Investigating the Surface of Titan with the Descent Imager/Spectral Radiometer onboard Huygens

Dissertation
zur Erlangung des Doktorgrades
der Mathematisch-Naturwissenschaftlichen Fakultäten
der Georg-August-Universität zu Göttingen

vorgelegt von
Stefanus Ewoud Schröder
aus Amsterdam / Die Niederlande

Göttingen 2007

Contents

Summary

On 14 January 2005 the Huygens spacecraft landed on the surface of Saturn's largest moon Titan. Its Descent Imager/Spectral Radiometer (DISR) was equipped with various up- and downward looking instruments to observe the atmosphere and surface during the descent. Titan's thick nitrogen atmosphere contains a few percent methane. Photodissociation of methane in the stratosphere leads to the formation of aerosols, which slowly fall to the surface. The result is a global haze that makes the atmosphere virtually opaque at visible wavelengths. Little is known about the surface; it is presumed to be composed of water ice and covered by organic material ('tholins'). It can only be observed in narrow wavelength intervals in the near-IR where methane absorption is low. DISR was optimized to these 'methane windows', and has given us the first close-up views of the surface. Its first results were described by Tomasko et al. (2005), and this thesis follows up on that paper. It presents an analysis of DISR observations of the surface in three chapters, concentrating on data from the downward looking visual and infrared spectrometers (DLVS and DLIS).

DISR countered the effects of atmospheric absorption by illuminating the surface just before landing. One chapter is devoted to the reconstruction of the reflectance in the 0.5-1.5 μm range from spectra that show evidence of lamp light. I find a significantly higher overall reflectance than other workers, and attribute this to a phase angle dependance. The spectrum has a red slope in the visible that is consistent with the presence of organic material, and a featureless blue slope in the near-IR that, so far, has defied interpretation. A single absorption line at 1.5 μm may be due to either water ice or tholins. From the depth of the methane bands I derive a mixing ratio of 4.5 ± 0.5% in the atmosphere close to the surface. Liquid methane appears to be absent from the surface. Another chapter puts the focus on two special observation cycles in which DISR acquired spectra as fast as possible in about one probe rotation. These spectrophotometric maps offer the highest possible spatial resolution, and are ideal for creating false color maps of the surface. By comparing the two maps, which were acquired at different altitudes, I eliminate the contribution of atmosphere to the observed intensity, and reconstruct the surface Bidirectional Reflectance Distribution Function (BRDF), which is similar to that found other dark solar system bodies, like Callisto and the Moon. Hapke (1981, 1984, 2002) models that fit the BRDF require both shadow hiding and coherent backscatter.

After landing, DISR observed changes in the amount of lamp light reflected off the surface for a few seconds. In the final chapter I attempt to reconstruct the sequence of events by simulating the lamp reflection spot. I find that the most likely cause for the variability is continued probe movement and/or rotation, and that the probe impact did not develop a cloud of large (>0.1 mm) dust particles. The DISR spectrometers did not detect significant changes in the probe environment in the hour that followed.

1 Introduction

"*Saturno luna sua circunducitur diebus sexdecim horis quatuor.*" This is how Christiaan Huygens announced in March 1656 his discovery of a moon orbiting Saturn, first seen a year before, on March 25, 1655. To him, Titan appeared as no more than a speck of light, and his first drawing of this new world was simply a cross (Fig. 1.1). Mankind had to wait for more than three hundred years before it obtained more detailed images of Titan. A major contribution to our knowledge of this enigmatic world would come from the small European spacecraft Huygens, which landed on Titan in 2005. This thesis describes my investigation of the surface of Titan using observations made by the Huygens camera.

Titan is Saturn's largest moon. It is one of the largest moons in the solar system, second only to Ganymede, and larger even than the planet Mercury (although not as massive). It is unique in that it has a thick atmosphere, which is remarkably Earth-like; not only is it primarily composed of nitrogen, but the surface pressure is one and a half bar. Nevertheless, with a surface temperature of 94 K we would not be comfortably walking on Titan. The other dominant constituent of the atmosphere is methane, present in substantial quantities (a few percent). Methane is continuously destroyed by Sunlight in the upper atmosphere, so it must be replenished from a source still unknown. This process of photodissociation creates methane radicals that react with each other and other molecules to form complex organic molecules, collectively known under the name of tholins (a word coined by the late Carl Sagan). In other words, the atmosphere is a natural laboratory for
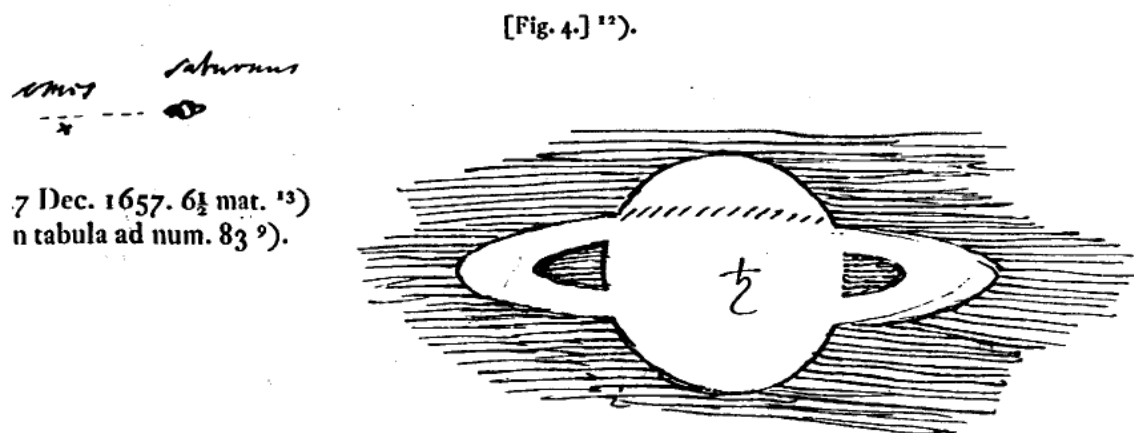

Figure 1.1: The first image of Titan (at far left), drawn by Christiaan Huygens on the night of 27 December, 1657 (source: *Recueil des observations astronomiques de Christiaan Huygens 1657-1694*, p. 57, `http://gallica.bnf.fr/`.).

organic chemistry. These organic reaction products coalesce into aerosols, which slowly descend to the surface under the influence of gravity, creating a global haze which appears pale yellow to the human eye. Because the haze almost completely obscures Titan's surface at visible wavelengths virtually nothing was known about it before the space age.

Only four spacecraft have seen the Saturnian system up close. The first was Pioneer 11 of NASA/Ames, which flew by Saturn in September 1979. Pioneer 11 was meant to serve as a pathfinder for the NASA/JPL Voyager mission. Its "camera" was a simple photometer, and images were built up line-by-line by scanning the photometer of the spinning spacecraft across the object. Titan appeared to Pioneer 11 as a tiny yellow disk (Fig. 1.2). A potential Pluto encounter was sacrificed to enable a close fly-by of Titan by Voyager 1 in November 1980. Somewhat disappointingly, its camera merely obtained close-ups of Titan's featureless yellow haze. Only a decade later it was realized that there are 'windows' in the spectrum of Titan, where absorption by haze and methane are low, through which the surface can in fact be seen. Nevertheless, Voyager 1 made many important discoveries, such as a north polar hood and detached haze layers. Its infrared spectrometer confirmed the presence of numerous species of organic molecules in the atmosphere. The Voyager 2 fly-by of Titan in August 1981 was much more distant than that of Voyager 1, and added little to our knowledge. The Voyager observations were extremely important for preparing the next mission to Titan thirteen years later. The NASA/JPL Cassini spacecraft with the ESA Huygens spacecraft attached to its side entered into orbit around Saturn in July 2004. Half a year later, on 14 January 2005, Huygens successfully descended through the atmosphere to gently land on the surface of Titan. The DISR camera gave us the first close-up view of the surface of this strange world. The landing site proved to be eerily earth-like, with abundant evidence for fluvial activity in the form of channels, a coast line, and a dry lake bed.

The DISR camera was a versatile, ingeniously constructed instrument, which contained a variety of sub-instruments looking up, down, and sideward at various wavelengths. It was built by Principal Investigator Martin G. Tomasko and his team at the *Lunar and Planetary Laboratory* (LPL) in Tucson (AZ), USA, with contributions from Co-Investigators from France and Germany. DISR's focal plane was developed under leadership of Co-I Horst Uwe Keller of our *Max-Planck-Institute für Sonnensystemforschung* (MPS, formerly MPAe). With Herr Keller as my principal supervisor I have been a member of the DISR team for the last three years, which, among others, has offered me the exhilarating experience to be one of the first to see images from the surface of a new world. This thesis describes my study of the surface of Titan, which concentrates on analysis of data from the DISR downward-looking spectrometers. One chapter is devoted to my reconstruction of the reflectance spectrum of the surface at the landing site, which can provide important clues on the composition of the soil. Another analyzes how the surface reflects Sunlight under different angles. The last chapter of this thesis investigates the changes over time observed by various DISR sub-instruments after landing. But first, in the next section, I give an overview of the current state of knowledge of Titan's surface. In the remaining sections I briefly describe the Huygens mission and the DISR instrument, and provide a summary of the first results of all instruments as they were reported in the *Nature* journal. As I felt that this thesis would not be complete without introducing the reader to the discoverer of Titan, after whom the mission was named, a short biography of Christiaan Huygens forms the last section of this chapter.
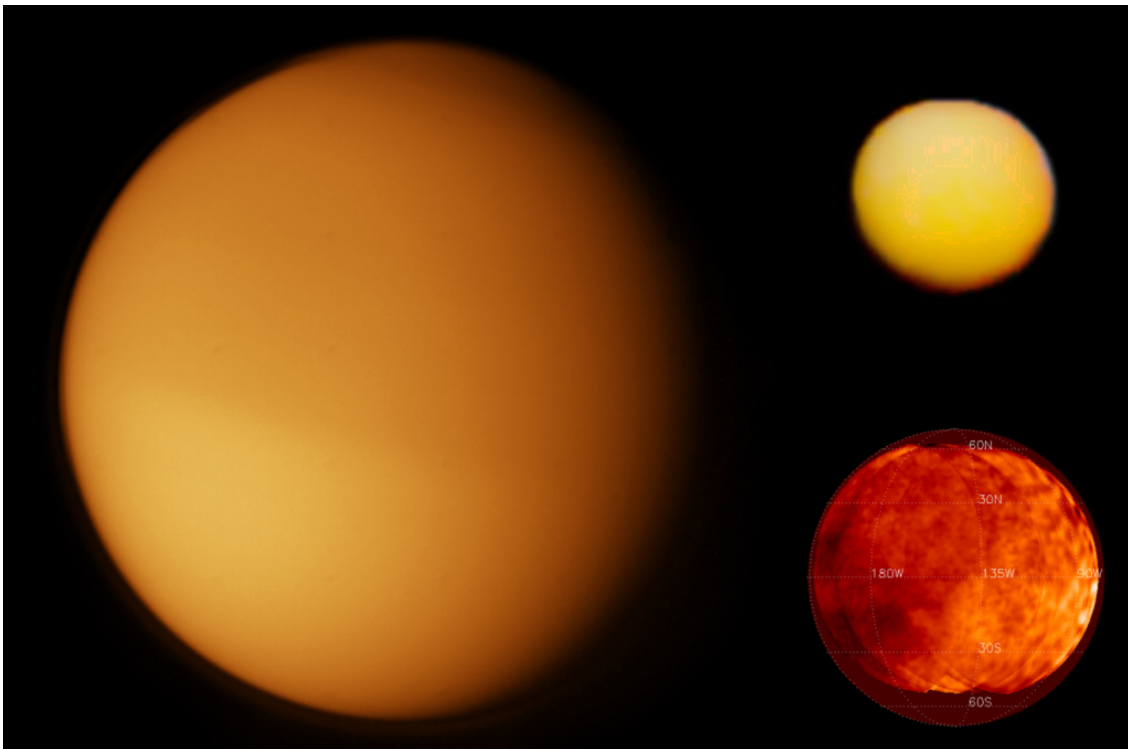
Figure 1.2: Pre-Cassini-Huygens spacecraft images of Titan. **Left**: Voyager 1 image (November 1980). Note the north-south brightness asymmetry and the north-polar hood (copyright Calvin J. Hamilton, `http://www.solarviews.com/`, data NASA/JPL). **Top right**: Pioneer 11 image (September 1979) (image processing by Ted Stryk, data NASA/Ames). **Bottom right**: Recently, Richardson et al. (2004) uncovered surface features from the Voyager 1 orange filter images.

1.1   A new view of Titan

Titan is large enough to have differentiated early in its history, and we expect its surface to be made up of water ice, just like that of the similarly sized galilean satellites. A major difference with Ganymede and Callisto is that Titan' surface is not exposed to deep space. Kuiper (1944) discovered Titan has an atmosphere by detecting absorption lines of methane. The atmosphere is substantial (surface pressure 1.5 bar), and primarily composed of nitrogen (N_2, ~98%) and methane (CH_4, ~2%). Photodissociation of methane in the upper atmosphere leads to the formation of global haze layer, which gives the moon its yellow color. Methane is key to the existence of the thick atmosphere. Without warming provided by the haze in the stratosphere and the opacity in the infrared (particularly by CH_4-N_2 and N_2-N_2 collisions in the troposphere), the atmospheric pressure would only be a few tens of millibar (Atreya et al. 2006). Photodissociation would destroy all present methane within ten to a hundred million years (Yung et al. 1984). So, unless we are witnessing a unique event in Titan's history, this requires the presence of a stable methane reservoir. Since methane and ethane (a major photochemical product) are liquid at the 94 K surface temperature, the existence of a deep, global ocean seemed long reasonable (Sagan and Dermott 1982, Lunine et al. 1983). Because the haze is vir-

Figure 1.3: Methane windows explained. Shown is the albedo of Titan from Karkoschka (1998) in black, and the solar flux at the t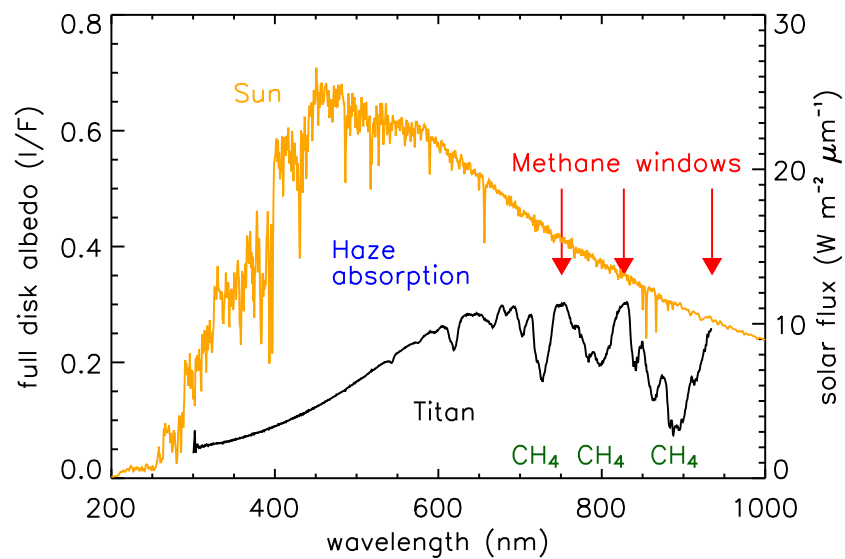op of Titan's atmosphere in orange. At visible and near-IR wavelengths we observe primarily reflected Sunlight. Even though the irradiance is high between 300 and 600 nm, the atmospheric haze absorbs and scatters mainly at these wavelengths, and so creates Titan's yellow appearance. At higher wavelengths the albedo is dented by methane absorption bands. In the near-IR methane windows both haze and methane absorption are low, and the surface can be observed from outside the atmosphere. Indicated are the 751, 829, and 935 nm windows; there are several more beyond 1 μm (e.g. at 1.07, 1.28, 1.6 μm).

tually opaque at visible wavelengths, spacecraft flybys at the time had not revealed the surface. A decade later Muhleman et al. (1990) disproved a global ocean by obtaining significant radar echoes from the surface, which are inconsistent with a deep ethane ocean. Around the same time it was realized that Titan surface can in fact be observed in so-called methane windows, narrow wavelength intervals in the near-IR wavelength range in which haze and methane absorption are low (Griffith and Owen 1990, Grundy et al. 1991). The principle of methane windows is illustrated in Fig. 1.3. Subsequent observations finally revealed the surface, and exposed a dichotomy between Titan's leading and trailing hemisphere (Griffith 1993, Smith et al. 1996, Gendron et al. 2004). The leading hemisphere features a bright region, dubbed Xanadu, and dark terrain is mainly concentrated around the equator on the trailing hemisphere. Initially it was thought that Xanadu exposes water ice (Griffith et al. 2003), and that the dark equatorial regions are bodies of liquid hydrocarbons (Campbell et al. 2003). This picture was about to change with the arrival of Cassini/Huygens in the Saturnian system.

With Huygens attached to its side, Cassini was launched on 15 October 1997 from the Cape Canaveral launch pad in Florida, USA. After a seven year journey the spacecraft entered into orbit around Saturn on 1 July 2004. Most of the orbits feature a Titan flyby, as Titan is the only satellite massive enough to allow for a significant adjustment of Cassini's flight path. The Cassini mission has so far been extremely successful, and its observations have challenged many preconceived notions about Titan. The Imaging Science Subsystem
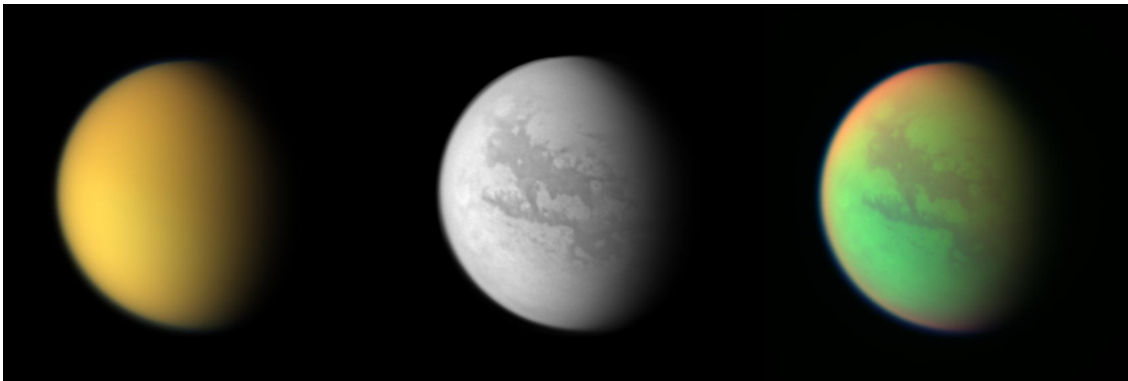
Figure 1.4: Cassini images of Titan. **Left**: Approximately true color view. **Middle**: The surface observed in the 938 nm methane window. **Right**: A false-color composite created by combining images taken at 420 nm (blue), 938 nm (green), and 889 nm (red). Green represents areas where Cassini is able to see down to the surface. Red represents areas high in Titan's stratosphere where atmospheric methane is absorbing sunlight. Blue along the moon's outer edge emphasizes the organic haze. (Image PIA06227, credit: NASA/JPL/Space Science Institute.)

(ISS) and Visual and Infrared Mapping Spectrometer (VIMS) are optimized for imaging the surface in the near-IR methane windows. The use of different filters allows to discern haze from methane absorption, or to image the surface directly (Fig. 1.4). With each Titan flyby adding a piece, ISS and VIMS are slowly building global maps of the moon (Porco et al. 2005, Barnes et al. 2007). The monochrome ISS map (Fig. 1.5) clearly shows the contrast between dark terrain distributed around the equator and bright Xanadu. All brightness contrast in the map is due to albedo differences; no shading is visible due to the diffuse illumination caused by atmospheric scattering. Note that the north pole region has not been imaged yet, because it was hidden in darkness at the beginning of the mission. Huygens landed at longitude 167.6° E (192.4° W in Fig. 1.5) and latitude 10.2° S (Karkoschka et al. 2007). The multi-wavelength VIMS map (Fig. 1.6) shows the same dichotomy. Conspicuous are the two 5 μm bright regions Tui Regio (130° W, 25° S) and Hotei Arcus (80° W, 20° S), which are thought to be fresh surface deposits, possibly of cryovolcanic origin (Barnes et al. 2005, 2006). Because the atmosphere is transparent at cm wavelengths, Cassini's Synthetic Aperture Radar (SAR) is ideal for studying the surface. Figure 1.7 shows some of its most significant discoveries: impact craters, equatorial dunes, cryovolcanism, and polar lakes.

Together, the ISS, VIMS, and SAR instruments start to paint a clearer picture of the surface of Titan and the dominant processes that shape it. It is still not clear what the surface is actually made of. As mentioned above, the crust is expected to consist of water ice, and observations in the methane windows have hinted at its presence (e.g. Griffith et al. 2003), but so far the evidence is inconclusive. The reflectance spectrum of the dark regions is consistent with the presence of water ice, but the spectrum of Xanadu, for example, is not (McCord et al. 2006). Moreover, recent General Circulation Model results are inconsistent with water ice dominating the surface (Tokano 2005). At least one prediction has been confirmed; radar observations point at the ubiquitous presence of organic material (Elachi et al. 2005). So far, all instruments have acquired evidence for widespread
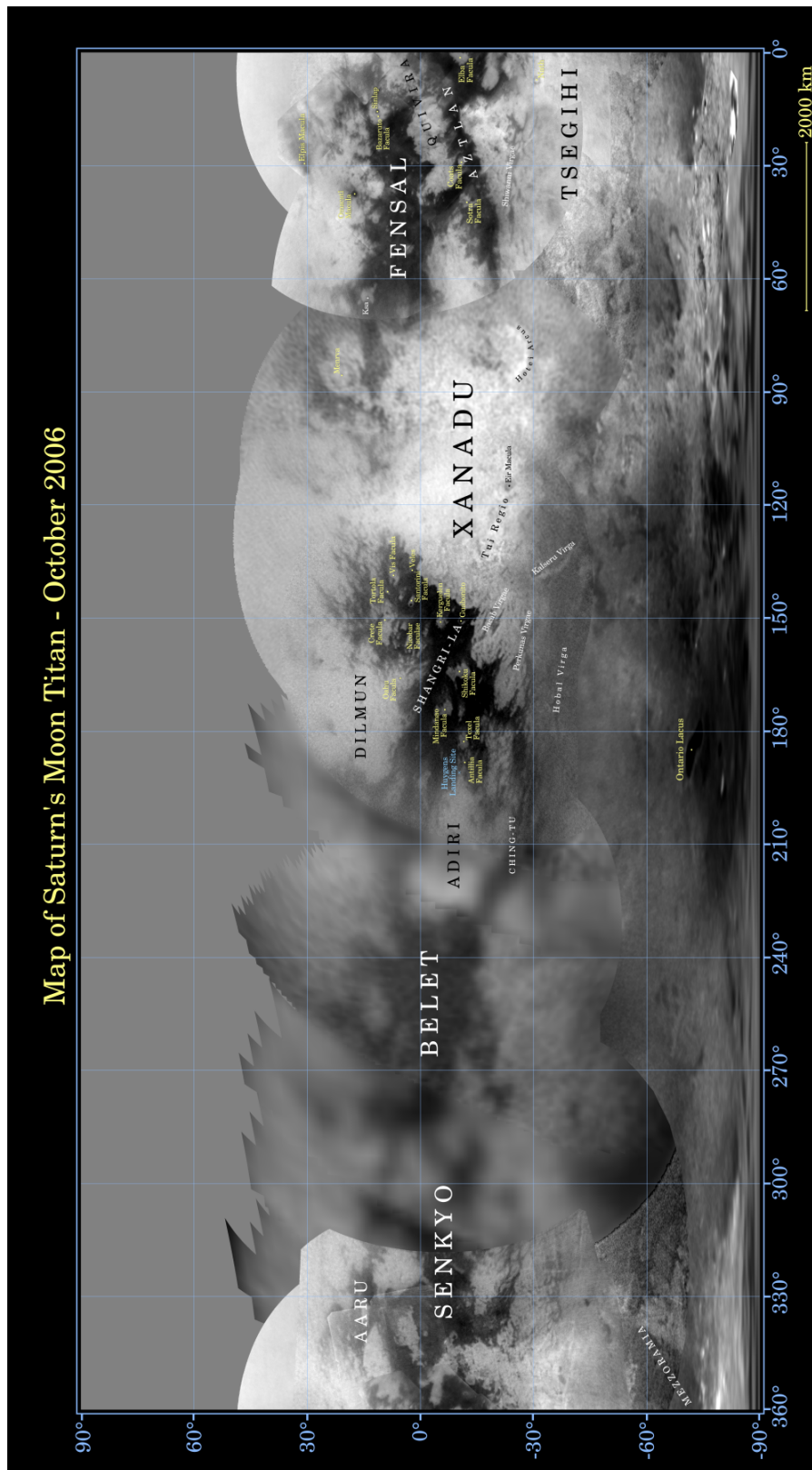
Figure 1.5: A recent map of Titan's surface compiled of Cassini ISS images in the 938 nm methane window, with feature names designated by the International Astronomical Union. The Huygens landing site is just below the center, indicated in blue. (Image PIA08346, credit: NASA/JPL/Space Science Institute.)
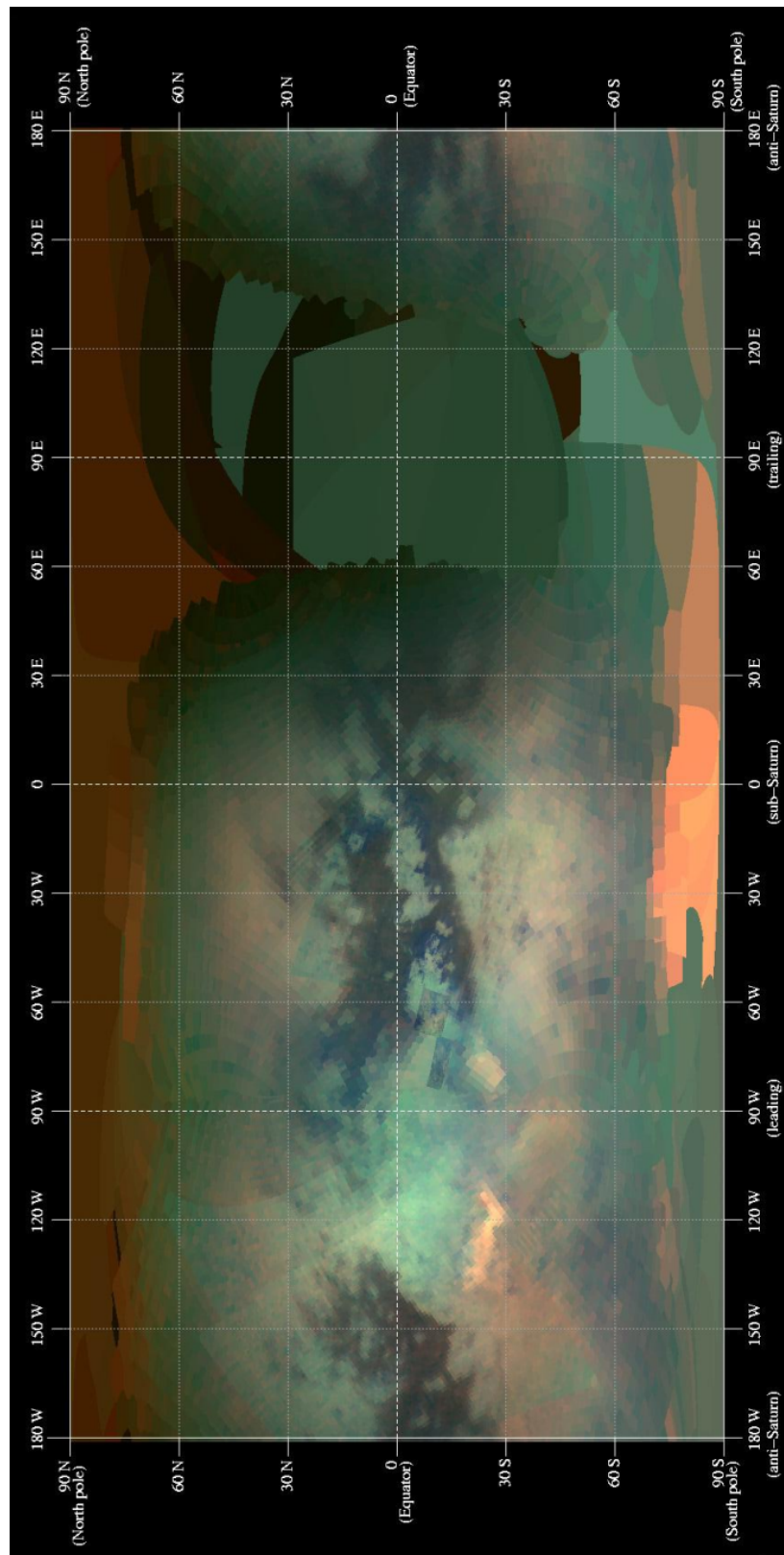
Figure 1.6: A map of Titan's surface compiled of Cassini VIMS images in the 1.6 μm (blue), 2.0 μm (green), and 5 μm (red) methane windows, acquired during flybys T9 and T10 (see Barnes et al. 2007). (Image PIA02147, credit: NASA/JPL/University of Arizona.)

13

fluvial activity and erosion on the surface, and a scarcity of impact craters. Many circular features in the ISS images are thought to be impact craters, but only with SAR can they be unequivocal identified because of its high effective spatial resolution (Fig. 1.7). The surface had been predicted to be densely cratered (Lorenz 1997), but so far only three impact craters have been confirmed (Stofan et al. 2006). The paucity of craters implies that the surface is geologically very young. Processes that lead to modification of surface morphology are erosion by fluids, cryovolcanism, and tectonic activity (deformation of the crust). All over Titan Cassini has found evidence for fluvial activity, in the form of channels, erosion patterns, and recently, lakes. Once thought to be thoroughly wet, Titan's oceans have proved elusive. Hence, a sense of relief pervaded the scientific community when standing bodies of liquid were finally found. First there was the tentative discovery of a lake near the south pole by ISS, then SAR revealed an abundance of lakes around the north pole (Stofan et al. 2007; Fig. 1.7). On the other hand, not all on Titan is wet. When SAR observed the dark equatorial regions, it found them covered by radar-dark linear features, nicknamed "cat scratches" (Fig. 1.7). Instead of hydrocarbon seas, the dark equatorial terrain turned out to be desert, covered by longitudinal dunes (Lorenz et al. 2006b). The dunes are created by the prevalent winds blowing from west to east (and sometimes in the opposite direction), and are probably composed of 100-300 μm sized particles of unknown origin. Even though at places dunes are only tens of kilometers apart from channels (Elachi et al. 2005), their presence implies the prevalence of dry conditions. The fact that the poles are wet and the equator is dry is probably related to the equator-to-pole 3-4 K temperature gradient (Courtin and Kim 2002, Tokano 2005).

The most likely candidates for surface liquids are methane and ethane. Ethane is the dominant photodissociation product of methane, and is expected to be present on the surface in large quantities. Methane may either rain down or be expelled from the interior by cryovolcanism. Over the past decade, potential rain-producing clouds have mainly been observed over the poles (Bouchez and Brown 2005, Schaller et al. 2006, Griffith et al. 2006) and concentrated around certain temperate latitudes (Griffith et al. 2005, Roe et al. 2005). The present dearth of clouds around the equator means that while rainstorms may be frequent at the poles, on the equator they are a rare event, consistent with the observed distribution of dunes and lakes. It is worth mentioning here that Tokano et al. (2006) predict a slow, persistent drizzle of methane reaching the surface over about half the globe (including equatorial regions). Even though this precipitation (~5 cm per year) is not expected to contribute significantly to erosion, it may be sufficient to keep the surface wet. But no evidence for this drizzle has been found so far, and it is difficult to reconcile with the existence of dunes. As mentioned above, an alternative source of methane is the interior of Titan. This implies the existence of low-temperature volcanism, or 'cryovolcanism'. Features seen with VIMS (Barnes et al. 2005, Sotin et al. 2005, Barnes et al. 2006) and SAR (Stofan et al. 2006, Lopes et al. 2007), e.g. the suspected dome *Ganesa Macula* (Fig. 1.7), are suggestive of cryovolcanism. Also the appearance of clouds at certain temperate latitudes have been associated with cryovolcanism (Roe et al. 2005). Cryovolcanism involves the emergence from the interior of water as a liquid or slush, and subsequent flow over the surface. To have water acting as lava at such low temperatures (90-94 K) requires an agent to lower its melting temperature. It is generally assumed that ammonia (NH_3) performs this function (Lunine and Stevenson 1987, Lopes et al. 2007), but even though the atmosphere protects ammonia on the surface
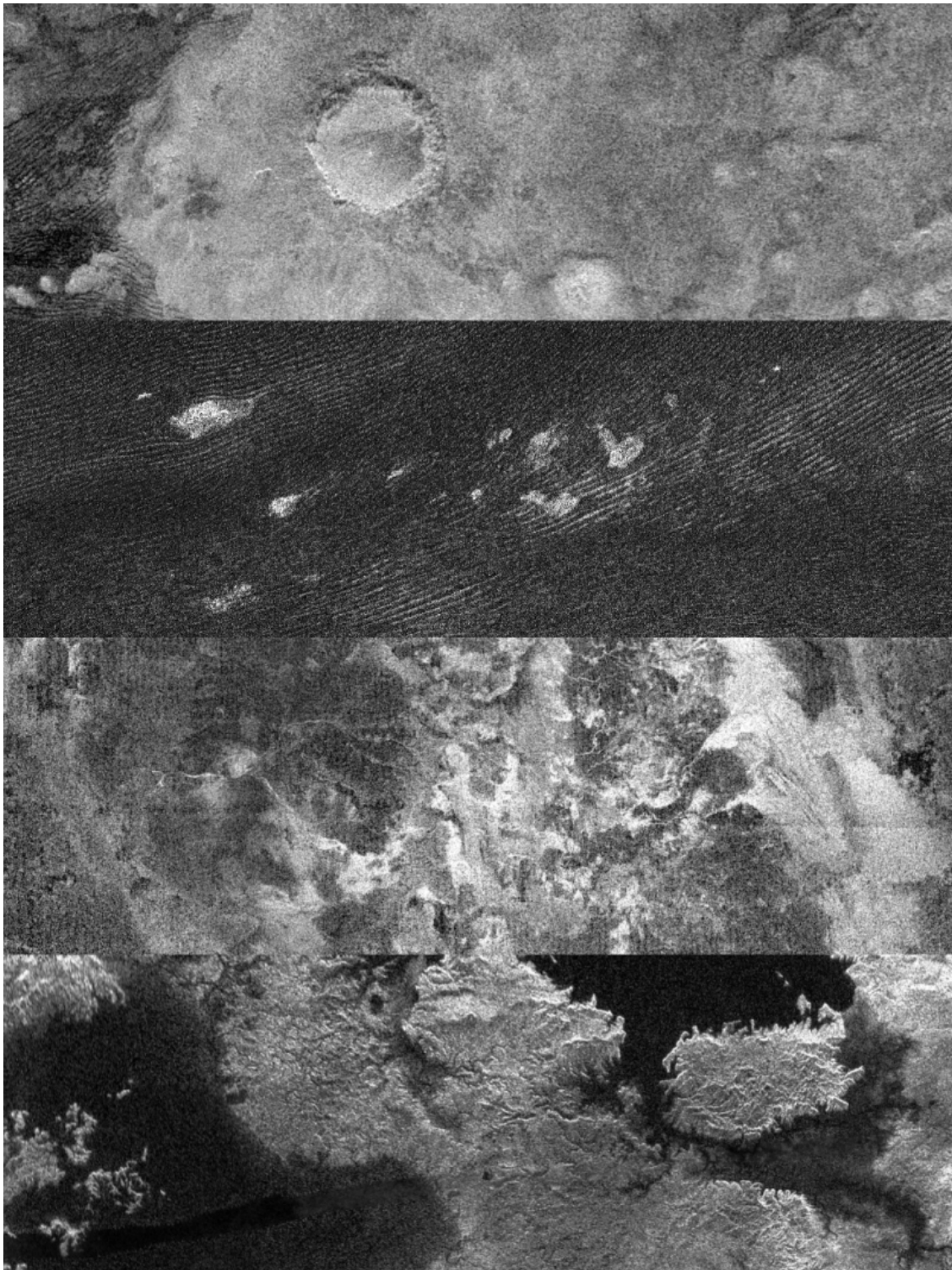
14

Figure 1.7: A collection of Cassini radar images. From **top** to **bottom** (Titan flyby in brackets): The impact crater *Sinlap* (T3), equatorial dune field (T8), the proposed cryovolcanic feature *Ganesa Macula* (Ta), north-polar lakes (T25). Images are not on the same scale. (Credit: NASA/JPL.)

from rapid destruction by energetic particles, its presence has yet to be demonstrated. While cryovolcanism may be a dominant process shaping the surface, tectonic activity does not seem to be widespread. Little evidence for it has been found so far (e.g. Stofan et al. 2006). Up to 1.5 km tall mountains may recently have been observed by VIMS (image PIA09032). As mountains on Titan are expected to be subdued (the strength of water ice is smaller than that of silicate rock), their existence would be evidence for recent tectonic activity.

The study of Titan's surface is ultimately aimed at elucidating the global methane cycle. Questions we strive to answer are: What is the source of the methane? What are the photochemical end-products, and where do they end up? (This is essentially the subject of this thesis.) And, why is there no global methane/ethane ocean? A recent theory provides an answer to the first and the last question. The ocean had been postulated on the assumption that photodissociation of methane has been going on for billions of years at the rate observed at present. One explanation for its absence is that the moon's icy regolith is able to absorb massive quantities of liquid (Kossacki and Lorenz 1996). Another is that Titan's thick atmosphere is a recent phenomenon. According Tobie et al. (2006) we are indeed witnessing a special moment in Titan's history. They propose the existence of a subsurface water-ammonia ocean sandwiched between a layer of water ice on top of a silicate core and a crust composed of methane clathrate (water ice with methane integrated in the crystal structure). There must have been three major episodes of methane outgassing. The first (~0.2-1 Gyr after formation) was sustained by core overturn, i.e. the internal differentiation of the core after its formation. The second (2-2.5 Gyr) resulted from the onset of core convection due to heating by radiogenic elements. The third (after 3.9 Gyr) continues to date, and was triggered by the growth of an ice layer (Ice I) below the clathrate crust. This layer quickly became unstable against thermal convection, and relatively hot (250 K) icy plumes, enhanced by tidal dissipation, welled up towards the clathrate crust, penetrating it and inducing clathrate dissociation. The predicted current rate of outgassing (i.e. cryovolcanism) is consistent with the observed methane atmospheric abundance. Note that an alternative origin for the methane is advocated by Atreya et al. (2006), who suggest it is synthesized in the interior ocean by a process called serpentinization.

At the time of writing we are one year away from the end of the Cassini mission. But an extension has been approved, and at least 21 Titan flybys are to follow (barring spacecraft failure). Every flyby will add a piece to the puzzle that is Titan, but it is certain that we will continue to be surprised.

1.2 Huygens, the mission

During Cassini's second orbit (Tb) around Saturn, a spring-loaded separation mechanism released Huygens on a collision course with Titan. A subsequent 'orbiter deflection manoeuvre' ensured that Cassini would miss Titan by 60.000 km. Huygens was aimed to land on the boundary of dark and bright terrain west of Xanadu. On 14 January 2005 it entered the atmosphere of Titan, protected by its heat shield from the heat of the fiery entry (Fig. 1.8). Two parachutes of different size were deployed in sequence to make the duration of the descent match the lifetime expectancy of the on board batteries. Spin vanes attached to its underside were to ensure a counter-clockwise rotation, so that DISR would
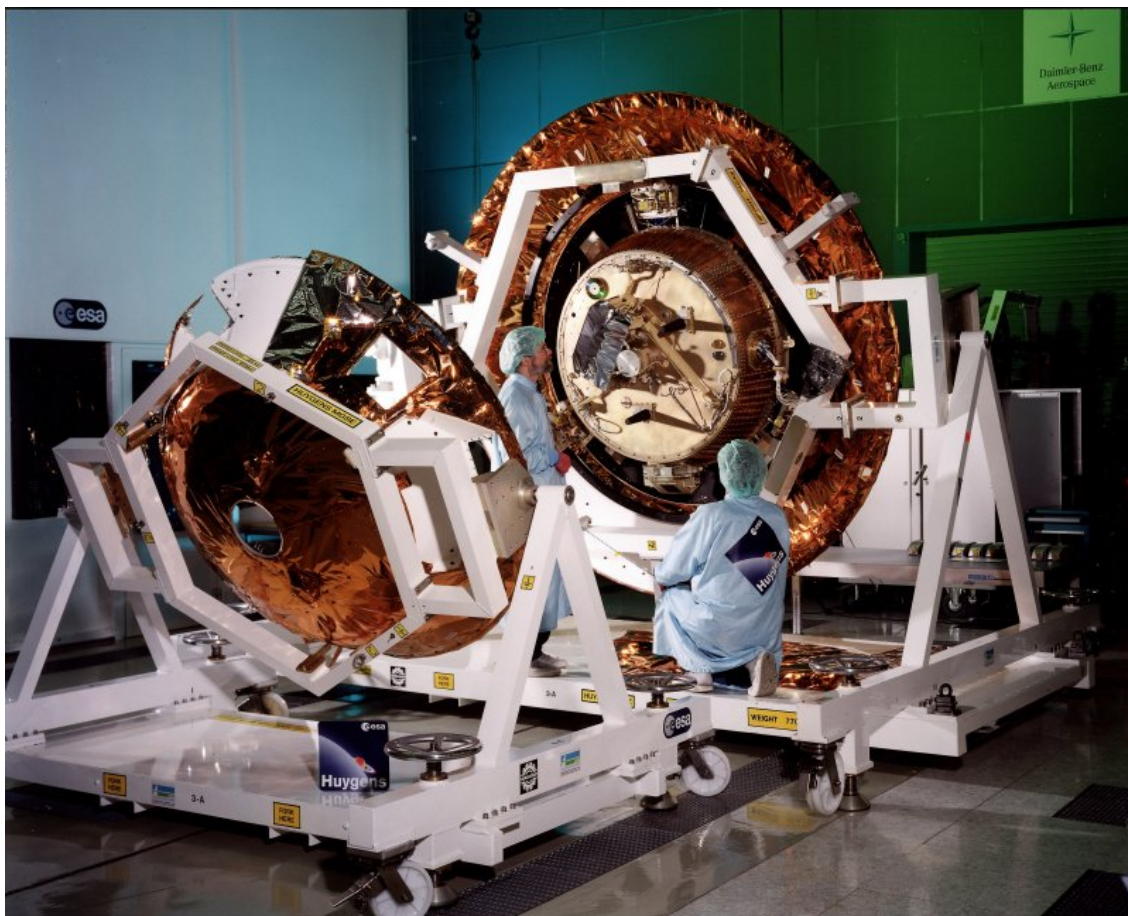
Figure 1.8: Mating the back shell to the Huygens descent module, which is already attached to the heat shield (ESA photo SEMQWJ2VQUD).

have the full 360° field of view of the surroundings. A Sun sensor would keep track of the position of the Sun in the sky to inform other DISR instruments when to acquire their exposures. The descent was not without surprises (see Lebreton et al. 2005, for a technical overview of the mission). A few weeks after the mission end DISR team member Bashar Rizk confirmed the suspicion that the probe had actually rotated clockwise (for reasons still unknown). Together with an unexpected low sensitivity of the Sun sensor, this made the probe unaware of its attitude for almost the entire mission. Fortunately, the altitude was derived through alternative means, and redundant radar altimeters enabled the probe to predict its impact time accurately. Huygens not only survived the landing, but continued to take measurements and transmit these to Cassini for more than an hour. After Cassini had set below the horizon as seen from Huygens, Earth-based telescopes continued to receive a signal for two more hours (Bird et al. 2005).

Huygens was primarily an atmospheric mission (it was referred to as a lander only after it had successfully landed), and was equipped with six instruments to study the atmosphere *in situ*. Even though beforehand the chances of Huygens surviving the impact of landing were thought to be slim, one instrument was devoted to studying the surface. The instruments are

- Descent Imager/Spectral Radiometer (DISR)

- Gas Chromatograph/Mass Spectrometer (GCMS)

- Aerosol Collector and Pyrolyzer (ACP)

- Huygens Atmospheric Structure Instrument (HASI)

- Surface Science Package (SSP)

- Doppler Wind Experiment (DWE)

The first results of these instruments were reported in a special issue of the *Nature* journal in a series of articles with the Principal Investigators as the lead authors, with an overview provided by Owen (2005). DISR was the mission's camera, and consequently had the highest data rate of all instruments. The next section of this chapter describes DISR and discusses the first findings reported by Tomasko et al. (2005). The GCMS determined the elemental composition of the atmosphere (Niemann et al. 2005). The gas chromatograph seems not to have operated as intended, but the mass spectrometer performed well, providing insights into the origin of the atmosphere. It detected no noble gases other than ^{36}Ar and ^{40}Ar. The former is primordial, but the latter originates only from the decay of ^{40}K, which has a half-life of 1.28 billion years. The amount of ^{40}Ar detected implies that it has been produced over the lifetime of the Solar System. This suggest that the atmosphere originates in the moon's interior, and was released, possibly episodic, by cryovolcanism. The low abundance of primordial noble gases suggests that the atmospheric N_2 is not primordial, but derives from photolysis of NH_3. The GCMS survived the impact of landing, and detected a range of organic molecules on the surface (C_2H_6, C_2N_2, C_6H_6). The ACP was essentially a small oven. The instrument would take a sample of Titan's atmosphere and lead it into the oven to pyrolyse the aerosols it hopefully contained. The contents of the oven would subsequently be flushed into the GCMS for analysis. While Israël et al. (2005) reported the detection of carbon and nitrogen-rich aerosols, Biemann (2006) has recently cast their results into doubt. In their reply, Israël et al. (2006) acknowledged the need for additional experiments with the spare instruments. HASI provided complete temperature and density profiles of the atmosphere from an altitude of 1400 km down to the surface (Fulchignoni et al. 2005), from which the probe's altitude throughout the mission could accurately be reconstructed. It measured the surface temperature to be 94 K, and found hints of lightning. Even though the primary goal of the SSP was the study of the surface, it carried accelerometers (as did HASI) providing data throughout the descent (Zarnecki et al. 2005). The instrument was designed to cope with a variety of surfaces (liquid, solid), and eventually found the surface at the landing site to be solid yet soft. Its penetrometer was the first part of Huygens to touch Titan, and its signal indicated that it had probably first touched a cobble. A sonar found the descent speed just before landing to be 4.6 m s^{-1}, a relatively gentle landing. The DWE experiment was nearly rendered a complete failure by the "Channel A anomaly" (a crucial command to switch on the Cassini receiver had not been transmitted), but Earth-based radio telescopes came to the rescue. Bird et al. (2005) reported on the detection of prograde zonal winds, confirming superrotation on Titan, and weak winds (<1 m s^{-1}) below 5 km altitude.

1.3   Descent Imager/Spectral Radiometer

DISR was Huygens' principal remote sensing instrument and had the highest data rate of all during the descent. It was developed and built by Principal Investigator Martin Tomasko and his team at the LPL in Tucson (AZ), USA, with several subsystems supplied by European Co-Investigators. DISR's main tasks were to determine the thermal balance of Titan's atmosphere by measuring the upward and downward radiative flux in the visible and near-IR, determining the properties of the haze aerosols and the atmospheric methane mixing ratio, and imaging the surface. For this, DISR was equipped with a wide range of sub-instruments: panoramic imaging cameras, solar aureole cameras, violet photometers, and visual and infrared spectrometers. This section provides a short overview of all DISR (sub-)instruments, a full description is given by Tomasko et al. (2002). The workings and calibration procedures of those instruments relevant to this thesis are described in more detail in Chapters 3 and 4.

The three DISR panoramic imaging cameras

- High Resolution Imager (HRI)

- Medium Resolution Imager (MRI)

- Side Looking Imager (SLI)

simultaneously imaged a narrow swath from 6° to 96° nadir angle with a width of 25° at the horizon. Rotation of the probe would ensure a full 360° azimuth coverage, allowing for the composition of complete panoramas of the surrounding landscape. Optical fibers led light from the camera windows towards a CCD developed by Co-I Horst Uwe Keller and his team at the MPS (then MPAe) in Lindau, Germany. The CCD flight model was built by the US company LORAL Fairchild. The cameras were sensitive over a wavelength range of about 660-1000 nm, the upper limit determined by the CCD, the lower limit chosen to avoid too much interference by the haze. Huygens transmitted data to Cassini through an omnidirectional antenna, which relatively low data rate forced DISR to compress its images (typically by a factor of 8-12 late in the descent). The Discrete Cosine Transform hardware compressed images by means of a JPEG-like scheme, and was built by the Technical University of Braunschweig in Germany.

The other instruments are classified according to whether they are looking up or down. Instruments looking upward are:

- Upward Looking Violet photometer (ULV)

- Upward Looking Visual Spectrometer (ULVS)

- Upward Looking Infrared Spectrometer (ULIS)

- Solar Aureole Cameras (SA)

- Sun Sensor (SS)

In this thesis I am mainly concerned with the downward looking instruments. They are the ULV, ULVS, and ULIS counterparts:
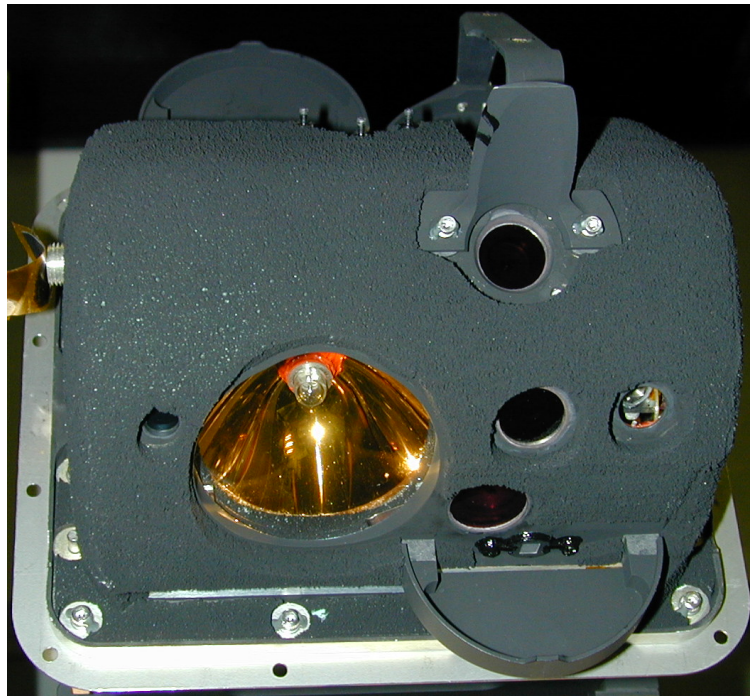
Figure 1.9: Photograph of the underside of the sensor head of the DISR#3 flight model. The camera was covered by a dark porous foam to absorb stray light. Clearly visible are the gold-coated SSL, the sunshade of the SLI, and the baffle of the DLV. Compare to Fig. 3.1 for identification of the instruments. Dimensions: 16.7×13.5 cm (width $\times$ height). (Credit: LPL.)

- Downward Looking Violet photometer (DLV)

- Downward Looking Visual Spectrometer (DLVS)

- Downward Looking Infrared Spectrometer (DLIS)

In addition, the DISR underside featured the Surface Science Lamp (SSL) to illuminate the surface just before landing. A photograph of the underside of the DISR flight model is shown in Fig. 1.9. The Violet photometers were silicon photodiodes, sensitive in the 350-480 nm wavelength range. As the intensity was expected to be very low due to the strong scattering and absorption of the aerosols in this wavelength range, the field of view of the Violet photometers was half the upper and lower hemisphere. To achieve this they were equipped with diffusing plates and baffles, nicknamed "bear's ear" baffles because of their appearance. The ULV shared a baffle with the ULVS, whereas the DLV had its own. The ULV/ULVS baffle included a shadow bar to permit separation of the direct and diffuse downward flux. Hence the field of view of the ULVS was the same as that of the ULV. The slit of the DLVS mapped into a 4° wide by 40° long region on the ground centered at 30° nadir angle. Its spatial resolution depended on the mode of operation, and either 1, 4, 8, or 16 spectra were returned per exposure. Light was led by optical fibers from the grating to a section of the CCD next to the MRI. The upward and downward looking infrared spectrometers were provided by Co-I Bruno Bézard of the *Observatoire de Paris* in Meudon, France. The field of view of the ULIS was restricted by a baffle

to half the hemisphere. Because of the long exposure times a shadow bar was deemed useless. Careful timing of the exposures was meant to separate the direct and diffuse downward flux by using the shade provided by the probe. The slit of the DLIS mapped into a 3° wide by 9° long region on the ground centered at 20° nadir angle. Generally, exposures were summed on board to increase the S/N, and only in special operational modes one spectrum was returned from a single exposure. Light was led by optical fibers from the grating to two linear arrays of InGaAs elements (one for each spectrometer). The four SA Cameras imaged a rectangular 6° × 50° area around the Sun at two different wavelengths and polarization angles to constrain aerosol properties, more specifically the number of monomers that are thought to be the aerosol building blocks. The SA images occupied a small section in the upper left corner of the CCD. The Sun Sensor (a silicon detector) would monitor the position of the Sun in the sky by means of a three-slit reticle and a shadow bar, and was to time the operation of all DISR sub-instruments.

A little less than a year after Huygens' successful descent, Tomasko et al. (2005) reported the first results of the DISR experiment in the *Nature* journal. I briefly summarize the paper here. The failure of the Sun Sensor to keep track of the Sun and the loss of half the images had severely complicated the data analysis. Nevertheless, the imaging team led by Bashar Rizk had been able to reconstruct the probe trajectory, and to compile several mosaics of the landing site at different resolutions[1]. The variety of surface features seen in the images exceeded all expectations (Figs. 1.10 and 1.11). The landscape witnessed by Huygens is dominated by a rugged, relatively bright landmass incised by rivers and creeks terminating in a dark lakebed along a well defined coast line. Note that the brightness and contrast in Figs. 1.10 and 1.11 have been enhanced. In reality, the surface is almost as dark as asphalt and the contrast between the brightest and darkest features is only 10%. The lakebed is covered by bright islands, with dark channels in between. Huygens landed in the lake, 3.5 km south of the coastline, on a plain littered with pebbles and cobbles, some of which are rounded. Close-ups of the soil reveal it to consist of grains. At all scales the imagers found evidence for fluvial activity, but neither the rivers nor the lake appear to contain liquid at present. Stereographic rendering of a section of land shows it to be extremely rugged. The slopes in the bright terrain incised by rivers are of the order of 30°. It is not clear what feeds the rivers. Those west of the straight channel are stubby and appear spring-fed, whereas the dendritic network east of the channel is suggestive of precipitation. The second half of the paper deals with the results from the photometers, spectrometers, and SA cameras. A preliminary reconstruction of the surface reflectance reveals a red slope in the visible (indicative of organic material) and an enigmatic featureless blue slope in the near-IR. Apart from methane bands only a single absorption feature (at 1.5 μm) can be identified with certainty, which may be associated with either water ice or tholins. The blue slope defies explanation, and is not matched by any combination of laboratory spectra of ices and organics. The overall ground reflectivity is low (peaking around 0.18 at 830 nm), and the atmospheric methane abundance is 5% near the surface. The paper further reports the first result of an ongoing effort to model the atmosphere.

---

[1]Having been assembled shortly after the descent, these mosaics incorporated an early generation of processed images which showed many compression artifacts. Shortly after publication of the paper DISR team member Erich Karkoschka perfected the calibration of the images, and created a grand seamless mosaic of the landing site using an improved trajectory reconstruction (Karkoschka et al. 2007). Figure 1.10 shows almost the entire mosaic, Fig. 1.11 zooms in on the center.

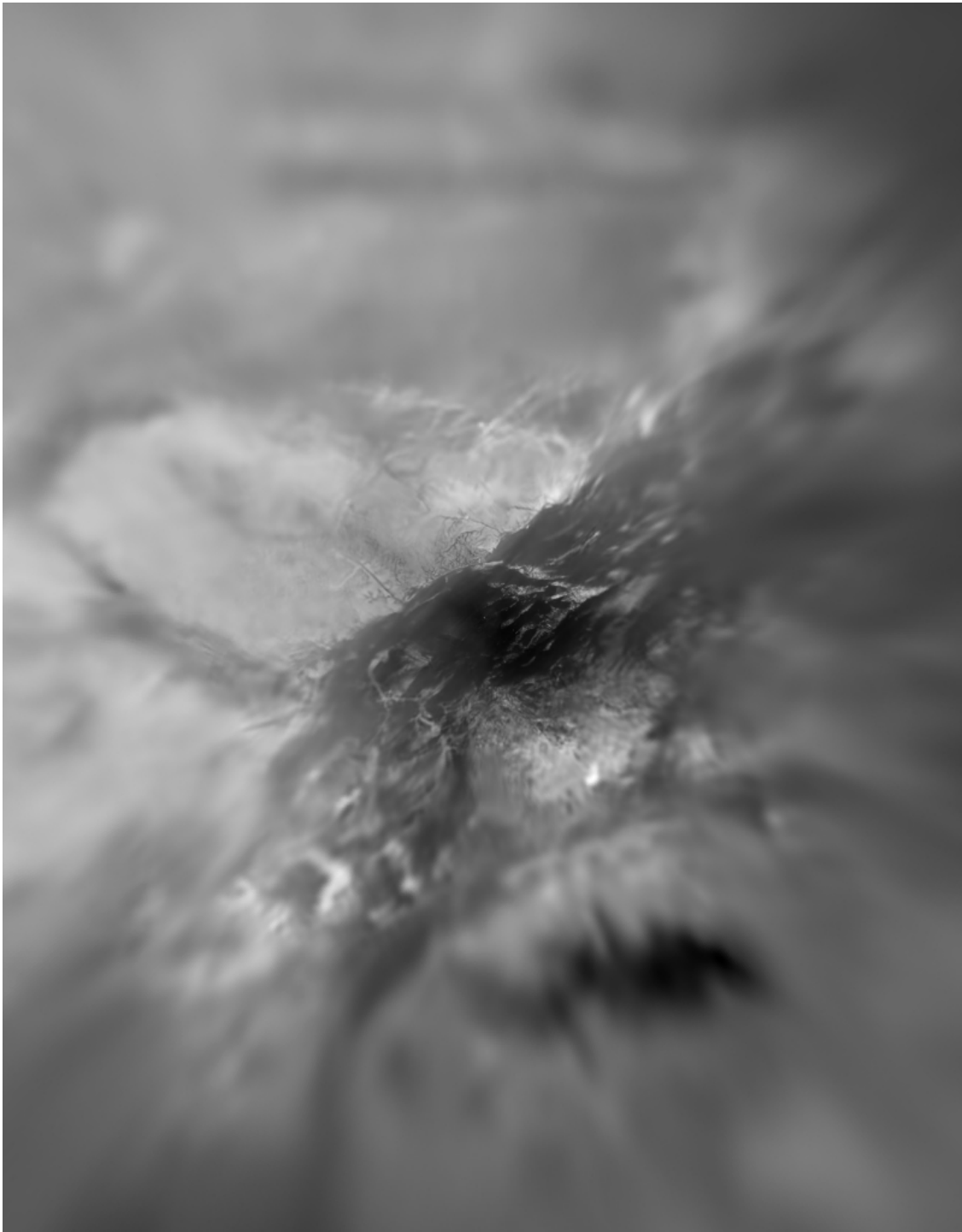Figure 1.10: A panorama of the Huygens landing site (62.5 × 80.0 km), reconstructed from DISR images (Karkoschka et al. 2007). North is at the top, east at the right. Huygens entered the scene approximately halfway the mosaic from the left, and landed exactly in the middle. Note the two "cat scratches" (dunes) at the top.
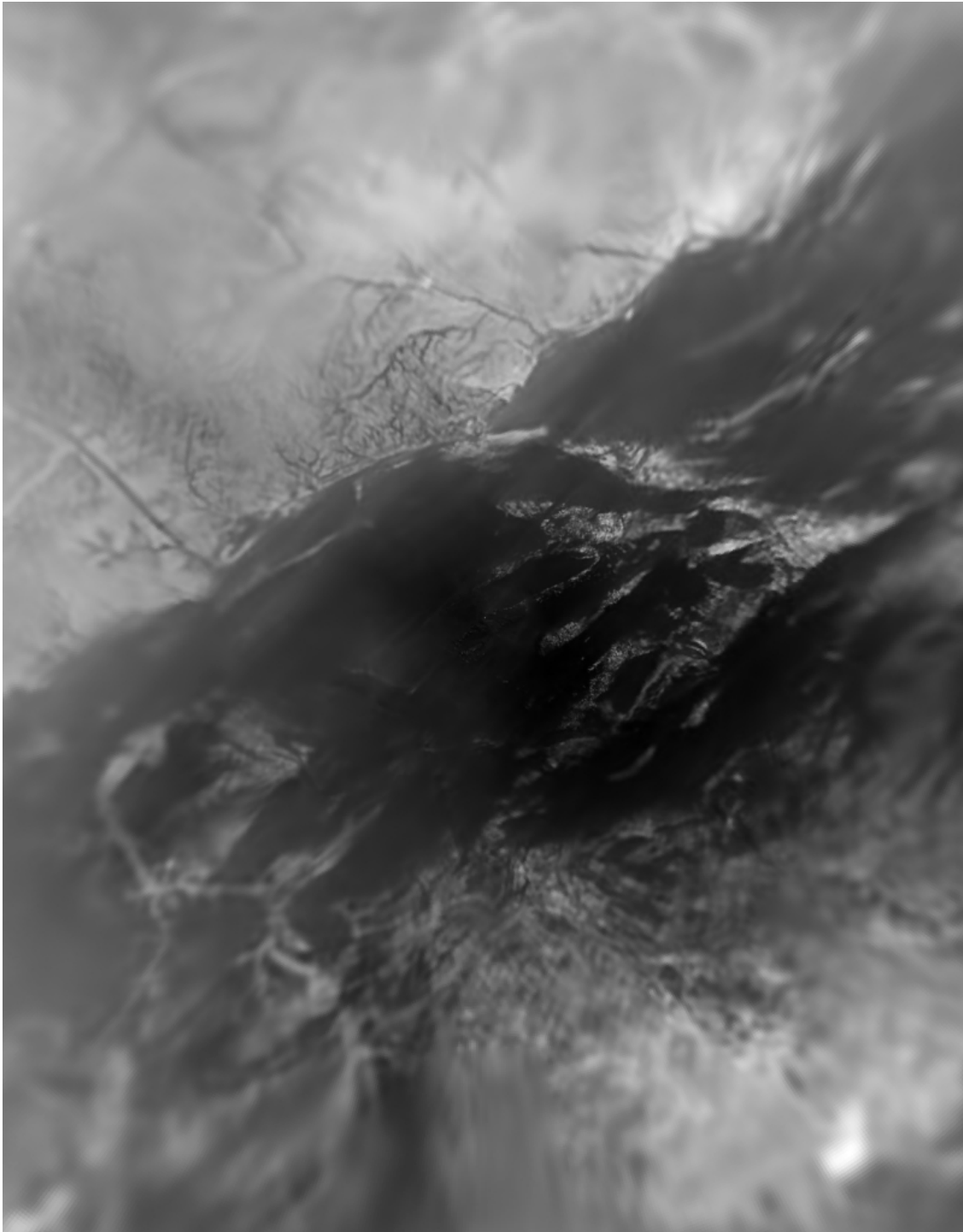
Figure 1.11: A zoom of the panorama in Fig. 1.10 (18.75 × 24.00 km). Huygens landed exactly in the middle.

The haze optical depth was determined as a function of altitude. The haze extends all the way to the surface, and a discrete haze layer was found around 21 km altitude. The degree of polarization of light scattered by the haze aerosols indicates they are composed of a large number (hundreds) of 0.05 μm small monomers. Note that these results are preliminary; the team is presently preparing a publication on an updated version of the atmosphere model (Tomasko et al., in preparation).

My own contribution to the *Nature* paper dealt with DLVS observations. Using spectra that were recorded closely in time with images within a panoramic cycle, I was able to accurately position their footprints on the surface mosaic, and to colorize the latter with either true or false colors. The true color of the surface (i.e. as seen by the human eye) proved to be orange, primarily as a consequence of the illumination by the orange sky. Furthermore, the DLVS perceived the land to be slightly redder than the lake, with redness expressed as the ratio of the intensity in the 827 nm and 751 nm methane windows. The work described in this thesis expands on the *Nature* paper. I improve the reconstruction of the surface reflectance spectrum in Chapter 5, and revisit the topic of surface color in Chapter 6 (Sec. 6.4).

1.4   Huygens, the scientist

The greatest Dutch physicist of all time, Christiaan Huygens' contributions to science are enormous. He was one of the pioneers of the *Scientific Revolution* in the 17th century, from which modern science was born. At first he was mostly dedicated to mathematics (he was one of the founders of probability theory), and later he also ventured into astronomy. He built the best telescopes of his time, devising a new and better way of grinding and polishing lenses, and was an avid observer. He was also mentor of Antoni van Leeuwenhoek, pioneer of the microscope. Most fundamental was his discovery that light can be described as a wave phenomenon, which put him at odds with Isaac Newton. His discoveries in the field of astronomy are numerous: he described the first feature on Mars (*Syrtis Major*) and estimated its size, he proposed that Venus was covered by clouds, he discovered the Orion nebula, the true nature of Saturn's "appendices", and most importantly in light of this thesis, Saturn's largest moon Titan.

Christiaan Huygens is born on 14 April 1629, in the middle of the Dutch Golden Age, in The Hague as a son of Constantijn Huygens and Suzanna van Baerle. The marriage is a good one and the pair have five children. When Christiaan is only eight years old his mother dies shortly after giving birth to his sister Suzanna. The Huygens family is a dynasty of influential civil servants in the service of the Princes of Orange, predecessors of the current Dutch royal family. Father Constantijn is a civil servant too and a well-known poet, who teaches Christiaan and his older brother Constantijn music and elementary mathematics at home. Counting René Descartes, Rembrandt van Rijn, and playwright Pieter Corneliszoon Hooft among his friends, he creates a stimulating atmosphere at home for young Christiaan, favorable to the arts and sciences. It is said that Christiaan conversed happily with his brothers in Latin and started composing at the age of nine.

As father Constantijn envisions a similar career for his children, Christiaan and his brother Constantijn embark upon the studies of Law and Arts at the University of Leiden in 1645. Christiaan receives training in mathematics and physics from Frans van

Figure 1.12: *Portrait of Constantijn Huygens (1596-1687) and his five children* by Adriaen Hanneman (1640), with Christiaan Huygens at top left. (Collection Mauritshuis, The Hague, `http://www.mauritshuis.nl/`.)

Schooten, whose teachings are heavily influenced by his friend Descartes. After two years their father pulls them out of Leiden and has them continue their studies in Breda, at the *Illustere School*, then recently established by stadtholder and Prince of Orange Willem II. When Prince Willem dies in 1650, the Republic of the Seven United Netherlands is promptly proclaimed. The influence of the royalist Huygens family wanes, and after completing his studies 21 year old Christiaan fails to find a good position. This is a blessing in disguise as he can now devote himself to full-time research, supported by the family fortune. What follows is the most productive time in his career, in which Huygens makes some of his most remarkable discoveries. One of these is the discovery of Saturn's moon Titan on 25 March 1655, which he announces in the pamphlet *De Saturni Luna* a year later (Fig. 1.13). Because he is not yet completely sure about his discovery, he establishes his priority in the form of an anagram (a common practice in those days), inspired by an Ovidius verse:

Admovere oculis distantia sidera nostris uuuuuuu cccrrhnbqx

which solution is the first line of this thesis. Huygens simply refers to the moon as 'the moon of Saturn' or 'my moon'; only two centuries later was Titan given its name by

CHRISTIANI HVGENII DE SATURNI LVNÂ OBSERVATIO NOVA.

HAG. COM. ADRIANUS VLACQ. 1656. IN 4°.

Figure 1.13: The title page of Huygens' pamphlet announcing the discovery of Titan, included by publisher Adriaan Vlacq as a supplement to *De Vero Telescopii Inventore* by Pierre Borel (source: *Recueil des observations astronomiques de Christiaan Huygens 1657-1694*, p. 165, `http://gallica.bnf.fr/`.). No copies exist of the original pamphlet that was published by Vlacq on 5 March 1656.

Herschel (1847). Later that year Huygens provides the correct explanation for the "appendices" of Saturn that had puzzled observers since Galileo. From his observations, recorded in *Systema Saturnium* (1659), he deduces that a ring surrounds the planet, but is not physically connected to it.

In those years (1655-1664) Huygens undertakes several travels to Paris and London, sometimes accompanied by his brother Constantijn, meeting distinguished astronomers and mathematicians (Blaise Pascal, Robert Hooke, Robert Boyle amongst others). Then in 1666 the French king Louis XIV invites him to Paris to establish the *Académie Royale des Sciences*, an honorable task that comes with a substantial salary. Huygens accepts and becomes on of the principal actors in French scientific circles. In Paris he meets Giovanni Cassini (later Jean-Dominique), who has likewise been invited by the king to become director of the newly established Paris Observatory. They jointly observe Saturn at the Paris Observatory in 1671, on which occasion Cassini discovers another moon of Saturn, Iapetus. He works hard and fruitful, but his health suffers setbacks. He becomes gravely ill in 1669 and returns to his family in The Hague, to return to Paris only after a year. Then in 1672 Louis XIV declares war against the Dutch Republic, which puts Huygens in the peculiar situation that his employer wages war against his home country. Chaos ensues in the republic in what is known to the Dutch as the *rampjaar* (disaster year), as at the same time it has to fight off English and German invaders. A popular uprising ends the republic and puts Prince of Orange Willem III, son of Willem II, into power as stadtholder. This restores the influence of the royalist Huygens family. But even though Willem III is no friend of Louis XIV, this has no direct consequences for Huygens' position. However, the mood in France gradually turns against foreigners, and when illness forces Huygens once more to retreat to The Hague in 1681, he decides better not to return.

Living in the Netherlands once more Huygens continues his work as an internationally respected scientist. He finally publishes his wave theory of light as *Traité de la lumière* (1690). In 1689 he visits London for the last time, where he meets Isaac Newton at the Royal Society. He has great admiration for Newton, but at the same time does not believe his theory of universal gravitation, which he says *"appears to me absurd"*. In 1695 Huygens becomes ill and dies on 8 July at an age of 66 years. He is laid to rest in a shared grave with his father in the *Grote Kerk* church in The Hague. He had never married, which was not unusual for a 17th century scientist. After his death *Cosmotheoros* (1698) was published, which speculates on the existence of extraterrestrial life.

2 Theory

Before reporting the results of my analysis of DISR data in the next three chapters, I first give an overview of the nomenclature I use throughout this thesis to describe physical quantities relating to radiation and its interaction with matter. Furthermore, in Chapter 6 I use the Hapke reflectance theory for particulate soils to study the properties of the surface at the Huygens landing site. Rather than interrupting the flow of that chapter, I prefer to describe the theory here, in Sec. 2.2. In that same chapter I employ a special type of phase function to prescribe the scattering behavior of aerosols, the so-called double Henyey-Greenstein function. I describe this function briefly in Sec. 2.3.

2.1 Nomenclature

The SI unit of **radiance** is [W m^{-2} sr^{-1}]. In my work I am often more interested in the radiance per infinitesimal wavelength interval. I call this quantity the **intensity** (unit [W m^{-2} μm^{-1} sr^{-1}]), for which I use the symbol I. The SI unit of **irradiance** is [W m^{-2}]. I simply call the irradiance per infinitesimal wavelength interval the **flux** (unit [W m^{-2} μm^{-1}]), for which I use the symbol F. For clarity I do not use the subscript λ to denote wavelength dependence, but the reader should keep in mind that all intensities and fluxes are wavelength specific.

Definitions for reflectance abound. Hapke (1981) provides an overview of reflectance nomenclature, and I will discuss here some I find most useful. Consider a collimated (parallel) beam irradiating a surface element da at an angle ι with the surface normal. We call the flux received by a plane perpendicular to the travel direction of the beam J. The surface element reflects a beam of radiation with intensity I in a solid angle $d\Omega$ at an angle ϵ with the surface normal. The **bidirectional reflectance** of the surface is then defined as

$$r(\iota, \epsilon, \phi) = \frac{I(\iota, \epsilon, \phi)}{J} \tag{2.1}$$

with ϕ the angle between the incident and reflected beam, or **phase angle**. The flux received by da is

$$F = \mu_0 J \tag{2.2}$$

where we have defined $\mu_0 = \cos \iota$. Likewise we define $\mu = \cos \epsilon$. The **hemispheric albedo** A_{H} is defined as the ratio of the specific power (in [W μm^{-1}]) reflected in all directions (in the upper hemisphere) by a surface element to that received from a collimated source in a specific direction:

$$A_{\mathrm{H}} = \int_{2\pi} \frac{I(\iota, \epsilon, \phi)}{\mu_0 J} \cos \epsilon \, d\Omega = \frac{2\pi}{\mu_0} \int_0^1 r(\mu_0, \mu, \phi) \mu \, d\mu. \tag{2.3}$$

Now consider the simple case of a Lambert surface. By definition, this surface looks equally bright from all angles (intensity is constant), and reflects all light incident on it (Lambert 1760). Thus

$$F = \int I \cos\theta d\Omega = I \int_{\varphi=0}^{2\pi} d\varphi \int_{\theta=0}^{\pi/2} \cos\theta \sin\theta d\theta = \pi I. \tag{2.4}$$

Let the bidirectional reflectance of a Lambert surface be called the Lambert reflectance r_L, then

$$r_L = \frac{\mu_0}{\pi} \tag{2.5}$$

and $A_H = 1$. We can now describe the reflectance properties of an arbitrary surface by means of the bidirectional **radiance coefficient** r_C, which is the bidirectional reflectance of the surface relative to that of an identically illuminated Lambert surface:

$$r_C(\iota, \epsilon, \phi) = \frac{r(\iota, \epsilon, \phi)}{r_L} = \frac{\pi}{\mu_0} r(\iota, \epsilon, \phi) \tag{2.6}$$

or in terms of the flux received by the surface

$$r_C(\iota, \epsilon, \phi) = \frac{\pi I(\iota, \epsilon, \phi)}{F}. \tag{2.7}$$

In the literature, "reflectance" is often given as "I over F". This reflectance really is the radiance coefficient calculated as $r_C = I/\mathcal{F}$, in terms of an alternative version of the flux which has units of intensity, defined by $F = \pi\mathcal{F}$. The hemispheric albedo of a surface in terms of the radiance coefficient is

$$A_H = 2 \int_0^1 r_C(\mu_0, \mu, \phi)\mu d\mu. \tag{2.8}$$

In atmosphere models that have a surface as lower boundary, the surface is often presumed to reflect radiation isotropic. Then a "surface albedo" A_{iso} is defined analogous to Eq. 2.4 by

$$A_{iso}F = \pi I. \tag{2.9}$$

It follows that the radiance coefficient for this surface is $r_C = A_H = A_{iso}$.

If the surface is that of a planet at heliocentric distance R_h with $F_\odot$ the solar flux at 1 AU, then

$$J = \frac{F_\odot}{R_h^2} \tag{2.10}$$

and

$$r_C(\mu_0, \mu, \phi) = \frac{\pi I(\mu_0, \mu, \phi)}{\mu_0 F_\odot / R_h^2}. \tag{2.11}$$
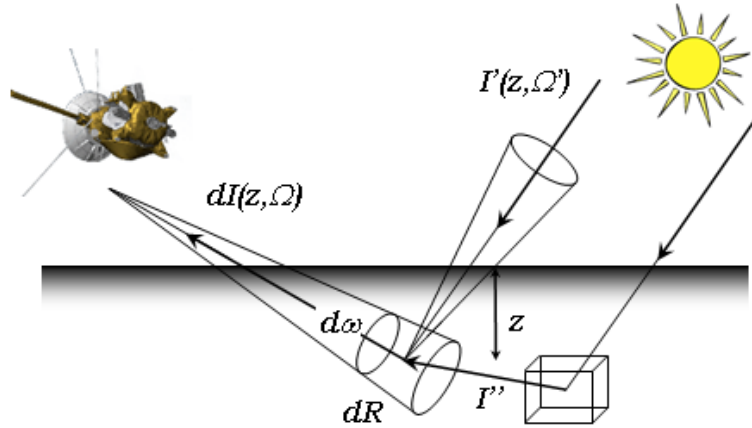
Figure 2.1: Cartoon illustrating the derivation of the Hapke reflectance model for a particulate surface. We consider the subsurface volume element $dV = R^2 d\omega dR$ located at a depth z and distance R from the detector (in this case Cassini). This element scatters light of intensity I' from the direct beam and scattered light of intensity I'' with efficiency G towards the detector. See text for details.

2.2 Hapke model

Bruce Hapke of the University of Pittsburgh has set up a theoretical framework to model scattering of light in a planetary regolith, or soil, in a series of articles on bidirectional reflectance spectroscopy (Hapke 1981, 1984, 1986, 2002). The full model, described in Hapke (2002), gives the radiance coefficient of a particulate surface as a function of the particle phase function and includes the Shadow Hiding Opposition Effect (SHOE) and the Coherent Backscatter Opposition Effect (CBOE).

Hapke (1981) develops his model as follows. We start off with the equation of radiative transfer for a dispersed particulate medium

$$\frac{dI(r,\Omega)}{ds} = -EI(r,\Omega) + \int_{4\pi} I(r,\Omega')G(\Omega',\Omega)d\Omega' \tag{2.12}$$

The first term in this equation is the extinction term, with E the **extinction coefficient**. As extinction includes all processes that remove photons from the light beam, it is the sum of absorption and scattering. The probability of any of these processes taking place upon interaction of a photon with a particle with cross section σ (in [m^2]) is given by the (dimensionless) efficiencies. With the **extinction efficiency** Q_E, the **absorption efficiency** Q_A, and the **scattering efficiency** Q_S, we thus have $Q_E = Q_A + Q_S$. For a medium composed of different type of particles the extinction coefficient E, **absorption coefficient** K, and the **scattering coefficient** S (all in [m^{-1}]) are given in terms of the efficiencies as

$$E = \sum_i n_i Q_{E,i} \sigma_i \tag{2.13}$$

$$K = \sum_i n_i Q_{A,i} \sigma_i$$

$$S = \sum_i n_i Q_{S,i} \sigma_i$$

where n_i is the number density of particles of type i (in $[\text{m}^{-3}]$). We can write these coefficients in terms of the average particle properties, e.g. the average extinction cross section $\langle \sigma_{\text{E}} \rangle = \langle Q_{\text{E},i} \sigma_i \rangle$:

$$E = n\langle \sigma_{\text{E}} \rangle, \tag{2.14}$$

with n the number of particles per unit volume. The second term in Eq. 2.12 represents photons scattered into the path. It includes the **differential volume scattering coefficient** G, which has dimensions $[\text{m}^{-1}\ \text{sr}^{-1}]$ and describes the probability that a photon coming from direction Ω' is scattered in direction Ω, or

$$G(\Omega', \Omega) = \frac{1}{4\pi} Q_{\text{S},i} \sigma_i p_i(\phi) \tag{2.15}$$

Consider a volume element $dV = R^2 d\omega dR$ located at distance R from the detector at a depth z below the surface, in the solid angle $d\omega$ in the line of sight (Fig. 2.1). From Eq. 2.12 we derive the equation of radiative transfer for the radiation $\bar{I}$ scattered in the direction of the detector. Since the detector is not in line with the direct beam the first term on the right hand side is zero, and

$$\frac{dI(z, \Omega)}{dR} = \int_{4\pi} [I'(z, \Omega') + I''(z, \Omega')] G(\Omega', \Omega) d\Omega' \tag{2.16}$$

where we have distinguished between the (collimated) incident light I' and diffuse light I''. The **single-scattering albedo** is $\varpi_i = Q_{\text{S},i}/Q_{\text{E},i}$ for particle type i, and its average is then $w = \langle \varpi \rangle = S/E$. Furthermore we define the average phase function by $P(\phi) = \langle p(\phi) \rangle = 4\pi G/S$. With these definitions and $dz = \mu dR$ we can write Eq. 2.16 as

$$dI(z, \Omega) = \frac{wE}{4\pi\mu} \int_{4\pi} [I'(z, \Omega') + I''(z, \Omega')] P(\phi') d\Omega' dz \tag{2.17}$$

We want to integrate this equation over the depth z to find the intensity towards the detector. Before we do this we have to realize that part of the light emitted by dV in the line of sight will be absorbed on its way to the surface by overlying particles. We have to multiply the right hand side of Eq. 2.17 with the attenuation term $e^{Ez/\mu}$ (remember that $z < 0$ for locations below the surface). Integrating over z we find the intensity reaching the detector as the sum of the singly and multiply scattered intensity

$$\bar{I} = \bar{I}_{\text{S}} + \bar{I}_{\text{M}} \tag{2.18}$$

with

$$\bar{I}_{\text{S}} = \frac{wE}{4\pi\mu} \int_{-\infty}^{0} \left[\int_{4\pi} I'(z, \Omega') P(\phi') d\Omega' \right] e^{Ez/\mu} dz \tag{2.19}$$

$$\bar{I}_{\text{M}} = \frac{wE}{4\pi\mu} \int_{-\infty}^{0} \left[\int_{4\pi} I''(z, \Omega') P(\phi') d\Omega' \right] e^{Ez/\mu} dz.$$

The integral over all solid angles in the equation for the singly scattered intensity can be evaluated exactly. As the light is considered to be collimated, the integrand is nonzero only in a single direction, and

$$\int_{4\pi} I'(z, \Omega') P(\phi') d\Omega' = J e^{Ez/\mu_0} P(\phi), \tag{2.20}$$

30

where we have multiplied J with an attenuation term to account for absorption by overlying material. Then the singly scattered contribution to the intensity is

$$\bar{I}_S = \frac{w}{4\pi} \int_{-\infty}^{0} J e^{Ez(\mu_0^{-1}+\mu^{-1})} P(\phi) \frac{E}{\mu} dz = \frac{w}{4\pi} \frac{\mu_0}{\mu_0 + \mu} J P(\phi). \tag{2.21}$$

For isotropic scattering $P(\phi) = 1$ and Eq. 2.21 becomes the **Lommel-Seeliger law**:

$$\bar{I}_S = \frac{w}{4\pi} \frac{\mu_0}{\mu_0 + \mu} J. \tag{2.22}$$

The evaluation of the contribution of multiply scattered light to the intensity observed by the detector is more complicated. Hapke (1981) derives for isotropic scatterers

$$\bar{I}_M = \frac{w}{4\pi} \frac{\mu_0 J}{\mu_0 + \mu} [H(\mu_0)H(\mu) - 1] \tag{2.23}$$

in which appears the so-called Ambartsumian-Chandrasekhar H-function (Chandrasekhar 1960). A second-order approximation to the exact H-function is given by

$$H(\mu) = \left[1 - w\mu \left(r_0 + \frac{1 - 2r_0\mu}{2} \ln \frac{1+\mu}{\mu} \right) \right]^{-1} \tag{2.24}$$

with $r_0 = (1 - \gamma)/(1 + \gamma)$ and $\gamma = \sqrt{1 - w}$. Contrary to the singly scattered term, the multiply scattered term cannot be evaluated exactly for an arbitrary phase function. However, it is relatively insensitive to it, as the more times a photon is scattered, the more directional effects are averaged out. The brighter the surface, the more the multiply scattered term approaches the isotropic case. A first order approximation to the intensity observed coming from a surface of non-isotropic scatterers consists of the exact evaluation for the singly scattered term, and the isotropic evaluation for the multiply scattered term:

$$I(\mu_0, \mu, \phi) = \frac{w}{4\pi} \frac{\mu_0 J}{\mu_0 + \mu} [P(\phi) + H(\mu_0)H(\mu) - 1]. \tag{2.25}$$

Using Eqs. 2.1 and 2.6 we can write the radiance coefficient of this surface as

$$r_C(\mu_0, \mu, \phi) = \frac{w}{4} \frac{1}{\mu_0 + \mu} [P(\phi) + H(\mu_0)H(\mu) - 1]. \tag{2.26}$$

Hapke (1981, 1986, 2002) expands and improves this model to include the **Shadow Hiding Opposition Effect** (SHOE) and the **Coherent Backscatter Opposition Effect** (CBOE), which make the surface appear brighter at lower solar phase angles. The radiance coefficient in the full model is

$$r_C(\mu_0, \mu, \phi) = \frac{w}{4} \frac{1}{\mu_0 + \mu} [P(\phi)B_{SH}(\phi) + M(\mu_0, \mu)]B_{CB}(\phi). \tag{2.27}$$

In this equation $B_{SH}(\phi)$ is a factor correcting for the SHOE, which acts on singly scattered light only. The contribution of multiply scattered photons is given by $M(\mu_0, \mu)$, and is a

function of the phase function. $B_{CB}(\phi)$ is a CBOE correction factor, acting on both singly and multiply scattered photons. If the CBOE can be ignored, Eq. 2.27 becomes

$$r_C(\mu_0, \mu, \phi) = \frac{w}{4} \frac{1}{\mu_0 + \mu}[P(\phi)B_{SH}(\phi) + M(\mu_0, \mu)] \qquad (2.28)$$

If the soil particles scatter isotropically then $P(\phi) = 1$ and

$$M(\mu_0, \mu) = H(\mu_0)H(\mu) - 1, \qquad (2.29)$$

which reduces Eq. 2.28 to

$$r_C(\mu_0, \mu, \phi) = \frac{w}{4} \frac{1}{\mu_0 + \mu}[B_{SH}(\phi) + H(\mu_0)H(\mu) - 1]. \qquad (2.30)$$

Hapke (1986) derives an expression for $B_{SH}(\phi)$. He starts by calculating the extinction coefficient of a particulate layer of soil. The result is effectively that of Eq. 2.14 with the particle number density n replaced by the effective particle number density n_{eff}:

$$E = n_{eff}\langle\sigma_E\rangle = -n\langle\sigma_E\rangle\frac{\ln P}{1 - P}, \qquad (2.31)$$

with P the **porosity** of the soil, defined as the proportion of the non-solid volume to the total volume of material. A solid has $P = 0$, fresh snow has $P = 0.75$ - 0.99. Hapke proceeds by realizing that for small phase angles the probability that a light ray penetrates to the surface of a soil particle is not independent of the probability that it is subsequently scattered towards the detector, as close to the particle part of the ray's in- and egress paths overlap. This is readily understood for phase angle zero, in which case the light ray exits the same way as in which it has entered, with zero loss of intensity. This dependency was ignored in the derivation of Eq. 2.21, and gives rise to the factor $B_{SH}(\phi)$ in Eq. 2.27. Note that the SHOE will cause the soil to appear brighter than predicted by Eq. 2.21 when observed at small phase angles. If the effective density follows a step function ($z > 0$: $n_{eff}(z) = 0$, $z < 0$: $n_{eff}(z) = n_{eff}$), B_{SH} is written in terms of the error function, but can be accurately approximated by

$$B_{SH}(\phi) = 1 + B_{S0}B_S(\phi) = 1 + \frac{B_{S0}}{1 + \tan(\phi/2)/h_S}. \qquad (2.32)$$

The amplitude of the SHOE peak is determined by B_{S0}, the ratio of the light scattered from the near-surface of the particle to the total scattered light. If the particles are opaque, then all of the scattered light comes from the surface, and $B_{S0} = 1$. In transparent particles light can be reflected inside the grain, and B_{S0} will be smaller. For narrow opposition peaks the half width of the peak is given approximately by $\Delta\phi = 2h_S$. The width parameter h_S is the ratio of the effective particle radius r_{eff}, defined by $\pi r_{eff}^2 = \langle\sigma_E\rangle$ (see Eq. 2.14), to the extinction path length $l_E = 1/E$:

$$h_S = \frac{r_{eff}}{l_E}. \qquad (2.33)$$

But since r_{eff} and l_E are interdependent, h_S is not easily interpreted in this form. Alternatively, it can be formulated in terms of the porosity and a parameter Y which depends on the particle size distribution:

$$h_S = -\frac{3}{8}Y \ln P. \qquad (2.34)$$

Hapke (1986) gives some examples of size distributions and their associated Y. A soil consisting of equally sized particles has $Y = 1$, the maximum value. A comminuted soil like lunar regolith has a low Y, around 0.25. Generally, soil with a narrow particle size distribution has a broader SHOE peak compared to soil with a broad size distribution.

The Coherent Backscatter Opposition Effect arises from constructive interference of light rays which are scattered via different paths by the soil particles towards the observer in exactly the same angle. If the scatterers at the location where the rays leave the soil are within a few wavelengths of each other, the CBOE peak can be several degrees wide. Even though this process requires multiple scattering, low albedo bodies, like the Moon, can show a pronounced CBOE (Hapke et al. 1998). Hapke (2002) provides an analytical expression. Like the SHOE (Eq. 2.32) the CBOE can be written as a function of the phase angle ϕ in terms of an amplitude (B_{C0}) and a peak width parameter (h_C):

$$B_{CB}(\phi) = 1 + B_{C0}B_C(\phi), \tag{2.35}$$

where

$$B_C(\phi) = \frac{1 + [1 - e^{-f(\phi)}]/f(\phi)}{2[1 + f(\phi)]^2}, \text{ with } f(\phi) = \frac{\tan(\phi/2)}{h_C}. \tag{2.36}$$

Width parameter h_C is a diagnostic for the properties of the soil, and is a function of the wavelength λ and the transport mean free path in the medium Λ:

$$h_C = \frac{\lambda}{4\pi\Lambda}. \tag{2.37}$$

The latter may be thought of as the mean distance a photon travels in the soil before its direction is changed by a large angle (larger than a radian). An expression for Λ exists in terms of particle density, cross section, and scattering efficiency, but it is of limited use because Λ is strongly affected by scattering inhomogeneities internal and on the surface of the particles. Generally, the CBOE amplitude B_{C0} cannot be calculated from soil properties and must be regarded as a free fitting parameter, with $0 \leq B_{C0} \leq 1$.

In a separate paper Hapke (1984) calculates an expression for **macroscopic roughness**. In this model the particulate soil is assumed not to be perfectly flat, but to consist of facets that build up macroscopic structures ("fairy castles"). Macroscopic roughness is a function of the facets' mean slope angle Θ, and the angles of incidence and reflection. It leads to extensive modification of Eq. 2.27, which I will not reproduce here.

2.3   Henyey-Greenstein phase function

Phase functions in the Hapke model are normalized so that

$$\int_{4\pi} P(\phi)d\Omega = \int_{\varphi=0}^{2\pi} d\varphi \int_{\theta=0}^{\pi} P(\phi)\sin\theta d\theta = 2\pi \int_{\phi=0}^{\pi} P(\phi)\sin\phi d\phi = 4\pi. \tag{2.38}$$

For isotropic scatterers $P(\phi) = 1$. A type of phase function that was used by the LPL team to model the scattering behavior of Titan aerosols is the double Henyey-Greenstein function. Actually, two different versions of the "double Henyey-Greenstein phase function" exist, and the one used is

$$P_{dHG}(\psi, f, g_1, g_2) = fP_{HG}(\psi, g_1) + (1 - f)P_{HG}(\psi, g_2) \tag{2.39}$$
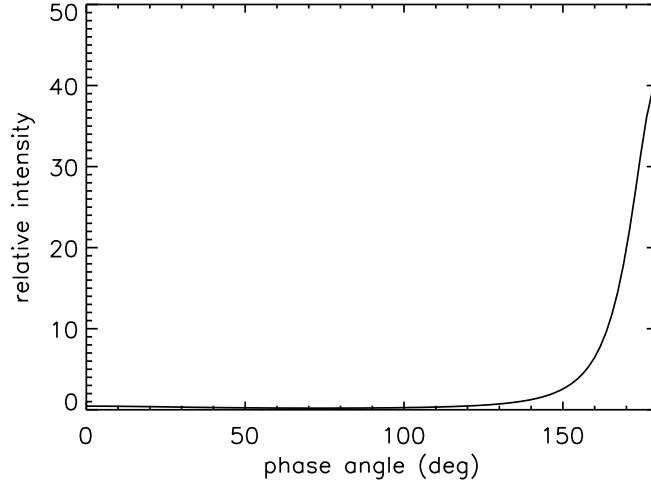
Figure 2.2: Example of a double Henyey-Greenstein phase function used to model the scattering properties of Titan aerosols in an early version of the LPL atmosphere model (Lyn Doose, personal communication). Shown is the phase function for aerosols at 1.28 μm with Henyey-Greenstein parameters $f = 0.9$, $g_1 = 0.8$, and $g_2 = -0.4$. The aerosols are strongly forward scattering, but also exhibit a small backscattering peak.

with

$$P_{\mathrm{HG}}(\psi, g) = \frac{1 - g^2}{(1 + g^2 - 2g \cos \psi)^{3/2}} \qquad (2.40)$$

and ψ the scattering angle, which is related to the phase angle by $\psi = \pi - \phi$. Forward scattering is in the direction of $\phi = 180°$, backward scattering is towards $\phi = 0°$. In terms of the phase angle these equations become

$$P_{\mathrm{dHG}}(\phi, f, g_1, g_2) = f P_{\mathrm{HG}}(\phi, g_1) + (1 - f) P_{\mathrm{HG}}(\phi, g_2) \qquad (2.41)$$

with

$$P_{\mathrm{HG}}(\phi, g) = \frac{1 - g^2}{(1 + g^2 + 2g \cos \phi)^{3/2}}. \qquad (2.42)$$

An expansion of this version into Legendre polynomials P_n is

$$P_{\mathrm{dHG}}(\phi) = 1 + \sum_{n=1}^{\infty} [f(-g_1)^n + (1 - f)(-g_2)^n](2n + 1)P_n(\cos \phi). \qquad (2.43)$$

The double Henyey-Greenstein function does not have a physical basis, but is merely descriptive. Figure 2.2 shows an example of such a function, that was used in an early version of the LPL atmosphere model.

3   DISR Instrument Calibration

Three versions of DISR have been built at the LPL in Tucson, Arizona, of which the third (DISR#3) is the flight model. At the time of writing, the first model (DISR#1) is attached to a Huygens engineering model stored in Darmstadt, Germany, and the second (DISR#2) is at the LPL. DISR#2 was originally meant to be launched, but was eventually replaced by DISR#3 because of severe internal light leaks ('crosstalk'). It now serves as a test bed, and it has been used to perform several of the experiments described in this thesis. A schematic of the DISR#3 flight model and its location on the probe is shown in Fig. 3.1. On the front is the **Side Looking Imager** (**SLI**, with the sun shade), below which we find the **Medium Resolution Imager** (**MRI**) and the **High Resolution Imager** (**HRI**). In addition to the three cameras, DISR houses the upward looking instruments Upward Looking Violet photometer (ULV), Upward Looking Visual Spectrometer (ULVS), Upward Looking Infrared Spectrometer (ULIS) and the Solar Aureole Cameras, and the downward looking instruments **Downward Looking Violet photometer** (**DLV**), **Downward Looking Visual Spectrometer** (**DLVS**), and the **Downward Looking Infrared Spectrometer** (**DLIS**). Tomasko et al. (2002) provide a technical overview of DISR and all its sub-instruments. This thesis concentrates on the downward looking instruments. In this chapter I describe their operation and data calibration procedures. For this I made extensive use of the calibration reports that were compiled and published internally by the LPL DISR team. For details on the image calibration the reader is referred to Karkoschka et al. (2007). Observation sequential numbers are printed **bold** throughout this thesis; details can be found in Appendix A.

3.1   Downward Looking Violet Photometer

The Downward Looking Violet Photometer is a silicon photodiode, sensitive in the 350-480 nm wavelength range. It is located directly below the HRI, under a baffle to make its field of view the lower hemisphere. The detector is read out instantaneously, and the raw data numbers can be converted to intensities by subtracting a dark current and dividing the result by the responsivity.

3.1.1   Dark current

Before launch, the dark signal of the DLV was measured in several tests at LPL, and found to be different for each of the DISR operation modes. The modes relevant for this thesis are the VLNS and surface modes. The dark signal for the VLNS mode was determined to have a bimodal distribution, with peaks at 38 and 51 DN, the latter almost uniquely
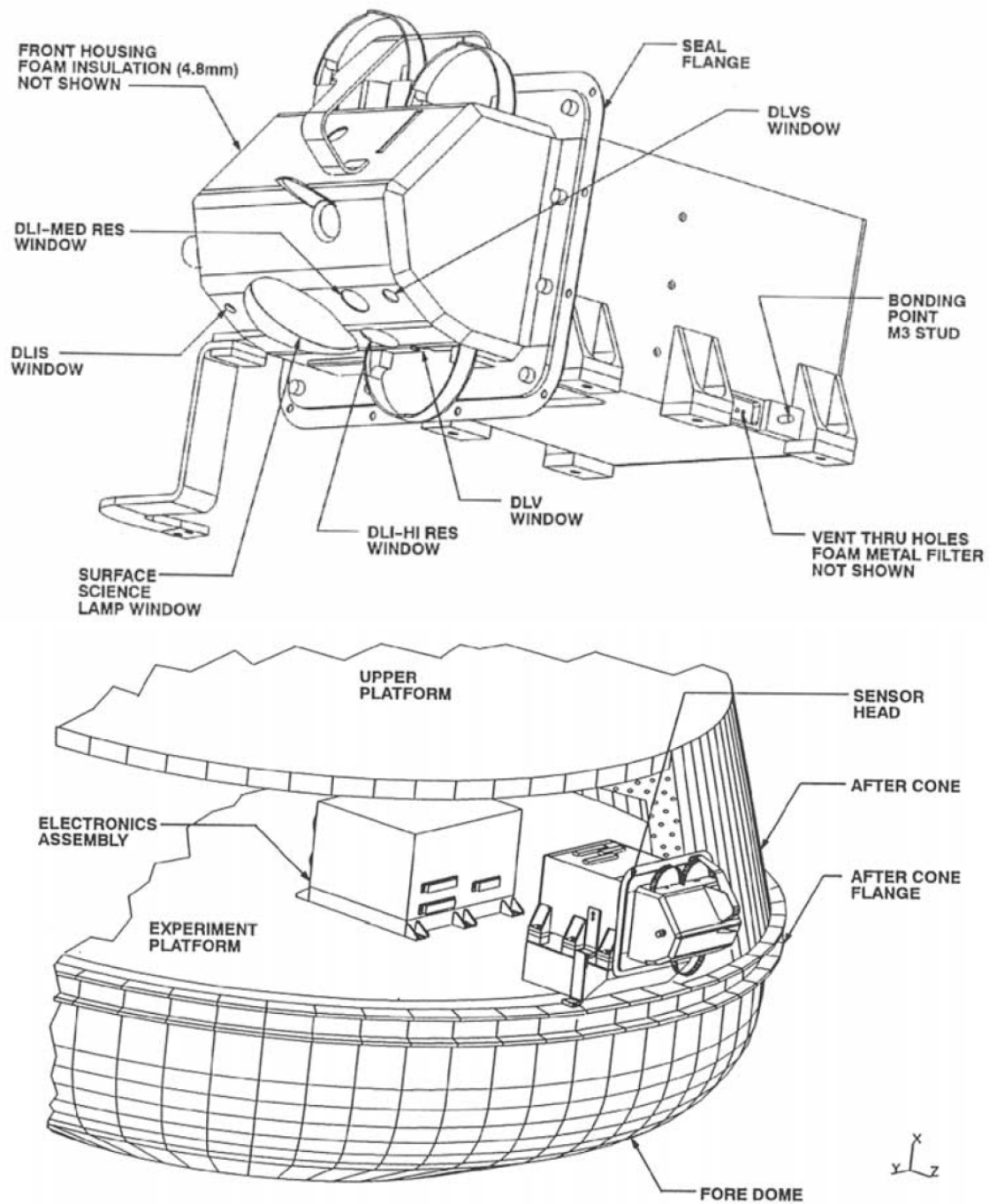
Figure 3.1: The Descent Imager/Spectral Radiometer (DISR). **Top**: DISR as seen from below. The Medium Resolution Imager (MRI) and High Resolution Imager (HRI) are labeled as 'DLI-MED RES' and 'DLI-HI RES', respectively. The Side Looking Imager (SLI) is not labeled and is located above the MRI. **Bottom**: The location of DISR on the Huygens experiment platform. The sensor head protruded through the after cone. Figures from Tomasko et al. (2002).

Table 3.1: The exposed area of the CCD, sized 524×256 pixels, occupied by the different DISR sub-instruments. The pixel in column and row zero is at the bottom left in Fig. 3.2.

instrument	columns	rows
DLVS	14-33	1-200
ULVS	38-45	1-200
Column 49	49	1-200
MRI	52-227	1-254
SLI	234-361	1-254
HRI	364-523	1-254

associated with a single test. After launch, an inflight DISR checkout (F4) showed the dark signal for the VLNS mode to have only a single peak at 41.5 ± 1.6 DN ($n = 36$). The VLNS measurements on Titan are unimodal, and I used the inflight dark values. The distribution of the pre-launch surface mode dark signal was found to have three peaks (at 39, 49, and 62 DN), one of these (62 DN) uniquely associated with the test mentioned above. The inflight dark for the surface mode was 41 DN ($n = 2$). Presumably, had there been more measurements, a second peak would have been found at around 51 DN. The surface mode measurements on Titan are bimodal, and I made no effort to convert them into intensities.

3.2   CCD layout

Central to the DISR focal plane is the 524×512 pixel sized CCD. It was read out by means of an electronic shutter, not involving any mechanical action. For this the lower 524×256 pixels were covered by an opaque metal film, with the upper 524×256 pixels being the exposed area. After exposure, the charge was transferred from the top to the covered lower part to be subsequently read out by means of a serial register and digitized. Transfer took about 2.2 seconds for image data, time during which extra charge could accumulate in rows not yet transferred due to light exposure, which is known as the electronic shutter effect. The CCD was not only used for imaging Titan's surface, but also served as detector for solar aureole cameras and the visual spectrometers DLVS and ULVS, their light being led to the focal plane by optical fibers. Furthermore, to gauge the spill of light from the MRI to the spectrometer columns, known as 'crosstalk', the lower 200 pixels of the 49th column were also transmitted. Inadvertently, this column served as an additional camera, its 'images' being linear brightness profiles. Figure 3.2 shows the location of the sections reserved for the downward looking instruments on the CCD. Note that viewed in the CCD coordinate system the images are upside down. Table 3.1 lists the columns and rows occupied by the different sub-instruments relevant to this thesis.
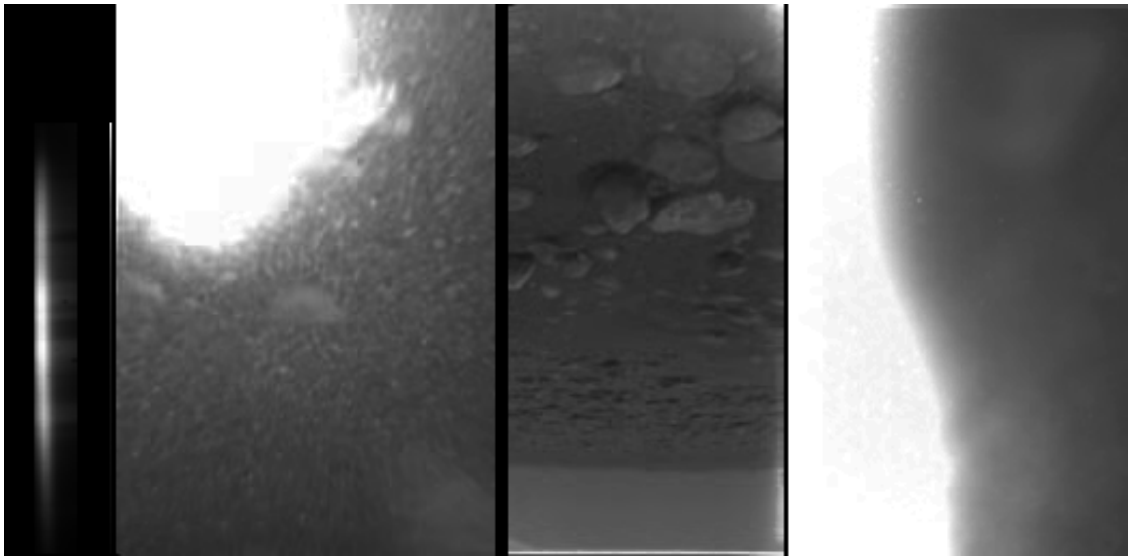
Figure 3.2: Layout of the DISR CCD, shown with a typical post-landing signal. The pixel in the lower left corner has coordinates (0,0). The imager sequence from right to left is HRI/SLI/MRI. Column 49 is located immediately left to the MRI, and the DLVS is at far left. Not shown are the ULVS (left of the DLVS) and the solar aureole camera sections in the top left corner of the CCD. See Table 3.1 for column and row numbers.

3.3 Column 49

The lower 200 pixels of column 49 of the CCD were read out at the same time as the DLVS and its contents stored in a separate file. This column is known as 'the extra column', but I will refer to it as 'Column 49'. Located between the MRI and the ULVS (see Fig. 3.2), it provides a measure of the amount of 'crosstalk', or light spilled over from the MRI to the ULVS and DLVS. Like the DLVS it was read out in a fast mode, and therefore does not suffer from the 'electronic shutter effect' (the accumulation of charge during read-out) which affects the images. The CCD temperature was so low for all measurements relevant to this thesis that the dark current was essentially zero. Even though the primary function of Column 49 was to provide a correction for the visual spectrometers, it acted as a camera in its own right, reflecting the brightness distribution of the rightmost column of the MRI. Interestingly, it was the only 'camera' active around the time of landing, and I analyze its brightness profiles in Section 7.1.

3.3.1 Bias

The pre-landing bias for each pixel of Column 49 was estimated by the LPL team to be 9 DN for all measurements relevant to this thesis. The post-landing bias can be determined empirically. Possibly, the probe moved for a few seconds after landing, but after that DISR essentially viewed the same spot on the surface for the remainder of the mission. By comparing a set of measurements recorded closely in time, but with different exposure times, we can derive the (constant) bias level (Fig. 3.3). I used Column 49 measurements **827**, **829**, **831**, **833**, **835**, and **837**, recorded around 2 minutes after landing. These were
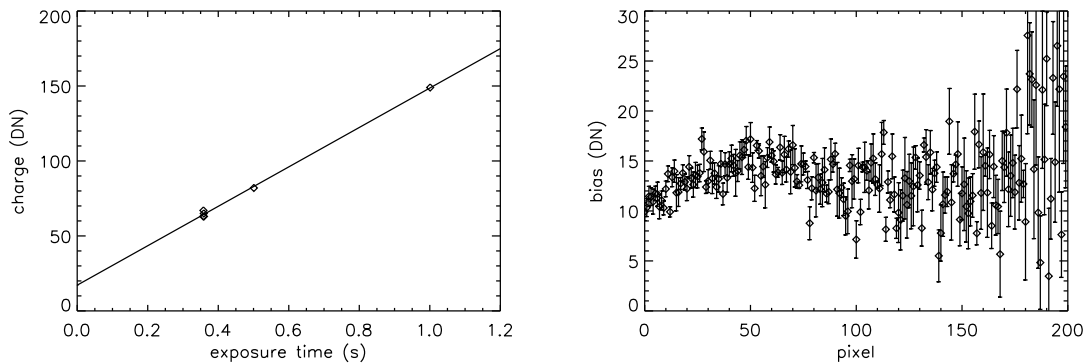
Figure 3.3: The extra charge, or bias, of Column 49 after landing was estimated by fitting a line to measurements at different exposure times. **Left**: A linear fit to the intensity for pixel 50. The intercept is equal to the bias. **Right**: The bias derived for all pixels of Column 49. The error bars provide a 1σ measure of the goodness-of-fit.

recorded at the same mission time and with the same exposure time as the DLVS spectra with the same sequential number (see Table A.8). I assumed the bias not to have changed for the remaining time on the surface.

3.4   Downward Looking Visual Spectrometer

The DLVS is sensitive in the 480-980 nm wavelength range. Its field of view is rectangular, ranging from 12° to 45° in nadir angle, and being approximately 6° wide at the top and 17° at the bottom. Its slit is imaged on a 20×200 pixel sized section on the CCD. Generally, adjacent columns were summed on-board before being transmitted, yielding an array of 10 columns by 200 rows. Exceptions are the Spectrophotometric Map mode, in which all 20 columns were returned, and the Very Low Near Surface mode, which returned only 2 out of 10 summed columns. The different modes of observation are discussed in more detail in Chapter 4. The DLVS was read out in a fast mode (in around 300 ms), and therefore, like Column 49, does not suffer from the 'electronic shutter effect' that affects the images (accumulation of charge during readout). There are two issues complicating the calibration of DLVS spectra. The first is that the spectra are projected slightly warped on the CCD, which necessitates rectification by a geometric correction. Second, light spills over from the MRI to the DLVS section on the CCD ('crosstalk'), and has to be removed. Then the intensity, in units of [W m^{-2} μm^{-1} sr^{-1}], is calculated from the raw data as

$$\text{intensity} = \frac{\text{raw data} - (\text{dark current} + \text{bias}) - \text{crosstalk}}{\text{exposure time} \cdot \text{responsivity}} \tag{3.1}$$

The raw data, dark current, bias, and crosstalk are all in DN. Exposure time is in seconds, and responsivity in [J^{-1} m^2 μm sr]. Dark current is calculated from a model, but for all measurements relevant to this thesis the CCD temperature was so low that the it was essentially zero. As calculated, the dark current does not include bias, which has to be added separately. The spectrum wavelength scale is a function of the camera optics temperature, and has to be determined for each exposure. The different aspects of the
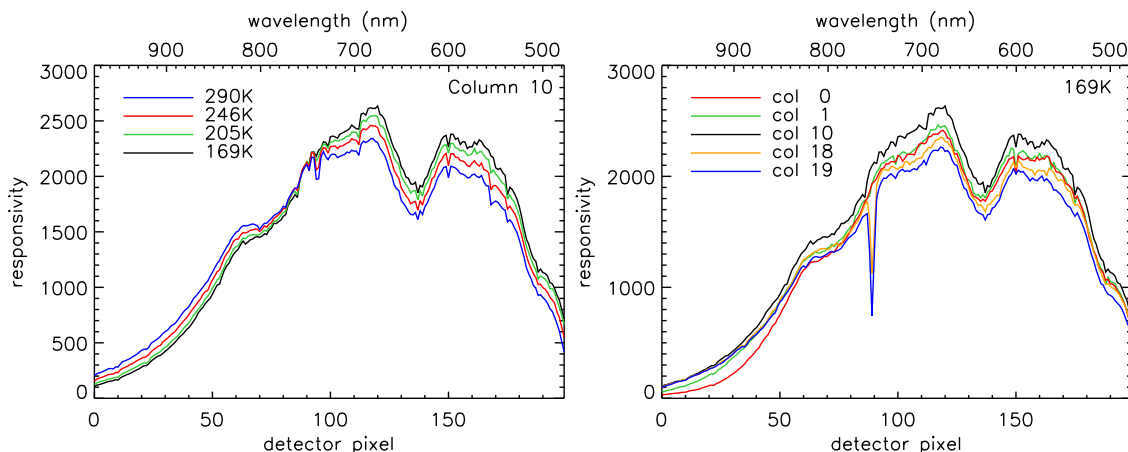
Figure 3.4: The responsivity of the 200 DLVS rows (pixels) as determined for various CCD temperatures (**left**, column 10), and columns (**right**, CCD temperature 169 K). The wavelength scale at the top is that for the standard temperature of 200 K. Division by the responsivity converts DN to intensity in [W m^{-2} μm^{-1} sr^{-1}].

calibration are covered in more detail in the following subsections. The spectral resolution was determined before launch: a thin spectral line was observed by the DLVS as a Gaussian profile with a FWHM of 5.5-6.0 nm, valid over the whole wavelength range.

3.4.1   Responsivity

The responsivity of the 20 columns × 200 rows DLVS section on the CCD was determined before launch by the LPL team at nine different CCD temperatures between 169 and 290 K. Figure 3.4 shows how the responsivity strongly depends on row number (i.e. wavelength), but weakly on temperature and column number. Note that the wavelength scale runs opposite to row number. The temperatures at the end of the descent were were low (ranging from 183 K for the SM2 mode to 170 K for the VLNS mode), but above the minimum calibration temperature, so no extrapolation was necessary. The responsivity for each pixel was found by cubic spline interpolation to the measured CCD temperature. The uncertainty in the responsivity determinations is unknown, but we can safely assume that the errors are largest where the responsivity is lowest. We have to be careful interpreting results for wavelengths at which the responsivity is relatively low. The figure shows that this is roughly below 500 nm and above 900 nm.

3.4.2   Geometric correction

The spectrum as it is projected on the DLVS area on the CCD is warped, with different rows looking at different zenith angles. The situation is sketched in Fig. 3.5. The lower half of the figure represents the 200 rows on the CCD, with the zenith angle of the center of some pixels (columns) indicated. The vertical dotted lines delimit the zenith angle range that is common to all rows. The intensities within this range are interpolated to one of the standardized grids of footprints associated with the mode of observation, depicted in the upper half of the figure. The numbering convention used in this thesis for the standardized

footprints runs opposite for that of the CCD columns. The column number runs from 0 at the left end of the DLVS section on the CCD, where light coming from the highest zenith angles is projected, to 19 at the right end of the DLVS section (compare Fig. 3.2). If the columns are summed the column number runs from 0 to 9. In contrast, the numbers of the standardized footprints are defined to increase towards higher zenith angles (or decreasing nadir angles). The 20-column Spectrophotometric Map mode has 16 standardized spatial footprints of approximately the same spatial extent as the original CCD pixels. In the regular 10-column mode, used in panoramic cycles, the DLVS returned only the sum of adjacent columns. The intensities were interpolated to 8 footprints half the size of those of the Spectrophotometric Map mode. The 5-column mode, used early in the descent, returned only the sum of 4 adjacent columns, and has therefore 4 footprints. In the VLNS 2-column mode the DLVS returned only the sum of columns 4 and 5, and that of column 6 and 7. Only a very narrow zenith angle range, centered on $159.6°$, is common to all rows, and finding the intensity at both end of the spectrum actually involves extrapolation. The extent in zenith angle of the single footprint of a VLNS spectrum is (approximately) given by the short vertical dotted lines in Fig. 3.5. Whereas for 10-column mode spectra intensities are found by cubic spline interpolation, those for 2-column mode spectra are determined by linear interpolation. The availability of only two instead of ten columns does not affect the end result significantly before landing, but becomes problematic in the presence of a strong brightness gradient over the columns on the CCD, such as that caused by the SSL. This is why the 2-column and 10-column mode post-landing spectra look very different, even though their footprints approximately cover the same patch of ground (see §3.6.2 for further details).

The most recent 'official' release of the DLVS calibrated data by the LPL team (3 May 2005) interpolates the Spectrophotometric Map spectra to 8 footprints, and gives two spectra for the 2-column VLNS mode. My reduction improves on this, as it yields Spectrophotometric Map spectra at the full spatial resolution of 16 footprints and treats the 2-column mode spectra correctly.

3.4.3   Wavelength calibration

The wavelength is a function of the DISR optics temperature. Prior to launch the wavelength scale was calibrated for five temperatures in the range of 189 to 290 K. During flight, the optics temperatures dropped to values as low as 165 K. In fact, all of the SM2 and VLNS spectra were recorded with optics temperatures below 169 K. The wavelength scale for these spectra may be incorrect, even though the extrapolated scale for 165 K is only marginally different from that of 189 K (less than 1 nm). Of the spectra considered in this thesis only the temperatures of the SM1 and surface spectra from **874** onward are within the calibrated range.

3.4.4   Bias

The pre-landing bias for each pixel of the DLVS section on the CCD was estimated by the LPL team to be 9 DN for all measurements relevant to this thesis. Like that of Column 49, the post-landing bias can be determined empirically. The measurements used to determine the bias are **825**, **827**, **829**, **831**, **833**, and **835**. They were chosen to have a wide
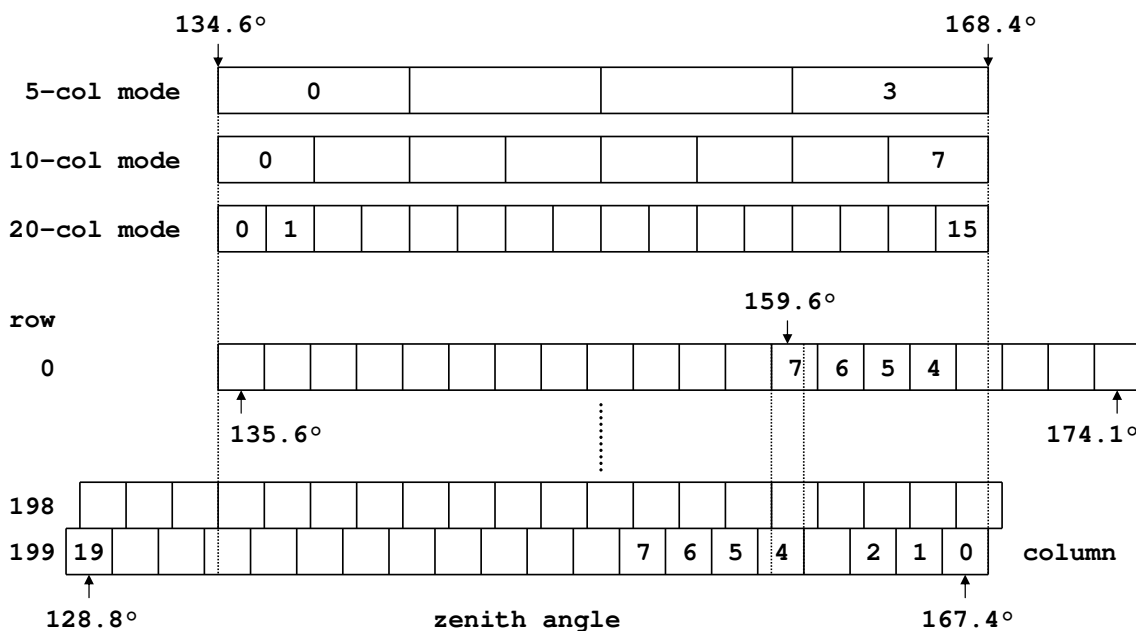
Figure 3.5: The principle of the DLVS geometric correction. See text for details.

range in exposure times, and a short range in mission times (see Table A.8). Figure 3.6 demonstrates the method and shows the results for two out of ten summed columns. The bias appears to be similar for each column, but not identical. Moreover, it is not constant in time as the figure shows for column 9. But since the variability is relatively small I assume that the post-landing bias of all columns is is constant and equal to that of summed column 7.

3.4.5   Crosstalk

Crosstalk, light leaking from the MRI to the visual spectrometers, is much more of a problem for the ULVS than the DLVS. Nevertheless, a correction is calculated from Column 49 (see also Section 3.3), using coefficients determined before launch at LPL. Figure 3.7 shows that crosstalk hardly affects pre-landing spectra, but that it becomes significant after landing due to the strong lamp signal on the MRI (see Fig. 3.2). The fact that Column 49 was read out at the same time as the DLVS enables us to precisely predict the amount of crosstalk. However, correcting the VLNS mode DLVS spectra required special treatment. Only half of the Column 49 and DLVS files were transmitted to Earth, but not in pairs. That means that not for every DLVS spectrum a Column 49 is available. Especially around the time of landing, when the amount of crosstalk jumps dramatically, we must take care to interpolate crosstalk as accurately as possible.
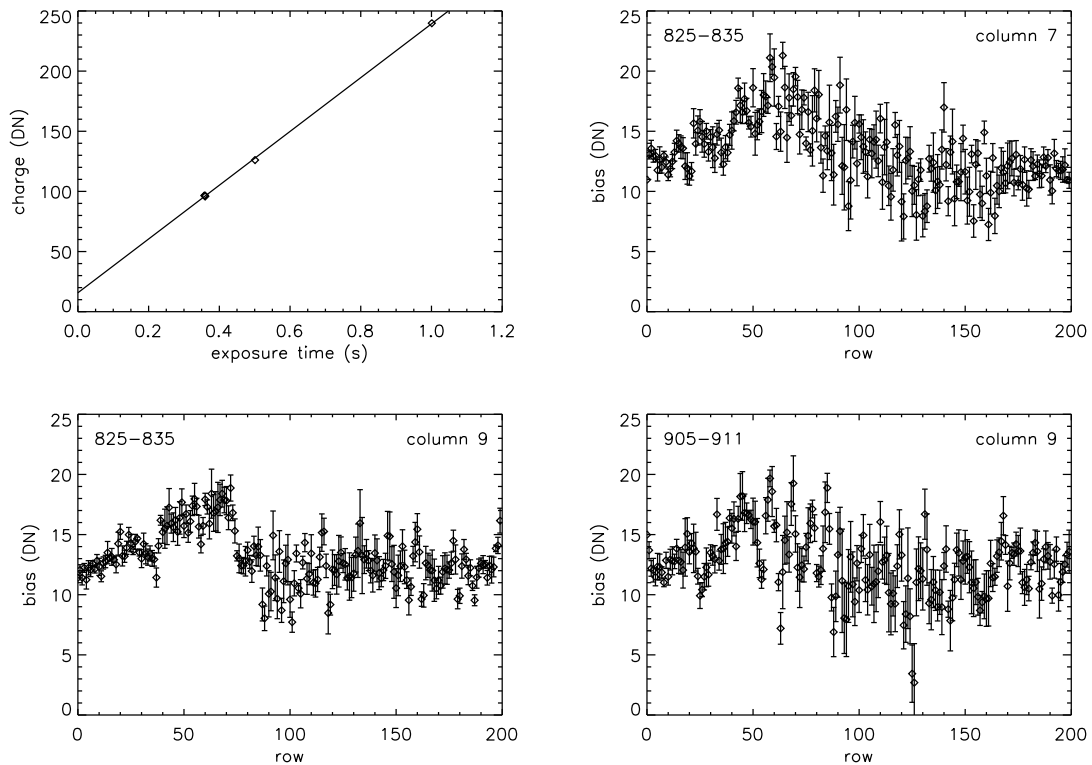
Figure 3.6: The extra charge, or bias, present on the DLVS spectra after landing was estimated by fitting a line to measurements at different exposure times. **Top left**: An example linear fit to the intensity for row 50 of summed column 9 (out of 10). The intercept is equal to the bias. **Top right**: The bias derived for summed column 7 from **825-835** (mission time 8949-8991 sec). **Bottom left**: The bias derived for summed column 9 from **825-835**. **Bottom right**: The bias derived for column 9, but now from **905-911** (20 minutes later). Even though the error bars are larger, we see significant changes.

3.4.6   Overexposure

Many of the DLVS spectra acquired after landing suffer from overexposure. As it struggled to deal with the flood of reflected lamp light, the instrument varied the exposure time. At the time of landing DISR was operating in the Very Low Near Surface mode, in which the DLVS returned spectra in the 2-column mode. For a little less than a minute after landing it continued to do this, after which it switched to the 10-column mode for the remaining 69 minutes of the mission. Both modes involve on-board summing of two consecutive columns. This sum reaches a certain maximum value in case of overexposure. But if in reality only one of the two column was overexposed, we cannot determine which one, as we have only their sum. This is why we cannot judge from the raw data numbers alone whether a certain intensity value is reliable or not. We can find out though, by comparing correctly exposed and certain overexposed 10-column mode spectra, as shown in Fig. 3.8. Overexposure occurs in the central region of the spectrum in the form of a depression. Significantly, the figure shows that outside this region, in both flanks, the spectrum is fully reliable. Even though the same cannot be demonstrated for overexposed
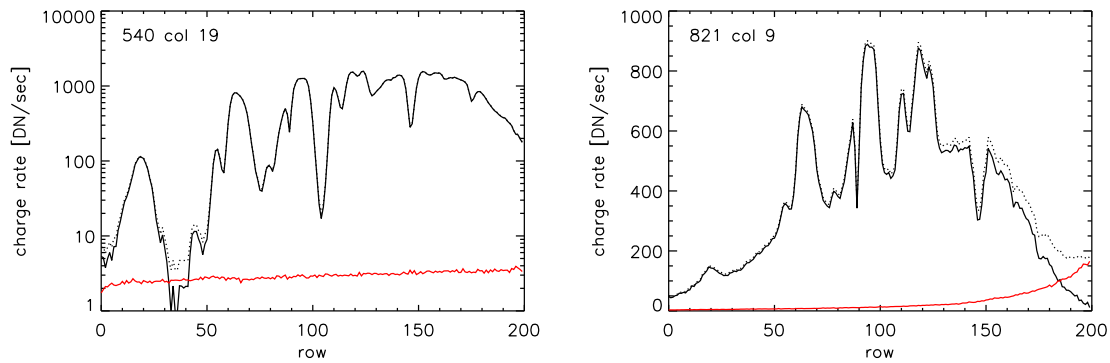
Figure 3.7: How crosstalk affects the DLVS. The corrected spectrum (drawn black line) is obtained by subtracting the crosstalk (red line) from the raw spectrum (dotted line). **Left**: For a typical pre-landing spectrum (SM1 spectrum **540**, column 19) crosstalk is minor, affecting only the strongest methane bands. (Note: logarithmic scale.) **Right**: For a typical post-landing spectrum (10-column mode spectrum **821**, summed column 9) crosstalk is significant, especially at the top end of the spectrum (low wavelength end), due to the strong lamp signal on the MRI. Note that wavelength runs opposite to the row number.
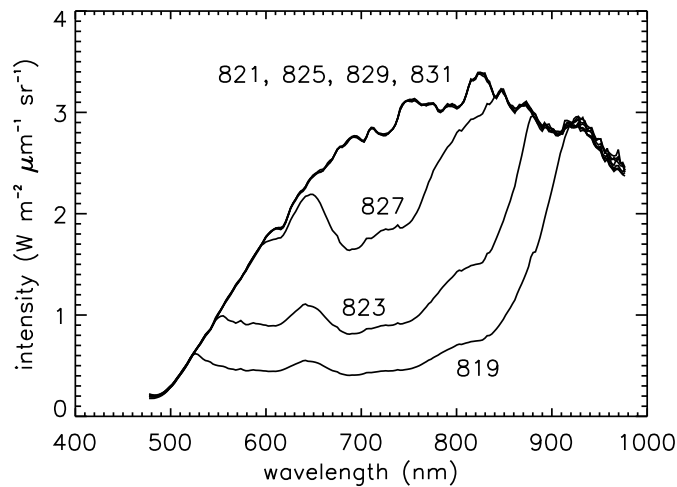

Figure 3.8: The first seven 10-column mode spectra acquired after landing were recorded at different exposure times, leading to the overexposure of some. The regions flanking the overexposed cores agree well with correctly exposed spectra. All spectra were recorded within one minute (labels denote sequential number).

2-column spectra due to a lack of data, I nevertheless assume it holds true.

3.4.7 Noise

Sources of noise are read noise, quantization noise, and shot noise. Read noise is the noise added to the signal on read-out of the CCD. Shot noise is the result of random
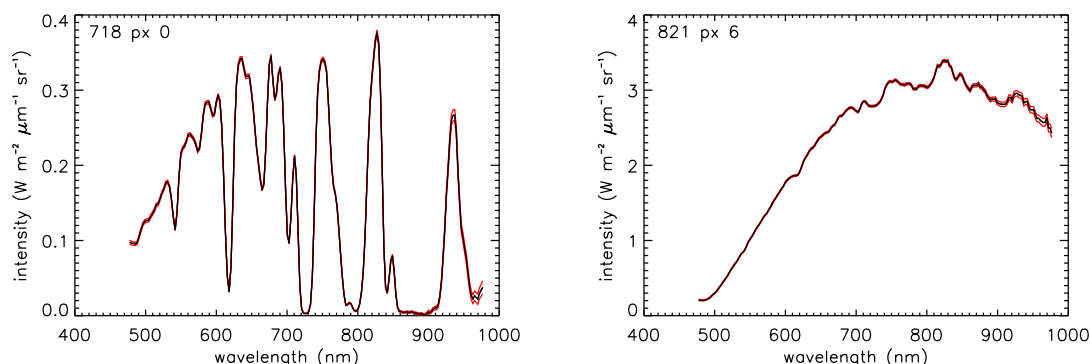
Figure 3.9: Two examples of how sensitive the DLVS calibration is to noise. The black line is the calibrated spectrum, the red lines delimit the 1σ confidence intervals. **Left**: Pre-landing SM2 spectrum **718**, footprint 0. **Right**: Post landing 10-column mode spectrum **821**, footprint 6.

fluctuations in the detected number of photons. It is significant only because the intensity of light near the Titan surface is so low. Quantization noise results from the analogue to digital conversion of the signal, and is basically a rounding error. If we assume that the noise is normally distributed around zero, the variance of the measured signal of a certain pixel on the CCD is the sum of the variances of the individual sources of noise:

$$\sigma^2_{\text{pixel}} = \sigma^2_{\text{read}} + \sigma^2_{\text{quant}} + \sigma^2_{\text{shot}} \tag{3.2}$$

The read and quantization noise have been determined from pre-launch and inflight tests to be $\sigma_{\text{read}} = 0.57$ DN and $\sigma_{\text{quant}} = 0.29$ DN. The shot noise is assumed to follow a Poisson distribution, so $\sigma_{\text{shot}} = \sqrt{N}$ electrons, or $\sigma_{\text{shot}} = \sqrt{d/30}$ DN, with d the DN value of the pixel of interest. Figure 3.9 shows two examples of how noise is expected to affect the DLVS calibration. The intensity at wavelengths above 900 nm appears to be most sensitive to noise. For example, noise typically constitutes 1.4% of the signal at 935 nm. Note that this analysis does not consider errors in the responsivities.

3.5 Downward Looking Infrared Spectrometer

The DLIS is sensitive in the 850-1700 nm wavelength range, but due to second order effects the effective wavelength range is 850-1600 nm. Its field of view is approximately 3° by 9° (azimuth × nadir angle), and is centered on 20° nadir angle. Its slit is imaged by a linear array of 150 InGaAs photodiodes, of which each element is connected to one pixel of a linear CCD array. Contrary to the DLVS, the DLIS has a shutter (the only moving part in DISR). A spring holds the shutter open unless an electromagnet is activated. Dark current is eliminated by subtracting shutter open from shutter closed exposures, and when the result is divided by the responsivity and the exposure time (shutter open) one obtains the intensity. The first and last 7 pixels of the CCD array are covered by an opaque resin to determine the dark current in case of shutter failure, which leaves 136 pixels for the spectral measurements. The DLIS spectral resolution was determined before launch: a

thin spectral line was observed as a Gaussian profile with a FWHM of circa 20 nm, valid over the whole wavelength range.

During the descent, exposures were generally summed on board over multiple probe rotations to yield azimuthal averages. However, all the observations relevant to this thesis were acquired in special, unsummed modes that yield a single spectrum with a relatively small footprint (see Chapter 4). In some of these (e.g. the spectrophotometric map mode) the instrument acquired four samples in sequence, two with shutter open and two with shutter closed, alternating between shutter states. The shutter-open and shutter-closed samples were summed on board and the sums were returned separately. Around landing (in the VLNS mode) the instrument acquired single samples with either shutter open or closed.

3.5.1   Responsivity

The first and second order responsivity of the DLIS was determined before launch by the LPL team at eleven different detector temperatures between 198 and 306 K (Fig. 3.10). Generally, responsivities at a certain measured detector temperature are determined by cubic spline interpolation. But since the temperature in the last stages of the descent dropped to values as low as 189 K, I resort to extrapolation to find the responsivities at these temperatures. The second order response becomes significant relative to the first order around detector pixel number 120, i.e. at around 1.6 μm. This is why, generally, I ignore measurements above this wavelength. The first order response is shown not to be very sensitive to the detector temperature, except for the regions where the responsivity drops sharply, mostly at the red end. The uncertainty in the responsivity determinations is unknown, but we can safely assume that the errors are largest where the responsivity is lowest. Therefore we have to be careful interpreting results for wavelengths beyond which the responsivity has dipped downward. The figure shows that this is roughly below 900 nm and above 1550 nm.

3.5.2   Wavelength calibration

The wavelength is a function of the DISR optics temperature. Prior to launch the wavelength scale was calibrated for twelve temperatures in the range of 187 to 288 K. During flight, the optics temperatures dropped to values as low as 165 K. In fact, all of the SM2, MNS, VLNS, and unsummed surface spectra (**249**-**254**) were recorded with optics temperatures below 169 K. The wavelength scale for these spectra may be incorrect, even though the extrapolated scale for 165 K is only marginally different from that of 187 K (less than 1 nm). Of the spectra relevant to this thesis, only the SM1 and summed surface spectra (**261**-**268**) temperatures are within the calibrated range.

3.5.3   Noise

The S/N level due to random noise is better than 1000 in the methane windows for the low detector temperatures relevant to this thesis. A source of systematic uncertainty is the shutter, the only moving part in DISR. The uncertainty in the time of opening and closing introduces an uncertainty in the measured intensity of typically less than 1%.
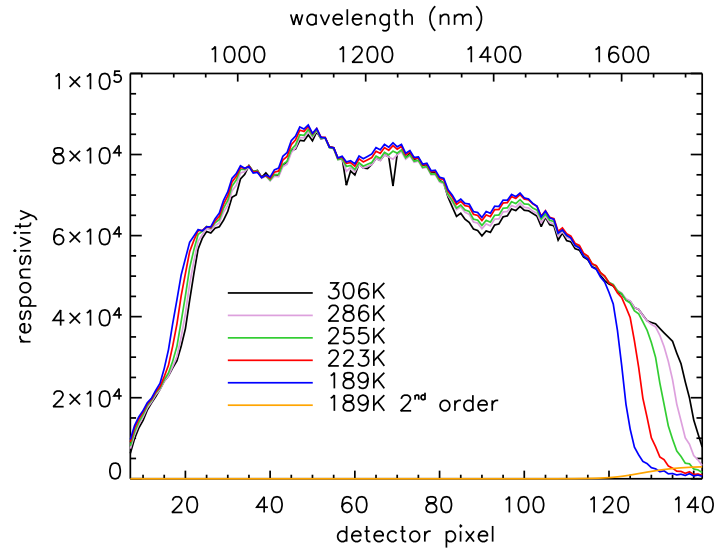
Figure 3.10: The first order responsivity of the 136 detector pixels of the DLIS as determined at various detector temperatures, including one second order response. The wavelength scale at the top is that for the standard temperature of 200 K. Division by the responsivity converts DN to intensity in [W m^{-2} μm^{-1} sr^{-1}].

3.6   Surface Science Lamp

DISR carried a Surface Science Lamp (SSL) to illuminate the surface just before landing. The SSL is a 20 W incandescent lamp with a gold-coated parabolic reflector. It serves a twofold purpose. First and foremost it allows for a study of atmospheric methane absorption by creating unsaturated absorption lines in DLVS/DLIS reflectance spectra acquired just before landing. Second, the reflectance of Titan's surface can be reconstructed from the same spectra by dividing out the spectrum of the SSL proper.

3.6.1   Calibration experiment

To determine the SSL spectrum an experiment was carried out in which the the DISR downward looking instruments observed a target illuminated by the SSL. The lamp beam is not collimated, and its flux is a function of distance. By knowing the reflectance of the target, the SSL flux at the distance of the target can be calculated. Combining Eq. 2.1 and Eq. 2.6 we find for the flux

$$F_{\text{SSL}} = \frac{\pi I}{r_{\text{C}}^{\text{target}}(\phi = 0°)} \qquad (3.3)$$

where $r_{\text{C}}^{\text{target}}(\phi = 0°)$ is the radiance coefficient of the target at phase angle zero, and I the intensity observed by the spectrometer.

The experiment aimed at determining the SSL spectrum was performed at LPL on 16 August 1996. The DISR#3 flight model observed an 95.3×147.3 cm (width × height) aluminum target with small (7.6×7.6 cm) dark Krylon squares, positioned at a distance of 4.68 m from the camera and perpendicular to the lamp beam. Measurements were acquired by all three cameras, the DLVS, the DLIS, and the DLV, with the SSL alternately

switched on and off. Housekeeping data (temperatures, currents) were recorded. The SSL current and voltage during the calibration experiments were nominal, and identical to those during the descent. Figure 3.11 (left) shows how the instrument viewed its target. Naturally, to retrieve the surface reflectance in absolute units one needs to scale the lamp flux to the distance to the surface at the time of observation. The catch however is that Titan spectra which show lamp light were acquired at distances to the surface greater than 4.68 m. Since the spectrometers and the SSL all have different lines of sight and locations on DISR, parallax effects are significant at close range. As can be seen on the Titan surface image (Fig. 4.7), moving the surface closer will shift the DLVS and DLIS footprints to the left and right, respectively. Moving the surface further away than 4.68 m will have the opposite effect, and this may cause the SSL flux to be different than that calculated from the calibration experiment. In Fig. 3.11 (right) I simulated the field of view of the instruments for a distance to the target of 25 m. The expected shift of the footprints is seen to be relatively small, but how exactly this translates to a change in flux cannot be determined because we only have the image with the target at 4.68 m. The problem is that although the pointing angles of the instruments have been well determined, the direction of the SSL beam is poorly known. However, from the surface image we can be sure that the reflectance spot follows the DLIS footprint. So at larger distances the DLIS flux is more reliable than the DLVS flux, and fortunately, the closest observations were those of the DLVS. How well the calibrated SSL flux suffices can be gauged from how well the reflectances from spectra recorded at the various altitudes agree.

The aluminum target was covered with an unknown type of paint. The plate's reflectance properties had been determined by the LPL team, and are recorded in the SSL calibration document. Due to some inconsistencies in the visual part of the reflectance spectrum I asked Co-I Bernard Schmitt of the *Laboratoire de Planétologie* in Grenoble, France, to measure the reflectance of the target with the LPG goniometer, which he was willing to do. Also Chuck See of the LPL responded positively to my request to sacrifice a piece of the target and send it to Grenoble. Initially Chuck wanted to send the whole target to preserve its integrity for history (did he envision a Huygens museum?), but he changed his mind when it became clear that it was too large for the goniometer to accommodate. The measurements were performed in April 2006.

During the calibration experiments, the target was positioned perpendicular to the lamp beam at a distance of 4.68 m. Since both spectrometer pupils are located within 6 cm of the SSL on DISR, we are most interested in an illumination incidence angle of 0° and reflection angles of 0-1°. Unfortunately, it was not possible to put the goniometer in this configuration. Therefore, fully characterize the calibration target material (both aluminum and Krylon) was measured in the following three geometrical configurations. The first was to illuminate the target at an incidence angle of 0°, and measure the reflectance at 10° to 40° degrees (configuration 1). The second was to set the incidence angle to 20°, and measure the reflectance at the opposite side, at 0°, −20°, and −40° (configuration 2). The 20°/−20° measurement determines the degree of specular reflection. The third set of measurements changed both the incidence and reflection angle, keeping the phase angle constant at 20° (configuration 3). The results are shown in Figs. 3.12 and 3.13 for the aluminum material and Krylon squares, respectively. The goniometer appears to suffer from noise in the wavelength range from 1000 to 1400 nm, and jumps around 700 nm, increasingly so for larger reflection angles. Bernard expressed the opinion that these
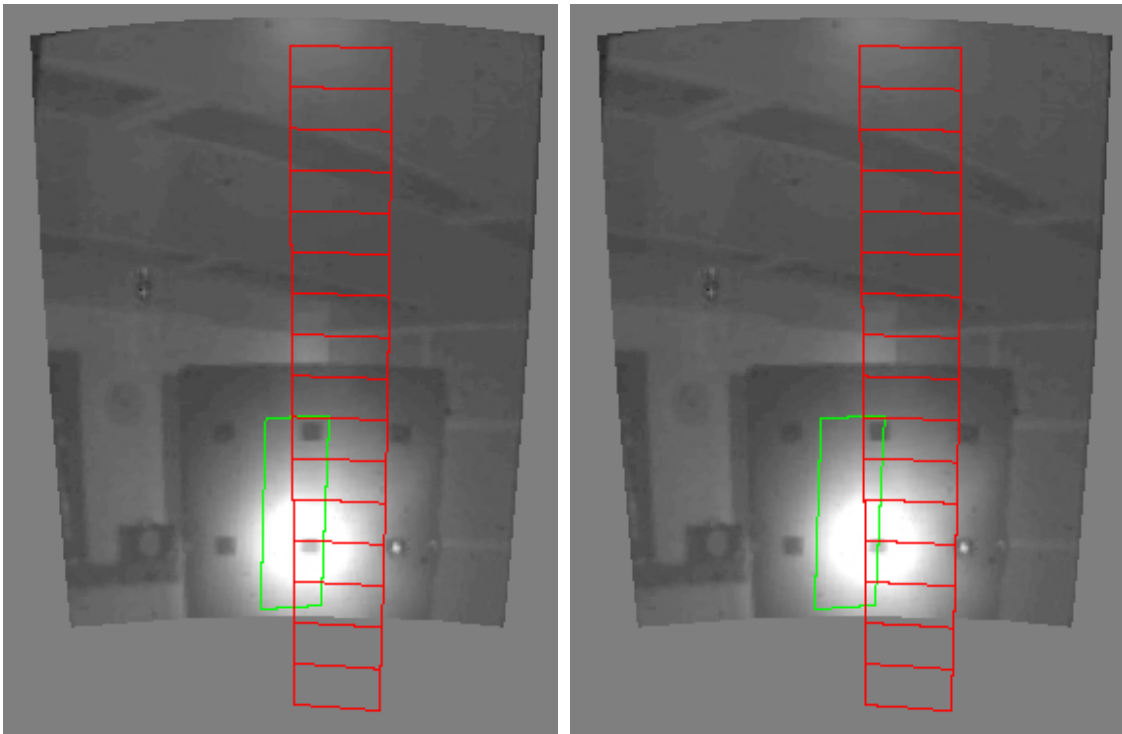
Figure 3.11: A MRI image in polar projection from the SSL calibration experiments with the DLVS (red) and DLIS (green) slits superposed. At **left** the actual situation, and at **right** the images and footprints projected as if the distance to the screen was 25 m, which gives an impression of the parallax effects involved (note that we do not know the SSL parallax). We see the 95.3×147.3 cm aluminum target with its dark Krylon squares positioned in a room at LPL. The lamp reflection spot is visible in the center of the target. The DLVS was operating in the 20-column mode, which yields 16 complete spectra (footprints are numbered 0 to 15 from top to bottom). The brightness and contrast of the image have been adjusted to bring out details in the scene.

changes are not real, and indeed, scaling all measurements to match reveals that the shape of the spectrum is roughly the same in all cases.

Since the target was oriented perpendicular to the lamp beam, we need to know the reflectance of the target at incidence and reflection angle zero. Unfortunately, this measurement was technically impossible. But we have measurements with incidence angle zero at various reflection angles, and one measurement with phase angle zero. When we compare these in Fig. 3.14 (left) it seems that the zero phase angle measurement is a good approximation for the desired one. However, it is very noisy, so I judge the best estimate of the calibration target reflectance to be a fit to the 20°/0° measurement scaled to the level of the 20°/−20° measurement. The procedure is illustrated in Fig. 3.14 (right). As a final adjustment, we need to account for the Krylon squares. The aluminum is about 3.4 times as reflective as the Krylon, the squares of which take up 3.5% of the space on the plate. The Krylon reflectance seems to have the same functional dependance on wavelength as the aluminum (Fig. 3.13, right), so we can simply scale down the reflectance. We arrive
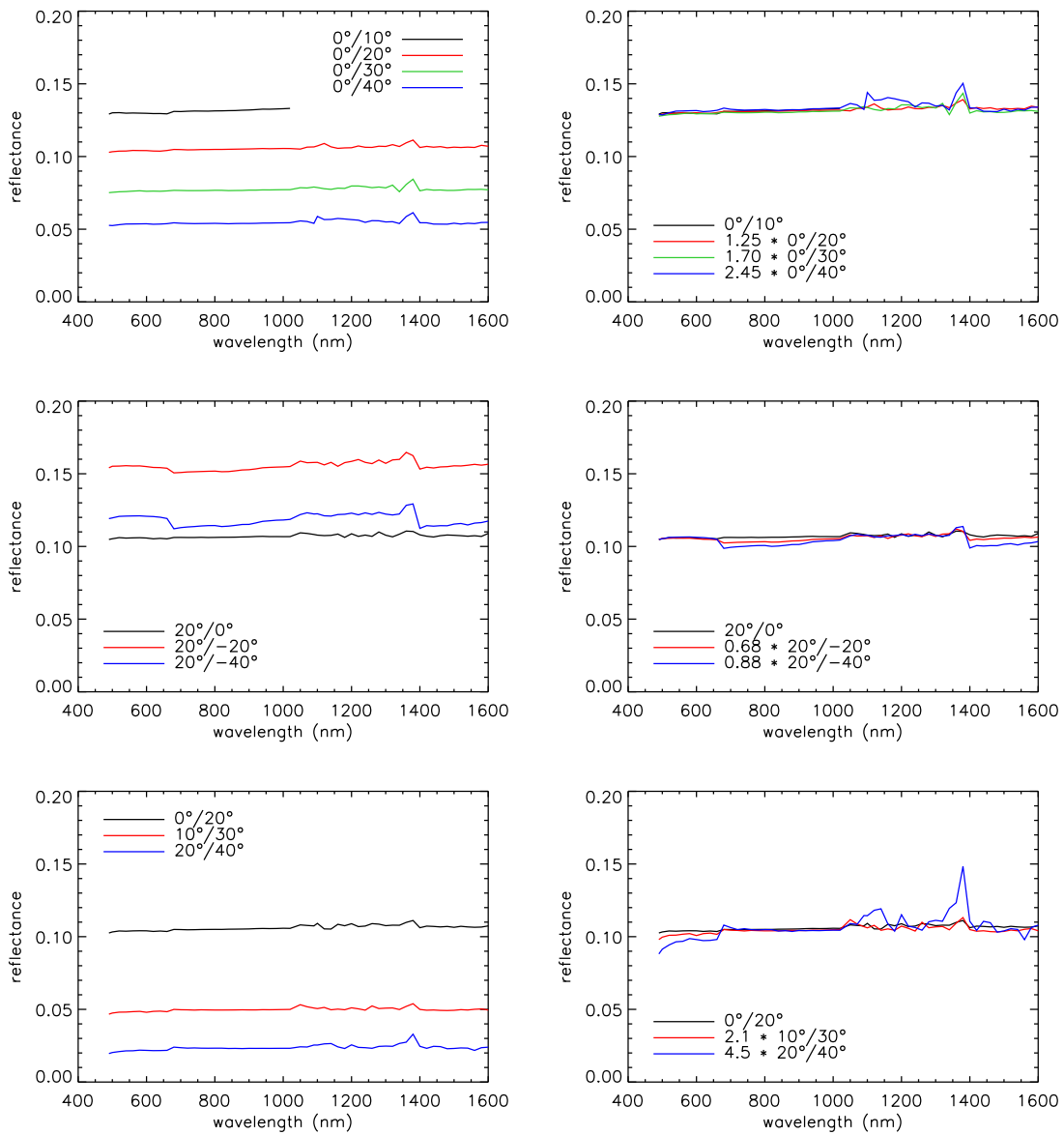
Figure 3.12: The reflectance (radiance coefficient) of the aluminum calibration target in the DISR wavelength range as measured by the Grenoble goniometer. We have from **top** to **bottom** the goniometer configurations 1, 2, and 3 described in the text, with at **left** reflectances, and at **right** scaled reflectances. The first and second number in the legend are the incidence and reflection angle, respectively.
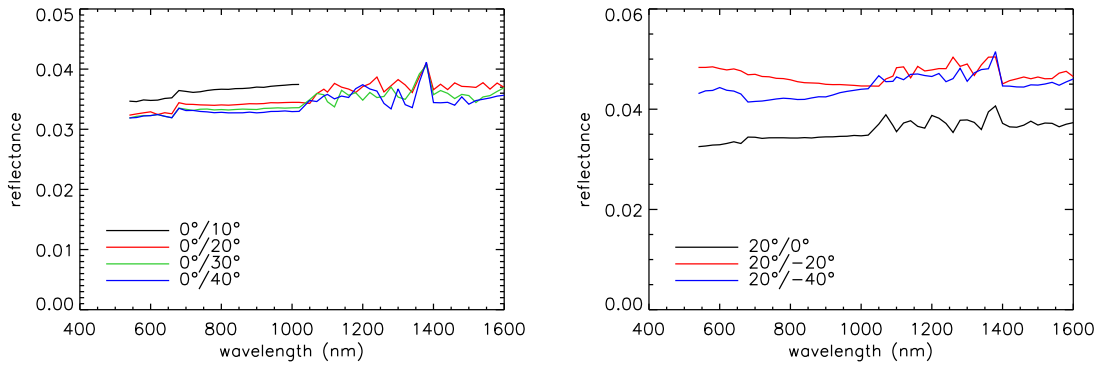
Figure 3.13: The radiance coefficient of the Krylon squares on the calibration target as measured by the Grenoble goniometer. The first and second number in the legend are the incidence and reflection angle respectively. **Left**: Incidence angle 0°. **Right**: Incidence angle 20°.
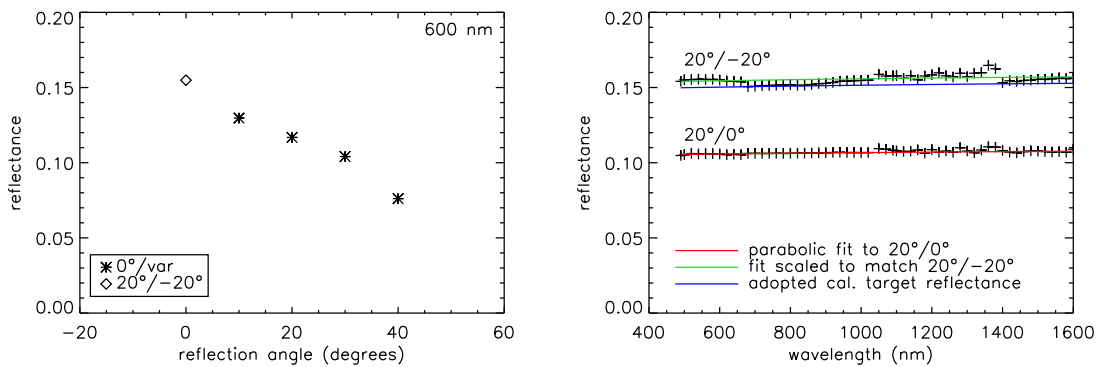

Figure 3.14: **Left**: The radiance coefficient of the aluminum target at 600 nm, measured at incidence angle 0°. The reflection angle was varied, except for the data point at 0°, which has both incidence and reflection angles 20° to measure specular reflection. **Right**: To determine the calibration target radiance coefficient I first fit a parabola to the 20°/0° data (which is least noisy) in the wavelength intervals 520-1020 and 1400-1600 nm, then scale this fit to match the 20°/−20° data, and again scale this curve down slightly to accommodate for the Krylon squares.

at the following expression for the average radiance coefficient of the calibration target:

$$r_C^{\text{target}} = 0.148 + 4.87 \cdot 10^{-6}\lambda - 1.06 \cdot 10^{-9}\lambda^2 \tag{3.4}$$

with λ the wavelength in nm. This is the reflectance I use to determine the SSL spectrum.

3.6.2   DLVS SSL spectrum

For the calibration experiment the DLVS was set to the 20-column mode, which offers the highest spatial resolution. During the actual descent this mode was used only for the two spectrophotometric maps. Spectra showing lamp light were acquired either in the

2-column mode (around the time of landing), or the 10-column mode (after one minute on the surface). It is therefore important to characterize how the instrument behaves in the different modes when observing the reflected lamp signal. I simulate the 2- and 10-column modes by summing columns of the 20-column mode spectra. When the spectra are processed in regular fashion the appearance of the SSL spectrum depends strongly on the mode; Figure 3.15 shows that it is retrieved well in the 20-column mode, but that it shows odd dips and kinks at the red end in the 2- and 10-column modes. This behavior can be understood in the following way. The lamp reflection spot has a finite size on the CCD, and creates steep gradients on its edges along the spatial dimension of the DLVS (Fig. 3.16). When the geometric correction is applied (see §3.4.2) the detailed shape of the lamp spot can be accurately reconstructed from 20 data points, but errors result when only 10 data points are available, even though cubic spline interpolation is used. The situation is much worse in the 2-column mode; it is impossible to reconstruct the peak of intensity by inter- and extrapolation from only two data points (Fig. 3.17). When reconstructing the surface reflectance from the 2-column mode spectra acquired around landing, it is imperative to divide out the lamp spectrum before applying the geometric correction. Save real surface brightness gradients, the resultant 2×200 pixel array will be mostly flat in intensity, minimizing extrapolation errors. So to process the 2-column spectra we need two lamp spectra, one for each of the summed columns. We must calculate these in units of observed intensity (instead of DN) since the calibration was done at room temperature and the responsivities are temperature dependent. Figure 3.15 (bottom right) shows the two adopted SSL spectra, corrected for the reflectance of the calibration target (Eq. 3.4).

3.6.3   DLIS SSL spectrum

Deriving the SSL spectrum for the DLIS range is more straightforward compared to the DLVS, because the DLIS features only a single footprint. During the calibration experiment the reflectance of the target was measured twice with the DLIS window uncovered (Fig. 3.18, left). The experiment was carried out in the LPL lab at room temperature, with the detector and optics temperature being in the range of 304-306 K and 294-297 K, respectively. Even though the air in Tucson is generally very dry, atmospheric water is clearly detected, and its absorption lines can be modeled well. After converting the observed intensity into the flux at 4.68 m, I remove the absorption lines, saturated pixels, and the second order response from the SSL spectrum by fitting a cubic spline (Fig. 3.18, right).

Merely switching on the SSL imposes an extra charge on the DLIS (Fig. 3.19). I used a linear fit to the observed extra intensity (in W m^{-2} μm^{-1} sr^{-1}),

$$I_{\text{extra}} = 0.0014 - 6.4 \cdot 10^{-6} \times \text{pixel}, \tag{3.5}$$

to correct the Titan observations. Here I assume the effect is not temperature dependent.

3.6.4   Full SSL spectrum

Combining the DLVS and DLIS observations we arrive at the complete SSL spectrum in Fig. 3.20. The DLVS peaks at a higher intensity than the DLIS because a relatively larger fraction of its footprint is covered by the brightest part of the lamp spot (see Fig. 3.11).
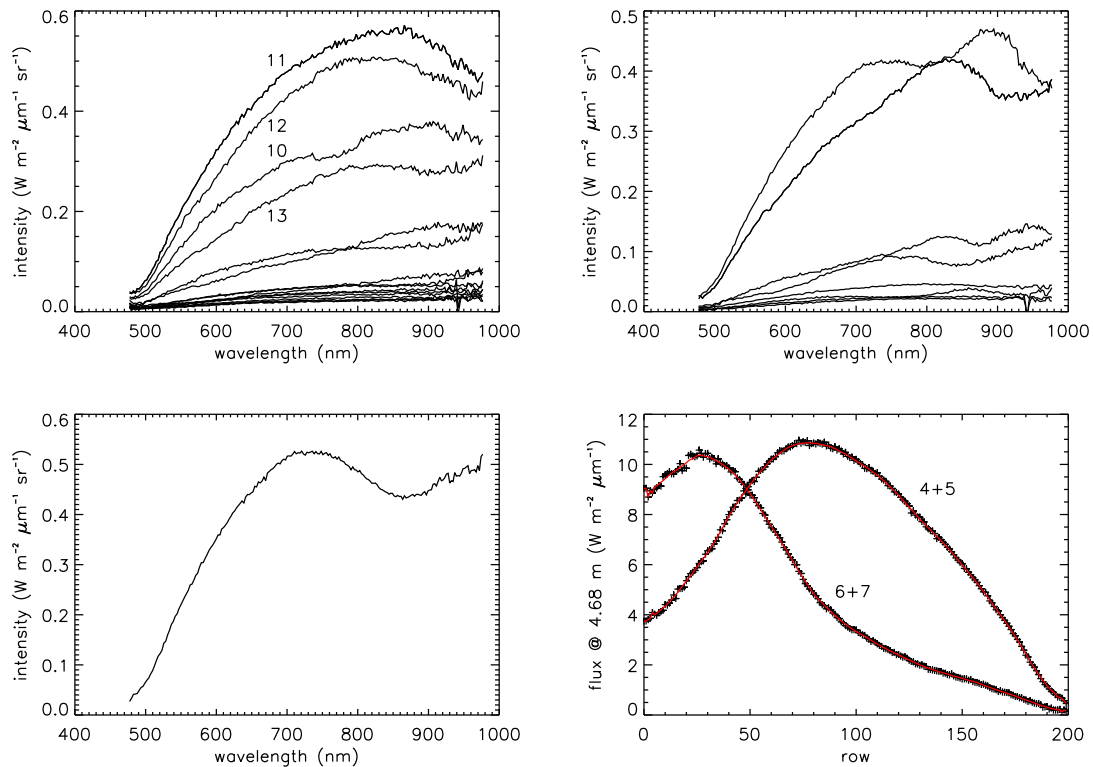
Figure 3.15: The Surface Science Lamp spectrum as observed by the DLVS. **Top left**: The calibrated spectra of all 16 footprints of the DLVS in the 20-column mode, with some footprint numbers indicated (see Fig. 3.11). Pixel 11 offers the best reconstruction of the true SSL spectrum. **Top right**: The lamp spectrum as it appears to the DLVS in the (simulated) 10-column mode. **Bottom left**: The lamp spectrum as it appears to the DLVS in the (simulated) 2-column mode. **Bottom right**: The adopted lamp spectrum (red), with the labels referring to which of the original 20 columns were summed. The observed intensities have been converted to the flux at 4.68 m from the lamp. Note that wavelength decreases with increasing row number.

If we scale the DLVS spectrum to match the DLIS spectrum, both should agree in the wavelength range where they overlap. Clearly they do not; the DLVS spectrum drops more rapidly beyond 850 nm than the DLIS. The fault probably lies with the DLVS. Either the responsivity, which drops steeply beyond 830 nm, is incorrect, or the geometric correction. The reconstructed lamp spectrum is especially sensitive to the latter because of the aforementioned steep brightness gradient on the CCD. It is therefore best to divide the lamp spectrum out of observed spectra before the geometric correction, i.e. before reducing the two summed columns to a single spectrum. The SSL flux adopted for each of the two columns is shown in Fig. 3.15 (bottom right).

3.6.5 Proximity correction

The SSL calibration experiment was done with the target positioned at 4.68 m from the DISR sensor head. The calibrated SSL spectrum can be used to derive the surface re-
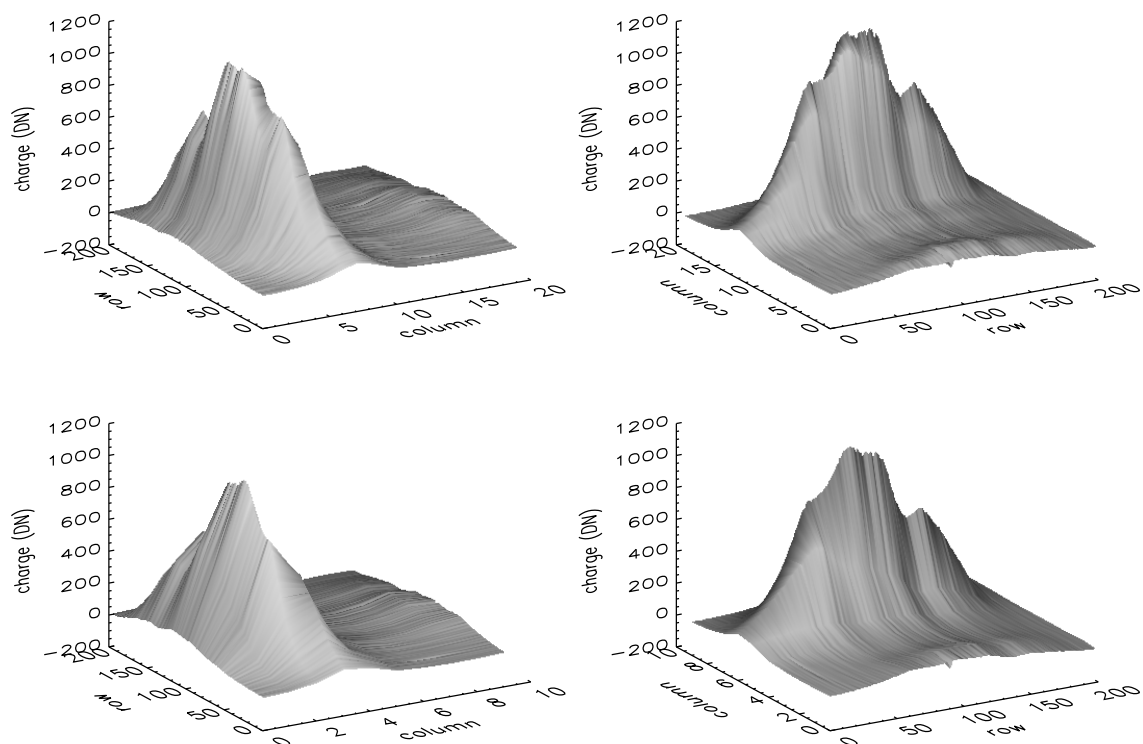
53

Figure 3.16: The Surface Science Lamp signal as it appeared on the 20×200 pixel DLVS section of the CCD during the SSL calibration experiment (corrected for dark signal). **Top**: The DLVS in the 20-column mode. **Bottom**: The DLVS in simulated 10-column mode (with the sum of consecutive columns divided by two). **Left** and **right** are different views of the same surface. Rows and columns represent the spatial and spectral dimension, respectively.

flectance from spectra recorded before landing, when the surface was sufficiently distant. After Huygens had landed however, DISR found itself approximately half a meter from the surface, a distance at which parallax effects are significant. To the DLVS the lamp spectrum looked completely different; the brightness distribution across the columns of the CCD had changed as the lamp reflection spot was observed at a different angle (compare Fig. 3.11 with Fig. 4.7). The situation was aggravated by the onboard summing of columns; if after landing the DLVS had been switched to spectrophotometric map mode (which returns all 20 columns), it would have been possible to use the lamp spectrum in Fig. 3.20 to reconstruct the surface reflectance from the high S/N post-landing spectra. The situation is different for the DLIS. Since the DLIS is a linear array of detectors, looking at a different part of the lamp reflection spot will not change the brightness distribution on the detectors, unless the lamp spectrum is variable within the beam. As the flight model is currently unavailable, a spare camera was kept in working condition at LPL for testing purposes. I hoped that experiments with the DISR#2 spare could provide clues to how the DISR#3 downward looking instruments responded to the bright lamp spot at close range.

Aided by Chuck See I performed several experiments with the DISR#2 model at LPL
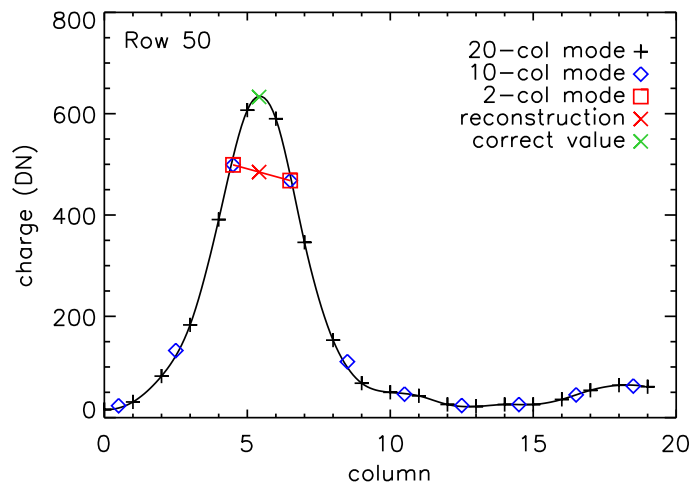
Figure 3.17: The intensity peak on the DLVS section of the CCD imposed by the SSL cannot be accurately reconstructed from only two columns. The figure shows the data in the twenty columns of the DLVS in a transect through row 50, with a spline fit drawn in black. Shown in blue are simulated values (divided by two) that would be returned in the 10-column mode. In the 2-column mode only two of these would be returned (red squares), in which case the geometric correction interpolates the charge (red cross) to be much lower than the real value (green cross).
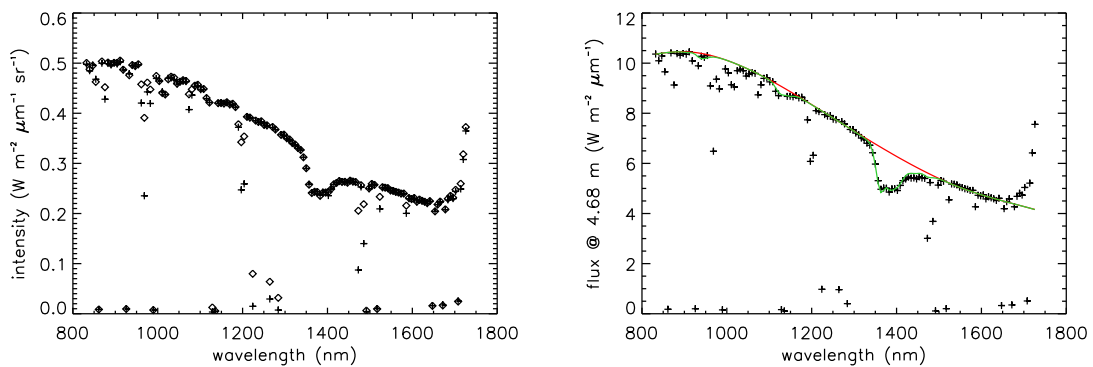

Figure 3.18: The Surface Science Lamp spectrum as observed by the DLIS. **Left**: Calibrated intensities from two separate DLIS exposures. Visible are water absorption lines (most clearly around 1.4 μm), saturated pixels, and the second order response beyond 1600 nm. **Right**: The adopted SSL spectrum (red) was obtained by fitting a spline through the average of the two spectra at left (black). The green line is the spline fit including water absorption (coefficients from the GEISA database, courtesy Emmanuel Lellouch). The observed intensities have been converted to the flux at 4.68 m from the lamp.
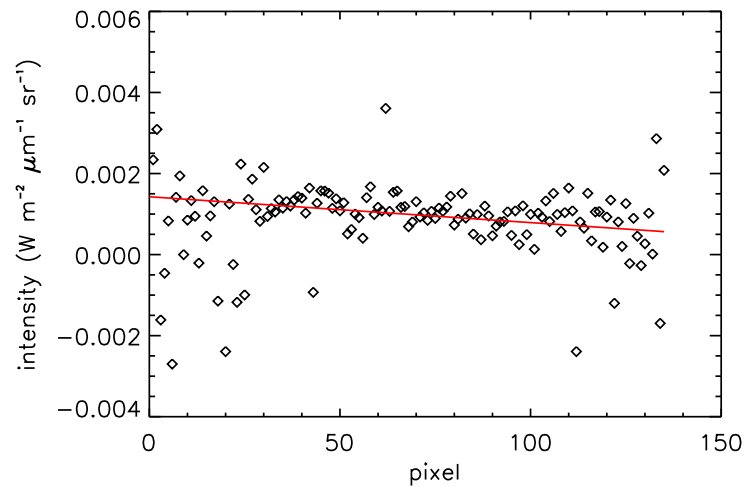
Figure 3.19: The extra intensity observed by each of the 136 DLIS detectors (pixels) due to the SSL being switched on. This was determined as part of the calibration experiment by covering the DLIS window and switching the SSL alternately on and off. In red a linear best fit to the data, which was used to correct the Titan spectra.
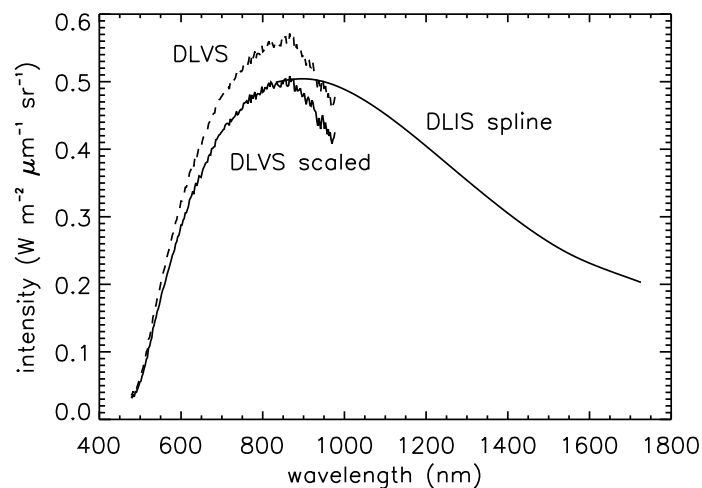

Figure 3.20: The full spectrum of the SSL as observed by the DLVS and the DLIS during the calibration experiment. The dashed DLVS spectrum is that of footprint 11 (Fig. 3.15, top left). The DLIS spectrum is a spline fit (Fig. 3.18, right). The drawn DLVS spectrum has been scaled to match the DLIS spectrum at 850 nm.

in December 2005. On 9 December a cardboard target sprayed with white Krylon paint was placed perpendicular to the lamp beam at 4.46 m, and measurements were performed with all downward looking instruments with the SSL switched alternately on and off. After the target was moved in a position parallel to the camera at 51 cm (as measured from the SLI tip), the same set of measurements was repeated. The ratio of the intensity observed by the DLIS at far and close distance to the target is shown in Fig. 3.21 (left). Like in the calibration experiment (Fig. 3.18), the result shows absorption lines from water vapor present in the 4 m optical path. Assuming the lamp flux scales from 4.68 to 4.46 m according to $1/d^2$, we find that at close range the SSL is perceived to be 3.04 times weaker as would be expected from the calibration experiment (again, scaling according to $1/d^2$); a clear consequence of parallax. In addition, the ratio appears to oscillate at lower wavelengths. The responsivity is low here, so dividing probably amplified fringes, which are known to plague the flight model. The ratio shows a significant change around 1.5 μm. The responsivity is nominal here, and the reason why the intensity measured with the target at close range is relatively low is not clear. A spline fit was used to correct the SSL spectrum for processing the post-landing DLIS spectra.

On 19 December the procedure was repeated at distances of 4.48 m and 50 cm to acquire the DLVS ratios in Fig. 3.21 (right). The DLVS was in the 20-column mode, and to simulate the 2- and 10-column modes I summed consecutive columns. I then divided the summed columns of the far exposure by those of the near exposure. Only the summed columns 4+5 and 6+7 (the 2-column mode columns) were of use, as the others were too noisy. Apart from the noisy edges (where the responsivity is low), the ratio curves are quite smooth, except for some features of unknown origin around row 130. To get rid of the noise I constructed spline fits to the data, and used these to convert the calibrated pre-landing SSL spectrum into a hypothetical post-landing spectrum for processing the 2-column mode spectra. Note that the correction factors were applied to the two summed columns before performing the geometric correction.
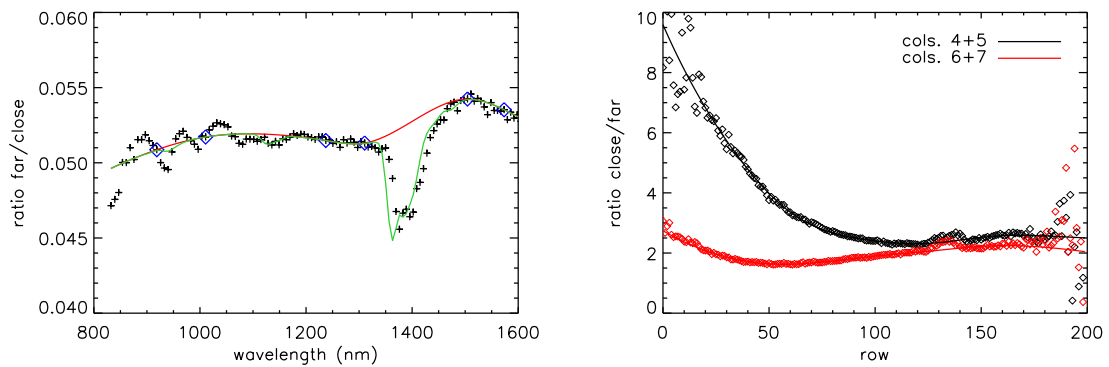
Figure 3.21: The SSL of the DISR#3 flight model was never calibrated with a target at close range. We performed an experiment with the DISR#2 spare with targets at both far (4.5 m) and close (50 cm) range, and calculated the close/far ratio of the SSL spectra as measured by the DLIS (**left**) and DLVS (**right**; 2-column mode). Drawn through the data are cubic spline fits. The DLIS spectrum shows water absorption lines, outside of which the spline points (blue) were chosen; the green line is the spline fit including water absorption (courtesy Emmanuel Lellouch).

4 DISR Observations

During the descent DISR switched between different modes of operation to maximize the science return. The main trigger for this was the probe altitude. The mode determined which sub-instruments were active, the way in which they acquired data, and the format in which data was returned. Close to the surface the camera interchanged modes rapidly to make optimum use of the limited bandwidth available for data transfer to Cassini. As the focus of this thesis is the surface we are primarily interested in the modes active late in the descent. In the next section I provide an overview of these modes, concentrating on their effect on the operation of the downward looking instruments. Especially the operation of the DLVS and the DLIS was altered substantially, altering the number and spatial extent of their footprints. In Sec. 4.2 I determine the surface coverage of the spectrometer footprints in various near-surface modes, and project them on DISR mosaics of the surface. In the following chapters I will frequently refer to the maps presented in this section.

4.1 Operational modes

Measurements by the various DISR sub-instruments were organized in cycles. Huygens data stream 524b contains 165 cycles, each labeled with a sequential number. A single cycle generally contains measurements by multiple instruments. The cycle numbers, and other details, of all measurements relevant to this thesis are tabulated in Appendix A. DISR operational modes consist of multiple cycles, with the exception of the spectrophotometric maps. Modes early in the mission were optimized for observing the atmosphere. In the second half of the descent DISR entered various "near surface" modes, better suited for observing the surface. Then just before landing it switched modes rapidly to ensure that a diverse set of measurements would be recorded of the landing site itself. In all modes the imagers and the violet photometers operated in the same way, with the exception of the HRI returning only half images just before landing. The spectrometers, however, operated in distinctly different ways depending on the DISR mode. Two modes that affected their operation most strongly are the spectrophotometric map mode, the Medium Low Near Surface (MNS) mode (DLIS only), and the Very Low Near Surface (VLNS) mode. In the next paragraph I provide a detailed overview of the DISR modes in chronological order, but first I explain the different operational modes available to the downward looking spectrometers. The DLVS shared the CCD with the DISR imagers, occupying an area of 20 columns by 200 rows. Generally, adjacent columns of the DLVS section on the CCD were summed, and the resulting 10 columns were returned. I refer to this DLVS mode of operation as the **10-column mode**. Due to the fact that the slit projection on the CCD was warped (see §3.4.2), these 10 columns yield 8 complete spectra. Around the

time of landing only 2 out of 10 summed columns (4+5 and 6+7) were returned, from which a single spectrum is retrieved. I refer to this mode of operation as the **2-column mode**. The full set of 20 columns, which yields 16 individual spectra, was only returned in the spectrophotometric map mode. The DLIS had its own linear array of sensors. Its regular mode of operation was to sum observations acquired at (perceived) identical azimuth intervals over multiple probe rotations. The failure of the Sun sensor meant that the instrument actually summed contributions acquired at different azimuth angles, yielding azimuthal averages for most of the descent. However, in three special modes it operated distinctly different. In the spectrophotometric map and MNS modes the DLIS summed only two exposures acquired over a very short time. The operation included acquisition of two dark exposures (with shutter closed). In the VLNS mode it just acquired a single, brief exposure without summing at all. Dark exposures were acquired separately.

In the first half of the descent DISR alternated between the imaging mode, in which all instruments acquired measurements, and the non-imaging mode, in which the three imagers were not active, interspersed with calibration cycles. In the latter stages of the descent the camera went into a series of special modes, depending on the probe altitude. These modes are listed in Table 4.1 and their sequence is depicted in Fig. 4.1. The first was the High Near Surface (**HNS**) mode, activated at 23.3 km altitude, which lasted for almost 50 minutes. Imaging in this mode was strictly panoramic, i.e. images were acquired in groups for the duration of around 100 seconds with 200 seconds in between. A 10-column mode DLVS spectrum was always recorded within a second of an image triplet. DLIS exposures were summed over many rotations on board, resulting in azimuthal averages. The HNS mode is of limited relevance to the work described in this thesis. More important are the two special, single cycle modes called **spectrophotometric map** 1 and 2 (**SM1** and **SM2**). In the spectrophotometric map mode only the DLVS and DLIS acquired spectra, as fast as possible. They were meant to cover the full range of azimuths in one rotation, to build a complete picture of the surface below. Due to the failure of the Sun sensor the spacecraft did not know where it was pointing at any time, but fortunately, full azimuthal coverage was almost achieved for both maps. Only in the spectrophotometric map mode the DLVS achieved full spatial resolution by transmitting all 20 columns. The operation time of the DLIS was very short, only half a second, in which it acquired two samples which were summed on board. The SM1 cycle interrupted the HNS mode at an early stage. The SM2 cycle was sandwiched in between the HNS and the **Medium Near Surface** (**MNS**) mode. Apart from images, the MNS mode returned regular, 10-column mode DLVS spectra. The DLIS obtained spectra similar to those in the spectrophotometric maps, only with larger sampling time, effectively integrating over an azimuth range of about $50°$. The Surface Science Lamp (SSL) was switched on at the end of this mode, at mission time 8734 s, and was left on for the remainder of the mission. The Low Near Surface (**LNS**) mode was very brief (13 seconds) and had DISR only return four half HRI images, the last images of the descent. The subsequent **Very Low Near Surface** (**VLNS**) mode was initiated 210 m above the surface and remained active past landing. It was a strictly non-imaging mode, in which only the visual and infrared spectrometers and the violet photometers were gathering data. The DLVS returned 2-column mode spectra, while the DLIS recorded single, brief exposures, either with shutter open or closed. After landing at mission time 8869.77 s (Zarnecki et al. 2005), the DLVS quickly reduced its exposure time to deal with the flood of reflected lamp light. It obtained correctly exposed
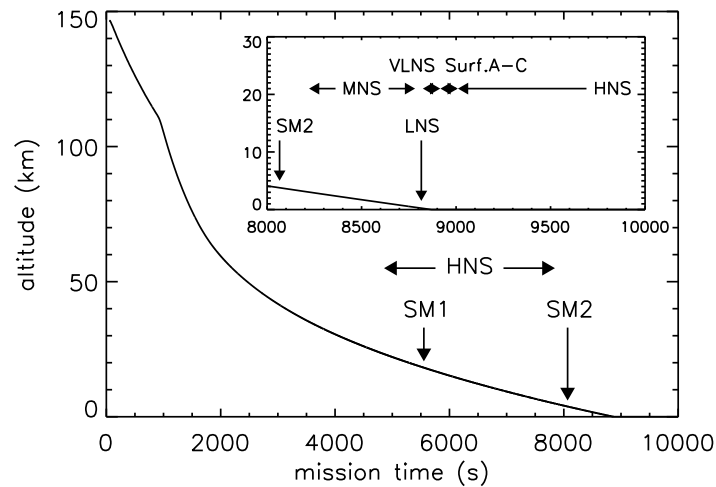
Figure 4.1: The altitude profile of the Huygens probe as determined by the HASI experiment (Fulchignoni et al. 2005), with the low altitude operational modes indicated. The inset zooms in on the time of landing.

spectra throughout this phase, apart from two partly overexposed spectra directly after landing. All the post-landing DLIS spectra in this mode, however, are overexposed. After 46 seconds after landing DISR ran through various brief surface modes (A/B/C), at the end of which imaging was resumed. The DLVS returned to the 10-column mode, initially varying its exposure time, leading to a series of overexposed spectra. The DLIS returned to the summing mode, adding very brief exposures on board for a duration of 2 seconds. As a safeguard (the probe's software might have been wrong about having landed!) the HNS mode was activated again after 2 minutes and 20 seconds on the surface. The DLVS continued to operate in the 10-column mode, while the DLIS summed thousands of samples in operations lasting over 70 seconds. Both spectrometers again initially varied their exposure (sampling) times, leading to a series of overexpose spectra. Sadly, no more spectrophotometric maps were acquired, which would have given us the complete set of 20 (unsummed) columns for the DLVS.

In the next chapter I reconstruct the surface reflectance spectrum from DLVS and DLIS spectra recorded in the VLNS and Surface B modes. Then Chapter 6 investigates how the intensity coming from the surface depends on the solar phase angle, using DLVS and DLIS spectra from both spectrophotometric maps, the MNS mode (DLIS only), and the VLNS mode. Chapter 7 concludes this thesis by looking into the rapid temporal changes observed around landing by various downward looking instruments (VLNS mode), and their long term behavior on the surface (Surface B and second HNS mode).

4.2   Context

The Huygens attitude and trajectory reconstruction of Karkoschka et al. (2007), shown in Fig. 4.2, was used to project the DLVS and DLIS footprints on DISR images of the surface. The probe drifted from west to east with ever decreasing velocity, to eventually

Table 4.1: DISR modes of operation in the latter stages of the descent (cycles 50-165 from data stream 524b). Note that the first HNS mode was interrupted by the SM1 mode. Cycle 62 was a 'dark' cycle. Landing occurred exactly in the middle of the VLNS phase at mission time 8869.77 s. See text for details.

mode	cycle	mission time (s)	duration	altitude (km)
HNS	50-60	4856-7845	49m 49s	23.3-4.9
SM1	52	5534-5571	37s	18.3-18.0
SM2	61	8046-8086	40s	3.9-3.7
MNS	63-86	8222-8783	9m 21s	3.0-0.39
LNS	87-90	8810-8823	13s	0.27-0.21
VLNS	91-140	8824-8916	1m 32s	0.21-0
Surface A-C	141-151	8917-9009	1m 32s	0
HNS	152-165	9010-13006	1h 6m 36s	0

land in a lake bed approximately 3.5 km south of the coastline visible in the DISR mosaic (Fig. 1.10). Figures 4.3 to 4.6 show the location of footprints of spectra acquired in selected special modes during the latter stages of the descent. All maps are in gnomonic projection and have the probe landing site exactly in the center. SM1 was acquired at 18 km altitude and covers both the lake bed and the land/river area north of the landing site (Fig. 4.3). Remember that the spectrophotometric map mode offers the highest spatial resolution for the DLVS: 16 spectra per exposure versus 8 for the regular mode. The DLIS acquired brief, single exposures with relatively small footprints. At the time of recording of the SM2 the probe had descended to 4 km altitude, hence it covers lake area only (Fig. 4.4). In Fig. 4.5 we zoom in on a small (1.4 × 1.4 km) area enclosed by the SM2. Here we find the MNS and VLNS spectra, spiraling inward towards the landing site. The VLNS mode offered the lowest spatial resolution for the DLVS, only a single spectrum per exposure. Hence the VLNS footprints can easily be identified; they are the small group of 11 single-footprint DLVS (red) and 7 DLIS (green) spectra in the center of Fig. 4.5, all acquired within a single probe rotation. This area is enlarged in Fig. 4.6, which shows the immediate surroundings of the landing site. Unfortunately, most of this area was imaged at very poor resolution; the last image to show the landing site itself (HRI **384**) was recorded at an altitude of 20 km. Consequently, none of the terrain covered by the VLNS footprints has been imaged at a resolution of better than circa 100 m per pixel. Most likely the probe landed in the featureless gray terrain that dominates the area, but we cannot exclude that it landed on an extension of the relatively bright ridge that runs diagonally through Fig. 4.5 from center right to bottom left.

Remarkably, the footprints of the last few pre-landing spectra may have been captured by the images transmitted from the surface. Figure 4.7, albeit not necessarily completely accurate in its positioning of the footprints, shows the view from the surface. The footprints of the last two DLVS and last DLIS spectra are located only a few meters from the probe. It is therefore reasonable to assume that these observations are representative for the terrain visible in the surface images. The rocks visible in the SLI image appear to be small boulders. This is because the probe's perspective is that of a crawling toddler, with DISR positioned a little bit less than half a meter above the surface. In reality the rounded
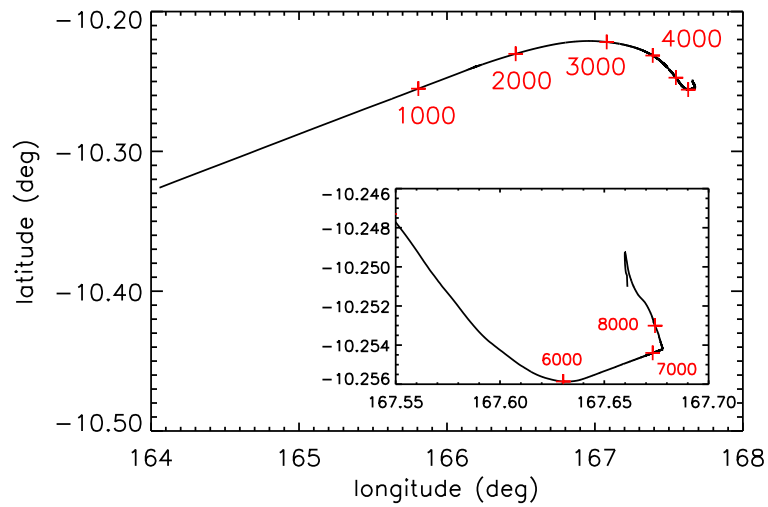
Figure 4.2: The trajectory of the Huygens probe according to the reconstruction of Karkoschka et al. (2007). The trajectory is given in Titan coordinates (latitude vs. east longitude), with a zoom on the last part (inset). Indicated in red are mission times in steps of 1000 s.

rock in the center is a decimeter sized cobble. To create a more natural impression of what the landing site looks like, I reproject the images to match a human's perspective in Fig. 4.7 on the right. Note that this vertically stretches rocks in the foreground that do not lie flat on the surface, but also makes the DLVS footprints appear closer to the probe.
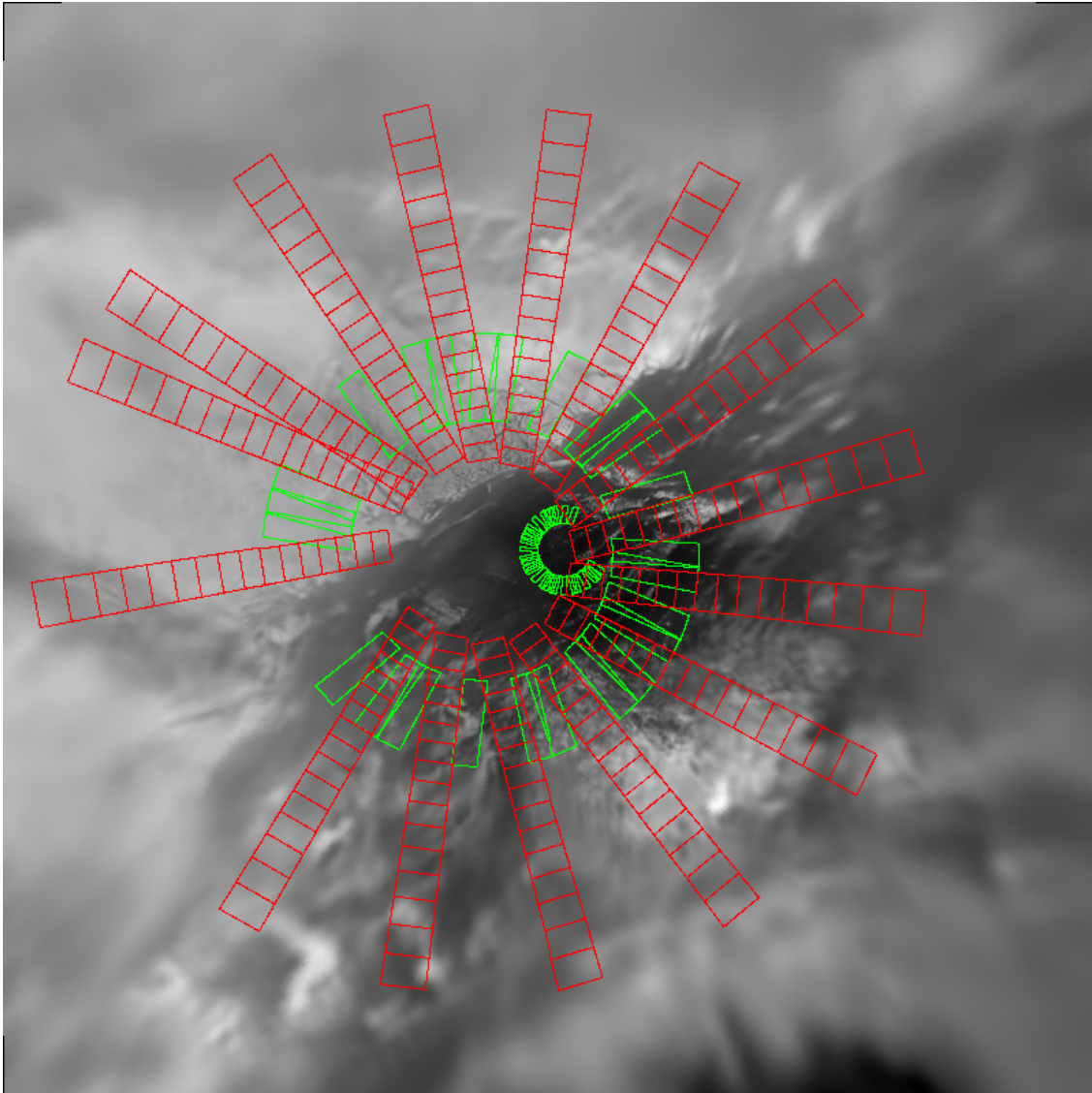
Figure 4.3: The area covered by the first spectrophotometric map in Gnomonic projection (45 × 45 km). The SM1 DLVS and DLIS footprints are overlayed in red and green, respectively. The SM2 DLIS footprints are shown in the center for reference. North is at the top, east at the right. Huygens landed exactly at the center (background mosaic from Karkoschka et al. 2007.)
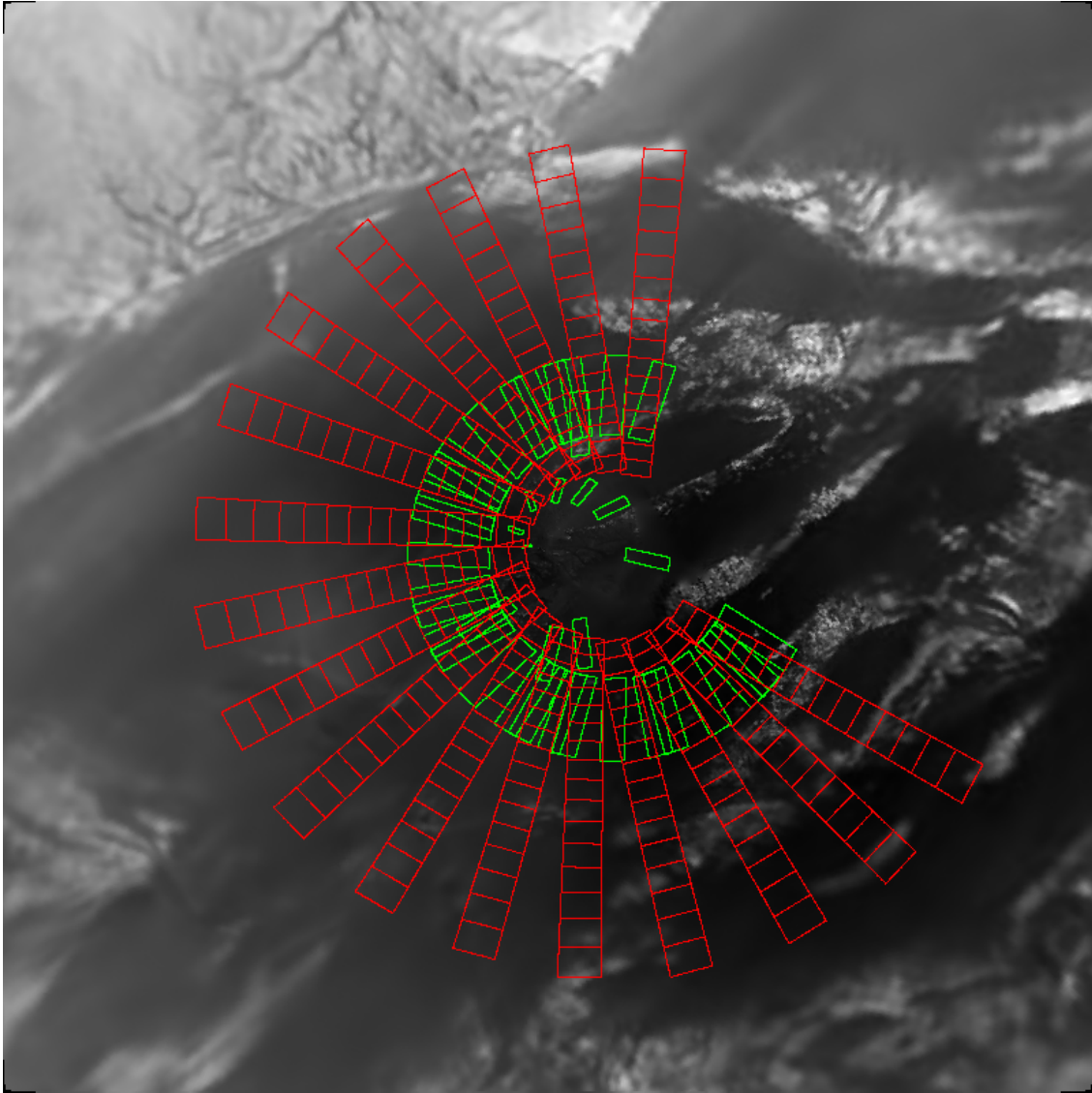
Figure 4.4: The area covered by the second spectrophotometric map in Gnomonic projection (10 × 10 km). The SM2 DLVS and DLIS footprints are overlayed in red and green, respectively. The MNS mode DLIS footprints (in reality wider than shown here) are shown in the center for reference. (Background Karkoschka et al. 2007.)
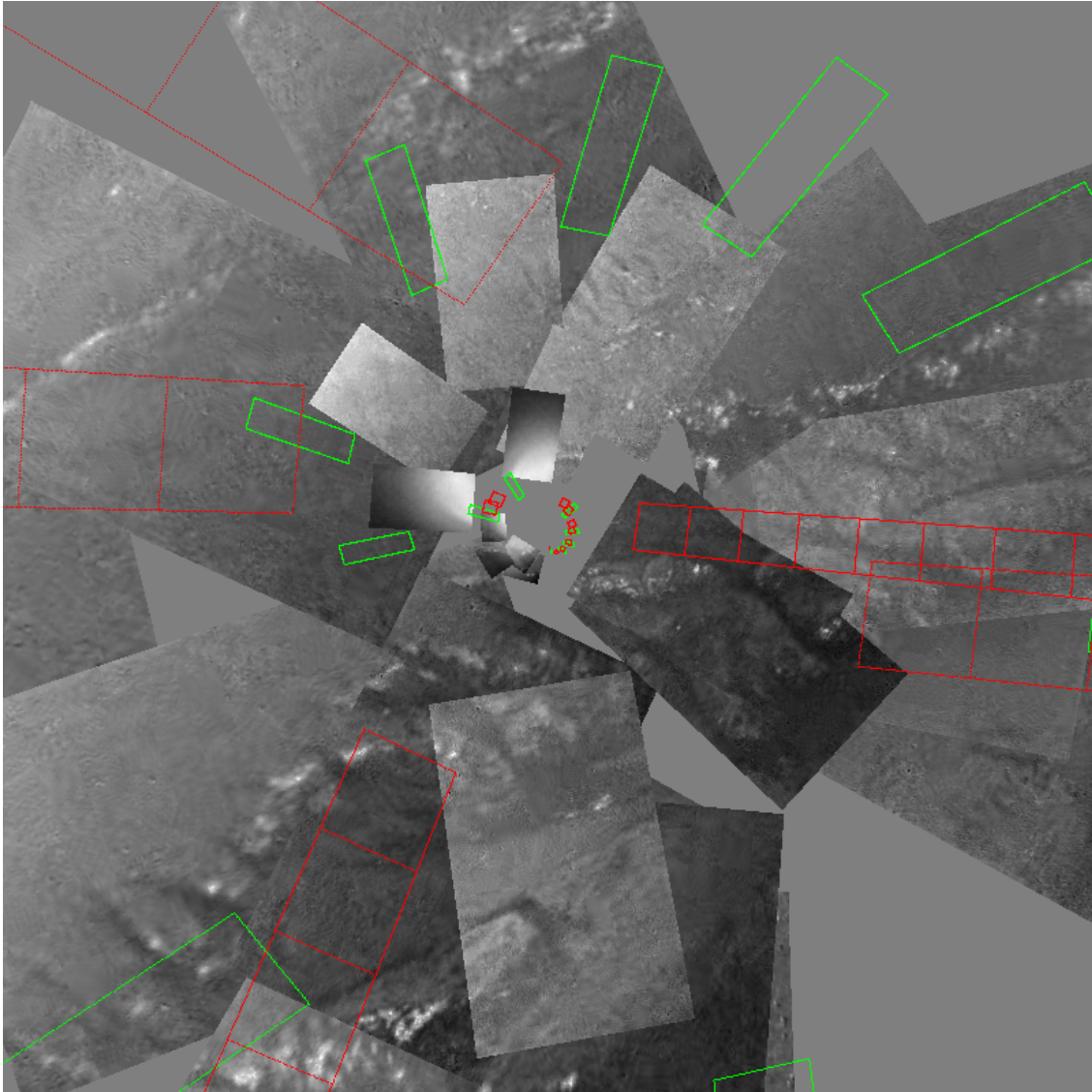
Figure 4.5: The area of the landing site in Gnomonic projection (1.4 × 1.4 km). The MNS and pre-landing VLNS mode DLVS (red) and DLIS (green) footprints are overlayed. The MNS DLVS spectra are 10-column mode spectra, the DLIS MNS footprints are wider in reality than shown here. The VLNS footprints are located in the center (see Fig. 4.6). All available high-res images (HRI **651-721**, MRI **664**-**700**) are shown. Terrain for which only low-res images are available is left gray. The last two full HRI images and the four half ones in the center (HRI **711**-**721**) show internally scattered lamp light at the bottom.

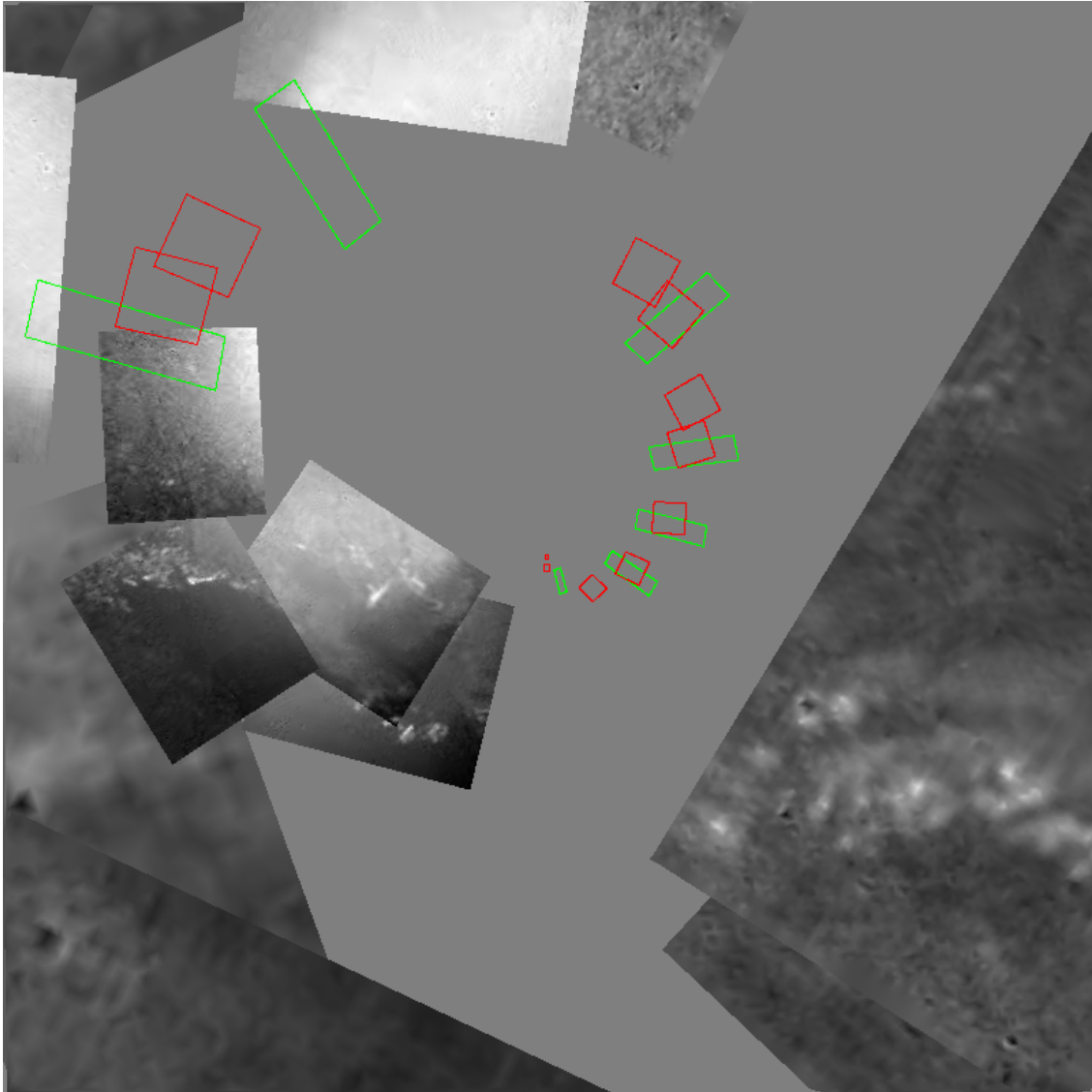Figure 4.6: A close up of the area of the landing site in Gnomonic projection (220 × 220 m). All pre-landing VLNS mode DLVS and DLIS footprints are overlayed in red and green, respectively. All available high resolution (low altitude) images (HRI **651**-**721**) are shown. The last two full HRI images and the four half ones (HRI **711**-**721**) show internally scattered lamp light at the bottom.
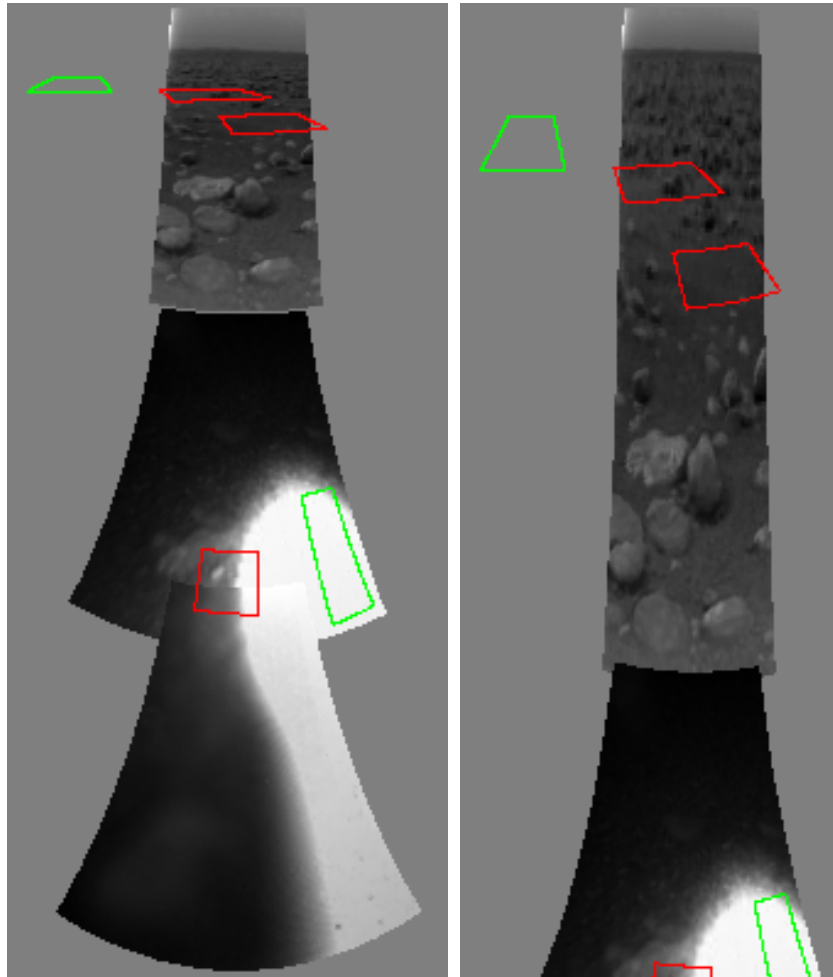
Figure 4.7: The view from Huygens after landing in Mercator projection (7°-100° nadir angle) from the probe's (MRI altitude 46 cm, **left**) and a human's (altitude 1.7 m, **right**) perspective. The last two DLVS and last DLIS pre-landing footprints are overlayed in red and green, respectively. The post-landing VLNS footprints are visible at the bottom. Images: HRI **1211**, MRI **1020**, SLI **742**. The intensity in the SLI image was scaled differently from the MRI and HRI for display purposes. The lamp reflection spot is more or less elliptical in shape; the lamp light at the bottom of the HRI image is internally scattered light (compare Fig. 3.2).

5 Surface Reflectance Spectrum

Attempts to investigate Titan's surface are generally hampered by its thick atmosphere. Aerosols generated by the photodissociation of methane in the stratosphere virtually obscure the surface at ultraviolet and visible wavelengths, while methane predominantly absorbs light in the near-infrared, except in certain narrow wavelength intervals. Ground based (Coustenis et al. 1995, Griffith et al. 2003, Lellouch et al. 2004) and Cassini (McCord et al. 2006) spectroscopic observations of the surface in these methane windows are usually interpreted in terms of water ice and a second, dark material. An important candidate for the latter are tholins, the solid end-product of the photodissociation of methane (Sagan and Khare 1979, Cruikshank et al. 1991, Bernard et al. 2006). In support, Cassini's radar (Elachi et al. 2005) and Huygens' GCMS (Niemann et al. 2005) have found evidence for the presence of organic material on the surface. But so far, tholins have not unequivocally been detected. And since the near-IR methane windows roughly coincide with the water absorption line cores, the lines themselves cannot be resolved and their existence has thus far been inferred. This is where DISR's Downward Looking Visual (DLVS) and Infrared (DLIS) Spectrometers enter the discussion. By actively illuminating the surface with its Surface Science Lamp (SSL) DISR could record a complete surface reflectance spectrum, albeit in a limited wavelength range. Complementary to ground based and Cassini observations, the DISR reflectance spectrum may better constrain the surface composition at the Huygens landing site, which will certainly lead to further understanding of the atmospheric methane cycle (Tobie et al. 2006, Atreya et al. 2006).

Tomasko et al. (2005) made the first attempt to reconstruct the surface reflectance spectrum from DISR measurements. They scaled the last DLIS spectrum acquired before landing, which shows a contribution of reflected lamp light, to the ratio of the up- and downward flux determined from spectra uncontaminated by the lamp. They went on to model the methane absorption in the reflectance spectrum using the Strong et al. (1993) coefficients to estimate the atmospheric methane mixing ratio close to the surface. Their treatment of the DLVS part of reflectance spectrum was preliminary, and led to significant artifacts. Their analysis leaves enough questions open to merit further investigation. For example, what do we find for the absolute reflectance if we take the lamp flux from the original calibration experiments? What is the shape of the visual reflectance spectrum as derived from the DLVS? What is the sensitivity of the reflectance reconstruction to the choice of background spectrum? How do newly available methane absorption coefficients and the revised altitude scale of Huygens' descent affect the analysis? And finally, what is the significance of the inconsistency between the reflectance derived from pre- and post-landing spectra that is seen around 1.5 μm in Fig. 15a in Tomasko et al. (2005)?

This chapter addresses all these questions. First I present my methods in detail in Section 5.1. Then, in Section 5.2 I explain how the DLVS spectra need to be processed with

special care, and why the reflectance cannot be reliably reconstructed from post-landing spectra. In Section 5.3 I re-analyze the DLIS spectra, including the second-before-last pre-landing spectrum which had not been analyzed previously, to arrive at an absolute reflectance scale which is very different from that of Tomasko et al.. In the last two Sections 5.4 and 5.5 I reconcile the DLVS and DLIS reflectances and interpret the result in terms of materials thought to be present on the surface (e.g. tholins, water ice).

5.1   Method

During the last 200 m of the descent DISR was in the Very Low Near Surface (VLNS) mode, in which it acquired DLV exposures, DLVS and DLIS spectra but no images (see §4.1). The SSL had already been switched on in the preceding Medium Near Surface (MNS) mode, but evidence of lamp light can be found only in a handful of spectra recorded just before landing. From these we can reconstruct the reflectance of the surface by subtracting a background spectrum and dividing the result by the lamp spectrum. The background spectrum is that which would have been observed if the lamp had been turned off. As it is obviously not available, it needs to be constructed. I approximate the true background by selecting a spectrum recorded closely in time with, and at approximately the same solar phase angle as the spectrum of interest, and then vary its intensity (by multiplying with a constant) to account for possible surface brightness variations. The criterion for judging the quality of a background spectrum is the smoothness of the final reflectance spectrum. That is, the shape and depth of the methane absorption bands which appear due to the intervening atmosphere, should conform to reasonable assumptions on methane absorption. I assess this by modeling methane absorption using the Karkoschka (1998) coefficients below 1050 nm, and the Irwin et al. (2006) coefficients above (Fig. 5.1).

The surface reflectance is reconstructed from spectra which show evidence of lamp light. For the DLVS these are spectra **785** and **786**, acquired at 16.1 and 8.2 m above the surface, respectively. The details of these and all other spectra mentioned in this chapter (sequential numbers are printed **bold**) can be found in Appendix A. As background spectra I use two spectra acquired shortly before (**772** and **779**), for reasons discussed in detail in the next section. The first three spectra acquired after landing are partly overexposed. I select the first correctly exposed post-landing spectrum (**791**) and three later spectra (including the last one returned) for additional analysis. Two DLIS spectra which show clear evidence for lamp light are **206** and **210**, acquired at 55 and 24.8 m above the surface, respectively. As background spectra I use two spectra acquired shortly before (**199** and **202**). After landing, spectra acquired prior to **249** are all severely overexposed. I select three correctly exposed post-landing spectra (including the first and the last) for additional analysis.

Figure 4.5 shows the footprints of the spectra acquired in the last stage of the descent projected on high resolution images of the surface. Shown is the small (1.4 × 1.4 km) area surrounding the landing site, which is located in the lake bed, approximately 3.5 km south of the coastline visible in the DISR mosaic (Fig. 1.10). The pre-landing VLNS spectra are the small group of eleven single-footprint DLVS (red) and seven DLIS (green) spectra in the center, all acquired within a single probe rotation. Unfortunately, the area

directly surrounding Huygens' landing site was imaged at very poor resolution; the last image to show the landing site itself (HRI **384**) was recorded at an altitude of 20 km. Consequently, none of the terrain covered by the VLNS footprints has been imaged at a resolution of better than circa 100 m. Most likely Huygens landed in the featureless gray terrain that dominates the area, but we cannot exclude that it landed on an extension of the relatively bright ridge that runs diagonally through Fig. 4.5 from center right to bottom left. Figure 4.7, albeit not necessarily completely accurate, shows the footprints of the last three pre-landing spectra to be located close to the probe, possibly in sight of the camera after landing. It is therefore reasonable to assume that reflectance curves we reconstruct for these patches of ground are representative for the terrain visible in the surface images.

To retrieve the reflectance in absolute units we need the lamp flux at Titan's surface, which is unknown. But we can work around this problem by scaling the SSL flux measured by the DISR#3 flight model prior to launch by $1/d^2$, with d the distance from the spectrometer window to the center of the footprint on the surface. This can be understood in the following way. Consider the lamp beam to be a cone. Then the lamp spot on the surface is the intersection of this cone with the surface plane, or ellipse. The intensity reflected back from the surface is then proportional to the inverse square of the area of the ellipse, itself proportional to d. This scaling is valid as long as parallax effects can be ignored (i.e. d is large enough), and tip and tilt of the probe are zero. The spectrometer windows are located a few centimeters apart from the lamp on the DISR sensor head, leading to parallax effects close to the camera. We calculated that parallax can be safely ignored for the DLIS beyond 4 m, but that it makes the lamp flux as observed by the DLVS decrease slightly more with distance than expected from the $1/d^2$ scaling. This effect of the DLVS footprint 'drifting away' from the lamp beam may lead to a lower reflectance as reconstructed from **785** (we did not correct for this). Swinging of the probe does not affect the reconstruction significantly; tilt values of less than a degree are predicted by Karkoschka et al. (2007). Then we can estimate d accurately from the altitude h and the nadir angle of the spectrometer θ_{Sp} if the surface is flat, as it appears to be in the post-landing SLI images (Fig. 4.7).

We reconstruct the reflectance as the radiance coefficient r_{C}, or the bidirectional reflectance of the surface relative to that of an identically illuminated Lambert surface (see Sec. 2.1), also known as "I/F". We would like to subtract from a spectrum I_1 with clear presence of reflected lamp light a background spectrum, i.e. one that would have been recorded if the lamp were off. As we do not have such an ideal background spectrum we approximate it by taking an earlier recorded spectrum I_2 with much less reflected lamp light. Both spectra contain reflected lamp light (at identical phase angle ϕ) and reflected sunlight (at different phase angles ϕ' and ϕ''). Then

$$\pi(I_1 - I_2) = r_{\mathrm{C},1}(\phi)F_{\mathrm{L}}(h_1) + r_{\mathrm{C},1}(\phi')F_\odot - r_{\mathrm{C},2}(\phi)F_{\mathrm{L}}(h_2) - r_{\mathrm{C},2}(\phi'')F_\odot \qquad (5.1)$$

with F_{L} the lamp flux and $F_\odot$ the solar flux at the surface (in W m^{-2} μm^{-1}). We now make two simplifying assumptions. The first is that the radiance coefficient is spatially constant: $r_{\mathrm{C},1} = r_{\mathrm{C},2} = r_{\mathrm{C}}$. The second is that the solar phase angle of both spectra is the same: $\phi' = \phi''$. This leads to

$$r_{\mathrm{C}}(\phi) = \frac{\pi(I_1 - I_2)}{F_{\mathrm{L}}(h_1) - F_{\mathrm{L}}(h_2)}. \qquad (5.2)$$
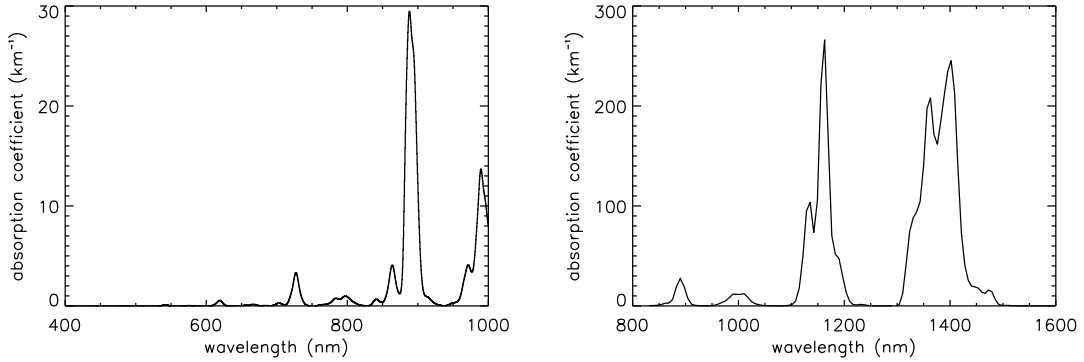
Figure 5.1: Methane absorption coefficients used in this chapter, convolved to the resolution of the instrument. Coefficients above 1050 nm are from Irwin et al. (2006), below from Karkoschka (1998). **Left**: The DLVS wavelength range. **Right**: The DLIS wavelength range. Note the difference in scale.

The first assumption is reasonable (see Chapter 6), and about the second we have to make sure by carefully selecting the background spectrum. What is left now is to determine the lamp flux on Titan's surface $F_L(d) = F_{SSL}(d) \cos \theta_{SSL}$ from the flux F_{SSL} measured prior to launch (see §3.6) and the SSL pointing nadir angle θ_{SSL}. With F_{SSL} having been measured at 4.68 m we find $F_{SSL}(d) = (4.68/d)^2 F_{SSL}(4.68\ \text{m})$, with distance d in meters. Then the lamp flux at the surface is $F_L(d) = F_{SSL}(d) \cos \theta_{SSL}$, and Eq. 5.2 becomes

$$ r_C(\phi) = \frac{(d_1^{-2} - d_2^{-2})^{-1}}{4.68^2} \frac{\pi(I_1 - I_2)}{F_{SSL}(4.68\ \text{m}) \cos \theta_{SSL}}. \qquad (5.3) $$

The distance to the surface is calculated as $d = h/\cos \theta_{Sp}$ from the altitude h and the spectrometer nadir angles (θ_{Sp}) to the center of the footprint on the surface ($\theta_{DLIS} = 21.4°$ and $\theta_{DLVS} = 20.0°$ for the VLNS mode). The DLVS and DLIS wavelength ranges overlap between 800 and 1000 nm. Agreement of the results for both spectrometers in this range would be an important confirmation of the validity of the reconstructed reflectance.

5.2 DLVS

The DLVS in the VLNS mode returned 2 out of 20 CCD columns from which a single spectrum is constructed. Table A.6 lists the VLNS spectra acquired before landing. The last two of these, **785** and **786**, show the presence of lamp light. The former was recorded 3.5 s before landing at an altitude of 16.1 m, the latter 1.8 s before landing at 8.2 m. From these spectra we can retrieve the reflectance of the surface by subtracting a background spectrum, and dividing the result by the lamp spectrum. However, finding a suitable background spectrum is not straightforward. Spectrum **772** appears to be a good choice, as Fig. 5.2 shows that it was recorded at approximately the same solar phase angle as **785** and **786**. But its altitude is more than twice as high as, for example, **779**. The additional absorption by haze particles in the last hundred meters may not be negligible. Since this predominantly affects the blue end of the spectrum, **779** may be the better
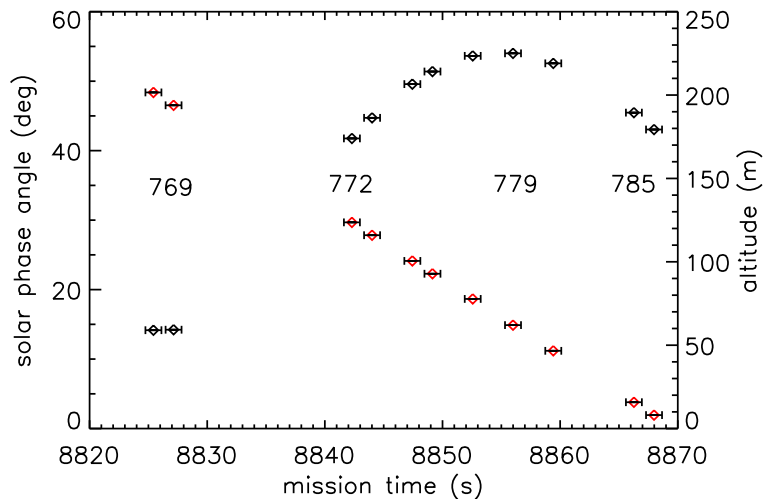
Figure 5.2: The altitude (red) and solar phase angle (black) of all VLNS DLVS 2-column mode spectra recorded before landing. The error bars delimit the exposure time. The sequential numbers of some spectra are indicated; the others may be identified by means of Table A.6.
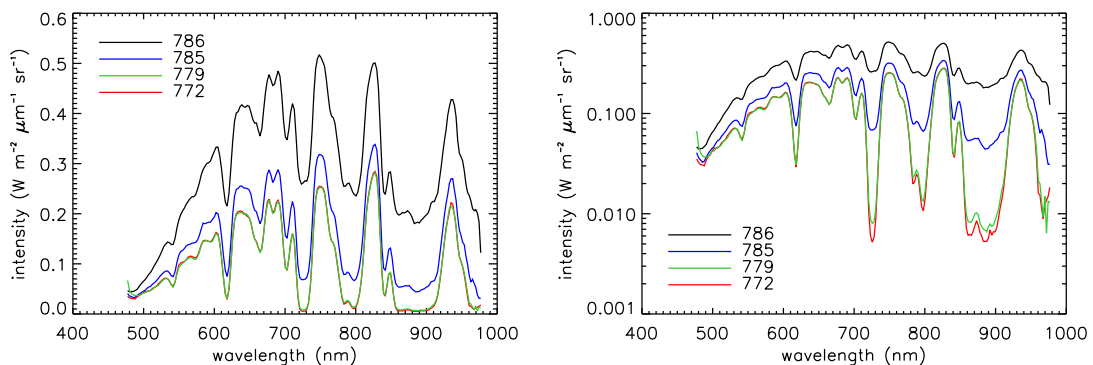

Figure 5.3: The DLVS spectra involved in the visible surface reflectance reconstruction on linear (**left**) and logarithmic (**right**) scale. The two pre-landing spectra in which the lamp signal is clearly present are **785** and **786**. The two spectra used as background are **772** and **779**; they appear to be virtually identical, except in the methane bands

choice at these wavelengths. Since neither spectrum is the perfect choice, I try out both as background. Figure 5.3 shows all the spectra involved in the reconstruction. The procedure to reconstruct the reflectance is illustrated in Fig. 5.4.

The reflectances reconstructed from **785** and **786** are shown in Fig. 5.5. It appears that the choice of background spectrum (**772** or **779**) hardly affects the end result, so in the remainder we use **772** because of the better phase angle. What matters more is how much background we subtract. Figure 5.6 (left) shows how changing the background by a few percent affects the reflectance of **785** in the methane windows; subtracting too much background creates "absorption lines" in the methane windows, whereas the opposite creates "emission lines". Hence our strategy is varying the background to achieve maximum smoothness of the reflectance. The effect on spectrum **786** is more subtle (Fig. 5.5, right);
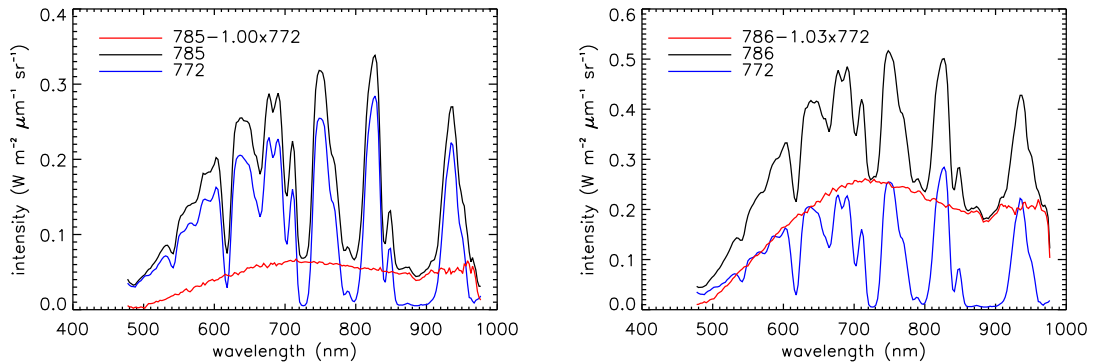
Figure 5.4: The procedure to reconstruct the reflectance is illustrated for the two pre-landing DLVS spectra (**left**: **785**, **right**: **786**). The lamp-only spectra (shown in red) are constructed by subtracting background spectra (blue) from the observed spectra (black). Compare the lamp-only spectra with the simulated 2-column mode lamp spectrum in Fig. 3.15 (bottom left).
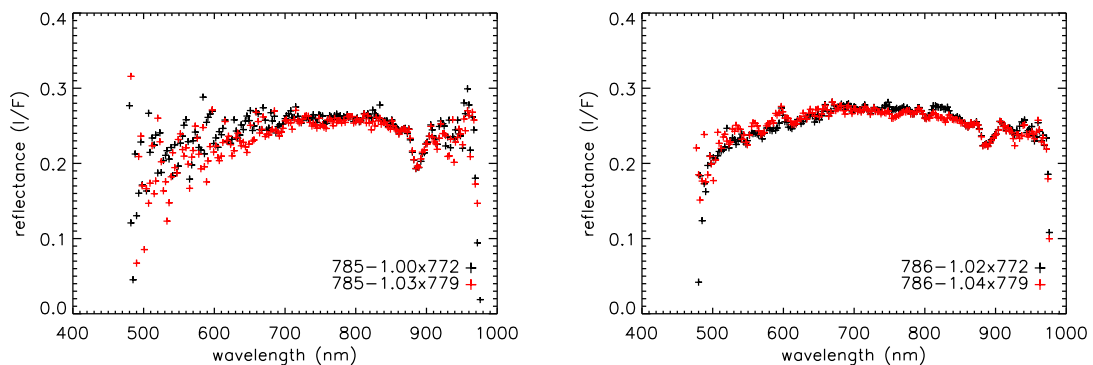

Figure 5.5: The visual surface reflectances derived from the one-before-last (**left**: **785**) and last (**right**: **786**) 2-column mode DLVS spectra before landing. Different background spectra (**772** and **779**) were subtracted before dividing out the lamp.

subtracting too much background makes the red slope below 700 nm less smooth, too little creates spurious emission lines. Another important factor in the reconstruction is the altitude at the time of acquisition of a spectrum. We calculated the altitude from the probe impact velocity of $4.60 \, \text{m s}^{-1}$ (as determined by the SSP), and the assumption of a constant descended velocity in the last fifty meters. Figure 5.7 show the consequences of changing the altitude slightly. Overall, the reflectances reconstructed from **786** and **786** are similar; increasing towards 800 nm and decreasing beyond. Naturally, the **785** reflectance is noisier, but the only significant difference is the depth of the 890 nm methane absorption band, as expected because **785** has an optical path length about four times longer. In Fig. 5.8 I model the optimal reflectance reconstructions by superposing methane absorption on a spline fit representing the true surface reflectance. The 890 nm methane absorption line in both spectra is modeled reasonably well with a methane mixing ratio of $6 \pm 2\%$.

How reliable are these reflectance reconstructions? In §3.6.4 we found that there
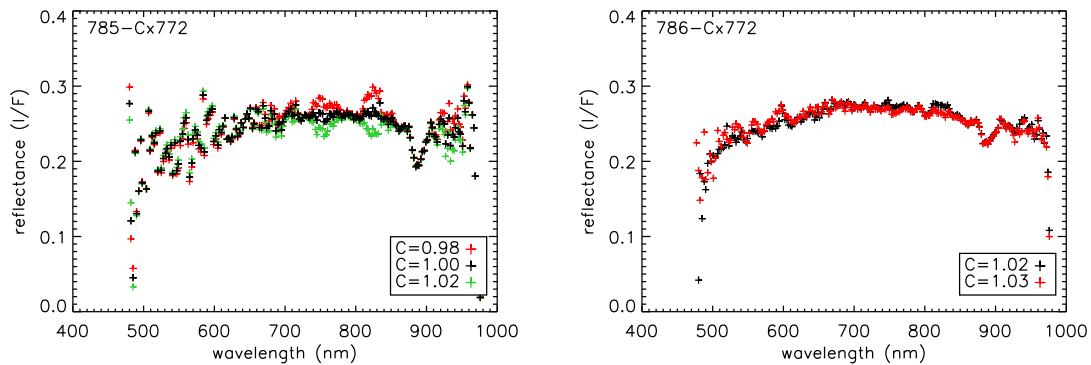
Figure 5.6: Varying the background by a few percent affects the reconstructed reflectance primarily in the methane windows. The legend lists the factors by which the background spectrum was multiplied before subtraction (**left**: **785**, **right**: **786**).
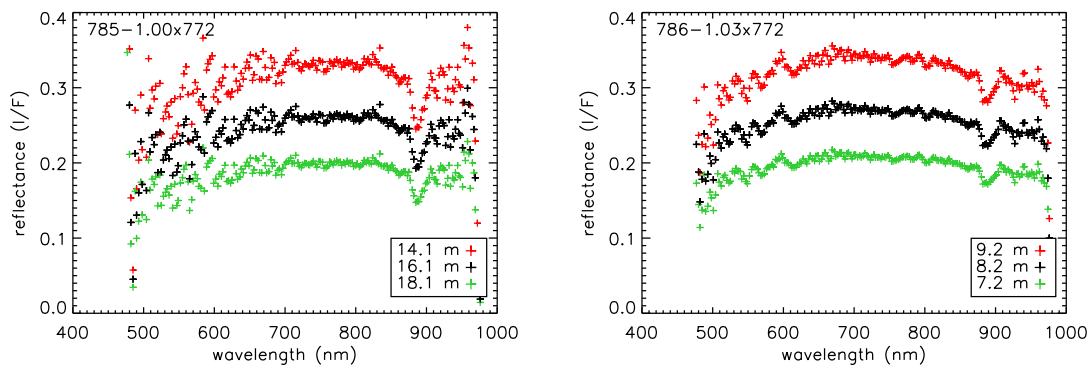

Figure 5.7: Varying the altitude affects the overall reflectance (**left**: **785**, **right**: **786**; nominal altitudes in black).

may be an error associated with the geometric correction of the lamp spectrum at the high wavelength end. This should not affect our reconstruction, since we divide out the lamp spectrum before the two summed columns are converted to a single spectrum. If the surface is uniform and lamp light has been divided out correctly, both these columns should be identical. However, Fig. 5.9 shows that the reflectance reconstructed from the individual columns of both **785** and **786** are very different. As **786** was acquired at a distance to the surface closest to that of the target distance in the calibration experiments, this is cause for concern. It probably indicates that we have not correctly accounted for the lamp signal, although we cannot exclude a problem with the responsivity. Figure 5.9 also serves as a reality check for putative absorption bands, such as those that appear to be present around 800 nm. Because these features do not appear in both summed columns, they must be considered artifacts.

How do the pre-landing reflectances compare with those derived from post-landing spectra? Even though the latter have a very high S/N ratio, they have the disadvantage that the lamp illuminated the surface at very close range (<1 m). The DLVS and the SSL are separated by 6.8 cm on DISR, leading to a parallax effect and a completely different
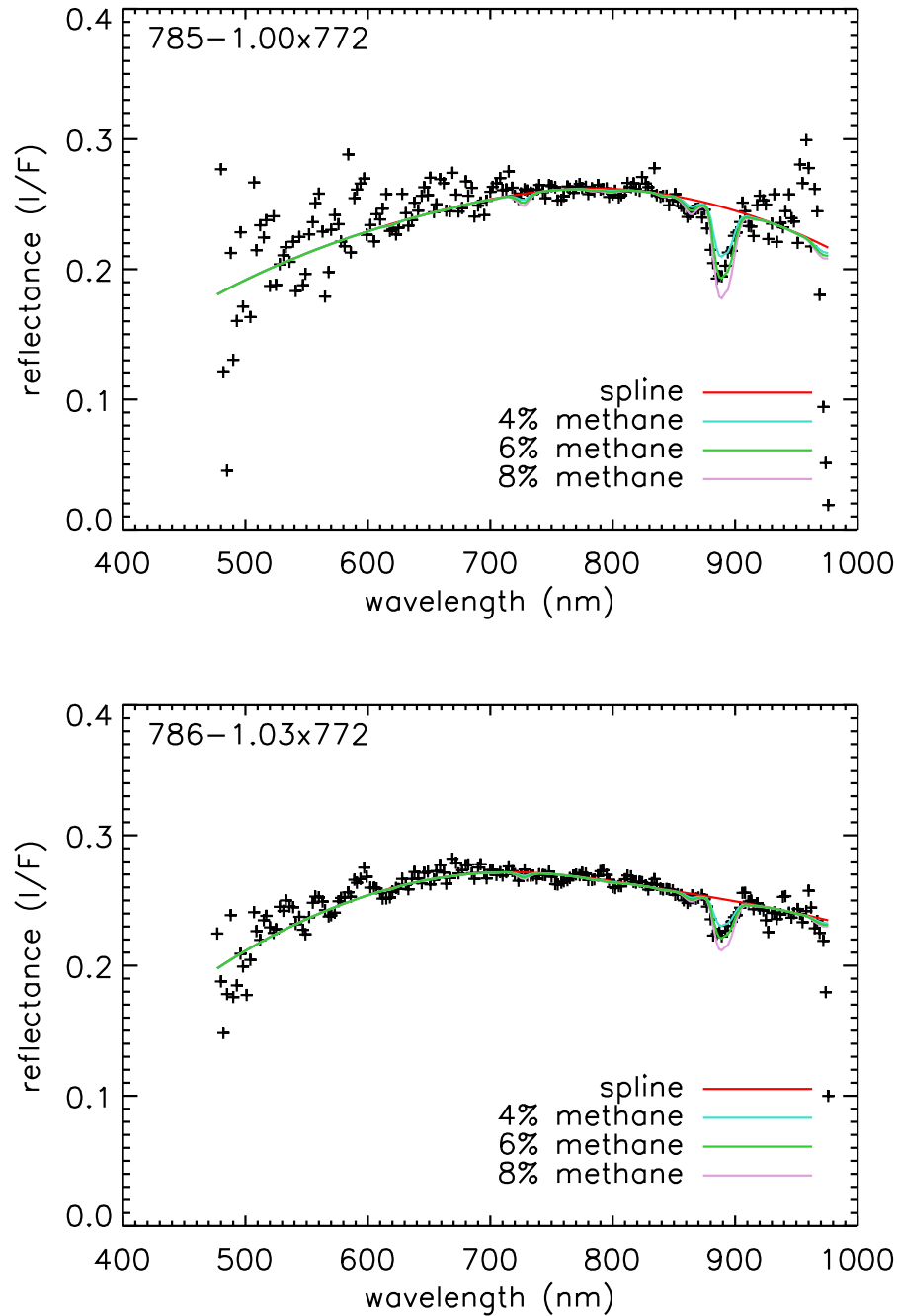
Figure 5.8: The reflectance reconstructed from the two last pre-landing DLVS spectra can be modeled by superposing methane absorption on a spline fit through the methane windows (red line), representing the surface reflectance. Reasonable fits are achieved for a 6 ± 2% methane mixing ratio. **Top**: **785**, **bottom**: **786**.
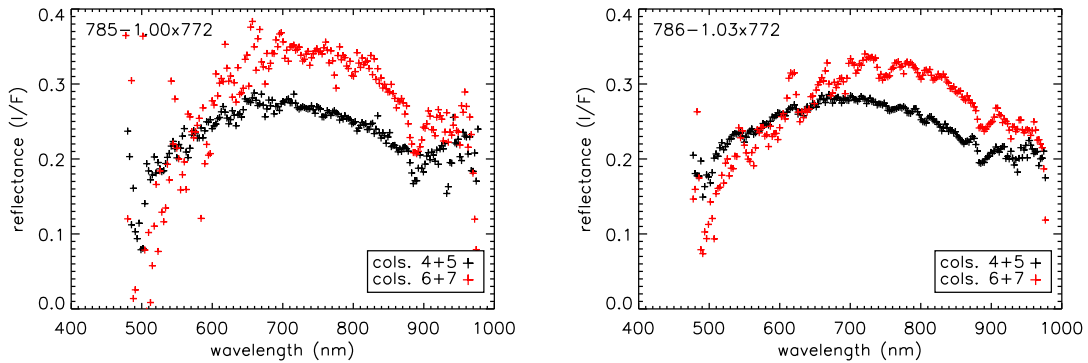
Figure 5.9: The reflectance reconstructed for each of the two columns of **785** (**left**) and **786** (**right**), each column being the sum of two adjacent CCD columns (as listed in the legend). These columns are converted into a single spectrum by the geometric correction. If the surface is uniform both columns should be identical. The absorption features around 800 nm in the **786** reflectance reconstruction are not real; the figure shows that they do not show up in both summed columns.

brightness distribution on the CCD when the surface is close by. Figure 5.10 (top left) shows how the changing proximity of the surface and the different acquisition mode of the DLVS (2 or 10 columns) lead to a completely different spectral shape. Especially the on-board summing of the columns is detrimental to retrieving the true shape accurately. Thus we cannot naively use the SSL spectrum in Fig. 3.15 (which was determined with a target at 4.68 m) to retrieve the reflectance. The problem is, however, that the lamp spectrum was never measured with a target at close range. The only thing we can do is measure these brightness changes on the CCD of a spare instrument, hoping that it is similar to the flight model. Unfortunately, Fig. 5.10 shows that the reflectances derived from a post-landing VLNS spectrum with and without such a correction do not compare well with the pre-landing reflectances. In all likelihood this does not mean that the post-landing surface reflectance is actually different, but that the flight and spare instruments are not sufficiently similar. The correction factors for columns other than the two VLNS columns are so noisy that it is not feasible to correct a 10-column mode post-landing spectrum. The relevance of the post-landing spectra is therefore limited. They merely demonstrate the absence of narrow absorption bands.

5.3 DLIS

In the VLNS mode the DLIS recorded single-exposure spectra with a relatively short sampling time. Since these exposures were not summed, they do not suffer from the Sun Sensor failure that garbled regular mode spectra. Dark exposures (which have the shutter closed) were recorded separately from bright exposures. Table A.13 lists all VLNS spectra acquired before landing (post-landing spectra are not listed as they are all severely overexposed). Two spectra in which lamp signal is clearly present are available: **206** and **210**. The former was recorded 12.3 s before landing at an altitude of around 55 m, the latter 5.4 s before landing at 24.8 m. Just 0.3 s before landing an additional spectrum
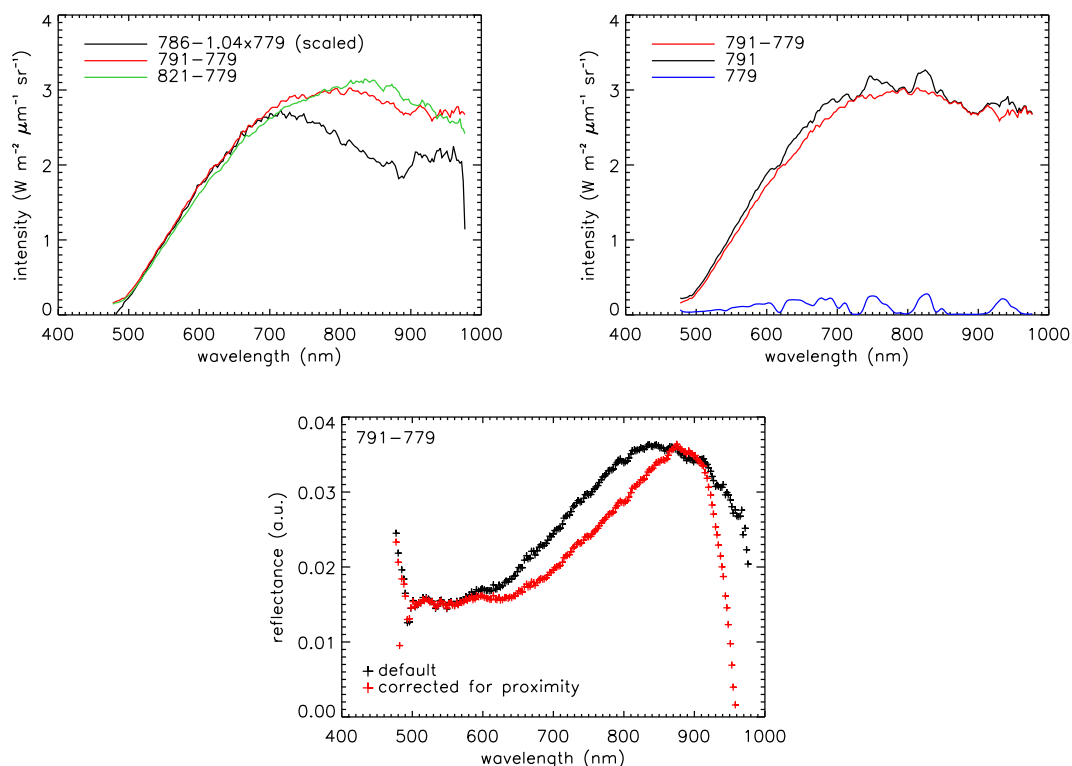
Figure 5.10: The reflectance cannot be reconstructed reliably from post-landing DLVS spectra due to the unknown shape of the lamp spectrum. **Top left**: Post-landing spectra **791** (2-column mode) and **821** (10-column mode; footprint 6) compared to pre-landing spectrum **786**, after background subtraction. Even though the footprints of all spectra cover approximately the same terrain, each spectrum appears different due to the different mode of acquisition. **Top right**: Spectrum **791** with background **779**. **Bottom**: Reconstructions of the reflectance from **791**, with and without a correction for proximity of the surface obtained with the DISR#2 flight spare (see Fig. 3.21), scaled to the same maximum.

was recorded and transmitted, but as luck would have it, this was a dark exposure. Again we are faced with the task of finding a suitable background spectrum for the reflectance reconstruction. Because it was recorded at approximately the same solar phase angle as **206** and **210**, spectrum **202** appears to be the best candidate (Fig. 5.11). We also try out an earlier spectrum, **199**, which was recorded at a slightly smaller phase angle. Figure 5.12 shows all spectra involved in the reconstruction, and illustrates the reconstruction process.

The sensitivity of the reconstruction to the choice of background is illustrated in Fig. 5.13. Like for the DLVS we find optimally smooth reflectances by varying the background spectra a few percent (Fig. 5.14): subtracting too much creates absorption bands in the methane windows, whereas too little leads to methane bands with an unphysical shape. The reflectance is similar for all reconstructions, decreasing steadily from 800 to 1500 nm. Methane absorption bands due to the intervening atmosphere are apparent, with a saturated 1400 nm band for **206**. Only the reflectance beyond 1500 nm appears to be sensitive to the choice of background spectrum (it can even become negative for **206**),
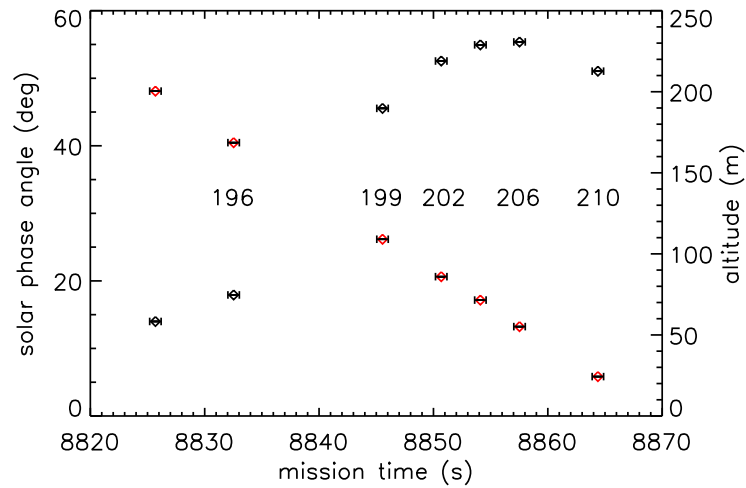
Figure 5.11: The altitudes (red) and solar phase angle (black) of all VLNS DLIS spectra recorded before landing. The error bars delimit the sampling time. The sequential numbers of some spectra are indicated; the others may be identified by means of Table A.13.
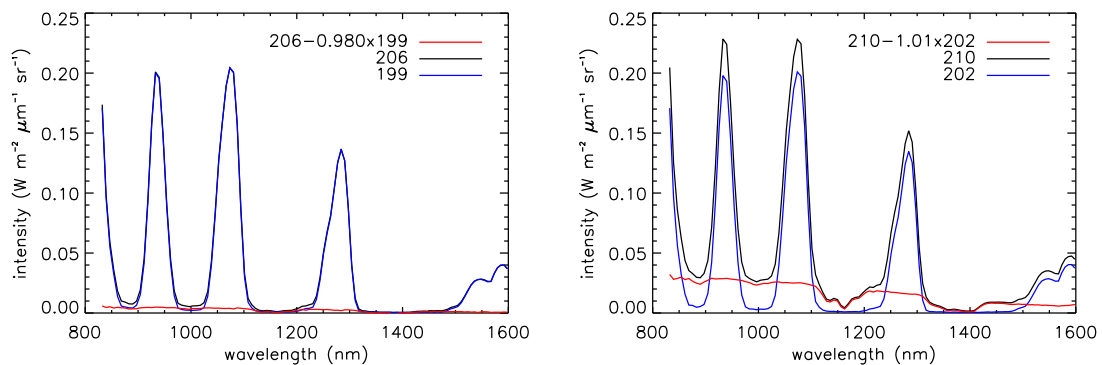
Figure 5.12: The procedure to reconstruct the reflectance is illustrated for the two pre-landing DLIS spectra in which the lamp signal is clearly present (**left**: **206**, **right**: **210**). The lamp-only spectrum (shown in red) is constructed by subtracting the background spectrum (blue), multiplied by a constant, from the observed spectrum (black). The surface reflectance is obtained by dividing the lamp-only spectrum by the lamp spectrum (see Fig. 3.18).

Figure 5.13: The reflectance reconstructions derived from the one-before-last (**left**: **206**) and last (**right**: **210**) DLIS spectra before landing using different background spectra (**199** and **202**). The reconstructions show methane absorption lines due to the intervening atmosphere.
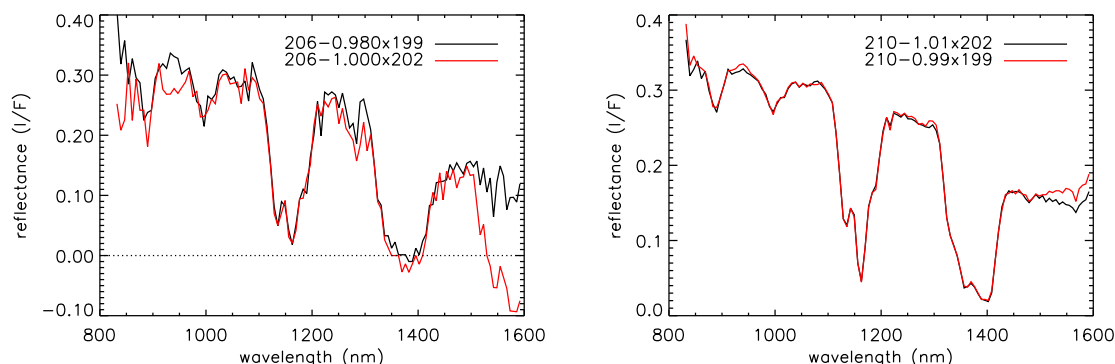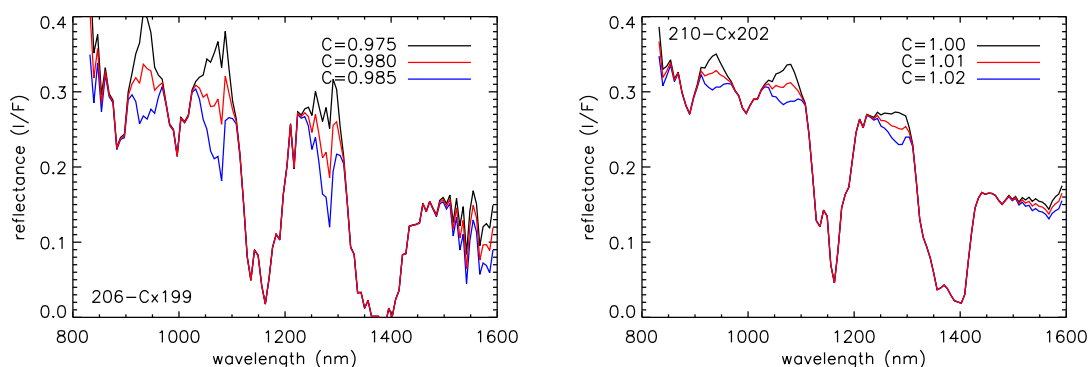

Figure 5.14: Varying the background by a few percent affects the reconstruction in the methane windows (**left**: **206**, **right**: **210**). The legend lists the factors by which the background was multiplied before subtraction.

and is therefore not fully reliable. The influence of altitude on the reconstruction is shown in Fig. 5.15. In Fig. 5.16 I model the optimal reflectance reconstructions by superposing methane absorption on a spline fit through the methane windows representing the true surface reflectance. The **206** and **210** reflectances are best modeled with a $4 \pm 1\%$ and $4.5 \pm 0.5\%$ methane mixing ratio, respectively. Spectrum **206** is quite noisy, and a smooth spline through the methane windows suffices as a model for the surface reflectance. In the high S/N spectrum **210** we need to introduce a slope around 1450 nm into the spline model to achieve a satisfactory fit. The resulting feature at 1500 nm likely represents an absorption band. Note that the depression is not required when we use the Strong et al. (1993) methane absorption coefficients instead of those from Irwin et al. (2006).

After landing the DLIS continued to operate, peering straight into the lamp reflection spot (see Fig. 4.7). By adjusting its sampling time, the DLIS was able to cope with the flood of lamp light reflected off the surface. As shown in Fig. 5.17 (left), the observed intensity was more than a hundred times larger than before landing. With the lamp signal
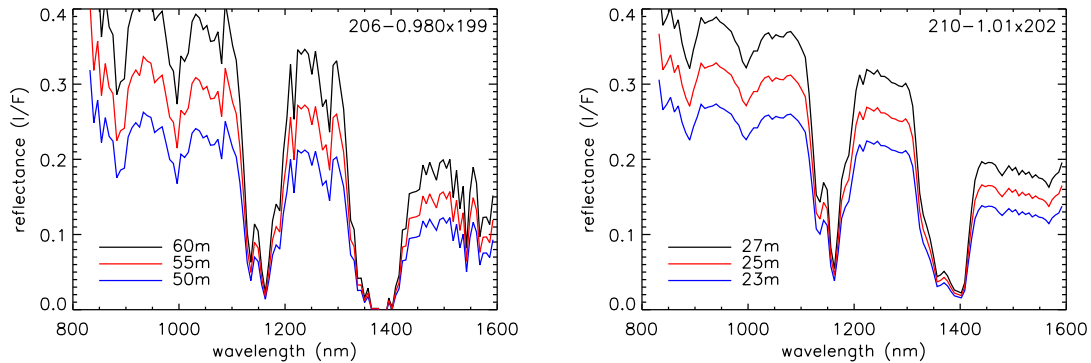
Figure 5.15: Varying the altitude at the time of observation affects the reconstruction (**left**: **206**, **right**: **210**).

so strong, the choice of background does not affect the end result. The reflectance reconstructed assuming a $1/d^2$ scaling of the SSL flux is about a third of that of the pre-landing spectra. However, when we apply the correction obtained from the DISR#2 spare camera (see §3.6.5), we find the level raised to that of the others (Fig. 5.17, right). Closely comparing the pre-landing **206** and **210** reflectances with the (corrected) **249** reflectance reveals a slight mismatch between 1450 and 1500 nm (Fig. 5.18. This difference of 7% (also present between **206** and **249**) is significant because here the responsivity is high, and the reconstruction insensitive to the choice of background (see Fig. 5.13). We have to be careful when interpreting this deepening, though. The DISR#3 SSL spectrum has not been measured with a target at close range, and DISR#2 observed a drop in intensity of 5% at 1500 nm (see Fig. 3.21; this is included in Fig. 5.18).

We find other absorption features in the post-landing reflectance around 1160, 1330, and 1400 nm. The 1160 nm feature is a methane band, and well modeled with a methane mixing ratio of 4.5 ± 1.0% (Figure 5.19, left), assuming the DLIS is positioned 45 cm above the surface (Karkoschka et al. 2007). This agrees with the mixing ratio determined before landing, implying that landing did not change the methane abundance in the DLIS optical path. We can also turn the argument around and presume the mixing ratio to be constant; then the optimal fit is achieved for a height of the DLIS above the surface of 45 ± 5 cm (Fig. 5.19, right). But where we also expect the presence of the 1400 nm methane band in the **249** reflectance, we find that it cannot be modeled satisfactory in the 1300-1450 nm range with our methane absorption model (Figure 5.19, left, inset). The nature of this region remains puzzling, and might even reflect imperfections in the responsivity. Assuming the methane mixing ratio is indeed the same before and after landing, this leaves very little room for absorption by liquid methane. The depth of the methane absorption lines in pre-landing spectra is governed by atmospheric methane, but after landing there is so little gaseous methane present in the optical path that the spectral signature of liquid methane present on the surface would leave its mark on the absorption lines. Using the coefficients of Grundy et al. (2002) I determine an upper limit of circa 20 μm for the thickness of a liquid layer on the surface, based on a fit to the 1160 nm complex.
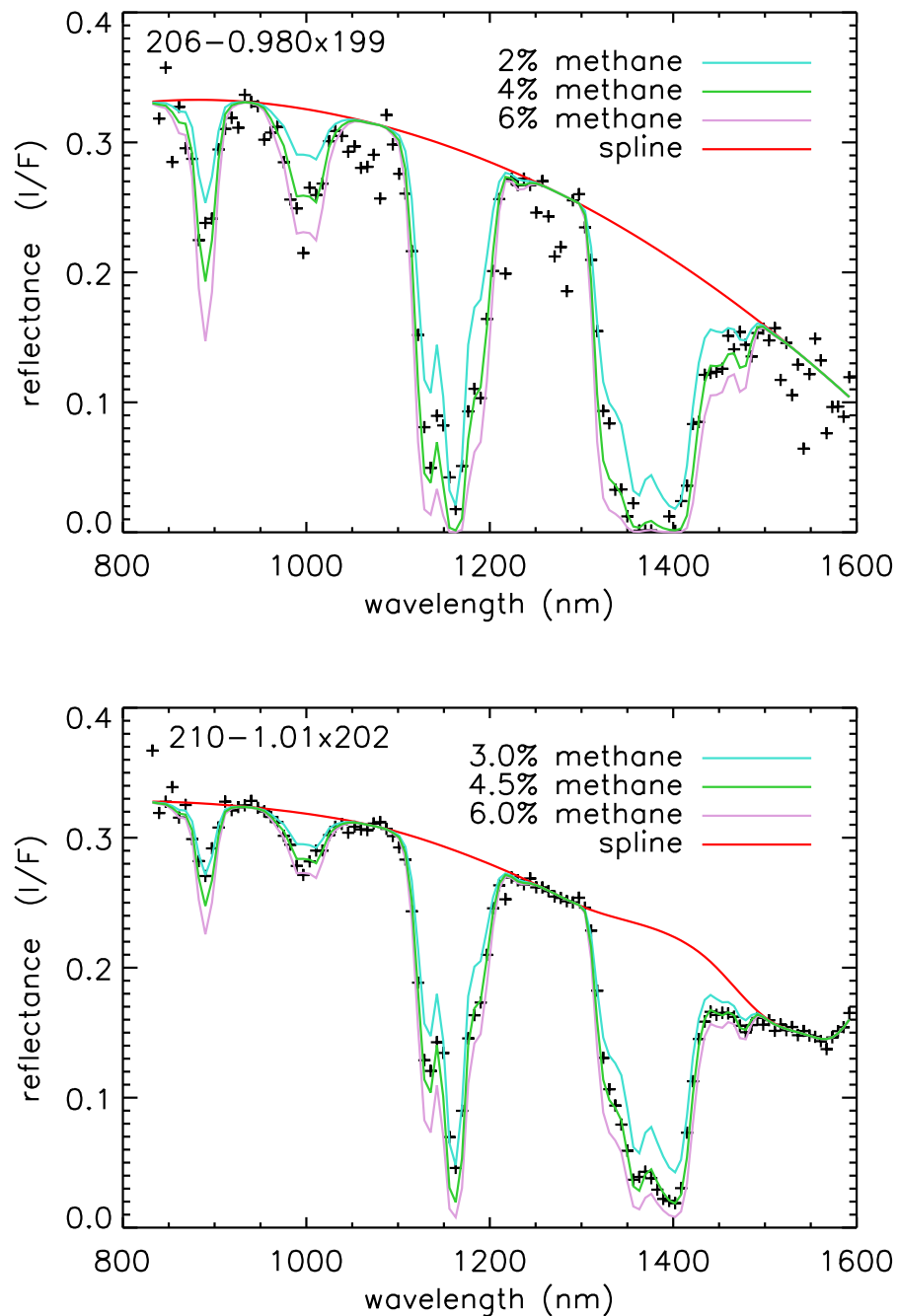
Figure 5.16: The reflectance reconstructed from the two last pre-landing DLIS spectra can be modeled by superposing methane absorption on a spline fit through the methane windows (red line), representing the surface reflectance. **Top**: The reflectance reconstructed from **206**, albeit noisy, is modeled with a 4% methane mixing ratio. **Bottom**: The reflectance reconstructed from **210** is modeled well with a 4.5% methane mixing ratio. A slope around 1450 nm was introduced into the spline to achieve a good fit.
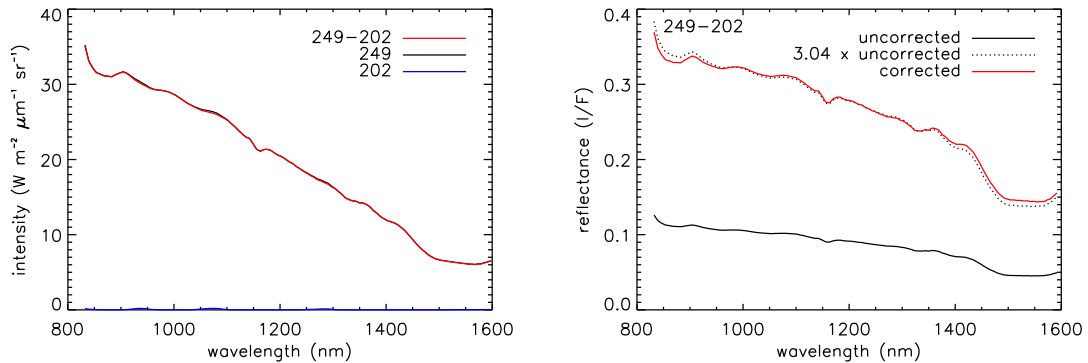
Figure 5.17: Reconstruction of the surface reflectance from **249**, acquired after landing. **Left**: The measured intensities. The background spectrum is **202**. **Right**: The reconstructed reflectance. Shown here are reconstructions with the SSL spectrum uncorrected (black) and corrected (red) for proximity of the surface, using results from the flight spare (DISR#2) experiment (see §3.21). The correction increases the reflectance by a factor of three, and changes the shape of the red end slightly.

Figure 5.18: The corrected post-landing spectrum **249** from Fig. 5.17 agrees very well with pre-landing spectra **206 (left)** and **210 (right)**. We find a mismatch only in the 1450-1500 nm range, where the reconstruction is insensitive to the choice of background (see Figs. 5.13 and 5.14).

Figure 5.19: Methane absorption in a post-landing spectrum. **Left**: The 1160 nm methane absorption line in the reflectance spectrum reconstructed from **249** is modeled we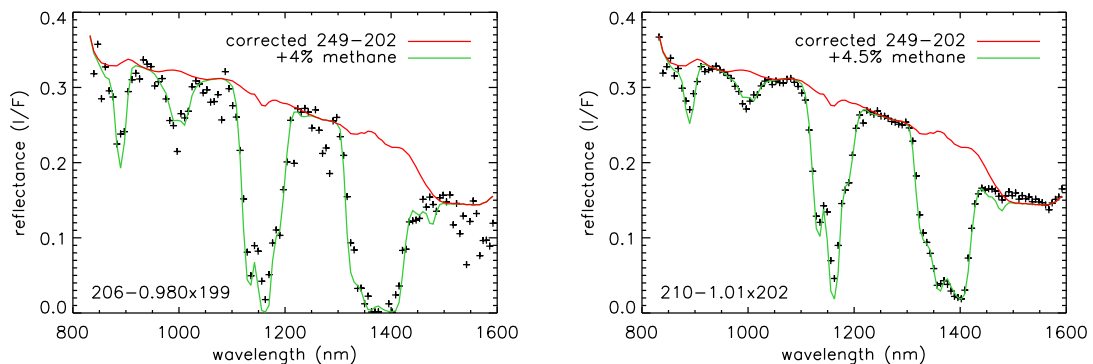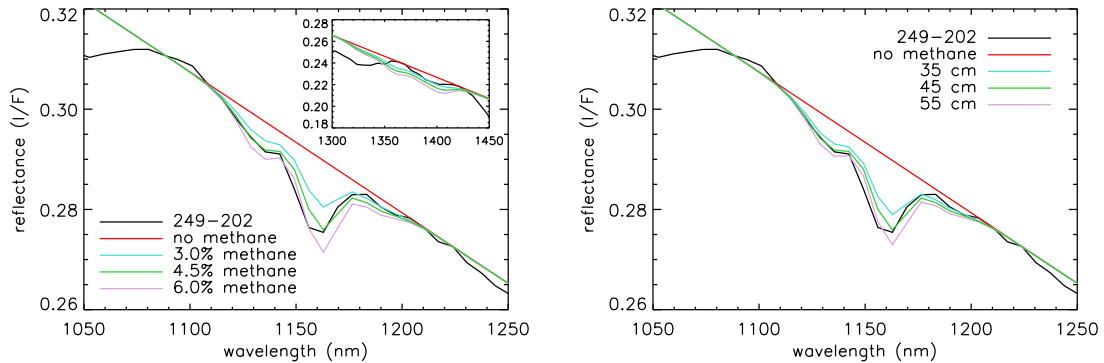ll with a 4.5% methane mixing ratio, assuming the DLIS is located 45 cm above the surface. It is difficult to define the continuum, therefore the zero methane model is a line with a slope similar to that of the observations. The methane absorption complex around 1400 nm is less revealing (**inset**). **Right**: Methane absorption as a function of height of the DLIS window above the surface, assuming a mixing ratio of 4.5%.

5.4   Synthesis

5.4.1   Surface reflectance

In the preceding sections I have reconstructed the surface reflectance from the last DLVS and DLIS spectra before landing, making as few and simple assumptions as possible. Ideally, all pre-landing reflectances should conform, with the DLVS and DLIS agreeing at overlapping wavelengths. Figure 5.20 (left) compares the DLVS and DLIS spline fits representing the true surface reflectance (the red curves in Figs. 5.8 and 5.16). The two DLVS reflectances (**785** and **786**) are quite similar, as are the three DLIS reflectances (**206**, **210**, and **249**). This suggests that the method of reflectance reconstruction by scaling the SSL flux is sound, and that we successfully corrected DLIS **249** for parallax effects. But the DLVS reflectances are somewhat lower that those found by the DLIS. Figure 5.20 (right) attempts to reconcile the results from both spectrometers. When we scale the DLVS **785** reflectance up by a factor 0.25 we find reasonable agreement with the DLIS **210** reflectance. A slight discrepancy occurs in the wavelength range of overlap, where the DLVS reflectance appears to drop and the DLIS reflectance is more or less constant (curiously, it is worse for DLVS **786**). The same trend can be observed in the reconstructed SSL spectrum (see Fig. 3.20). If, as we suspect, there it was due to a small error in the geometric correction, it would not affect the reflectance because the lamp spectrum is divided out before the correction is applied, and we do not expect steep gradients to remain after division. If it was caused by an incorrect responsivity (i.e. if the true lamp spectrum follows the DLIS curve in Fig. 3.20 instead of dipping down towards 1000 nm), it would make the DLVS reflectances bend downward even more. Note that errors affecting the reconstruction of the SSL spectrum do not necessarily affect the calibration of Titan spectra, because of the much lower temperatures involved (and, consequently,
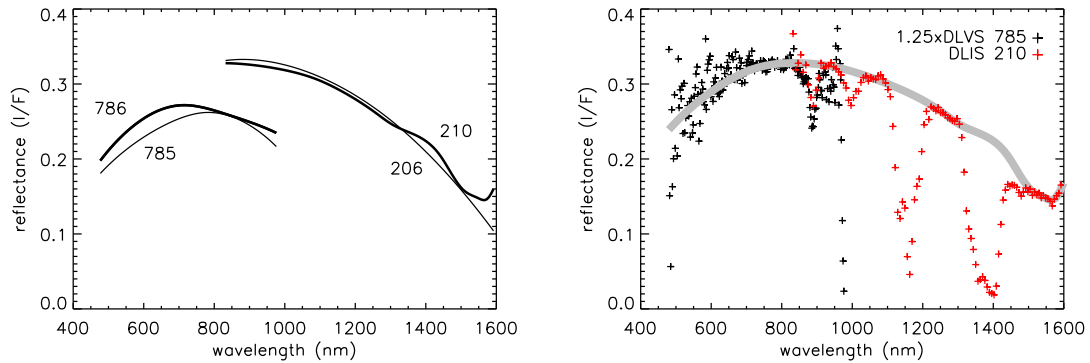
Figure 5.20: The reflectance of the surface around the landing site. **Left**: The spline fits through methane windows in the reflectance reconstructed from the last two pre-landing DLVS and DLIS spectra compared (see Figs. 5.8 and 5.16). Labels: 206: DLIS **206**−0.980×**199**, 210: DLIS **210**−1.01×**202**, 785: DLVS **785**−1.00×**772**, 786: DLVS **786**−1.03×**772**. Thick lines indicate the spectra with the highest S/N. **Right**: To find the reflectance over the full wavelength range (gray line), valid for phase angle zero, I scale the DLVS **785** spectrum to match the DLIS **210** spectrum.

different detector responsivities). In any case, the DLVS reflectance reconstruction is affected by uncertainties that are not relevant to the DLIS, so the fault likely lies with the DLVS calibration.

My reflectance reconstruction represents a refinement of the preliminary reconstruction by Tomasko et al. (2005). The shape of my spectrum is similar, with the DLVS part now properly calibrated and the DLIS part slightly improved. Even though the DLVS reconstruction is fraught with uncertainties I believe there is sufficient evidence for the presence of a red slope in the visible. The reflectance peaks between 800 and 900 nm, beyond which it slopes down to about half the peak value at 1500 nm. This blue slope is virtually featureless with the exception of an absorption feature at 1500 nm. Whereas I find the reflectance by scaling our result to the lamp flux measured before launch, Tomasko et al. scale their reconstruction to the average of the ratio of the up- and downward flux, derived from seven low-altitude DLIS and ULIS spectra. This method requires a good estimate of the probe azimuth at the time of observation, and an accurate knowledge of the ULIS spatial response, which in its turn depends on the input of an atmosphere model. Bruno Bézard (pers. com.) recently repeated this effort using the most recent azimuth and atmosphere models, broadly confirming the earlier values. Surprisingly, Fig. 5.21 shows that my approach leads to much higher values of the overall reflectance.

How does my reflectance spectrum compare to those found by other teams? Griffith et al. (2003) determined the surface albedo in near-IR methane windows of the leading and trailing side of Titan by means of a radiative transfer model. The leading hemisphere features the bright 'continent' Xanadu, and therefore has a higher average albedo than the trailing hemisphere, which has dark terrain distributed around the equator (Porco et al. 2005). Huygens' landing site is close to the equator on the trailing hemisphere, but the lake terrain observed by DISR is not covered by the very dark dunes which are ubiquitous in the equatorial dark terrain (Lorenz et al. 2006b). Hence, the albedo of the landing site
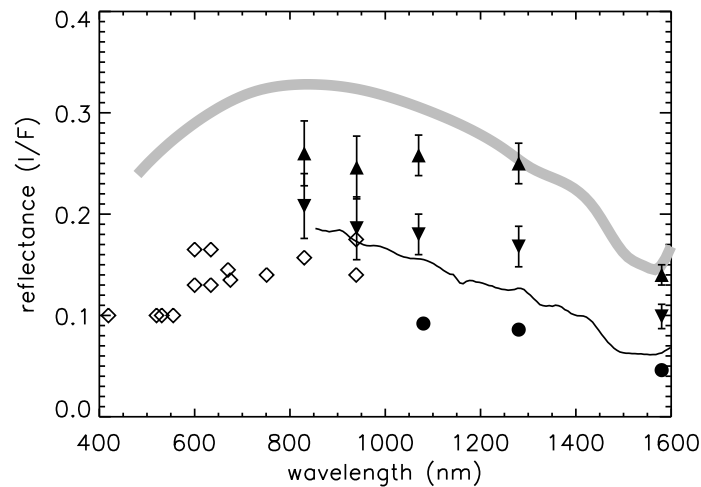
Figure 5.21: The zero-phase-angle reflectance spectrum from Fig. 5.20 (thick gray line) compared to reflectances from the literature. Plotted are the surface albedos from the LPL atmosphere model (Lyn Doose, pers. comm.) (◇), the albedos found by Griffith et al. (2003) for the leading (▲) and trailing (▼) hemisphere of Titan, the albedos found by McCord et al. (2006) for dark equatorial terrain (•), and the DLIS-derived reflectance from Tomasko et al. (2005) (thin line).

must be lower than that of the trailing hemisphere, but higher than that of the dune-covered terrain (reconstructed by McCord et al. 2006). Figure 5.21 shows that my reflectance spectrum does not meet this requirement; it is higher than the others, comparing only to that of Titan's leading hemisphere. The Tomasko et al. (2005) reflectance better meets the expectations. Recently, Tomasko et al. (2007) determined the visual part of the reflectance of the Huygens landing site by means of a comprehensive atmosphere model. Their results (Fig. 5.21, diamonds) confirm the low reflectance of the landing site, and we must accept that the discrepancy with my results is real.

The overall reflectance I find is higher over the full wavelength range than that determined by all other teams. Does my reconstruction fail? If there are problems associated with scaling the lamp flux and/or parallax effects, the reflectances derived from the two DLVS and three DLIS spectra would disagree more. Perhaps my altitude scale is incorrect. I use the SSP landing velocity of 4.60 m s^{-1} (Zarnecki et al. 2005, confirmed by Towner et al. 2006) to compute the altitude of the last observations before landing. Using the HASI velocity of 4.33 m s^{-1} (Fulchignoni et al. 2005) would decrease our reflectance only by 12%. Perhaps the probe was violently swinging? No, the Karkoschka et al. (2007) reconstruction predicts tilt values of less than a degree for the last part of the descent, which would change the result by less than a percent. Other unlikely explanations range from an unidentified problem with the SSL calibration to the last three footprints covering unusually bright terrain. There is no evidence for either. The most likely explanation has to do with the phase angle at which the observations were acquired. If the surface of Titan at the landing site exhibits an opposition effect (a strong increase in brightness towards zero phase angle), e.g. through a combination of shadow hiding and coherent backscatter (Hapke 1981, 2002), my reflectance can be much higher than those of other groups

because the phase angle of the last pre-landing spectra were less than a degree. We can calculate the phase angles from the size of the SSL window (5.2 cm diameter) and the distance of its center to the spectrometer windows on either side (DLIS: 3.2 cm, DLVS: 6.8 cm). DLIS spectra **206** and **210**, associated with the highest overall reflectance, were acquired at the smallest phase angles: $0.031° \pm 0.025°$ and $0.069° \pm 0.056°$, respectively. The phase angle of DLVS **786** is higher ($0.45° \pm 0.17°$) and its reflectance lower (~20%) than that of DLIS **210**, as would be expected in case of an opposition effect. The phase angle of DLVS **785** is intermediate to the previous two at $0.23° \pm 0.09°$, and we would expect its reflectance to be intermediate as well, contrary to what we observe. However, parallax would have pushed the lamp beam and the DLVS footprint away from each other (see Fig. 3.11), and the true SSL flux must have been lower in reality than that used, which makes the reconstructed **785** reflectance an underestimate. Post-landing DLIS spectrum **249** observed the surface over a wide range of phase angles (approximately 0.70°-6.7°), so the associated reflectance is expected to be lower than that of **210**. The fact that it is not could imply either surface heterogeneity (as seen in the post-landing images), or that DISR#2 is not sufficiently similar to DISR#3.

Albedos from other workers have all been derived from observations that were significantly affected by the atmosphere. For example, the ratio method employed by Tomasko et al. (2005) averaged eight DLIS observations of reflected sunlight at phase angles ranging from 13° to 57°. But the diffuse nature of Titan surface illumination would subdue shadow hiding, the dominant mechanism at these phase angles. Zero phase angle observations from outside Titan's atmosphere would not register an increased reflectance, because even though the surface is visible through the near-IR methane windows, hardly any direct sunlight reaches it, which is an essential prerequisite for coherent backscatter. Thus, we suggest that our high reflectance represents the opposition brightness surge, the apparent strength of which is within reasonable bounds. I explore this topic further in Chapter 6. Note that while I consider the opposition effect to be a natural explanation for our high reflectance, we cannot exclude the possibility that Huygens landed on a bright ridge, since the landing site was not imaged in detail (see Fig. 4.5).

5.4.2   Methane abundance

The methane mixing ratios found by fitting a methane absorption model to the various reflectance spectra in this chapter agree well. The $6 \pm 2\%$ mixing ratio estimated from the DLVS **785** and **786** spectra is not well constrained due to the fact that the main methane absorption line is located at the red edge of the spectrum, where it is difficult to define the underlying surface reflectance because of low responsivity. The $4\pm1\%$ ratio derived from DLIS **206** is relatively uncertain because the spectrum is very noisy; it was acquired at high altitude, when the lamp reflection was barely visible. The high S/N spectrum DLIS **210** gives us the most reliable determination of the mixing ratio: $4.5\pm0.5\%$. The post-landing DLIS **249** ratio of $4.5\pm1.0\%$ is agrees with this value, but is relatively uncertain because we can fit only one out of four methane bands. Since all determinations agree within the range of uncertainty, and the most reliable methane mixing ratio of $4.5\pm0.5\%$ is consistent with the $4.9 \pm 0.3\%$ measured by Huygens' GCMS instrument (Niemann et al. 2005), we can be confident that the altitude scale we use is correct. Interestingly, my estimate agrees with that of Tomasko et al. (2005), who derived a mixing ratio of 5% from

DLIS **210** at an altitude of 21 m. Adjusting the altitude to the 24.8 m I presume is correct, would decrease their mixing ratio by 0.8%. The authors used the Strong et al. (1993) methane absorption coefficients, which apparently overestimate the degree of absorption in the strong methane bands around 1150 and 1400 nm. Using the Irwin et al. (2006) coefficients would bring their mixing ratio back to around 5%. Compared to the Strong et al. coefficients the Irwin et al. coefficients model the 1320 nm absorption shoulder well. The detailed shape of the 1000 nm band, modeled with the Karkoschka (1998) coefficients, is not reproduced for **210**. The post-landing DLIS spectra do not support the presence of a layer of liquid methane on the surface of the landing site. If present, its thickness is in the order of micrometers. This suggests that while the soil may be wet at a depth of a few centimeters (Niemann et al. 2005, Zarnecki et al. 2005, Lorenz et al. 2006a), the surface itself is dry.

5.5   Surface composition

The reflectance spectrum in Fig. 5.20 offers us clues about the surface composition at Huygens' landing site. What spectral signatures do we expect to see? Titan is big enough to have differentiated after its formation, with metals and silicates sinking to the interior, pushing water and other ices out to the surface. This is how we think Ganymede, of similar size, has evolved. So presumably, Titan's surface is composed of water ice, and the rocks we see in the surface image are ice pebbles. Even though water ice behaves like rock at Titan's surface temperature, it is not as strong, and tall mountains cannot form since they would collapse under their own weight. The strongest relief around Huygens' landing site is only a few hundred meters (Tomasko et al. 2005). Other ices, like carbon-dioxide and ammonia, are possibly mixed in with the water ice. Ammonia is thought to be an important constituent of the proposed subsurface ocean (Tobie et al. 2006), and should be present on the surface if cryovolcanism occurs on Titan. Covering all this is a layer of organic material. Predicted on theoretical grounds, evidence for the presence of organics on the surface of Titan is overwhelming. Cassini's radar determined the relative permittivity of the surface to be close to 2, a value typical for organic material (Elachi et al. 2005), whereas Huygens' GCMS directly detected methane, ethane, cyanogen, and other more complex molecules on the surface (Niemann et al. 2005). The source of this organic material is the upper atmosphere. Here, at 500 km altitude, photodissociation of methane creates methane radicals, which react with other atmospheric constituents to form complex organic molecules. These then coagulate into small ($0.05\,\mu$m) spheres, or monomers, to form Titan's characteristic yellow haze. While the monomers slowly descend to the surface under the influence of gravity, they aggregate into aerosols. At around 100 km altitude organic ices (e.g. ethene, acetylene) may condensate out of the atmosphere onto the aerosols. Near the surface, an aerosol consists of hundreds of monomers (Tomasko et al. 2005). Many workers attempt to simulate the processes taking place in Titan's atmosphere. By subjecting gas mixtures of methane and other simple molecules to sparks or UV radiation, they create complex organic solids. Sagan and Khare (1979) were the first to do this, and they established that their solid brown, sometimes sticky residue was not a polymer, but something different which deserved a new name: **tholins**. Even though laboratory tholins are sticky, tholin aerosols on Titan are though to harden on their way to

the surface (Dimitrov and Bar-Nun 2002). Then on the surface, tholins might be found in the form of dust or sand. The thickness of the tholin layer on the surface is unknown, but it is clear that the constant drizzle of aerosols should leave its mark on the surface. The presence of ice rocks on the landing site indicates that it does not form a thick uniform blanket. Whether tholin particles adhere to the rocks is not clear; if indeed they behave like dust, wind may blow them off and expose clean water ice.

Each of the proposed surface materials has its own spectral characteristics. Let us first consider how the (presumably) dominant constituent of Titan's surface, water ice, reflects light. The reflectance spectrum of water ice frost is shown in Fig. 5.22 for different grain sizes. Clearly visible in all spectra are the 1.5 and 2.0 μm vibrational absorption bands. The shape of the spectrum is seen to depend strongly on the grain size; with increasing grain size the overall reflectance drops, the slope becomes more blue, and the 1.04 and 1.25 μm overtone bands become stronger. The drop of overall reflectance can be understood by considering how a powder exposes more surface to the incoming light than a coarse gravel, which covers part of its surface by shadows. A possible detection of water ice on Titan was reported by Griffith et al. (2003), who compared a reconstruction of the surface reflectance in near-IR methane windows with a spectrum of Ganymede. Even though they found an acceptable match, their method did not have the required spectral resolution to resolve the water absorption lines. The 1.5 μm absorption feature in the DLIS spectrum may be a water line. However, as already pointed out by Tomasko et al. (2005), the problem is that if the near-IR blue slope is due to water ice, the 1.04 and 1.25 μm overtone lines, conspicuously absent from the DLIS spectra, ought to be present. On the other hand, the blue slope might be caused by the presence of as-of-yet unidentified organic material (Roger Clark, pers. com.); then the overtone lines may simply be too weak to detect (very shallow depressions are actually present in post-landing spectra), considering the 1.5 μm absorption line is not very strong (especially in the pre-landing spectra). Bernard Schmitt (pers. com.) suggests the overtone water lines are present, but hidden from view by simple organic ices, like ethene and acetylene, which are theorized to condensate onto the surface of tholin aerosols in the lower layers of the atmosphere. Clark (1981a) experimented mixing water with charcoal and minerals. He found that, generally, when water is added the overall reflectance decreases, and the spectral slope becomes slightly more blue. Charcoal, when mixed with up to 30% (weight) water, completely suppresses the near-IR water absorption bands, but also the blue slope. A relatively small amount of charcoal sprinkled on water frost can dramatically lower the reflectance. A relatively small amount of dark material covering the water ice of Titan's surface may account for the low overall reflectance we observe.

Can we find evidence for organic material in the Titan reflectance spectrum? Characteristic for the spectrum of organics is a red slope over the visible and near-IR wavelength range. Simple organic molecules have absorption lines in the ultraviolet due to the excitation of covalent bonding electrons. The most common types of covalent bonds are π- and σ-bonds. In π-bonds two lobes of one involved electron orbital overlap two lobes of the other involved electron orbital. The π-bond is weaker than the σ-bond, which has a single lobe of one involved electron orbital overlapping a single lobe of the other involved electron orbital. A single bond is usually a σ-bond, and the carbon double bond often found in organic matter consists of one σ-bond and one π-bond. It is the latter that is responsible for the decrease in reflectance from the visible towards the UV. With increasing com-
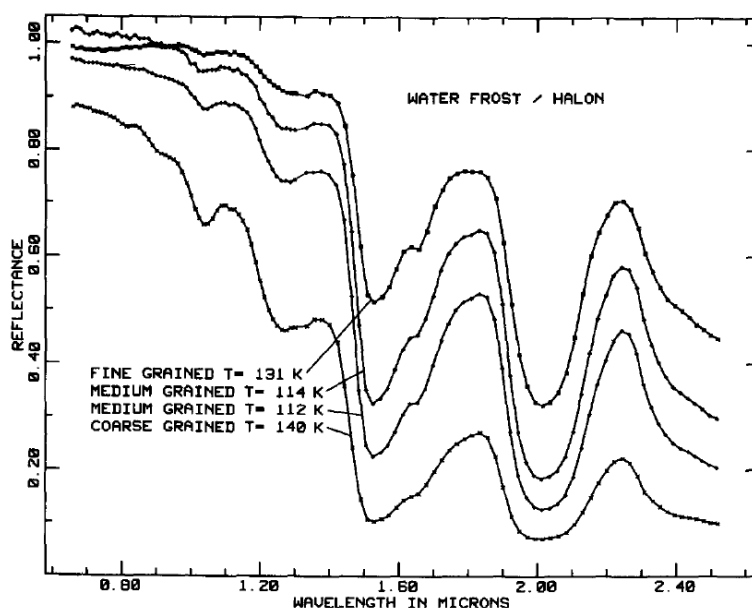
Figure 5.22: The observed reflectance spectrum of water ice frost of different grain sizes. Figure from Clark (1981b).

plexity of an organic molecule, individual absorption bands associated with π-electrons start to overlap, and absorption moves into the visible wavelength range. Note that some silicates also display a red slope in the visible (e.g. Fig. 5.25). Unfortunately, the predicted wavelengths (Cloutis 1989) of the most intense stretching and bending absorption bands of organic molecules, and their overtones, are outside the DISR wavelength range. Spectra of tholins display this red slope too. Figure 5.23 shows reflectance spectra of the Sagan and Khare tholins and those prepared by Bernard et al. (2006). The latter's experiment was set up to mimic the conditions in Titan's stratosphere, where tholins are thought to be formed. The reflectance spectra of the Sagan and Khare 'tholin 3' and 'tholin 4' are similar to those of the Bernard et al. yellow and black tholins, respectively. The color of these tholins is roughly correlated with elemental composition; nitrogen enriched tholins are dark, nitrogen depleted tholins more yellow (Eric Quirico, pers. com.). The red slope of tholin 3/black tholin continues all the way to 2.0 μm, and is relatively constant beyond up to 2.7 μm. Tholin 4/yellow tholin exhibits a blue slope in the near-IR and absorption bands. Its 1.5 μm band may be associated with the drop in reflectance at 1.5 μm in the Titan spectrum; then DISR did not find evidence for water. Our Titan reflectance spectrum also features a red slope in the visible, a tentative confirmation of the presence of organic material. However, it does not resemble that of the tholins in Fig. 5.23, most notably due to a lack of absorption bands (the featureless blue slope), and the low wavelength of the peak reflectance (0.8-0.9 μm versus 1.4-1.8 μm). To explain the latter, could temperature play a role? Although Roush and Dalton (2004) found that the reflectance spectrum of (hydrated) tholins hardly changed when the temperature was lowered from room temperature to 100 K, for the silicate kaolinite a decrease in temperature shifts the peak reflectance to lower wavelengths and decreases the overall reflectance (e.g. Fig. 5.25). The low overall reflectance of the Titan spectrum suggests that if tholins are present, the dark, nitrogen enriched, variety is prevalent. Note that grain size can play a

role here too; coarsely ground yellow tholin is darker, and grinding black tholin can make it twice as reflective (Eric Quirico, pers. com.).

The chances of identifying carbondioxide or ammonia are small. The carbondioxide frost reflectance spectrum is almost completely flat (Fig. 5.24, left). It has essentially no features in the DISR wavelength range, except for a tiny 1.4 μm band, which coincides with the strongest methane absorption line. The reflectance spectrum of ammonia frost has a moderate blue slope, with several small absorption lines at 1.05, 1.23, and 1.32 μm, and a deeper one at 1.5 μm (Fig. 5.24, right). In the Titan spectra a weak depression is visible around 1.05 μm (Fig. 5.18, right), but there is nothing around 1.23 μm. The other lines are not much use, as the 1.32 μm line coincides with a methane line (although there may be something present in the **249** reflectance), and the 1.5 μm line with the proposed water line. Since the strongest of the weaker absorption lines is absent, I conclude that pure ammonia frost is absent from the surface at the landing site.

Silicates are not expected on the surface, which, of course, does not mean we should not look for them. Titan's reflectance spectrum shows no evidence for common silicates like olivines and pyroxenes, that typically have broad absorption line complexes around 0.9-1.0 and 2.0 μm due to the presence of iron ions in their crystal structure. But the low temperature reflectance spectrum of a common clay mineral like kaolinite (used in toothpaste and glossy paper) uncannily shares many characteristics with the Titan spectrum: a red slop in the visible, a peak in reflectance around 800 nm, and a blue slope in the near-IR (Fig. 5.25). The only differences (in the DISR wavelength range) are the water absorption lines.

It is not clear whether the lake terrain seen in the DISR images can be identified with the dark terrain observed by Cassini to be distributed around the equator (Porco et al. 2005). The dark terrain is believed to be covered by even darker dunes (Lorenz et al. 2006b), which are absent from the lake. At least the reflectance spectrum of the dark terrain, as reconstructed by McCord et al. (2006) from Cassini VIMS data, is similar in shape to the lake spectrum. While their analysis is restricted to the methane windows, the advantage of VIMS is its wider wavelength range compared to that of the DISR spectrometers. Significantly, McCord et al. conclude that the dark material spectrum is not consistent with pure tholin, and may be composed of water ice mixed with a dark material. My conclusions concerning the lake spectrum are similar; it features a red slope in the visible wavelength range, which is consistent with the presence of organic material. The blue slope in the near-IR may be due to water ice, but an organic origin cannot be excluded. It is important to stress that even though the shape of the reflectance spectrum is now known with reasonable accuracy, not a single compound making up the surface has been identified with certainty. The main absorption feature at 1.5 μm absorption may be associated with water ice, but it is also present in the spectrum of (yellow) tholin, where it is *not* due to water. Due to uncertainties in the calibration, we tentatively conclude that this feature deepened after landing. It is tempting to speculate that the landing dispersed material from the landing site, exposing water ice.
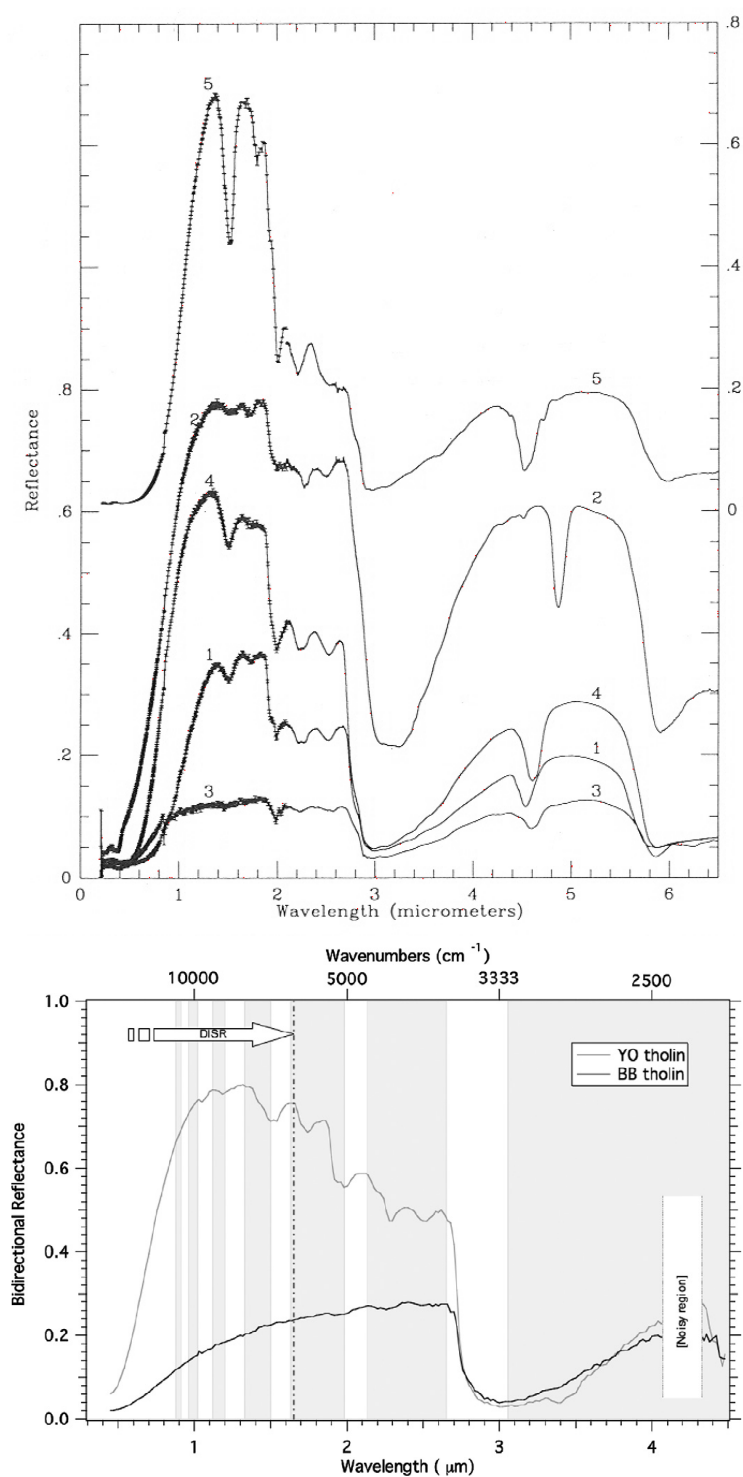
Figure 5.23: Tholin reflectance spectra. **Top**: Tholins prepared by Sagan and Khare from different mixtures under different conditions (labeled 1-4). Tholins 3 and 4 were made by subjecting a 9:1 nitrogen/methane gas mixture to an electrical discharge in different experimental setups. Figure from Cruikshank et al. (1991). **Bottom**: Bernard et al. (2006) prepared yellow ('YO') and black ('BB') tholins by subjecting a 98:2 nitrogen/methane gas mixture to an electrical discharge under low pressure to mimic Titan stratosphere conditions. (Figure from their paper.)

Figure 5.24: Reflectance spectra of CO_2 (**left**) and NH_3 (**right**) frost. Figures from Hapke et al. (1981).

Figure 5.25: Example of temperature affecting the reflectance of an intimate mixture of mineral and water. Spectra of the clay mineral kaolinite ($Al_2Si_2O_5(OH)_4$) mixed with 25% water at room temperature (labeled 'A' at **left**) and 150 K (labeled 'B' at **right**). Figures from Clark (1981a).
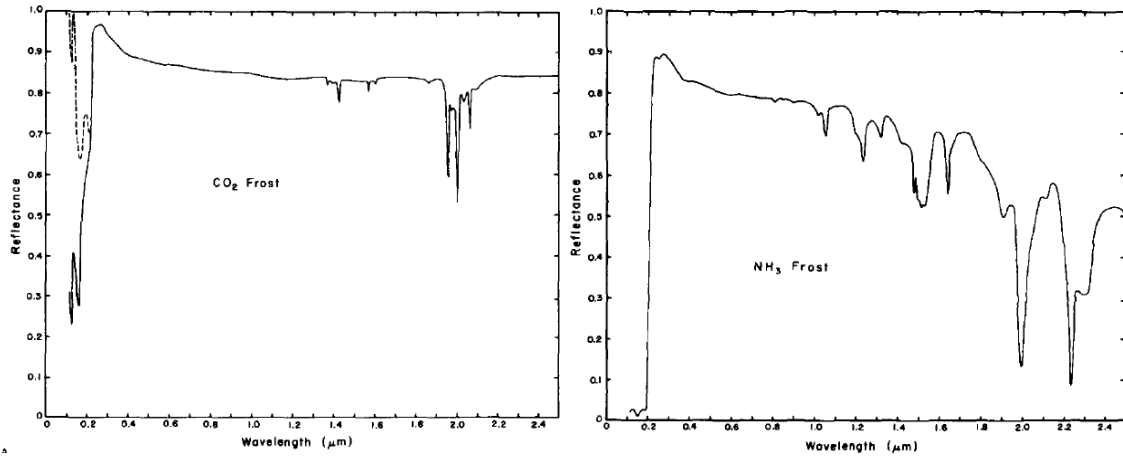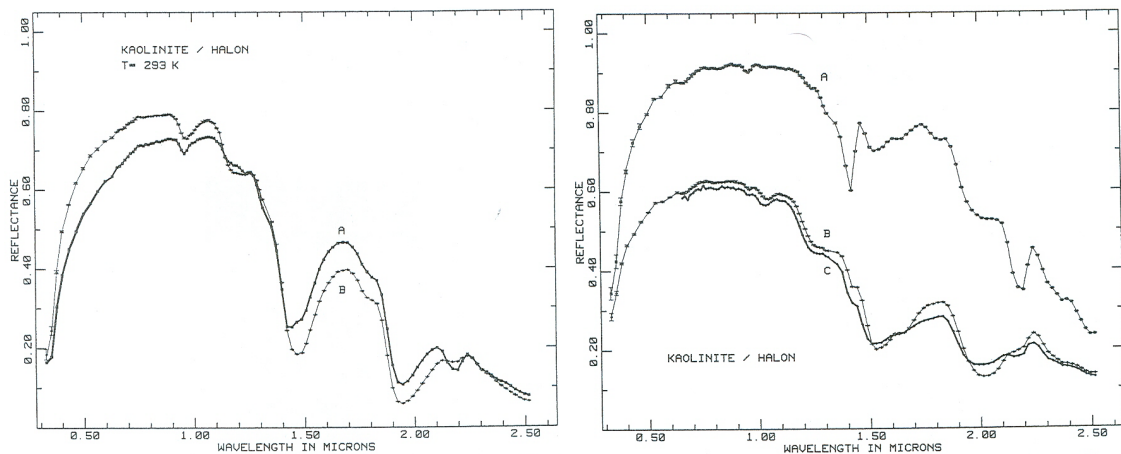
6 Surface BRDF

In the latter stages of the descent DISR acquired most of its images in so-called panoramic cycles. As the name suggests, these cycles were designed to build a full 360° panorama of the probe's surroundings in a relatively small number of rotations. In principle, this would require the acquisition of a total of twelve triplets. As the probe would be able to return only one to two triplets per rotation, the on board software needed to predict the pointing of each exposure as accurately as possible to avoid overlap, and therefore required good knowledge of the actual azimuth angle. Due to the failure of the Sun sensor, this scheme failed in flight, and pointing angles were calculated based on a pre-loaded model of rotation. With Cassini transmitting back only half of the images (the "Channel A anomaly" discussed by Lebreton et al. 2005), the resulting panoramas are far from perfect.

Below 25 km DISR recorded a total of nine panoramas. The task of reconstructing an accurate, seamless map of the surface from these panoramas is complicated by the fact that the observed intensity is a function of nadir and azimuth angle, and altitude. We can eliminate altitude as a complicating factor by regarding panoramas individually, since they were acquired within a relatively short time span, during which the probe descended only by a kilometer or so. Clues to the influence of nadir and azimuth angle can be found by collectively scaling the brightness of all images in a panorama. Figure 6.1 shows some examples: two panoramas taken at a relatively high altitude (23-28 km) and two lower ones (14-18 km). We see the familiar coast line running diagonally through the scene, with the land/river area in the northwest, and the lake area in the southeast (compare Fig. 1.10). On comparison, the muting effect of the atmosphere becomes clear; the panoramas acquired at lower altitude show the surface at higher contrast. Also, the image brightness generally increases outward (with increasing nadir angle) due to atmospheric scattering. Conspicuously, the brightest part in the panorama is always found in the northwest corner, and the darkest part just southeast of center. The fact that the location of these extremes is the same in each panorama leads to the suspicion that we are dealing with backscattering, either by the atmosphere, surface, or both. It is the subject of this chapter to disentangle the contributions of surface and atmosphere, and to retrieve the surface **Bidirectional Reflectance Distribution Function** (**BRDF**). By finding out how the surface reflects light under different viewing and reflection angles I hope to find clues to its physical nature.

With the imager passband roughly extending from 650 to 950 nm, DISR images of the surface are significantly affected by haze scattering. This is why we turn our attention to the downward looking spectrometers. The surface is best observed in the near-IR methane windows of the DLVS and DLIS. Ideally suited for our purpose are two special observing cycles, called spectrophotometric maps (see Sec. 4.1). Two maps were acquired; SM1 at
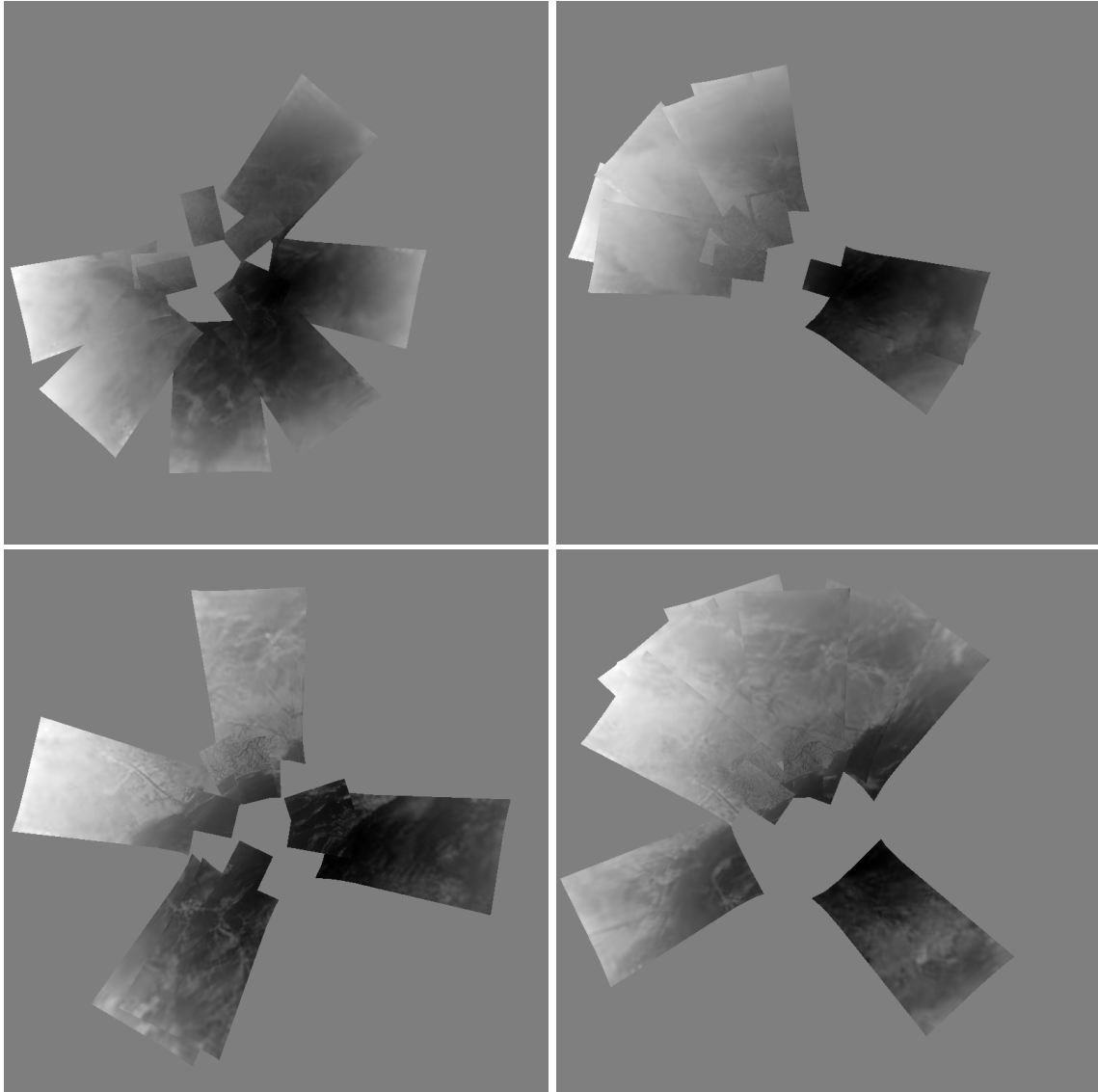
Figure 6.1: Examples of panoramic imaging cycles. For each panorama all MRI and HRI images are displayed in gnomonic projection, their brightness scaled such that pixels of minimum brightness (as determined for all images combined) are displayed as black, and pixels of maximum brightness as white. Clockwise from top left: panoramas acquired at 27-28 km, 23-24 km, 17-18 km, and 14-15 km altitude. North is at the top, and the Sun is at 4 o'clock.

18 km altitude and SM2 at 4 km. Apart from offering the highest possible spatial resolution, the maps have the advantage that the DLVS and DLIS recorded spectra in rapid succession in less than one probe rotation, thereby eliminating altitude as a complicating factor. The spectrophotometric map mode was especially important for the DLIS. Whereas in its regular mode of operation it summed exposures over many rotations on board, thereby averaging the intensity over all azimuth angles, the maps offer the clear advantage of spatial resolution.

This chapter is devoted to analyzing the DLVS and DLIS spectrophotometric maps of the landing site. To correctly interpret these maps it is essential to understand what we see in the images. This is why I attempt to better characterize the landing site by comparing DISR images with Cassini observations in the first section of this chapter (Sec. 6.1). The spectrophotometric maps contain a wealth of information. In Sec. 6.2 I show how they allow us to disentangle the atmospheric and surface contributions to the observed intensity, and proceed to reconstruct the surface BRDF. This analysis also includes Medium Near Surface (MNS) and Very Low Near Surface (VLNS) mode spectra. In the following section (Sec. 6.3), I model the BRDF using the well-known Hapke model for particulate soils to find out more about the surface properties. In the final section of this chapter (Sec. 6.4), I map the colors around the landing site and discuss the implications. This section is a follow-up on the preliminary analysis of the color of the surface I reported in Tomasko et al. (2005), where I dealt only with DLVS spectra within a single panoramic imaging cycle. Here I include the spectrophotometric maps of both the DLVS and DLIS, which provide better spatial coverage at a higher resolution.

6.1   Huygens landing site

Huygens landed at longitude 167.6° E and latitude 10.2° S, to 0.1° accuracy (Karkoschka et al. 2007). The DISR cameras provide clear images of the landing site and its surroundings. The covered area is large enough to allow for a comparison with the views offered by the instruments onboard Cassini. The Imaging Science Subsystem (ISS), Visual and Infrared Mapping Spectrometer (VIMS), and Synthetic Aperture Radar (SAR) instruments all have observed the landing site; ISS and VIMS many times and the SAR only twice, a close view during flyby T8 and a distant view during flyby T13. The VIMS images of the landing site are of relatively low resolution (Rodriguez et al. 2006), and only allow a comparison of large scale features. The resolution of the SAR and ISS images is sufficient to permit detailed comparison with the DISR mosaic of Karkoschka et al. (2007). Lunine et al. (2007) identify the location of the landing site by matching the dark lines seen in the north of the DISR mosaic to the "cat scratches", or dunes (Lorenz et al. 2006b), visible in the T8 SAR image. Here, we discuss the implications of this finding in terms of surface morphology and include ISS images of the landing site in the analysis.

DISR images reveal the presence of two major geological units (Tomasko et al. 2005): "land" terrain in the north, which is relatively bright and consists of hills incised with dark, river-like channels, and "lake" terrain to the south, which is dark, flat, and resembles a lake bed. Figure 6.2 shows how the DISR mosaic fits within the SAR and ISS images. A detailed comparison between the SAR image and the DISR mosaic is provided in Fig. 6.3. The good visual match with the ISS image and the dunes in the SAR image
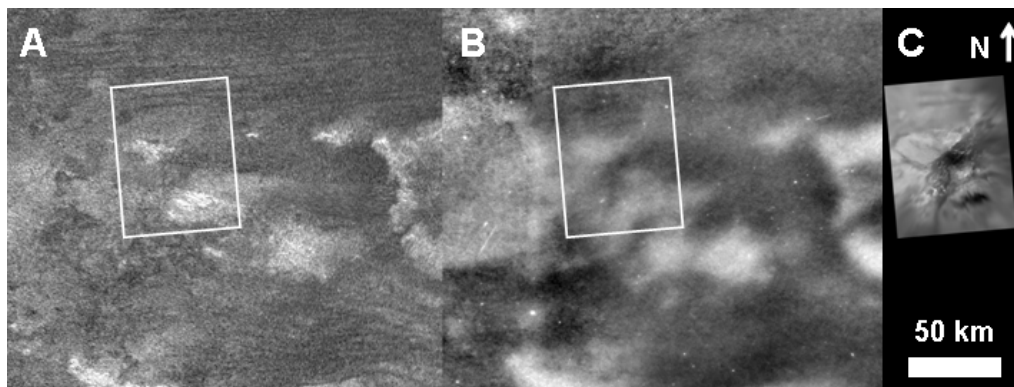
Figure 6.2: The landing site identified in the Cassini radar (**A**) and ISS (**B**) images. The rectangle outlines the location of the Huygens DISR mosaic (**C**), shown enlarged in Fig. 6.3B. (ISS image processing courtesy Travis Fisher.)

allow for accurate placement of the DISR mosaic. However, to match the orientation of the dunes in the ISS image with those in the DISR mosaic, the latter needs to be rotated 5° counterclockwise. However, this does not necessarily imply that the whole mosaic is off by 5°. Whereas the outer parts of the mosaic may contain significant distortions with orientations off by as much as 5-10°, the orientation in the center (within 5 km of the landing site) is probably good to 1-2° (Karkoschka, pers. com.). Our discussion is mainly concerned with the outer parts of the mosaic. The ISS and SAR images in Fig. 6.2 show good overall agreement, except west of the landing site, where ISS bright material shows up dark in SAR. The DISR mosaic ought to show good agreement with the ISS since the ISS filter wavelength (938 nm) is included in the DISR passband, but there are some notable exceptions. For example, the terrain in the north of the DISR mosaic should be darker. Its relative brightness is difficult to estimate since the MRI images that were used to construct this part of the mosaic brighten towards the top of the image due to atmospheric scattering. Note that the mosaic as originally published (Tomasko et al. 2005) suffers from the same deficiency. The most noticeable difference between DISR and ISS is an area southeast of the landing site which is seen dark by DISR, but bright by ISS. Significantly, this Dark Spot (DS; Fig. 6.5) is an area of high SAR brightness, as is the rugged terrain covered by rivers north of the landing site seen in detail by DISR. Given that the correlation between the DS and the SAR bright terrain is so strong (see Fig. 6.3), both terrains are probably similar. A natural explanation for the high SAR brightness is that the river area is rough on the scale of the SAR wavelength (2.17 cm) and/or features slopes.

The reason why the two river areas appear so different to DISR is the viewing and solar phase angle. Consider the river area north of the landing site. Figure 6.4 shows how it appeared bright relative to the lake early in the descent when observed at a low solar phase angle (22°). Just before landing, when observed at higher phase angles (typically 65°), it had darkened relative to the lake, most notably along the coast line and the rivers. This darkening appears to be restricted to the river area, and is not seen for the bright islands in front of the coast, whose nature seems to be fundamentally different. That the brightness of river and lake terrain has a different phase angle dependence implies that they cannot both scatter as Lambert surfaces. We can interpret this difference in terms of
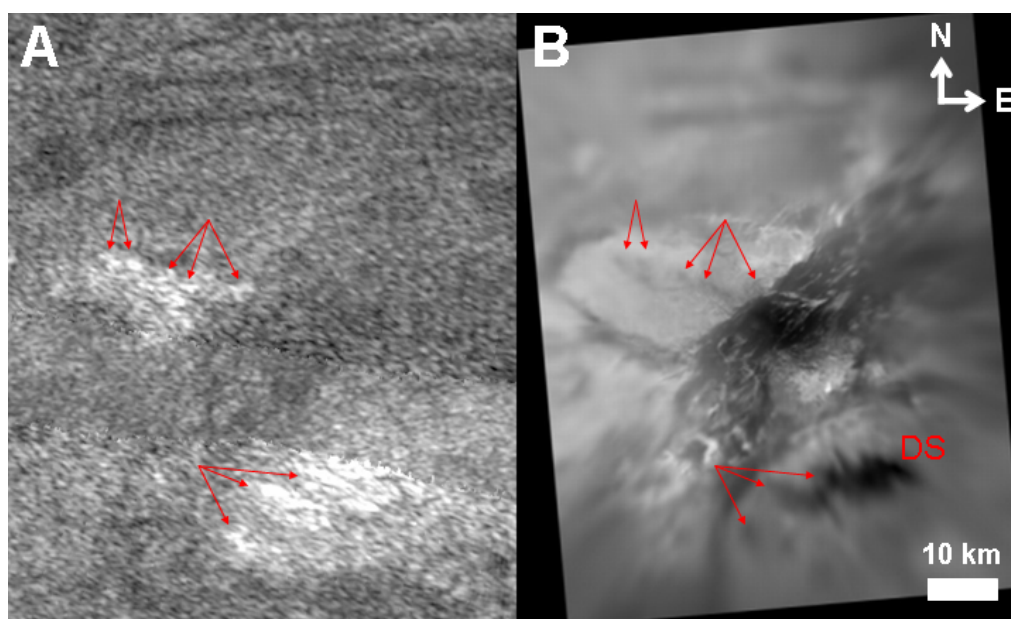
Figure 6.3: Detailed comparison between the Cassini radar (**A**) and Huygens DISR (**B**) images of the landing site. The top arrows point at the river terrain seen in detail by DISR, the bottom arrows point at the suspected river terrain seen by DISR as a Dark Spot (labeled DS). The DISR mosaic (Karkoschka et al. 2007) is centered on the Huygens landing site. We rotated the mosaic by 5° counterclockwise to make the dunes in the north have the same angle with the horizontal and to better match the DS with the radar bright features in the south.

surface roughness and shadow hiding (e.g. Hapke 1981, 1984). Higher surface roughness leads to stronger decrease in brightness with phase angle, with the implication that the river terrain is more rough than the lake, consistent with the radar observations (albeit at a different spatial scale). The fact that the strongest darkening is associated with the coast line and the rivers themselves, suggests that steep slopes also play a role. This hypothesis is consistent with the view that the river terrain is an old and eroded (perhaps original) part of the crust, and that the lake is sedimentary in nature.

The DS was imaged only by the SLI in the last stage of the descent, in the general direction of the Sun (Fig. 6.5). It was observed at even larger solar phase angles (90°-105°) than the rivers north of the landing site just before landing (65°, see Fig. 6.4). The fact that the DS is also dark in the visible, but bright in radar strongly suggests it is another river area; in the center SLI image a river can be discerned. So we have identified the nature of the SAR-bright terrain in the vicinity of the landing site; it is hilly terrain crisscrossed by rivers. It is also bright at visible wavelengths, but only at low solar phase angles. SAR-dark terrain is flat and lies below the bright terrain. The conclusion is that Huygens landed on a floodplain in between two river systems, one close by to the north, the second larger and further away to the southeast.
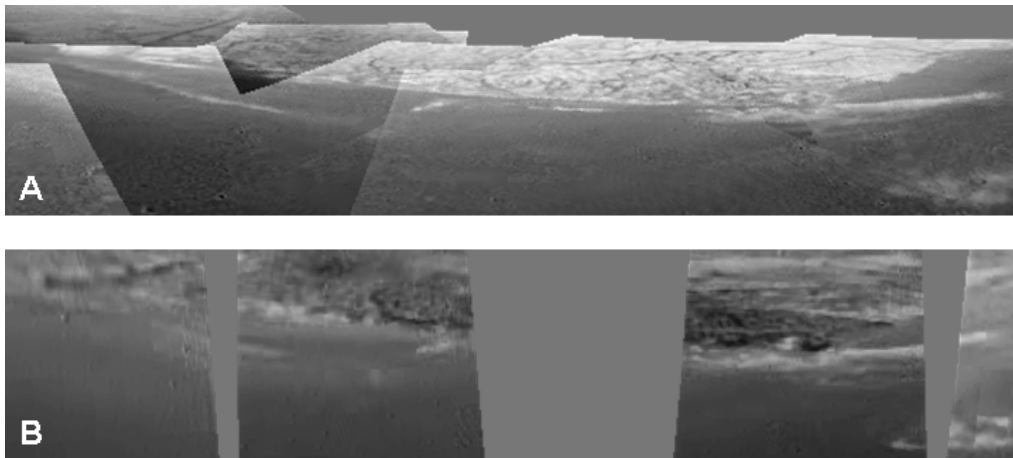
Figure 6.4: The brightness of the river area relative to the lake bed depends on the solar phase angle. These two panoramas show the same stretch of coastline in perspective view (Mercator projection), but one was recorded at high altitude (low phase angle) and the other at low altitude (high phase angle). They are reprojected to the same viewpoint 1 km directly over the landing site in the lake bed. Brightness and contrast have been adjusted to make the lake bed look the same in both panoramas. **A**: HRI **402–480** and MRI **436**, acquired at altitudes 12.4–16.7 km, typical solar phase angle 22°. **B**: SLI **698–710**, altitude 0.46–0.91 km, typical solar phase angle 65°.

Figure 6.5: Three SLI images of the Dark Spot (DS) in Fig. 6.3. The images have been processed to minimize the influence of the atmosphere (courtesy Erich Karkoschka). Note that SLI **524** shows river-like structures within the spot. The altitude at which the image was acquired and the DS solar phase angle can be found at the bottom of each image, and arrows denote the DS location.

6.2   Spectrophotometric maps
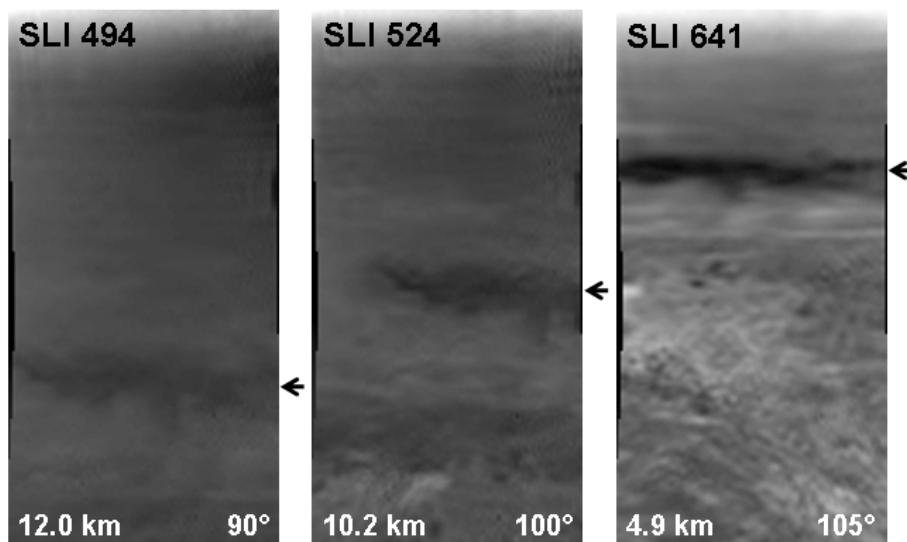
As outlined above, the intensity observed coming up from the surface not only depends on the local surface albedo, but also on the direction of observation due to the presence of the atmosphere; it varies with azimuth angle, generally increases with nadir angle, and decreases with altitude. Most strongly so at visible wavelengths because here the haze dominates. To disentangle the contributions of atmosphere and surface we turn our attention to the spectrophotometric map, MNS (DLIS only), and VLNS mode spectra. These special mode spectra offer specific advantages over spectra acquired during regular panoramic cycles. In the spectrophotometric map mode DISR acquired spectra at as rapidly as possible for the duration of about one probe rotation (see Chapter 4). In case of the DLVS, the CCD columns were not summed on board before transmitting, yielding spectra with the maximum spatial resolution. The decrease in altitude during acquisition of the maps was small compared to the starting altitude (SM1: 1%, SM2: 5%; see Appendix A), so that we may consider the altitude constant. This advantage comes at a price. In contrast to the usual panoramic cycles no images were obtained close in time to any of the map spectra. So whereas spectra recorded during panoramic cycles can each be tied to an image, here we need to rely on a probe rotation model to orient the maps and to determine the angle between the individual spectra. The Karkoschka et al. (2007) attitude model provides reliable azimuths, but the probe tip and tilt during acquisition of map spectra are unknown (but estimated to be smaller than $5°$). The VLNS spectra, which were acquired below 206 m altitude, suffer from the same uncertainties.

Without altitude as a disturbing factor, we can analyze how intensity varies with the viewing direction at different wavelengths. First we consider the intensity in methane windows observed by the DLIS; the results for the 0.93, 1.07, 1.28, and 1.59 μm windows are displayed in Fig. 6.6. In the figures on the left we find the intensity as a function of azimuth angle with respect to the Sun. First we note that at all wavelengths the SM1 intensities are higher than the SM2/MNS/VLNS intensities. Since SM1 spectra were acquired at a much higher altitude than the others (18 km versus <4 km), this implies that the atmosphere contributes to the intensity. This contribution becomes weaker with wavelength, and at 1.59 μm the lower atmosphere is virtually transparent. This behavior is typical for haze aerosol scattering. Below 4 km altitude the atmospheric contribution appears to be negligible since the SM2, MNS, and VLNS intensities overlap. Second we note that the intensity in Fig. 6.6 reaches a maximum at azimuth angle $180°$, and a minimum at $0°$, regardless of the mode of observation. Since at azimuth $180°$ the Sun is in our back, the rise in intensity from $0°$ to $180°$ must be caused by backscattering. Deviations from this smooth rise can be attributed to surface features with different intrinsic albedo. Most notable in the SM1 curve are the jumps in intensity at $80°$, and between $200°$ and $250°$, both related to the transition from lake to land and vice versa (see Fig. 4.3). Notice also the bump at $320°$, which covers a location in the lake area opposite to the land. A similar feature is present in the SM2 intensities between $90°$ and $140°$, where the footprints cover a relatively bright, elongated "island" in the lake (see Fig. 4.4). To compare these different types of terrain we consider how intensity varies as a function of solar phase angle in Fig. 6.6 (figures on the right). Judged from the SM2 observations (all of clean lake area, apart from the few mentioned above), the intensity is a smooth, almost linearly declining function of phase angle. At the SM2 altitude the surface dominates over the atmosphere

in all DLIS methane windows, which implies that at these wavelengths the surface itself is backscattering. The SM1 observations of the land/river area can be clearly distinguished from those of the lake. Figure 6.19 shows how each set of observations occupies its own phase curve, having the same shape as that associated with SM2 but a different slope. Note that for now we approximate the phase curve by a line, but we will refine our approach in the next section. Deviations from the line can be related to surface features. Examples are the aforementioned positive bump at 50°-55° and the negative bump around 20°, the latter associated with the relatively dark area directly east of the long, straight river (see Figs. 1.10 and 4.3). The slopes of the SM1 phase curves (affected by both surface and atmosphere) are steeper than that of the SM2 curve (dominated by surface), which implies that the haze aerosols are backscattering too. I use the fact that the lake terrain was both observed by SM1 and SM2 to devise a (crude) correction for the atmospheric contribution, and derive the color ratio of the different terrains in Section 6.4.

The situation is somewhat different for the intensity in methane windows observed by the DLVS, as here the influence of the atmospheric haze is much stronger. To enable a comparison between the spectrophotometric map with the VLNS mode, we approximate the spatial coverage of a VLNS spectrum by calculating the average of footprints 11 and 12 of each map spectrum. Figure 6.7 shows that the influence of the atmosphere reaches all the way down to the surface, as the SM2 intensities no longer coincide with those of the VLNS. We see the same phenomena and features as in the DLIS methane windows, albeit more subdued. There is some overlap in wavelength range between the DLVS and DLIS. If we compare the intensity in the 0.93 μm DLIS window (Fig. 6.6) with that in the 935 nm DLVS window (Fig. 6.7) we find that overall the DLVS shows the same features as the DLIS, but its data is much more noisy due to the low responsivity at this wavelength. Also, the DLVS intensities are higher than DLIS intensities due the former's higher spectral resolution. The DLVS covers a larger range of phase angles than the DLIS, reaching all the way up to phase angle zero; Figure 6.8 shows the full range. Note that the scattering behavior of the surface itself at small phase angles may be completely different than shown here. The reflectance of many solar system bodies sharply increases at small phase angles, a phenomenon known as the opposition effect. Two mechanisms proposed to contribute to the opposition effect are shadow hiding and coherent backscatter, and both are affected by the presence of an atmosphere. Shadow hiding is ineffective at visible wavelengths because of the predominance of diffuse illumination, and coherent backscatter (a form of constructive interference) requires a significant fraction of the direct solar beam to reach the surface (estimated to be only 1% at 830 nm, Lyn Doose pers. com.). I return to the opposition effect in the next section.

It is clear that if we want to reconstruct the BRDF of the surface we need to turn our attention to the low altitude DLIS observations. Close inspection of the SM2/MNS/VLNS measurements in Fig. 6.6 reveals that even though they all broadly overlap, the VLNS phase curve is always intermediate to that of the SM2; at low phase angle the VLNS intensities are lower than those of SM2, at high phase angle they are higher. This can be explained by the fact that there is an intrinsic large scale surface brightness gradient running across the lake, with the probe having landed in the midst of it (Fig. 6.9). By act of a cosmic conspiracy this gradient runs more or less along the Sun line, resulting in an expected drop intensity as observed by the SM2 of about 3%. The area covered by the VLNS measurements is very small compared to that covered by SM2 (compare Fig. 4.5

102

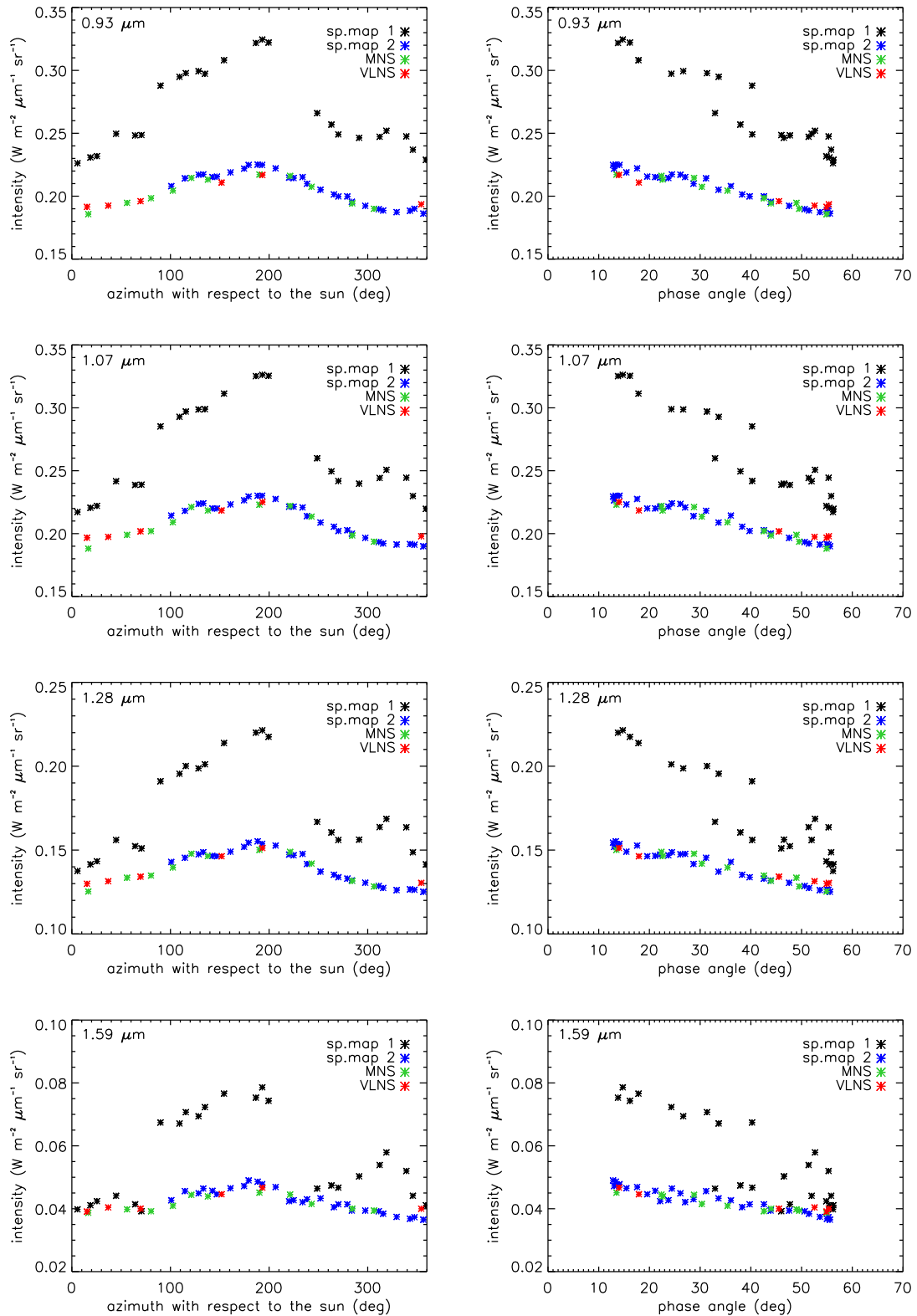Figure 6.6: The intensities in the 0.93, 1.07, 1.28, and 1.59 μm methane windows (**top** to **bottom**) plotted for all single (unsummed) DLIS measurements as a function of azimuth angle (**left**), defined running counterclockwise, and solar phase angle (**right**). The last pre-landing VLNS measurement was discarded because of lamp light, and the others had the intensity in a neighboring methane band subtracted.

103
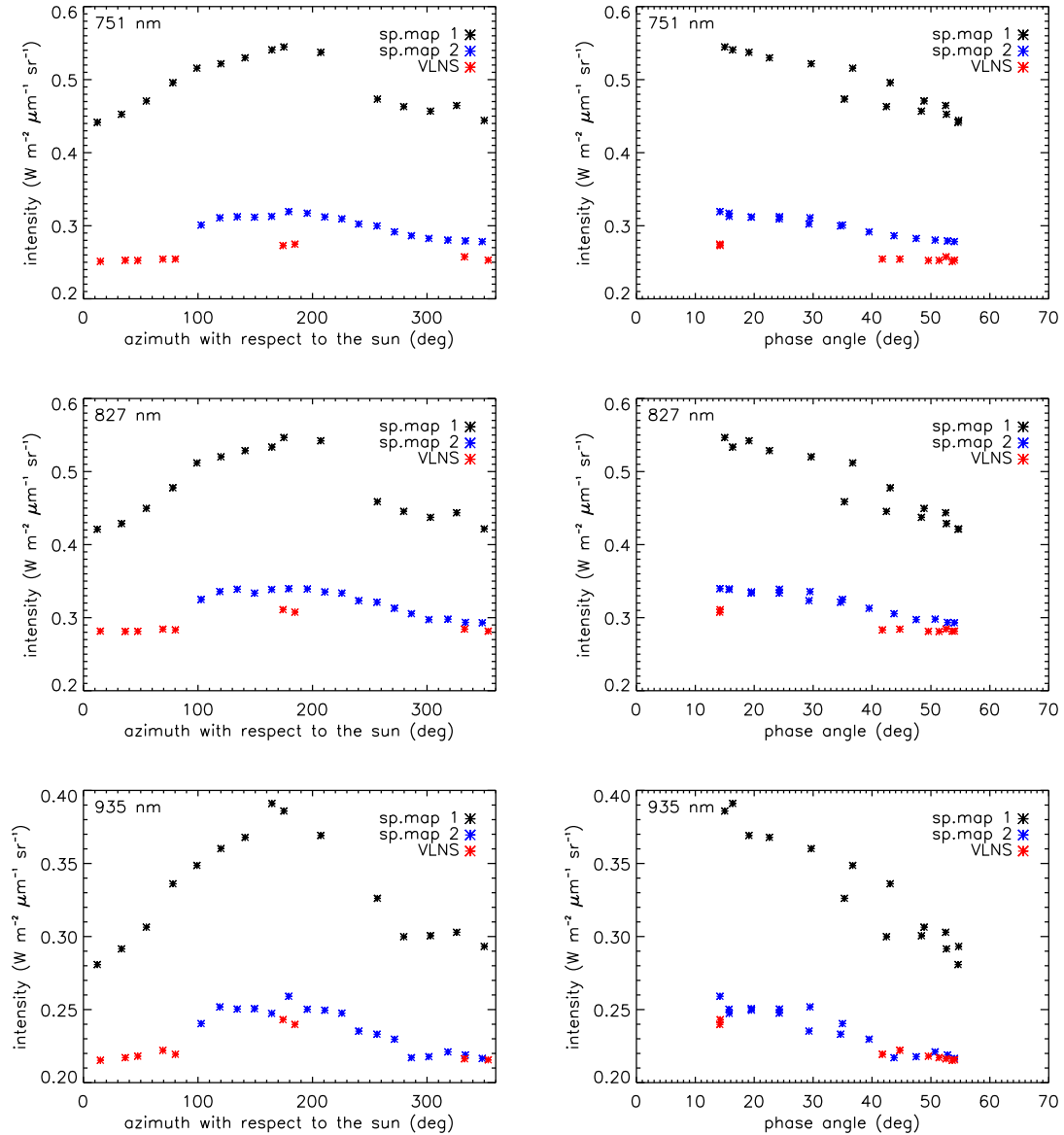
Figure 6.7: The intensities in the 751, 827, and 935 nm methane window plotted for the spectrophotometric map and VLNS mode DLVS measurements as a function of azimuth angle with respect to the sun (**left**) and solar phase angle (**right**). Azimuth angle is defined running counterclockwise. The last two VLNS measurements before landing were discarded because of the presence of lamp light. To enable comparison with the VLNS data the SM1/SM2 intensities are shown as the average of footprints 11 and 12 (footprint 15 is closest to nadir).
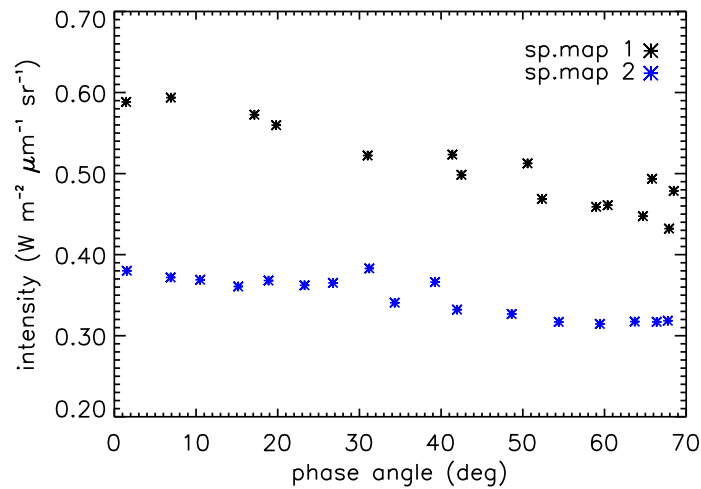
Figure 6.8: The intensities in the DLVS 827 nm methane window for footprint 5 of the spectrophotometric map measurements, showing the full solar phase angle range of the DLVS (footprint 15 is closest to nadir).
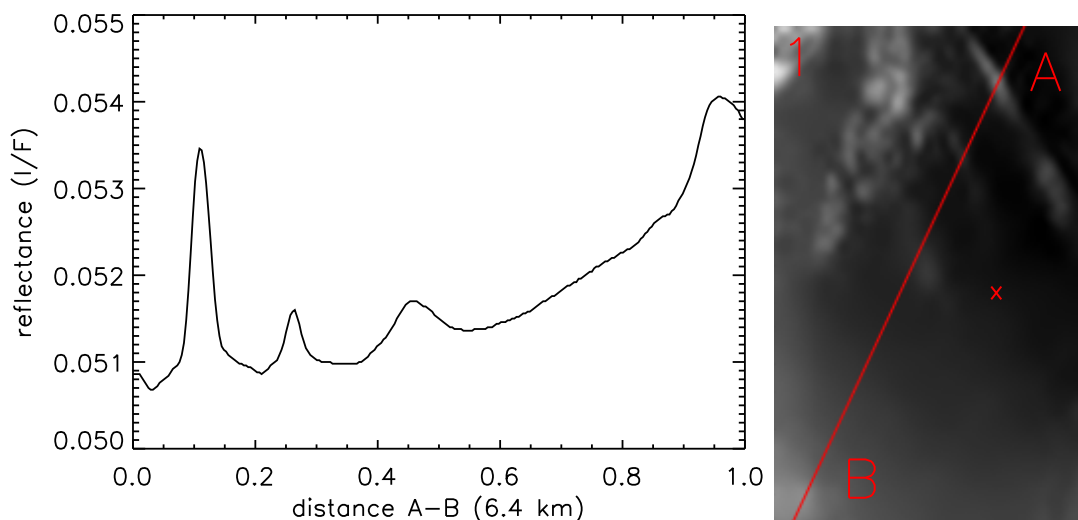
Figure 6.9: The lake area in which Huygens landed exhibits an intrinsic large scale brightness gradient. The figure on the **left** shows the brightness profile across HRI **384** on the **right**. The coast line is just beyond B. The landing site is indicated with a cross. Brightness is given as I/F, with πF the solar flux at the top of the atmosphere.

to Fig. 4.4), so if we consider only VLNS data we can ignore the large scale brightness gradient. Even though the phase angle coverage of the VLNS spectra is not as dense as that of SM2, it does extend over the full range subtended by the DLIS. From the SM2 spectra we can infer the regularity of the BRDF in between these extremes. The DLIS VLNS measurements then represent the surface BRDF for an incidence angle of 34° and phase angles in the range 13°-57°.

6.3 Modeling the BRDF

Having identified the BRDF, we may study the properties of the lake area around the Huygens landing site by modeling. First we take a closer look at Titan's surface to search for clues to its scattering behavior. The images acquired by DISR after landing offer a close-up view (Fig. 6.10). In the SLI image we see rounded, decimeter sized rocks, presumably made up of water ice, on a smooth soil. It appears that the most spherical rocks are resting on top of the soil, as if they have been rolling over the plain, whereas more elliptical rocks are embedded. The MRI images reveal the soil to be granular, perhaps made up of water ice 'sand'. Most likely, but invisible to the camera, everything is covered by organic matter (tholins?), which constantly 'drizzles' out of Titan's atmosphere. These images suggest that two factors contribute to the surface BRDF: the soil through its intrinsic scattering properties (microscopic shadow hiding and possibly coherent backscatter), and the cobbles through macroscopic shadow hiding. Our approach to modeling these processes is two-fold as well.

To investigate the effect of macroscopic shadows on the surface BRDF we employ the open-source *Persistence of Vision Raytracer* (POV-Ray 3.6, `www.povray.org`). We construct two types of surfaces, one with a Titan-like distribution of cobbles (*"realistic"*), and the other with identical 8 cm diameter spheres (*"spheres"*). The *realistic* surface emulates the observation that spherical cobbles are more elevated. Lighting is provided by a point source with parallel light rays, placed in the same direction as the Sun from Huygens' perspective. We make the simulated cobbles slightly more reflective than the surface, but both reflect isotropically. The model has no atmosphere and considers singly scattered light only, so shadows are black. In reality we would expect multiply scattered light to illuminate the shadows, hence our simulation represents a worst case scenario. Figure 6.11 compares the virtual surfaces with the SLI post-landing view. The simulations give us a sense of scale for the scene in the SLI image. On comparison with the *spheres* simulation, the diameter of the rounded cobble in the center can be estimated to be circa 10 cm. The distribution of light on the cobbles is well reproduced by the *realistic* simulation, as is the position of the shadows. The agreement becomes worse when we add specular reflection to the cobbles, the mismatch being most notable on the cobbles in the foreground. This implies that the cobbles do not exhibit specular reflection, but scatter diffusely. Surprisingly, since the simulated distribution of spheres is completely random, the post-landing viewing perspective creates the illusion of 'channels', devoid of cobbles. Especially the similarity of the *spheres* channel with that seen in the SLI image is striking, which serves as a warning against over-interpreting patterns seen in the Titan surface image.

We now view the simulated surfaces from the perspective of the probe during acquisition of the spectrophotometric maps. Figure 6.12 scales the simulated intensities to those observed by the SM2. As expected, the effect of the *spheres* shadows on the BRDF is larger than that of the *realistic* shadows, but the variability associated with both simulated surfaces is much smaller than that observed on Titan's surface. Remember that the *spheres* simulation is a worst case scenario, since it shows much more shadow than is visible in the SLI image, and its shadows are completely black. The true macroscopic shadow effect is most likely even smaller than that in the *realistic* simulation, since it too has black shadows, and Fig. 6.12 (right) shows that it must be very small indeed. This simple simulation
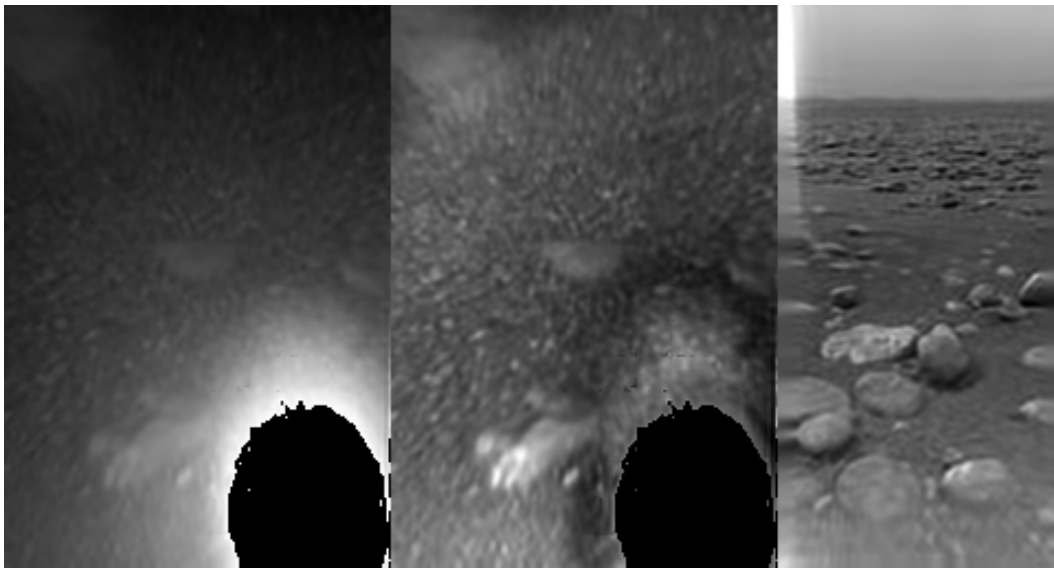
Figure 6.10: Titan's surface as seen by the probe after landing. The **left** and **middle** are MRI images, an SLI image is on the **right**. The black ellipse in the lower right corner of the MRI images is the overexposed lamp spot. The middle image was processed to remove the lamp brightness gradient (courtesy Michael Küppers); the dark ring around the lamp spot is an artifact.
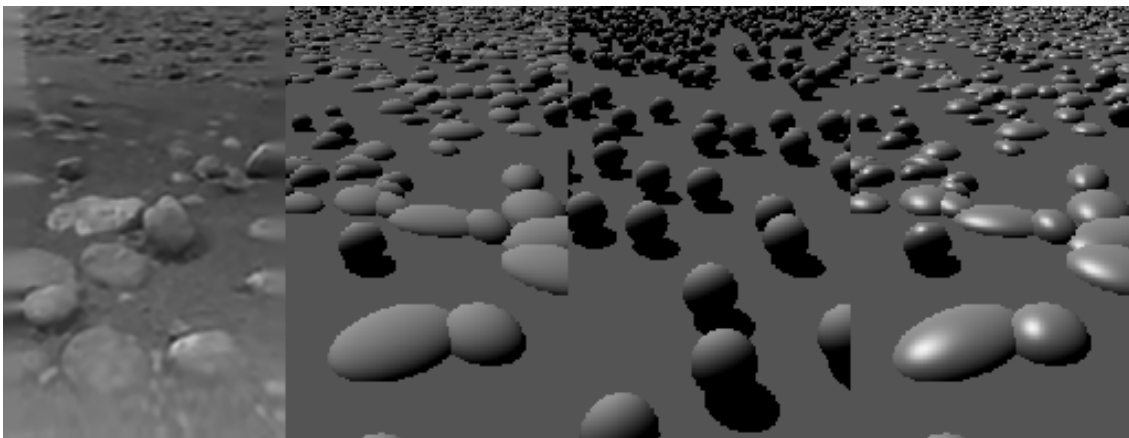
Figure 6.11: Titan's surface and two simulated surfaces with randomly distributed cobbles as seen from the DISR's perspective after landing, all displayed at the same image resolution. The Huygens SLI view (**far left**) is shown with a realistic (*"realistic"*, **center left**) and an idealized (*"spheres"*, **center right**) simulated surface covered with identical 8 cm diameter spheres. The simulation considers only singly scattered light, with rocks and surface reflecting diffusely. The simulation at the **far right** adds specular reflection to the *realistic* scene.

suggests that macroscopic shadows contribute very little to the observed surface BRDF, and that soil scattering properties dominate.

The theory of Hapke (1981, 1984, 1986, 2002) is widely used to model the BRDF of particulate soils (e.g. Buratti 1985, Domingue and Verbiscer 1997, Clark et al. 2002,

Figure 6.12: Simulations of the macroscopic shadow hiding effect compared to observations at 1.28 μm. **Left**: The brightness of the two surfaces in Fig. 6.11 relative to an empty surface as it would be observed by the DLIS for a full probe rotation. **Right**: The simulated intensities scaled to match the maximum of the SM2 1.28 μm observations.

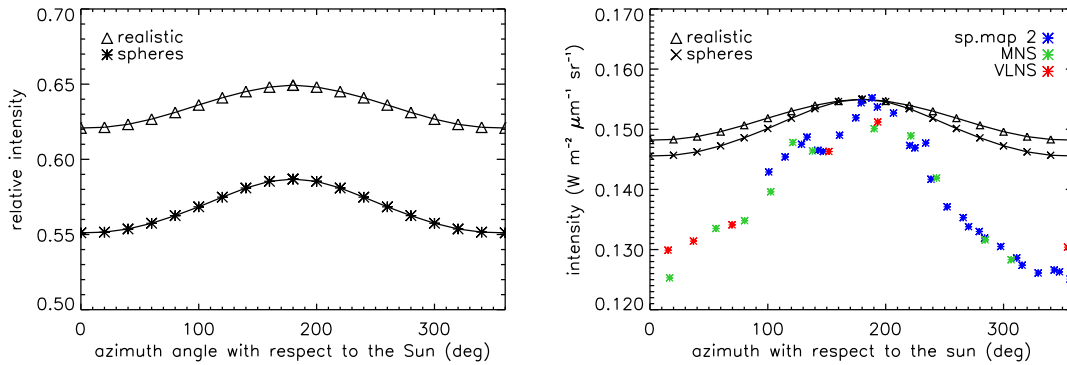Cruikshank et al. 2005). It offers a description of the microscopic Shadow Hiding Opposition Effect (**SHOE**), and the Coherent Backscatter Effect (**CBOE**), and a correction for macroscopic roughness. The SHOE is due to shadows cast by soil particles, the CBOE is the enhanced soil brightness observed near phase angle zero due to constructive interference of different light rays scattered in the same direction. While the SHOE is almost entirely caused by singly scattered light, the CBOE arises from both singly and multiply scattered light. Macroscopic roughness refers to structures ("fairy castles") composed of facets, and affects the observed intensity by means of shadows. Hapke's theory is explained in detail in Section 2.2. The basic model has input parameters the single scattering albedo (w_λ), the amplitude and peak half width of the SHOE (B_{S0} and h_S), and the amplitude and peak half width of the CBOE (B_{C0} and h_C). In addition, it allows for the specification of an intrinsic particle scattering phase function $P(\phi)$ as a function of the phase angle (ϕ). Inclusion of macroscopic roughness requires specification of the mean slope angle Θ of the facets. Note that the macroscopic roughness effect is not only a function of the phase angle, but also of the angles of incidence and reflection.

The data to which we fit the Hapke model are the DLIS VLNS observations in the methane windows at 0.93, 1.07, 1.28, and 1.59 μm. We discard the last measurement before landing because of strong lamp light, which leaves us with 6 data points between solar phase angle 13° and 57°. We convert the VLNS intensities to absolute reflectances by scaling their average to the average reflectance determined by Bruno Bézard (pers. com.), who calculated these from the ratio of up- and downward flux derived from early VLNS ULIS and DLIS spectra that show a negligible lamp contribution (average solar phase angle 40°). Figure 6.13 (left) shows that his reflectances compare well qualitatively with the last pre-landing DLIS reflectance spectrum, except at 1.28 μm where his is slightly higher. Bézard calculated the reflectance for 1.55 μm, and we scale our 1.59 μm data to this value. To these data points we add the single measurement at phase angle 0.069° ± 0.056° from the absolute reflectance reconstructed from the last pre-landing DLIS spectrum (to be called the zero phase angle data hereafter) to arrive at the surface BRDF in Fig. 6.13 (right). This gives us a total of 7 data points for each methane win-
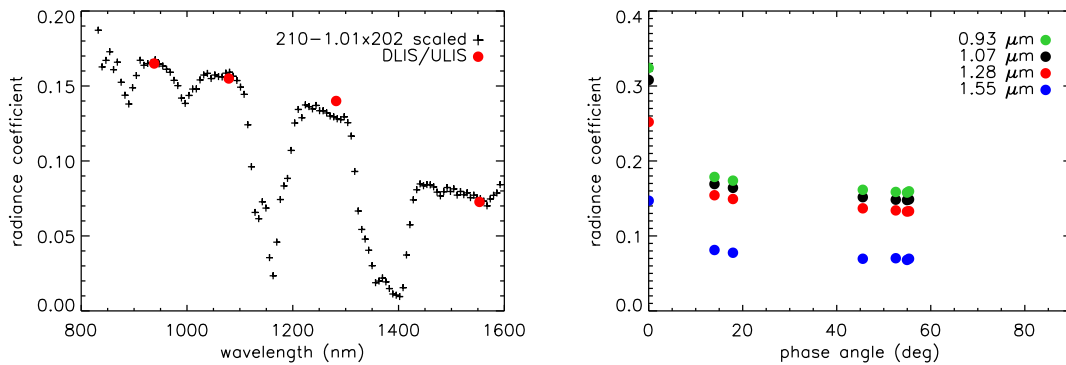
Figure 6.13: Reconstructing the reflectance in the DLIS methane windows as a function of the solar phase angle. **Left**: Reflectances calculated by Bruno Bézard from the ratio of DLIS and ULIS intensities just before landing (red dots) compare well with the scaled reflectance reconstructed from DLIS **210** (scale factor 0.51), except at 1.28 μm. **Right**: We scale the VLNS intensities (phase angles 13°-57°) to Bézard's reflectances, and combine these with the **210** reflectance at zero phase angle to reconstruct the surface BRDF in the methane windows.

dow. The VLNS intensities are averages over a small phase angle range because of the apparent size of the Sun in the Titan sky. In the discussion that follows I consider the Sun a point source, ignoring any diffuse illumination by the atmosphere. How reasonable this assumption is can be seen in Fig. 6.14, which shows that most of the diffuse illumination at 1.29 μm is contained within a relatively small solar aureole (width at half maximum is 20-30°). At higher wavelengths the haze is more transparent, so the situation should be better for 1.59 μm. Significantly, the zero phase angle measurements are not affected by this effect because the SSL acts essentially as a point source (its diameter is only 5.2 cm).

Clearly, the problem we face modeling the observed BRDF with the Hapke model is that we have a plethora of parameters, but a dearth of data. The three different scattering mechanisms we have to consider are shadow hiding (SHOE), coherent backscatter (CBOE), and macroscopic roughness. First I investigate the effect of macroscopic roughness in Fig. 6.15. In the top figure I try out different values for the mean slope Θ of the facets that build up the macroscopic structures. Because the model depends not only on the phase angle but also on incidence and reflectance angles, the reflectance is calculated for the viewing conditions for the DLIS during the VLNS phase of the descent. From the shape of the model curve we find $\Theta \leq 40°$; higher values do not fit the high phase angle data. Macroscopic roughness will always lead to a decrease in reflectance with increasing phase angle; the reflectance for a smooth surface ($\Theta = 0°$) is the maximum. From the figure it is clear that the model cannot reproduce the lower phase angle data points (extend the $\Theta = 0°$ model to phase angle zero); SHOE and/or CBOE must play a role as well. Hapke (2002) argues that a model with a broad SHOE and narrow CBOE peak around phase angle zero is the physically correct one. So in the bottom figure of Fig. 6.15 I add SHOE to fit the data points around 15° phase angle, adopting the maximum possible roughness ($\Theta = 40°$). Fitting this model involves fine-tuning w_λ for each methane window, while keeping B_{S0} and h_S constant. The SHOE model including macro-
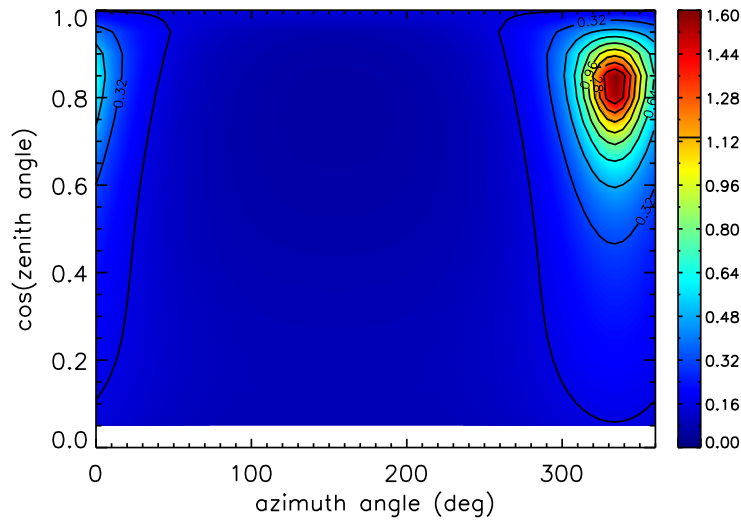
Figure 6.14: The intensity of the diffuse illumination in the sky at 1289 nm as seen from the Huygens landing site, predicted by an early version of the LPL atmosphere model (Lyn Doose, pers. com.). The direct solar beam accounts for 31% of the total downward flux at the surface (26% of the direct beam makes it to the surface).

Table 6.1: Best fit parameters for the Hapke macroscopic roughness models in Fig. 6.15 with $\Theta = 40°$. Particle scattering is isotropic; w_λ is the single scattering albedo at wavelength λ (in μm). h_S and B_{S0} are the peak width and amplitude parameters of the SHOE.

$w_{0.93}$	$w_{1.07}$	$w_{1.28}$	$w_{1.55}$	h_S	B_{S0}
0.700	0.680	0.640	0.410	0.01	1.0
0.695	0.670	0.630	0.400	0.04	0.5
0.705	0.680	0.640	0.410	-	0.0

scopic roughness fits the data well in all methane windows over the full VLNS phase angle range (fit parameters are listed in Table 6.1). The figure depicts limiting cases for the SHOE; whereas the amplitude is not well constrained, the half width parameter must be relatively small ($h_S < 0.05$).

If we assume the surface is perfectly flat (i.e. zero roughness) we can study the performance of the Hapke SHOE and CBOE models separately. First I consider SHOE only. The free model parameters are the single scattering albedo (w_λ), the SHOE amplitude and peak half width (B_{S0} and h_S), and the soil particle scattering phase function $P(\phi)$. As the surface must be covered by aerosols that continuously precipitate from the atmosphere, it seems reasonable to employ similar phase functions for both aerosols and soil particles. Whereas the aerosols are thought to be intrinsically backscattering while suspended in the atmosphere due to their fluffiness, on the surface they may be compacted or coated, and not exhibit internal reflections that lead to backscatter. In that case soil particles may scatter more or less isotropically, at least in the backscatter direction. Therefore, I consider two limiting cases for the particle phase function: isotropic scattering ($P(\phi) = 1$), and scattering according to the double-Henyey-Greenstein phase function
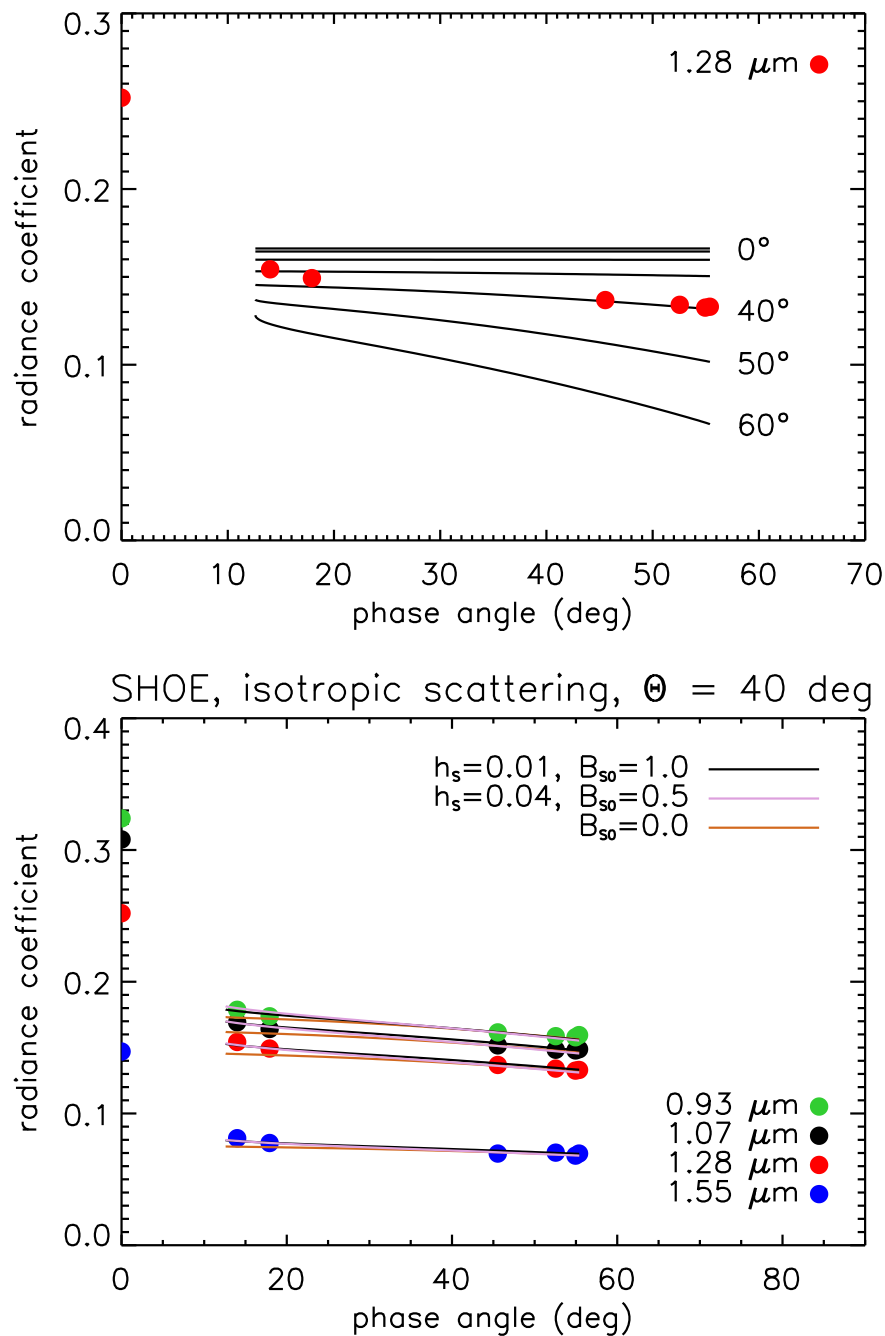
Figure 6.15: The Hapke (1984) macroscopic roughness model adapted for the viewing conditions of the DLIS during the VLNS phase of the descent. Surface particles scatter isotropically. **Top**: Macroscopic roughness (only) model compared to the reflectance at 1.28 μm. The mean surface slope angle Θ ranges from 0° to 60° with 10° increments (labels). The single scattering albedo ($w = 0.64$) was chosen to let the $\Theta = 40°$ model fit the data at high phase angles. **Bottom**: Macroscopic roughness models with $\Theta = 40°$ that include shadow hiding fit the reflectance in all methane windows well.

Table 6.2: Best fit parameters for the Hapke SHOE models in Fig. 6.16. w_λ is the single scattering albedo at wavelength λ (in μm), h_S and B_{S0} are the peak width and amplitude parameters. The double Henyey-Greenstein phase function is shown in Fig. 2.2.

particle scattering type	λ	w_λ	h_S	B_{S0}
isotropic	0.93	$0.605^{-0.015}_{+0.003}$	$0.06^{+0.04}_{-0.01}$	1.0
		0.600	0.10	0.8
	1.07	$0.580^{-0.02}_{+0.005}$	$0.07^{+0.06}_{-0.015}$	1.0
		0.565	0.15	0.8
	1.28	$0.540^{-0.03}_{+0.007}$	$0.08^{+0.12}_{-0.02}$	1.0
		0.532	0.15	0.8
	1.55	$0.335^{-0.025}_{+0.01}$	$0.08^{+0.12}_{-0.03}$	1.0
		0.330	0.15	0.8
double Henyey-Greenstein	0.93	0.652	0.01	1.0
		0.653	-	0.0
	1.07	0.635	0.02	1.0
		0.638	-	0.0
	1.28	0.610	0.02	1.0
		0.613	-	0.0
	1.55	0.460	0.01	1.0
		0.463	-	0.0

(dHG), i.e. the aerosol phase function at 1.28 μm in an early version of the LPL atmosphere model (Fig. 2.2). Figure 6.16 (top) shows model fits for isotropically scattering particles. The reflectance is fit for each methane window individually, and Table 6.2 lists the parameters. Many parameter combinations fit the data well, except at zero phase angle. The SHOE peak width h_S is found to inversely depend on the amplitude B_{S0}. For the maximum amplitude $B_{S0} = 1$ we find $0.05 \le h_S \le 0.20$, depending on the single scattering albedo, with the best fits achieved for $h_S = 0.06$-0.08. For the smaller amplitude of $B_{S0} = 0.8$ the best fitting values are $h_S = 0.10$-0.15. In Fig. 6.16 (bottom) we let the soil particles scatter according to the dHG phase function, and find that intrinsic particle scattering can almost completely replace the SHOE. Now only a very small degree of SHOE ($h_S = 0.01$-0.02) is required to fit the VLNS data (Table 6.2). Again, the zero phase angle data are out of reach of all models.

The fact that SHOE-only models fail to fit the zero phase angle data suggests that we have to take coherent backscatter into account. But the non-zero phase angle data should not be modeled with CBOE, because of the lack of direct (coherent) sunlight reaching the surface. Then the correct approach is to superpose a narrow CBOE peak on a broad SHOE model. In Fig. 6.17 I use the best fitting SHOE models from Fig. 6.16 (top), and restrict the CBOE peak width by adding a single data point at phase angle 0.45° to the 0.93 μm set. The reflectance of this point is derived by scaling down the DLIS 0.069° phase angle reflectance by a factor of 1.17, which is roughly the factor required to match the DLVS **786** reflectance to that of DLIS **210**. Even though this data point is rather speculative, it is our only means to estimate the CBOE peak width. The figure shows that
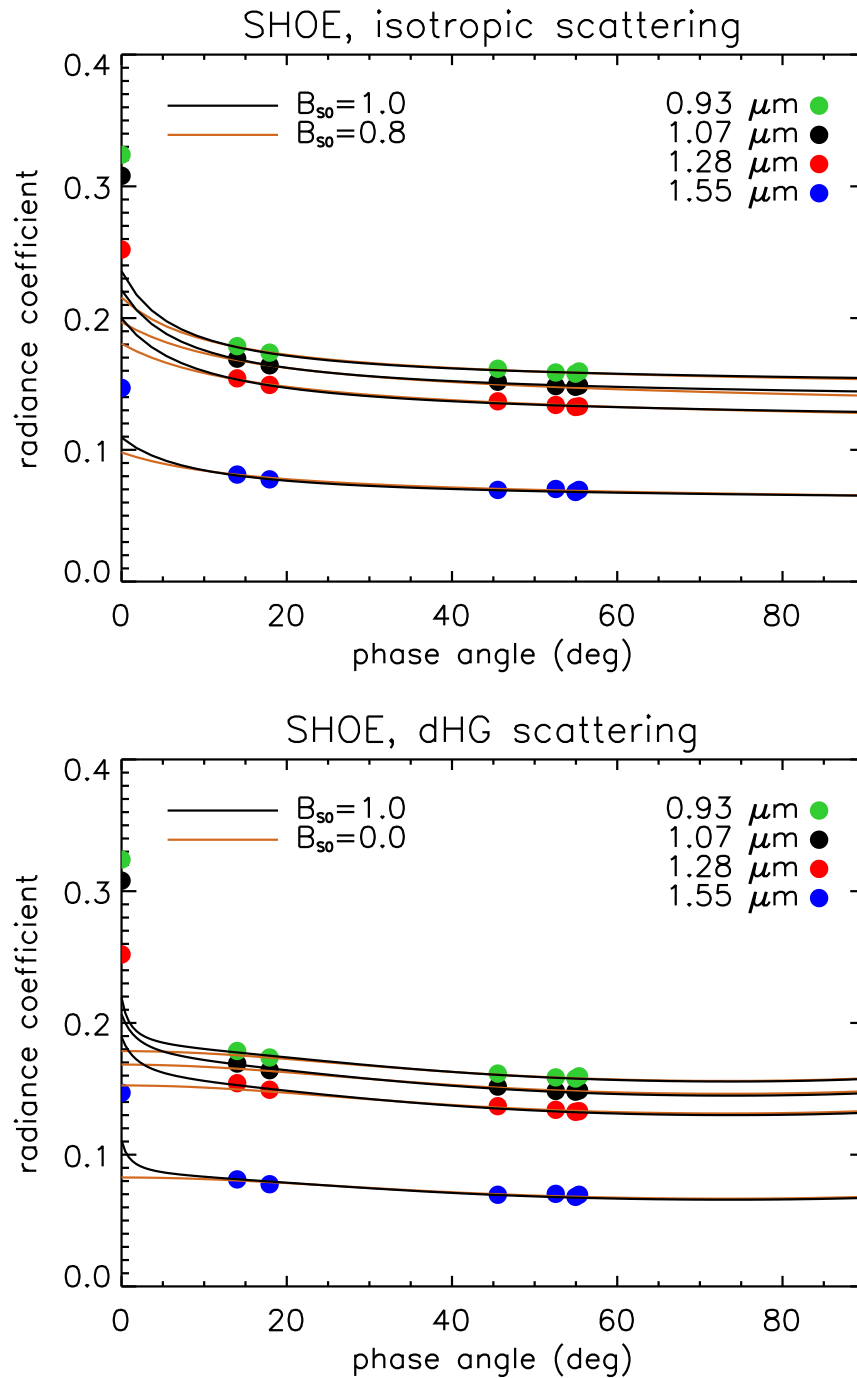
Figure 6.16: The Hapke shadow hiding model fitted to the reconstructed VLNS mode DLIS reflectances. The model does not include coherent backscatter and macroscopic roughness. **Top**: Soil particles scattering isotropically, Hapke model: Eq. 2.30. **Bottom**: Soil particles scatter like aerosols (phase function is the double Henyey-Greenstein function in Fig. 2.2), Hapke model: Eq. 2.28. All models were fit to the data around phase angle 50°; parameters are listed in Table 6.2.
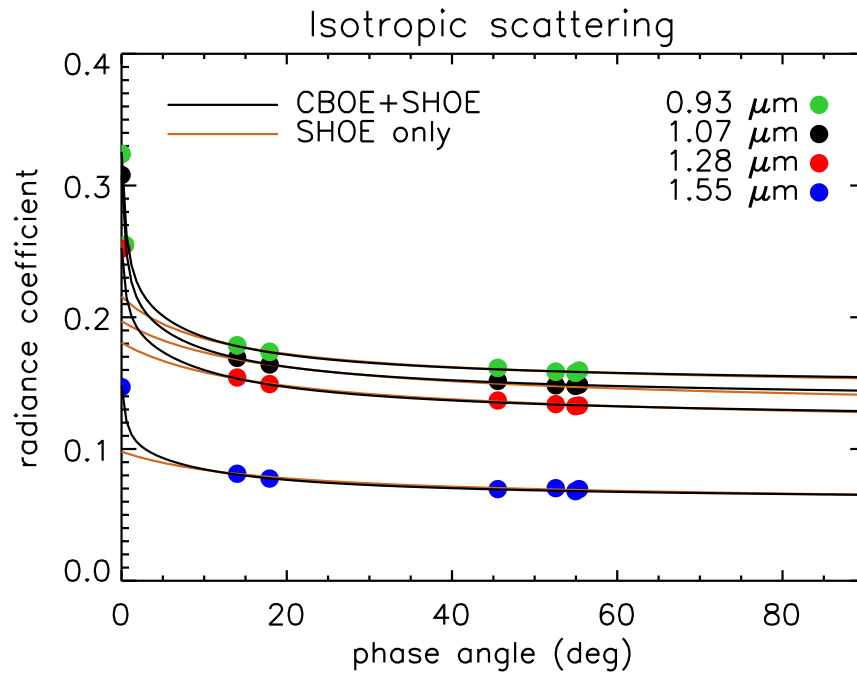
Figure 6.17: Where shadow hiding alone (brown line) fails to fit the zero phase angle data, coherent backscatter does the job (black line). The CBOE model (Eq. 2.27) does not include macroscopic roughness, and has soil particles scattering isotropically; parameters are listed in Table 6.3. All data are from the DLIS, except for the 0.93 μm data point at phase angle 0.45°, which is from the DLVS.

Table 6.3: Best fit parameters for the CBOE + SHOE Hapke models in Fig. 6.17. Particles scatter isotropically with single scattering albedo w_λ at wavelength λ (in μm). Parameters h_S and B_{S0} (h_C and B_{C0}) are the peak width and amplitude of the SHOE (CBOE).

| λ	w_λ	h_S	B_{S0}	h_C	B_{C0}
0.93	0.605	0.06	1.0	0.01	0.39
1.07	0.580	0.07	1.0	0.01	0.40
1.28	0.540	0.08	1.0	0.01	0.27
1.55	0.335	0.08	1.0	0.01	0.36

by including coherent backscatter we can fit all data perfectly. When we look at the fit parameters in Table 6.3 we find that regarding the CBOE amplitude (B_{C0}), the 1.28 μm data are the odd one out. This is a direct consequence of the mismatch between the the DLIS **210** reflectance spectrum and the reflectances derived from the DLIS/ULIS ratio method, visible in Fig. 6.13 (left).

Before we discuss the implications of our modeling exercise, we need to establish whether my BRDF is reasonable. After all, I made the bold move in the previous chapter to attribute the rather large difference between my reflectance reconstruction of Titan's surface and those of other workers to the opposition effect. To explain such a surge in reflectance towards phase angle zero I invoke coherent backscatter, which, because it

requires multiple scattering events, seems unlikely to occur in the low-albedo soil of the landing site. But then, my phase curve is very similar to that observed for another low-albedo body, the Moon; Pohn et al. (1969) found the reflectance of the surface as measured by Apollo 8 to drop by 35% from 0° to 7° solar phase angle, similar to what we find in Fig. 6.17. It has been proposed that both coherent backscatter and shadow hiding are required to explain the Lunar opposition surge (Helfenstein et al. 1997, Hapke et al. 1998). Similar in size to Titan, the reflectance of Jupiter's moon Callisto drops by roughly 40% from 0° to 10° solar phase angle at 0.47 μm (Domingue and Verbiscer 1997). Like Titan, Callisto's icy surface is also covered by a dark substance, possibly organic (McCord et al. 1997). So it appears that the phase curve in Fig. 6.17 is not at all unusual for a low albedo body.

What does Hapke modeling tell us about the physical characteristics of Titan's surface? Before drawing any conclusions I must emphasize that the aim of this chapter is not to evaluate or validate Hapke's theory. His theory is often criticized for being overly simplistic and not explicitly containing physical parameters as grain size or refractive index. Alternative theories for the scattering behavior of particulate soils exist (see e.g. Petrova et al. 2001, Shkuratov et al. 2002), but, because of our extremely limited data set, in this case simplicity is a virtue. However, the Hapke model has many free parameters and the best-fit solutions are not unique.

The first ambiguity we face is that of macroscopic roughness versus particle shadow hiding. The upper limit we find for the macroscopic roughness (mean facet slope angle $\Theta \leq 40°$) is not very constrictive as the theory is invalid for large slope angles anyway (Hapke 1984). Shadow hiding is required to fit the data, but its magnitude depends on the degree of macroscopic roughness. If, in reality, roughness is high then the SHOE is very narrow peaked ($h_S = 0.01$-0.05), but if roughness is low then SHOE peak can be broader ($h_S = 0.05$-0.20). By means of Eq. 2.34 parameter h_S can be interpreted in terms of soil porosity P and parameter Y which depends on the particle size distribution. On Earth, soil porosity varies with grain size; generally, larger grain sizes lead to lower porosities. Typically, the (total) porosity ranges from 0.28 for coarse gravel to 0.43 for fine sand, with clay porosities being as high as 0.57 (McWorter and Sunada 1977). The porosity of lunar regolith (which is highly comminuted, or pulverized) at the Apollo 11 landing site was measured in the laboratory to be 0.54 ± 0.06 by Wilson (1973), and theorized to be around 0.78 on the lunar surface. The natural lower limit for P seems to be around 0.3. Particle distribution parameter Y is not easily interpreted. Hapke (1986) calculates $Y = 0.25$ as typical for comminuted (lunar type) soils. Soils consisting of uniform sized particles have $Y = 1.0$, the maximum value. Hence, the porosity and parameter Y cannot be independent and certain (P, Y) combinations must be unphysical. I find h_S must be small (< 0.15), possibly close to zero depending on the macroscopic roughness. Figure 6.18 shows the full (P, Y) parameter space with curves corresponding to the h_S values we find. It shows that low values of h_S are generally associated with high porosity, unless Y is very small. As remarked above, the surface of the Moon and Callisto exhibit similar opposition peaks, and a modeling effort by Domingue and Verbiscer (1997), who assume a comminuted soil type ($Y = 0.25$), shows that the Hapke parameters for these bodies are within the range of the surface at the Huygens landing site. The other SHOE fit parameter, peak amplitude B_{S0}, appears to be inversely related to the peak width h_S. The amplitude is a measure of particle opacity (see Sec. 2.2), but is not well restricted in our case.
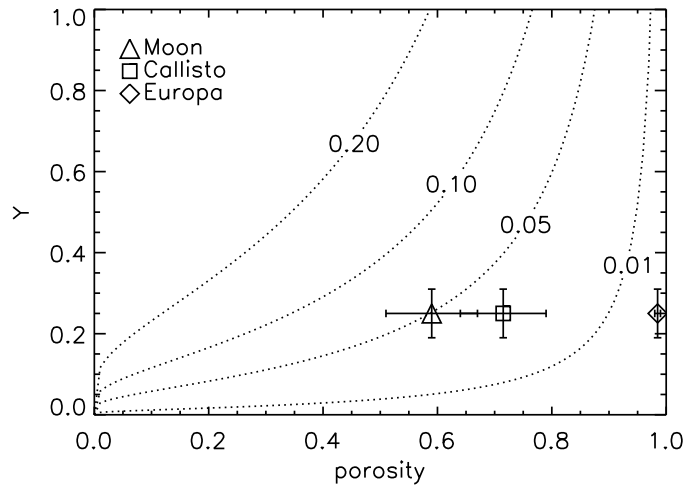
Figure 6.18: The (P, Y) parameter space with curves corresponding to the Hapke SHOE peak width (h_S values labeled). Parameter ranges found for the Moon, Callisto, and Europa by Domingue and Verbiscer (1997) are indicated.

The second ambiguity is whether particles scatter isotropically or are intrinsically backscattering. I assessed this by using a double-Henyey-Greenstein (dHG) phase function, characteristic of Titan aerosols. Once again, the data do not allow us to clearly distinguish between these two possibilities, but the bottom line is that it does not affect the results by much. Shadow hiding is still required (albeit with a smaller peak width as for isotropic scattering), and dHG scattering cannot explain the high reflectance at phase angle zero. Only the single scattering albedo is substantially increased (by roughly 10% at 0.93 μm to 40% at 1.55 μm).

Inclusion of coherent backscatter in the model is required to fit the data points at phase angle zero. A clear dependence on wavelength is not apparent in Table 6.3, but note that the 1.28 μm methane window behaves different from the others. As mentioned above, this indicates that the VLNS data at this wavelength have been scaled to a reflectance slightly too high. The CBOE peak width h_C is a better diagnostic of soil properties than the amplitude B_{C0} (see Sec. 2.2), but, unfortunately, here it is poorly constrained. If we accept the reality of the single 0.93 μm data point at 0.45° phase angle (Fig. 6.17) we find $h_C = 0.01$, with the implication (Eq. 2.37) that the transport mean free path in the soil (the mean distance a photon travels before its direction is changed by a large angle) is $\Lambda \approx 7 \mu$m. This implies that the scatterers are densely packed, seemingly in contradiction with the SHOE modeling results. But maybe both mechanisms act on different scales. Shadows may be cast by large (> 1 mm) particles, whereas the coherent scatterers may be placed micrometers apart on the surface of the larger particles. Measuring the polarization of light reflected off the surface could help to identify the dominant scattering mechanism (e.g. Shkuratov et al. 2002), but unfortunately, of all DISR instruments only the Solar Aureole cameras made such observations.

Even thought the Hapke models are very sensitive to the single scattering albedo of the soil particles ($w_\lambda^{\mathrm{soil}}$), requiring specification to three significant digits, I find different values for each of the models. To find an estimate for the true single scattering albedo I

Table 6.4: The single scattering albedo of the Hapke model soil particles we found compared with those of the aerosols in the LPL atmosphere model (Tomasko et al. 2007). The lower limit for w_λ^{soil} is from the SHOE+CBOE model (Table 6.3), the upper limit is from the macroscopic roughness+SHOE model (Table 6.1).

λ (μm)	w_λ^{soil}	$w_\lambda^{\text{aerosol}}$
0.93	0.60 - 0.71	1.00
1.07	0.58 - 0.68	0.99
1.28	0.54 - 0.64	0.98
1.55	0.33 - 0.41	0.96

look at the limits imposed by the most plausible models. As I have found that both SHOE and CBOE are required to model the scattering behavior of the soil, the SHOE+CBOE model in Fig. 6.17 sets the lower limit. Macroscopic roughness acts to increase the single scattering albedo. The true roughness of the soil is unknown, so the upper limit is set by the model with maximum roughness ($\Theta = 40°$) that fits the VLNS data (Fig. 6.15). Note that intrinsic particle backscattering increases w_λ^{soil} with respect to isotropic scattering, so this would increase the upper limit in case of maximum roughness. The resulting ranges for w_λ^{soil} in the different methane windows is listed in Table 6.4. The values we find for w_λ^{soil} are quite low for an icy satellite, certainly lower than that of the other Saturnian satellites (Buratti 1985). Also in this respect is Titan similar to Callisto. The table compares w_λ^{soil} with the single scattering albedo of the aerosols ($w_\lambda^{\text{aerosol}}$) in the LPL atmosphere model (Tomasko et al., in preparation), which suggests that the aerosols themselves are not responsible for the soil scattering behavior. Noteworthy is that w_λ^{soil} drops more steeply from 1.28 μm to 1.55 μm than $w_\lambda^{\text{aerosol}}$. Either a separate soil component is responsible for the additional absorption, or aerosols undergo substantial modification on the surface that alters their albedo.

The main conclusions of this section are the following. From an analysis of the Spectrophotometric Map and VLNS data I find the reflectance of the surface around the landing site to increase towards lower solar phase angles in the near-infrared methane windows. A substantial increase towards zero phase angle, commonly referred to as the "opposition surge", becomes apparent when I combine these data with the surface reflectance as reconstructed in Chapter 5. The resulting phase curves can be modeled with a Hapke model for light scattering in a particulate soil that includes both shadow hiding and coherent backscatter. However, the model has many free parameters, some of which perform similar roles, and there are insufficient data to infer any definite characteristics of Titan soil. What we can say is that the soil around the landing site has scattering properties similar to those found for the surface of other dark solar system bodies, like Callisto and the Moon.

6.4   Surface color

In the previous sections I showed how the observed intensity in spectra and images increases with decreasing solar phase angle ϕ. Superposed on this trend are the relatively small intensity variations that result from reflectance variability intrinsic to the surface.

Figure 6.19 shows an example of this for the intensity at 1.07 μm. Remember that SM1 covered both land and lake, whereas SM2 observed only the lake area. We now crudely model the increase of intensity towards lower phase angles with lines. Even though the previous section dealt with more advanced models, lines suffice for our purposes here. The lines labeled **1** to **3** in Fig. 6.19 are models for the SM1 land, SM1 lake, and SM2 lake observations. With the VLNS intensities being intermediate to those of the SM2 we can safely assume that the atmosphere does not contribute significantly to the observed intensity below 4 km, and that the SM2 intensities (line **3**) are surface only. Note that lines **1** and **2** are steeper than **3**, implying atmospheric backscattering. Observations which deviate from SM1 lake line **2** around phase angle 55° are associated with the bright terrain southwest of the landing site. Line **1** appears to be slightly steeper than **2**, reflecting the stronger darkening of land discussed in Section 6.1. From the observations in Fig. 6.19 we can estimate the ratio of reflectance of land and lake in the following way. Consider that at a certain altitude the observed intensity $I_{obs}(\phi)$ at solar phase angle ϕ is the sum of the intensity of the direct beam scattered from the surface and the intensity $I_{atm}(\phi)$ contributed by light scattered into the beam by the atmosphere:

$$I_{obs}(\phi) = \frac{F_0}{\pi} e^{-\Delta\tau} r_C(\phi) + I_{atm}(\phi) \tag{6.1}$$

where r_C is the radiance coefficient of the surface and F_0 is the downward flux at the surface. The direct beam is attenuated by the intervening atmosphere layer, which has optical depth $\Delta\tau$ along the optical path. The quantities I_{obs}, I_{atm} and r_C also depend on the angle of incidence and reflection, but I assume these to be constant within the spectrophotometric map. The contribution by the atmosphere is uncertain, but we can put limits on its magnitude. As the haze particles are known to be strongly forward scattering (Tomasko and Smith 1982), it is reasonable to assume that the atmospheric contribution to the observed intensity is stronger for light coming from the direction of the land. Hence I let the atmospheric intensity coming from the land be equal to the atmospheric intensity coming from the lake times a factor α. This factor represents our uncertainty concerning the degree of forward scattering of the aerosols, and has a minimum value of 1 (for identical atmospheric contributions), and a maximum of r_C^{land}/r_C^{lake}. Exactly how much the atmospheric contribution differs for land and lake can only be investigated by radiative transfer models that include a variegated surface. We can write a version of Eq. 6.1 for both land and lake and eliminate $F_0 e^{-\Delta\tau}$. We find

$$\frac{r_C^{land}}{r_C^{lake}} = \frac{I_{obs}^{land} - \alpha I_{atm}^{lake}}{I_{obs}^{lake} - I_{atm}^{lake}}. \tag{6.2}$$

This equation provides a rough estimate of the reflectance ratio of the bright land and the dark lake terrain. I estimate the different intensities from Fig. 6.6 at phase angle 35°; I read I_{obs}^{land} from line **1**, I_{obs}^{lake} from line **2**, and estimate I_{atm}^{lake} as the difference between lines **2** and **3**.

The estimated intensities and derived reflectance ratios are listed in Table 6.5 and shown in Fig. 6.20. First we note that the haze becomes increasingly dominant towards lower wavelengths, contributing only 10% to the observed intensity at 1.59 μm but almost half the light at 751 nm. The land/lake reflectance ratio in the methane windows steadily increases from around 1.10 at 751 nm to 1.25 at 1.28 μm, beyond which it jumps to 1.7
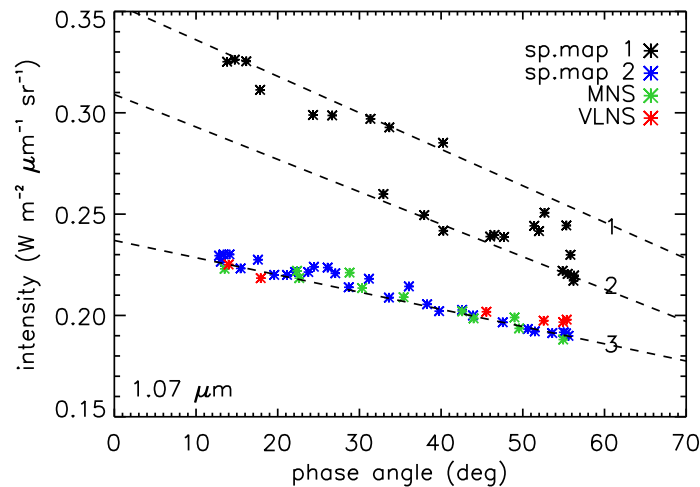
Figure 6.19: The intensities in the DLIS 1.07 μm methane window with lines (phase curves) fitted through SM1 land (**1**), SM1 lake (**2**), SM2 lake (**3**) intensities. Lines **1** and **2** are steeper than **3**, implying atmospheric backscattering.

at 1.59 μm. The ratio at 751 nm may not be significantly different from that at 827 nm, but clearly the land is redder than the lake over the whole near-IR wavelength range. In Fig. 6.21 we make a rough estimate of the shape of the land spectrum by multiplying the ratios with the reflectance reconstructed for the lake in Chapter 5. It is tempting to interpret this reddening in terms of tholins with the implication that they are more abundant on the land. Different types of tholins have been synthesized in the laboratory. The black tholins of Bernard et al. (2006) are red over the whole DISR wavelength range, whereas the reflectance spectrum of their yellow tholins feature an absorption line at 1.5 μm. The presence of both types of tholin cannot explain the jump in reflectance at 1.59 μm. Perhaps it is associated with water ice abundance or grain size, as the strongest water absorption line in the DISR range is the 1.5 μm line. Then water ice would be more abundant (or exposed) in the lake area, or it would be in the form of coarser grains (more about this below). However, Fig. 6.21 shows that the jump at 1.59 μm in the land spectrum completely erases the shallow absorption line that we find in the lake spectrum; it still features a blue near-IR slope, but it is not clear whether there is room for a water absorption line at all (though admittedly, we have only reliable information for the methane windows). The brightest terrain in the land area seems not to expose water ice as suggested by Tomasko et al. (2005).

How do these observations compare with the work of others? Rodriguez et al. (2006) report Cassini VIMS observations of the Huygens landing site in near-IR methane windows from 1.08 to 5.00 μm, several of which are in common with this study. The authors note a correlation of color with albedo in DLIS range band ratio images, and attribute it to a strong additive scattering contribution by the atmosphere. Even thought apparently they do not consider the possibility of an intrinsic color difference between bright and dark terrain, their ratios corrected for atmospheric scattering are broadly consistent with the surface color difference I have derived, although a detailed comparison is not possible due to the different resolution of the observations. McCord et al. (2006) present

Table 6.5: Albedo ratio of the bright land/river and dark lake terrains, derived from an analysis of the spectrophotometric map intensities (in W m^{-2} μm^{-1} sr^{-1}) in near-IR methane windows using Eq. 6.2. The lower limit of r_C^{land}/r_C^{lake} refers to $\alpha = r_C^{land}/r_C^{lake}$, the upper limit to $\alpha = 1$. The intensities were estimated from Figs. 6.6 and 6.7 at phase angle 35°.

type	wavelength	I_{obs}^{land}	I_{obs}^{lake}	I_{atm}^{lake}	$I_{atm}^{lake}/I_{obs}^{lake}$	r_C^{land}/r_C^{lake}
DLVS	751 nm	0.517	0.472	0.212	0.45	1.10-1.17
DLVS	827 nm	0.509	0.457	0.164	0.36	1.12-1.18
DLVS	935 nm	0.348	0.311	0.083	0.27	1.12-1.16
DLIS	0.93 μm	0.289	0.253	0.054	0.22	1.14-1.18
DLIS	1.07 μm	0.290	0.247	0.041	0.17	1.18-1.21
DLIS	1.28 μm	0.195	0.160	0.023	0.14	1.22-1.25
DLIS	1.59 μm	0.079	0.048	0.005	0.11	1.63-1.71
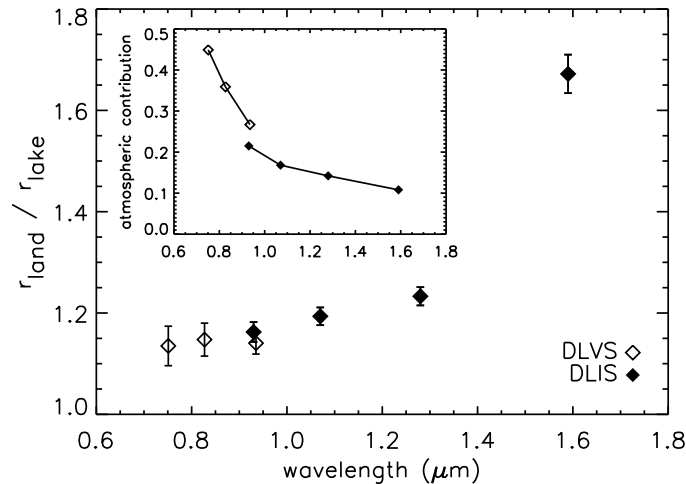
Figure 6.20: The ratio of land and lake surface reflectance in the near-IR methane windows, as derived from DLVS/DLIS measurements. The error bars denote the limiting cases from Table 6.5, with the symbols being their average. The true uncertainty in the DLVS 935 nm ratio is larger than indicated here. The insert shows the atmospheric contribution to the intensity (the fraction of light scattered into the beam by the atmosphere) observed at 18 km altitude (optical path length 19 km) coming from the lake terrain.

reflectance reconstructions from Cassini VIMS data for different types of surface seen on Titan (classified by their brightness in different atmospheric windows). My reflectance spectrum for lake terrain resembles their reflectance for dark terrain ("ddark") in shape, but the land reflectance in Fig. 6.21 does not look like any of theirs.

Even though the DISR images are monochrome and the camera did not carry color filters, we can put color on the images using spectra. The spectrophotometric map spectra were recorded closely in time, and are ideal for constructing false color maps from the ratio of the intensity measured in different methane windows. The DLVS offers a higher

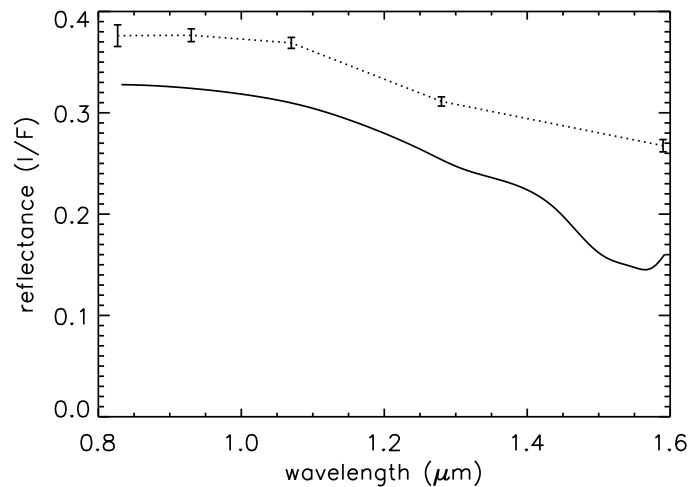Figure 6.21: The reconstructed land spectrum, obtained by multiplying the lake spectrum (the **210** spline fit from Fig. 5.16) with the land/lake ratios in the methane windows (Table 6.5). Note that the lake reflectance is that for (SSL) phase angle 0° whereas the ratios were determined at (solar) phase angle 35°, and that the lake reflectance beyond 1500 nm is uncertain (it could be off by as much as 20% at 1.59 μm). The 0.93 μm ratio is from the DLIS.

spatial resolution, but the DLIS covers more methane windows. Figures 6.24 to 6.27 show the DLVS and DLIS spectrophotometric maps overlaid on panoramas of the Huygens landing site, with their footprints colored according to the ratio of the intensities in the different near-IR methane windows. Table 6.6 provides a summary of the spectrophotometric map color analysis, and serves as a point of reference in the discussion below. The largest ratio in a map is represented by purple, the smallest by blue.

From the 0.751, 0.827, and 0.935 μm methane windows of the DLVS we can calculate the color ratios 0.827 μm / 0.751 μm and 0.935 μm / 0.827 μm (at lower wavelengths the atmospheric haze interferes too much). However, the responsivity at 0.935 μm is so low that calibration artifacts dominate the signal; when we calculate the average of each of the 16 footprints over all spectra in each map, we find that they show a similar dependence on zenith angle. This is clearly an artifact, since both maps viewed completely different terrains. As these artifacts dominate the 0.927 μm / 0.827 μm ratio, I exclude it from my analysis. The artifacts are minor for the 0.827 μm / 0.751 μm ratio, only significant for the footprints at lowest nadir angle. I devised a correction for each footprint by averaging the intensities of both maps, and its application improves the color balance within the maps. Note that the position and orientation of the individual spectra and the maps as a whole are not 100% accurate; no images were recorded close in time to either of the spectrophotometric maps, which could have constrained their orientation. The azimuth angle of each spectrum was calculated from the probe attitude reconstruction by Karkoschka et al. (2007), assuming zero tip and tilt. Note that the latter may lead to inaccuracies in the positioning of the footprints; the relative orientation of the spectra within a map is reliable due to the rapid acquisition of spectra, but we cannot account for a possible swinging motion of the probe. Figure 6.24 shows the DLVS spectrophotometric maps with the 0.827 μm /

Table 6.6: Summary of the results of the spectrophotometric map color analysis. Δ_{obs} is the difference between the maximum and minimum intensity ratio R, in brackets as a percentage of the maximum. Δ_{exp} is the difference expected from surface backscattering (Fig. 6.29), in brackets as a percentage of the difference observed for SM2.

ratio	SM1			SM2			Δ_{exp}
	$R_{\max}$	$R_{\min}$	Δ_{obs}	$R_{\max}$	$R_{\min}$	Δ_{obs}	
$\frac{827\text{nm}}{751\text{nm}}$	1.007	0.929	0.078 (8)	1.107	1.043	0.064 (6)	n/a
$\frac{1.07\mu\text{m}}{0.93\mu\text{m}}$	1.011	0.955	0.055 (5)	1.033	1.006	0.027 (3)	0.013 (48)
$\frac{1.28\mu\text{m}}{1.07\mu\text{m}}$	0.687	0.632	0.055 (8)	0.675	0.656	0.018 (3)	0.009 (50)
$\frac{1.59\mu\text{m}}{1.28\mu\text{m}}$	0.360	0.260	0.100 (28)	0.317	0.285	0.032 (10)	0.009 (29)

0.748 μm intensity ratio in false color. In the SM1 a high color ratio (pink footprints) is associated with the land area (labeled a), and the lowest ratios (blue footprints) with the lake area east of the landing site (b), confirming the findings in Tomasko et al. (2005). As mentioned before, at these wavelengths it is not clear whether the land area is truly redder or simply brighter than the lake area; the preferential absorption of light of lowest wavelength by the haze may merely make the land area appear redder. The DLVS color map is most useful for verifying the brightness distribution of the DISR landing site panorama. For example, lake bed associated with blue footprints in Fig. 6.24A is probably darker than lake bed overlayed by green footprints. The fact that the footprints that cover what appears to be lake bed north of the land area (c) are also blue suggests this terrain is as dark as the lake bed in the east (b), confirming our suspicion put forward in Section 6.1. The bright terrain southeast of the landing site (d) is characterized by orange footprints, with the broad dark channel immediately south of it traced out well by green footprints. The lake bed in front of the land area (e) is brighter, showing up in green and yellow footprints. In terms of the brightness gradient in Fig. 6.9 I interpret lake bed e to be less clean than b and c, being covered by outflow deposits from the mainland. This terrain was observed in detail by SM2. Figure 6.24B shows that the highest color ratio is found in front of the coast line, and the lowest ratio in the lake bed area south of the landing site. This color gradient is associated with the aforementioned large scale brightness gradient. Small scale color differences may be related to the presence of bright islands in the lake bed. However, the 'banded' appearance of the spectra along the spatial dimension suggests that calibration artifacts have not been completely removed.

The spatial coverage of the DLIS spectrophotometric maps is much smaller than that of the DLVS maps; one DLIS exposure yields only a single spectrum as opposed to 16 for the DLVS. Figures 6.25 to 6.27 show the DLIS footprints of both maps overlaid on panoramas of the landing site, colored according to the ratio of intensity in the four methane windows. For all three color ratios, SM1 confirms that the river area is redder than the lake area. This is mainly due to the intrinsic color difference between the two types of terrain; as expected from Fig. 6.20, it is most pronounced for the 1.59 μm / 1.28 μm ratio. This explains why the subtle color variations within the land area seen in the 1.07 μm / 0.93 μm and 1.28 μm / 1.07 μm ratios do not appear in the 1.59 μm / 1.28 μm ratio; if present, they are dwarfed by the large color gap between land and lake. It must be noted
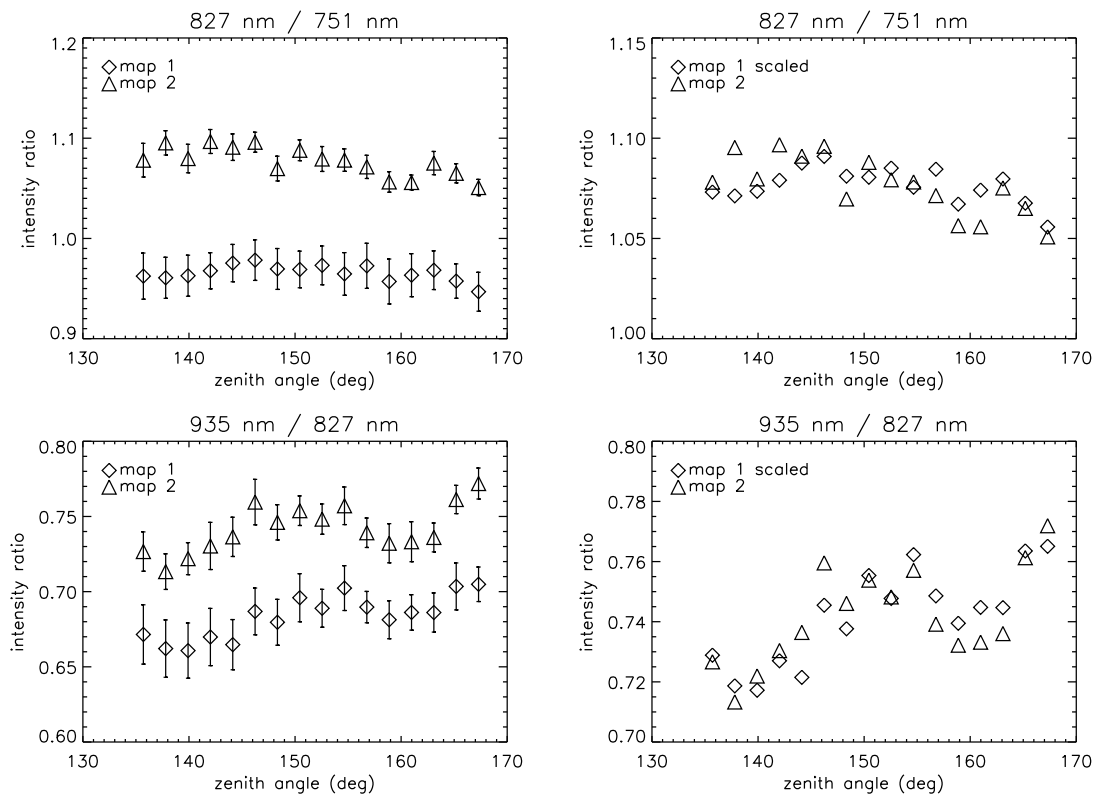
Figure 6.22: The intensities recorded by the DLVS in the 20-column spectrophotometric map mode show evidence for the presence of calibration artifacts. For each of the 16 footprints we calculate the average over all spectra in map 1 and 2. Shown are ratios of the intensity in three methane windows; at the **top** the 827 nm / 751 nm ratio, at the **bottom** the 935 nm / 827 nm ratio. On the **left** averaged intensities for the two maps, on the **right** the averaged intensities of SM1 multiplied by a constant to match those of SM2. To lower the level of noise, the intensities are calculated as the average of three spectral pixels around the wavelength of interest.

that the SM1 color variation is larger for the 1.07 μm / 0.93 μm ratio than for the 1.28 μm / 1.07 μm ratio, although it is unclear what this means. As is often done for spectra acquired from outside the atmosphere (e.g. Griffith et al. 2003, McCord et al. 2006), we can interpret the color difference in the methane windows in terms of water ice; when we compare the observed variability of the three ratios with that of water ice (Fig. 5.22, measured at methane window wavelengths), we find that it is broadly consistent with land consisting of fine and lake bed of medium grained water ice. But with the availability of a full lake bed spectrum (Fig. 6.21), this interpretation becomes questionable. As discussed above, the detection of water ice at the Huygens landing site is by no means certain, and the color difference between land and lake bed may also be related to tholin abundance.

Peculiar, since it does not show up in the DLVS SM1 (and hence is not associated with surface brightness), is the reddish terrain in the lake bed south of the landing site (labeled with an asterisk in Fig. 6.25). Its spectral behavior is different from the other lake terrain, but it does not stand out as unusual in the images (although admittedly it is difficult to interpret any feature in this part of the lake). Unfortunately, this part was not imaged at
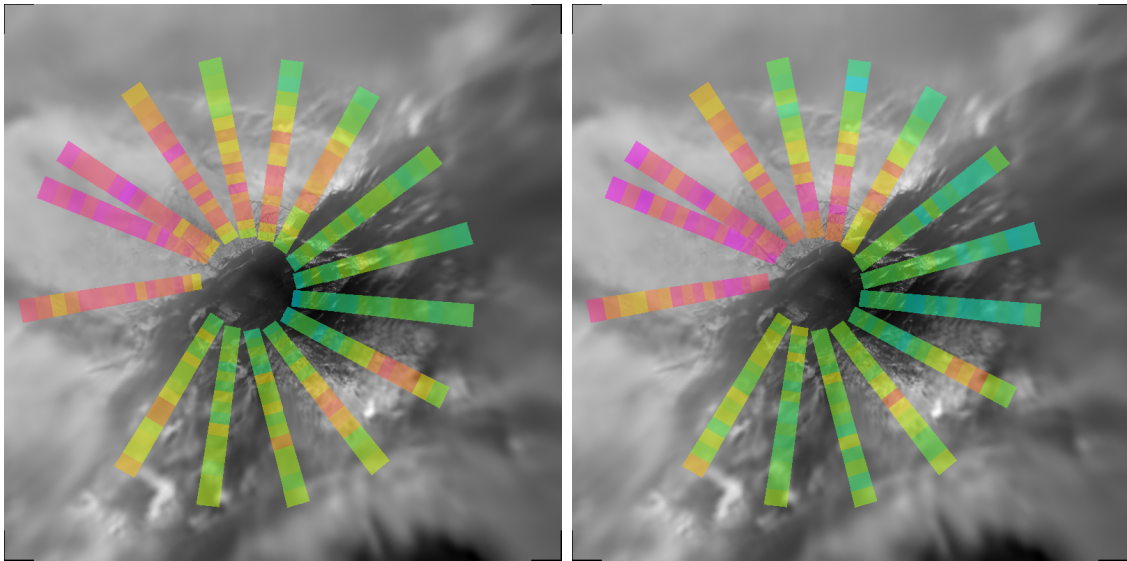
Figure 6.23: Calibration artifacts in the DLVS SM1. The figures at **left** and **right** show the map before and after applying a correction for the artifacts in the 827 nm / 751 nm intensity ratio (see Fig. 6.22). The correction is especially significant for the innermost footprints.

high resolution, but the close-up in Fig. 6.28 betrays the presence of rivers in this area. In the SM1 overview panorama (e.g. Fig. 6.27, top) it can be seen that these red DLIS footprints are closest to the very dark terrain (the Dark Spot) to the south, which I suggest is land/river terrain like that north of the landing site (see Section 6.1), and are located within what may be an outflow channel. An exciting possibility is that the red color is associated with outflow from the Dark Spot, with either the liquid itself being red or the sediment it transported.

The color variability in the SM2 is less pronounced than in the SM1, and the color spatial distribution is different for all ratios. Except for the highest color ratios, which often can be found in the northwest corner of most spectrophotometric maps, associated with spectra acquired at the lowest solar phase angles. This raises the question whether reddening is associated with surface backscattering. I calculated the degree of reddening for the best-fitting Hapke model, that for isotropically scattering particles, and show the results in Fig. 6.29. For the DLIS range of solar phase angles only a moderate amount of reddening is expected, accounting for roughly a quarter of that observed for SM2 (last column in Table 6.6). Apparently, most of the variability observed in the lake area by SM2 is intrinsic to the surface, although at DLVS wavelengths atmospheric backscattering may contribute. Other than the fact that higher ratios are generally found closer to the coast line, there is no obvious correlation with surface morphology. It is unclear how the color variability in the lake should be interpreted. It may be related to subtle chemical and/or particle size differences, likely associated with the flow features that abound in the dark terrain. Since we expect that aerosol deposition should completely cover the surface within a few decades, the fact that these color differences exist indicates that fluvial or aeolian processes creates or maintains them.

Figure 6.24: The ratio of the intensity in the methane windows at 827 and 751 nm, displayed for the two DLVS spectrophotometric maps. **A**: SM1 (45×45 km), **B**: SM2 (10×10 km). The ratios are corrected for the calibration artifacts in Fig. 6.22. Intensities are calculated as the average of three spectral pixels centered on the wavelength of interest. Projection is gnomonic, and the landing site is exactly at the center of each background mosaic (Karkoschka et al. 2007).

125
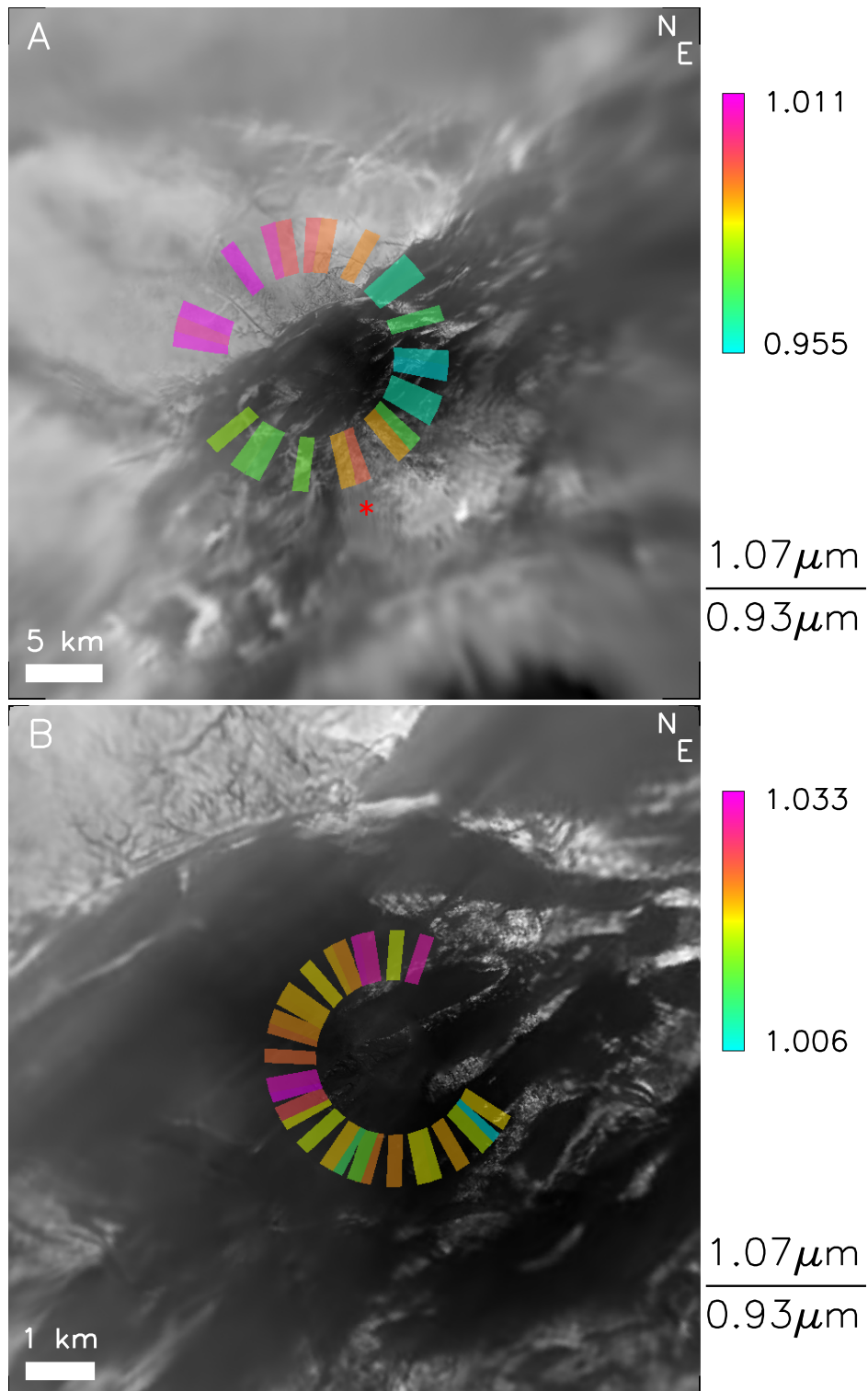
Figure 6.25: The ratio of the intensity in the methane windows at 1.07 and 0.93 μm, displayed for the two DLIS spectrophotometric maps (**A**: SM1, **B**: SM2).
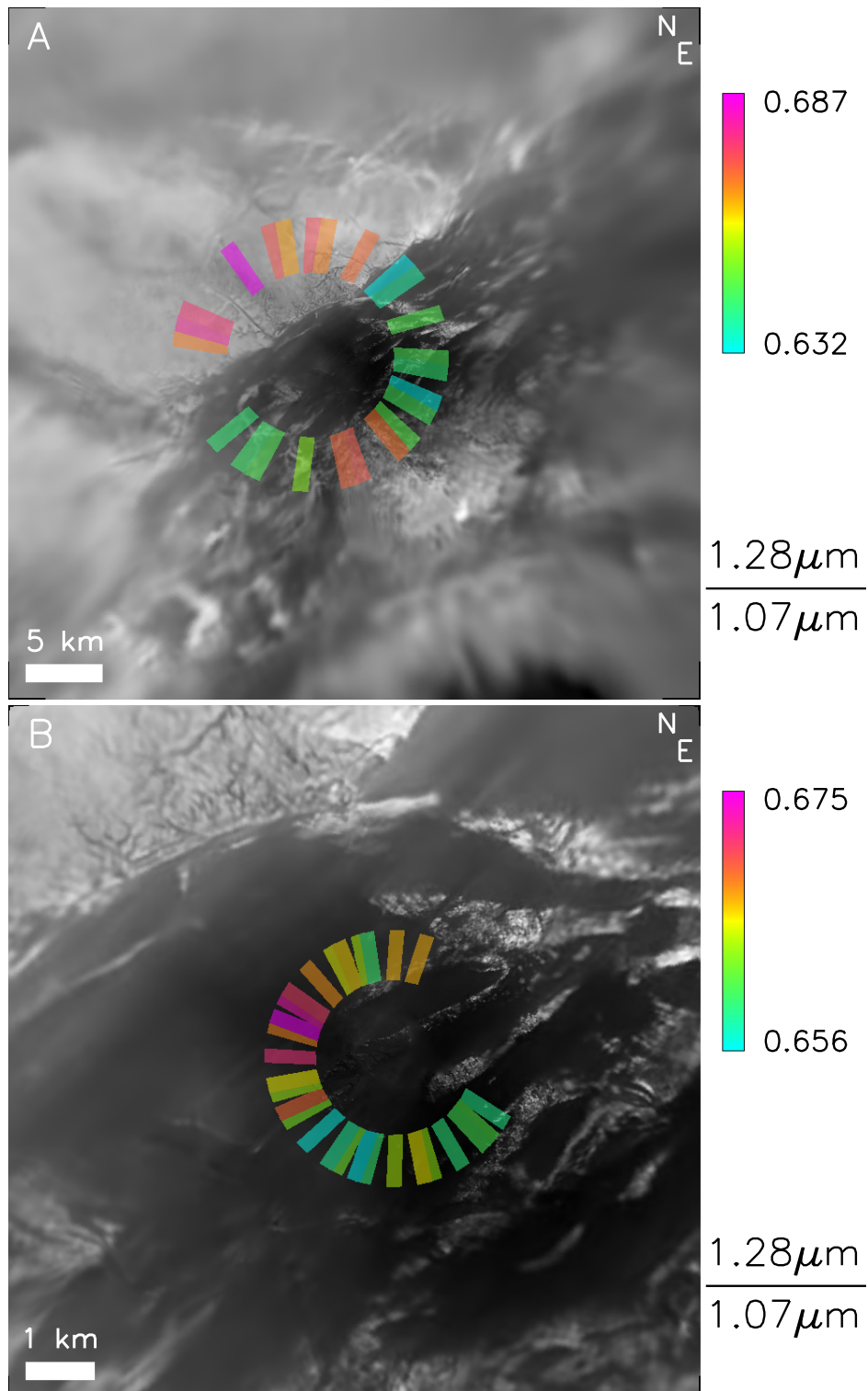
Figure 6.26: The ratio of the intensity in the methane windows at 1.28 and 1.07 μm, displayed for the two DLIS spectrophotometric maps (**A**: SM1, **B**: SM2).
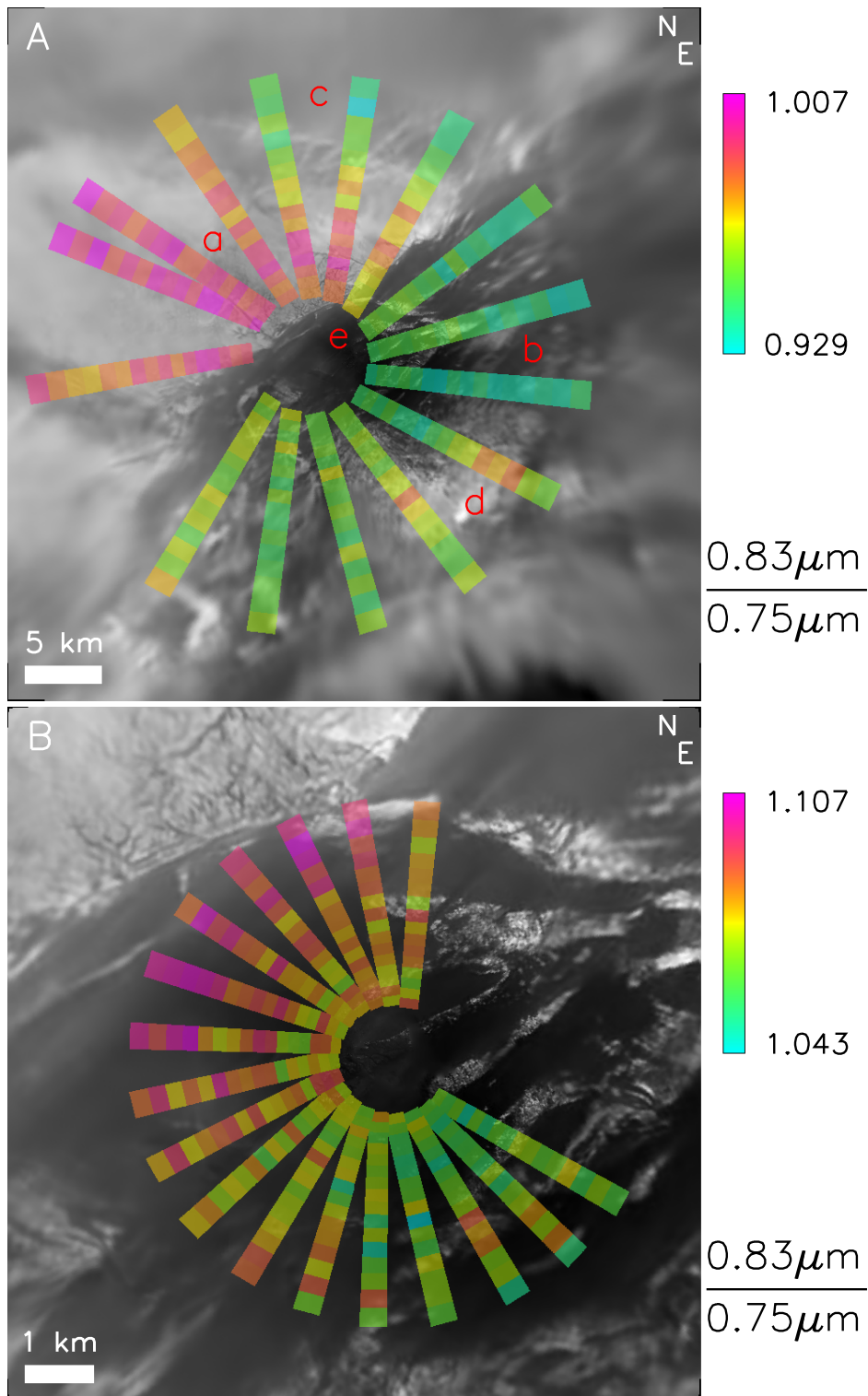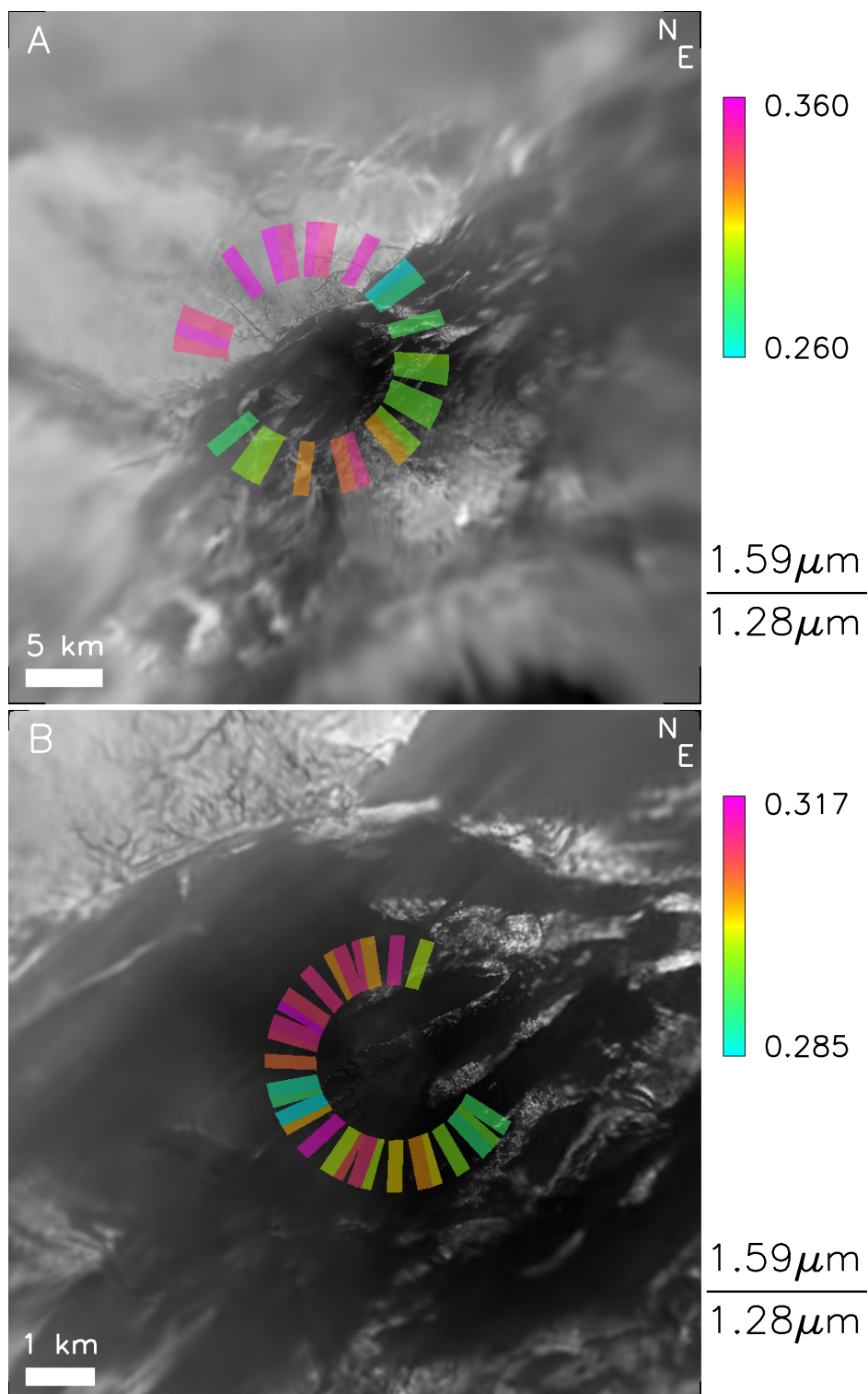
Figure 6.27: The ratio of the intensity in the methane windows at 1.59 and 1.28 μm, displayed for the two DLIS spectrophotometric maps (**A**: SM1, **B**: SM2).
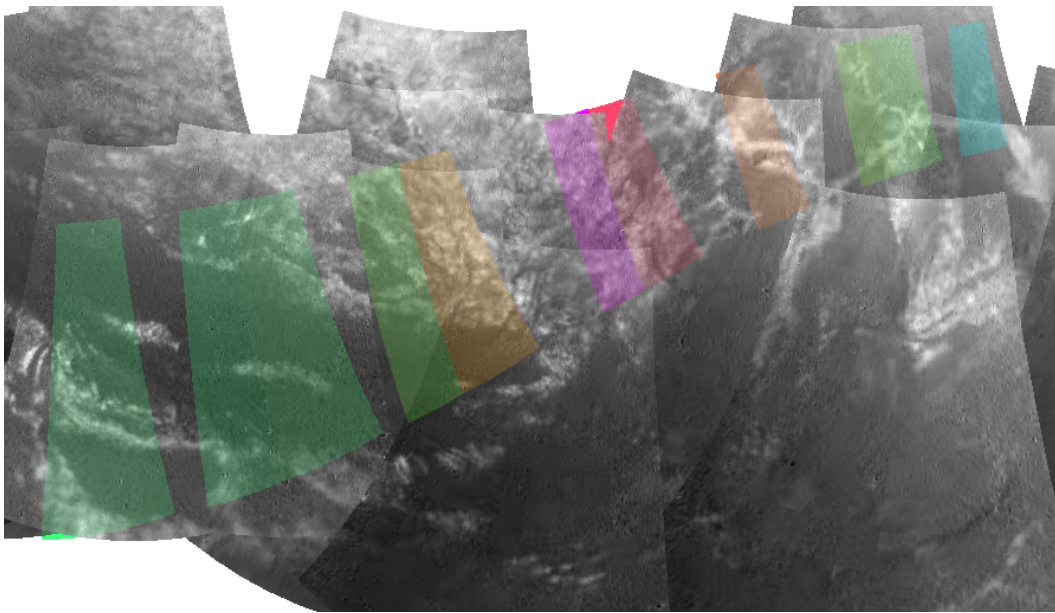
Figure 6.28: Close-up of the anomalous region south of the landing site which consistently shows up red in the DLIS SM1 color maps. Shown is the 1.59 μm / 1.28 μm intensity ratio of DLIS **86**-**105** overlaid in false color on MRI **487**-**613** in Mercator projection (color scale is slightly different from Fig. 6.27).
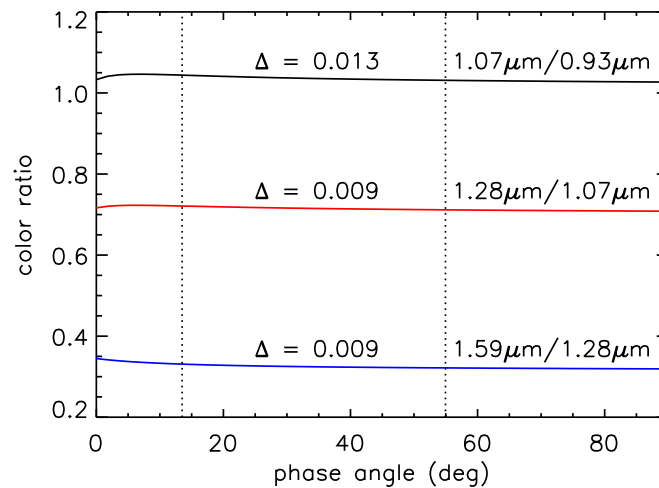
Figure 6.29: The color of the lake surface as a function of solar phase angle, as expected from the best fit Hapke SHOE model for isotropically scattering particles (Fig. 6.16, top). Color is expressed as the ratio of observed intensity in four near-IR methane windows. The scale has been chosen to facilitate comparison with the SM2 projections in Figs. 6.25 to 6.27. The vertical dotted lines indicate the phase angle limits of SM2, and Δ is the increase of the ratio over this interval.

7 Temporal Variability

After successfully landing on Titan's surface, Huygens continued to operate. About an hours worth of data was received from the surface, the communication eventually cut short by Cassini's disappearance below the horizon. Earth radio telescopes detected the telemetry carrier signal for several hours longer (Lebreton et al. 2005). DISR remained active too, and apart from 198 images a total of 49 DLV, 190 DLVS, and 36 DLIS measurements were returned from the surface (in data stream 524b). As the instrument initially needed time to adjust to the higher intensity levels due to the flood of reflected lamp light, many of the early spectra are overexposed. These post-landing measurements proved to be variable in time. In this chapter I analyze the short term temporal variability observed around landing, and the gradual changes observed over the course of the hour on the surface. The details of all measurements discussed can be found in Appendix A. Apart from the three aforementioned instruments I also include column 49 in the discussion. Strictly speaking not an instrument, column 49 was used as a measure of light spilling over from the MRI to the visual spectrometers ('crosstalk', see Section 3.3 and §3.4.5), and may be regarded as a one dimension camera. It is important to keep in mind the different field of view of the instruments. The DLVS samples a small fraction on the left side of the reflection spot visible in the post-landing MRI image, and the DLIS samples the reflection spot itself (see Fig. 4.7). Column 49 samples the right side of the MRI image (more specifically the upper 200 pixels), and DLV field of view is half the hemisphere. With the Surface Science Lamp (SSL) being the main source of light, it is paramount to establish that its output was constant. The probe housekeeping data provide the SSL diagnostics current and voltage. Figure 7.1 shows that these two indicators were steady. Being an incandescent lamp, this implies that the SSL brightness was constant from the moment it was switched on.

All active downward looking instruments recorded rapid changes within an interval of six seconds after landing. In the next section I discuss these in terms of two possible mechanisms. One is that after landing the probe moved for several seconds. The SSP found evidence that the probe landed on a cobble, like the ones we see in the post-landing images (Zarnecki et al. 2005). But the stable post-landing altitude of the DISR camera is consistent with the probe's bottom resting on the soil (Karkoschka et al. 2007). So it is reasonable to assume that either the probe pushed the cobbles it landed on into the apparently soft soil, or that it slid off of them while rotating (a 320 kg probe landing with 1 rpm carries a lot of angular momentum). Both movements would have changed DISR's attitude and distance to the surface significantly for a few seconds. An alternative mechanism is the development of a dust cloud. Lorenz (1993) investigated the likelihood of a dust cloud being generated by the impact of Huygens wake, and predicted that in the presence of fine particles at the landing site the formation of an optically thick cloud, lasting for some seconds, would be possible. The weak surface wind of <1 m s^{-1} (Bird
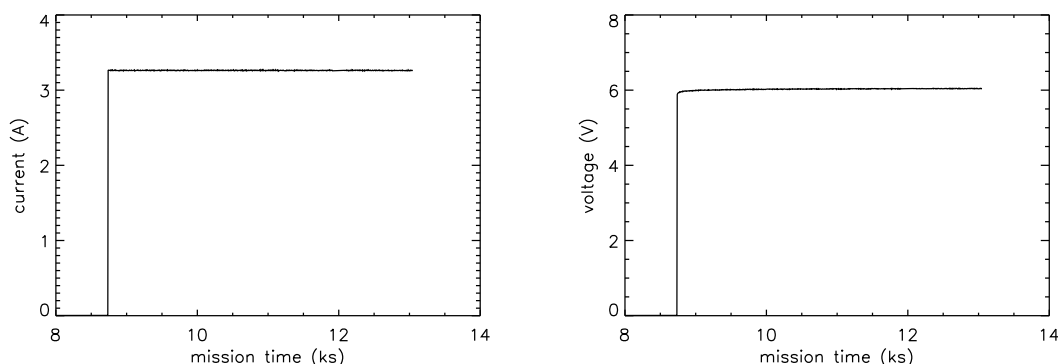
Figure 7.1: The current (**left**) and voltage (**right**) of the 20 W SSL were constant after it was switched on at mission time 8734 sec. These housekeeping data are from data stream 524a as the SSL current in stream 524b is corrupt (Chuck See, personal communication).

et al. 2005, Lorenz 2006) could have carried the dust away in a few seconds.

In the last section of this chapter I discuss the gradual changes observed by some of the downward looking instruments over the course of the hour in which Cassini continued to receive data from Huygens. Whether these changes are related to the environment of the landing site is questionable, but at least they provide us more insight into the workings of the instruments.

7.1   Variability around landing

Right after landing the instrument was still operating in the VLNS mode (see Section 4.1). All downward looking instruments were active in the 10 second time interval around landing, but only the DLV, DLVS, and column 49 yielded useful data (the DLIS just recorded a single dark measurement 0.25 s before landing). In the following paragraphs I first deal with each instrument individually, before I attempt to develop a comprehensive view of what transpired around landing.

7.1.1   DLV

In contrast to all other observation modes, the DLV dark current associated with the VLNS mode is unimodal. This means that the raw data numbers can uniquely be converted to intensities. Figure 7.2 shows all the DLV VLNS measurements, both before and after landing. The first intensity in this series, acquired at the lowest solar phase angle, is clearly higher than that of subsequent measurements, demonstrating that the opposition effect (due to backscattering of sunlight by the haze) was also observed by the DLV (see Chapter 6 for a discussion of the opposition effect). The last pre-landing intensity (**441**, at 3.5 m above the surface) is higher due to the proximity of the lamp reflection spot on the surface. After landing the intensity jumps to a higher level, reaching the stable value of 0.104 ± 0.002 [W m^{-2} μm^{-1} sr^{-1}] after about five seconds from **449** on. Small variations observed thereafter are within the limits of uncertainty. The first post-landing intensity (**445**, 0.100 [W m^{-2} μm^{-1} sr^{-1}] after 2.7 s) is significantly lower, whereas the second
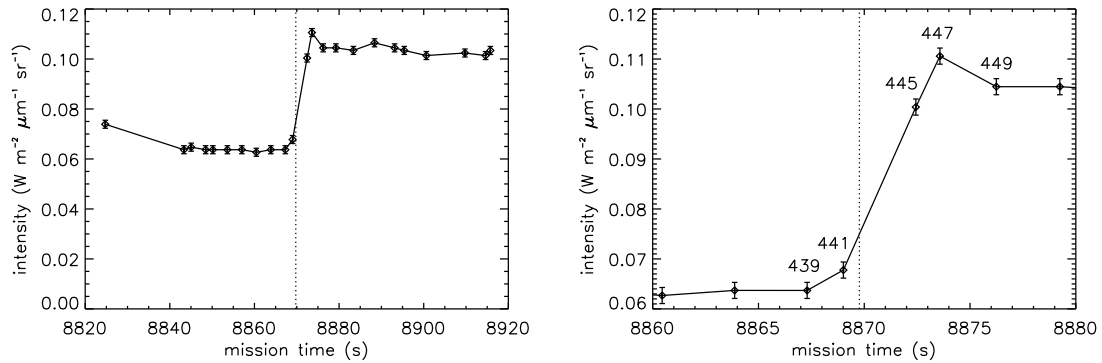
Figure 7.2: The VLNS mode DLV measurements, with errors indicating the uncertainty in the bias level. **Left**: All measurements. **Right**: Zooming in on the time of landing, with sequential numbers labeled.

(**447**, 0.111 [W m^{-2} μm^{-1} sr^{-1}] after 3.8 s) is significantly higher than the stable value. To explain the two anomalous post-landing data points we have to consider the two different mechanisms (probe movement and dust cloud formation), outlined in the previous section. With the field of view being half the hemisphere, it is difficult to distinguish between the effects of movement and dust. Dust would be bright close to the lamp, but at the same time obscure the lamp reflection spot. Probe movement could explain the data by changing the distance to the surface or bringing objects of different brightness into the field of view. We need to examine the measurements of other instruments for more clues.

7.1.2 Column 49

CCD column 49 is essentially a one-dimensional camera; it collects light spilled over from the MRI. This "crosstalk" is mainly a nuisance for the ULVS (a minor for the DLVS), and column 49 is used to gauge its magnitude. Figure 3.2 shows the location of column 49 on the CCD with respect to the MRI. Note that if an MRI image is projected in the correct orientation (raw images are upside down), light leaks from the rightmost columns.

Column 49 was read out several times around landing, and Fig. 7.3 shows the associated brightness profiles. Measurement **787** was actually acquired during landing, and its brightness profile appears smoothed, most likely because of smear (it was initiated before landing, while the probe was still rotating). In contrast, the first profile after landing (**790**, recorded after 4 s) is jagged, showing the same detailed structure as later ones (**791** and **792**). As the signal was strong due to reflected lamp light, the jagged nature of the profile must be due to surface features. It cannot reflect pixel-to-pixel variations in the responsivity of column 49 (which is unknown) because **787** is smooth, as expected for a smeared profile. The small variations superposed on the pre-landing profiles **783** and **784** are due to photon noise; their magnitude is in the order of a few DN, visible in only because of the use of the logarithmic scale in Fig. 7.3. Figure 7.4 examines the correlation between a post-landing MRI image and column 49. Shown are the top 200 pixels of the five rightmost columns of the MRI image together with column 49 **791**. The correlation of the detailed profile features is weak, but appears to be present, e.g. around pixel 170.
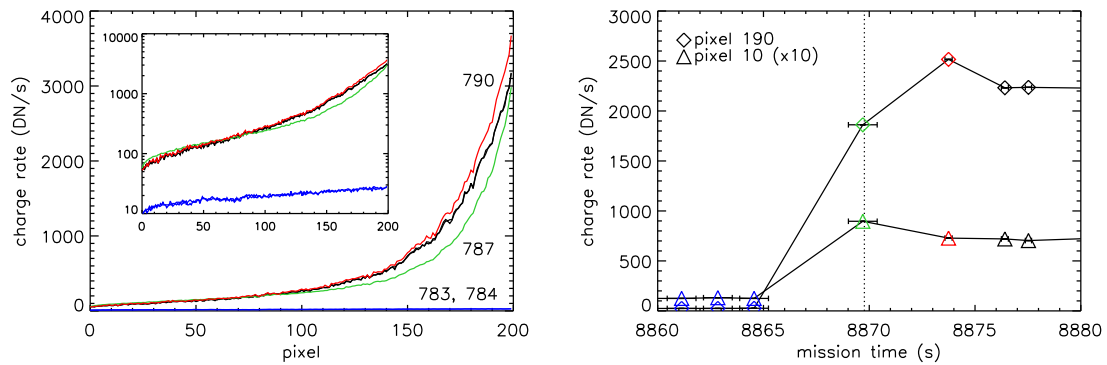
Figure 7.3: The variability of column 49 around the time of landing. **Left**: **783**, **784** (pre-landing), **787** (around landing), and **790**-**792** (post-landing). **791** and **792** are drawn in black. The inset shows the same figure in log-scale. **Right**: The variability of pixels 10 and 190. The scale of pixel 10 has been enlarged to show changes in the intensity gradient over the column. The colors are the same as in the figure on the left.
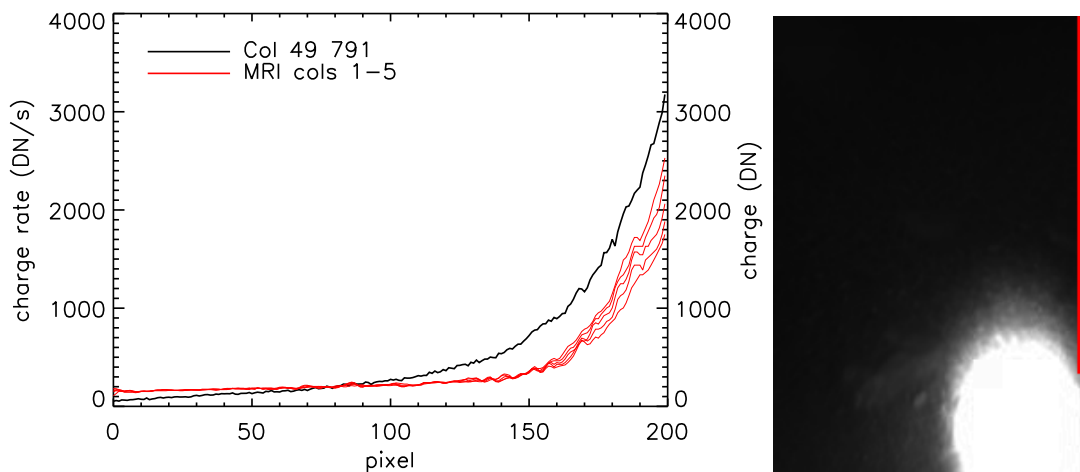
Figure 7.4: After landing, the small-scale details of the columns of the MRI that are located next to column 49 correlate reasonably weakly with the latter. **Left**: Column 49 **791** displayed in black, with the raw MRI **1191** columns 1-5 in red. **Right**: MRI **1191**, with the plotted columns in red. The overexposed lamp reflection spot is visible in the lower right corner. See Fig. 3.2 for the location and orientation of the MRI and column 49 on the CCD.

This tentatively confirms that the small-scale features in the column 49 profile correlate with surface features. All of this suggests that DISR was looking at the same spot on the surface from **790** onward. Yet **790** is brighter, mostly towards higher pixel numbers, i.e. close to the lamp reflection spot. In principle, this brightening could have been caused by a dust cloud, which would have increased the amount of lamp light scattered back into the camera. Because the detailed structure of profile **790** is similar to that of subsequent measurements, this cloud must have been optically thin.

7.1.3   DLVS

Directly after landing the DLVS signal oscillated for several seconds before reaching stability. Figure 7.5 shows how it started out low (**788**; 28% lower than the stable brightness), reached a maximum (**789**; 16% higher), and then reached a second minimum (**790**; 10% lower) before stabilizing somewhere between four to six seconds after landing (**791** and later). The first post-landing spectrum (**788**, recorded after 1.6 s) is not only a third lower in brightness, but its shape is also different (redder) than that of the stable spectrum, whereas the shape of the two subsequent spectra is virtually identical. In view of the two mechanisms proposed above (probe movement and dust cloud), it is difficult to envision how a dust cloud could have caused the brightness to oscillate. The DLVS did not look directly into the core of the SSL beam, but was aimed just to the left of it (see Fig. 4.7), so uniformly distributed intervening dust would have absorbed the light reflected off the surface. Turbulence within the dust cloud could have caused different degrees of darkening, but only in a special case (dust close to the ground) it could have lead to brightening. On the other hand, if we assume that Huygens was initially elevated above the surface by about 10 cm, perched on ice cobbles, it would lead to an intensity a third lower than the stable value, exactly what is observed for **788**. We can calculate this quite accurately because of the small field of view of the DLVS in the VLNS mode (see Fig. 4.7). That this spectrum is also redder than the stable spectrum strengthens the suspicion that DISR was looking at a different patch on the surface. As mentioned above, the higher brightness of the next spectrum (**789**) cannot reasonably be explained by dust. Together with the fact that it also is slightly redder than the stable spectrum (Fig. 7.5), this suggests that Huygens was still moving 3.0 s after landing. The brightening can be explained by DISR being closer to the surface (inclined forward?), or the presence of a relatively bright object in the field of view. The 10% lower brightness of **790**, recorded directly after **789**, can be explained by either probe movement or a dust cloud. The former would imply that the probe was still moving 4.0 s after landing.

7.1.4   Synthesis

Figure 7.6 shows how the signal of the downward looking instruments active around the time of landing (t_0) varied in a similar, but not identical, way. Seconds before landing the signal increased in strength due to the brightening of the lamp reflection spot on the approaching surface. Directly after landing the signal was variable for a period of four to six seconds, after which it stabilized. We now concentrate on three subsequent times of measurement within this brief interval of variability indicated in Fig. 7.6 ($t_1 = 1.6$ s, $t_2 = 3.0$ s, and $t_3 = 4.0$ s after landing). Initially all instruments recorded a relatively low signal. For column 49 (**787** at t_0) this was probably due to the fact that the measurement was initiated before landing. The low intensity of DLVS **788** (at t_1) with respect to the stable value is consistent with the probe being perched on 10 cm diameter ice cobbles. Its redder color compared to the stable spectrum supports the idea that the probe was initially looking at a different patch of surface. The DLV (**445**) and DLVS (**789**) observations at t_2 are more difficult to explain. The DLV measured a 10% lower intensity compared to the stable value, whereas the DLVS was actually 16% brighter. The DLV reading suggests that the probe's underside had not yet come to rest on the soil, but was still elevated a
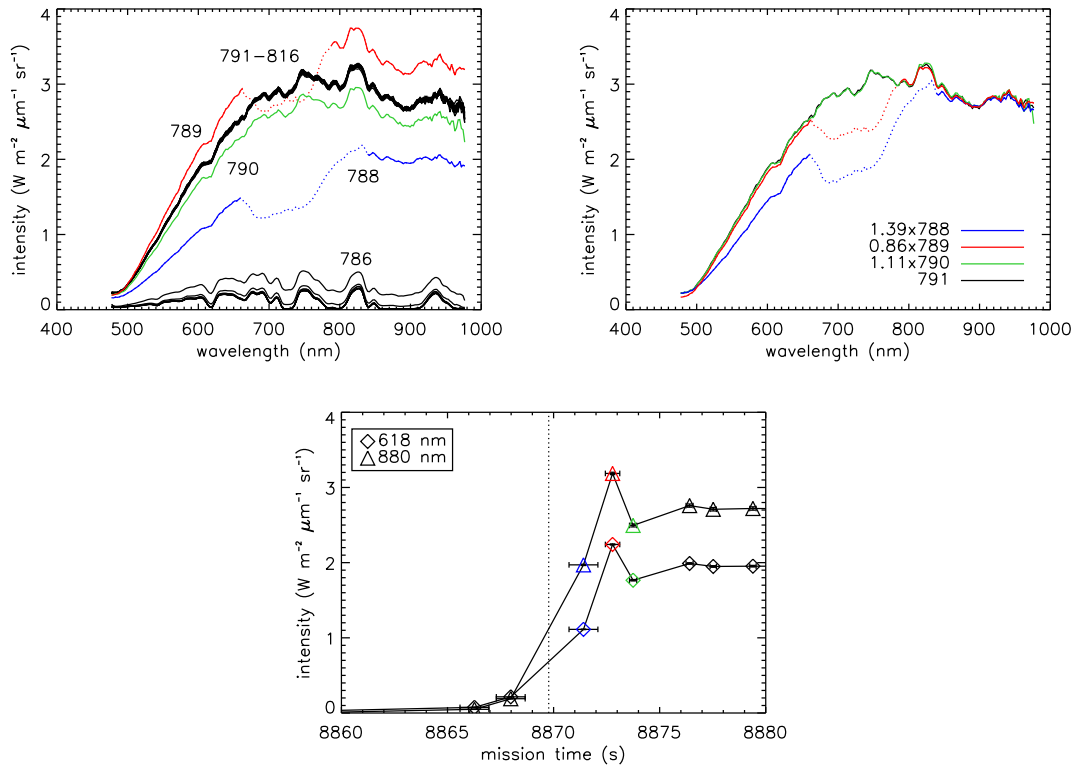
Figure 7.5: The DLVS spectra exhibit changes in intensity around the time of landing. **Top left**: All VLNS mode DLVS spectra. Unlabeled are **768**-**785** at the bottom, dotted lines indicate where the spectrum was overexposed. The spacecraft landed in-between the recording of **786** and **788**. **Top Right**: The first four spectra recorded after landing, scaled to match at the red end of the spectrum (**791** is behind **790**). The first spectrum after landing is significantly redder than the others. **Bottom**: The intensities in two methane bands, with the time of landing indicated by the vertical dotted line. The *x*-error bars delimit the exposure time. The *y*-error bars, while drawn, are hard to see as they are much smaller than the plotting symbols.

few cm above the surface. The bright DLVS spectrum may be explained by the presence of a bright, or elevated object (cobble?) in its small field of view. The fact that it is also slightly redder supports the idea that the probe had not yet come to rest. It appears that the observations at t_3 (DLV **447**, column 49 and DLVS **790**) are inconsistent with probe movement. The column 49 profile shows a brightening towards the lamp reflection spot, and has a detailed shape that resembles that of the stable profile, indicating that DISR must have viewed exactly the same terrain. The DLV detected brightening by a similar amount, but at the same time the DLVS darkened by 10%. How can the DLVS have experienced a local minimum while both the DLV and column 49 reached a maximum? The answer must have to do with the instruments' different field of view, and may be the temporary presence of a dust cloud.

To investigate this we simulate the post-landing illumination of the surface by the SSL with the open-source POV-Ray raytracer (version 3.6, `www.povray.org`). The simulation puts a spotlight in the same position as the SSL on DISR with Huygens resting on the

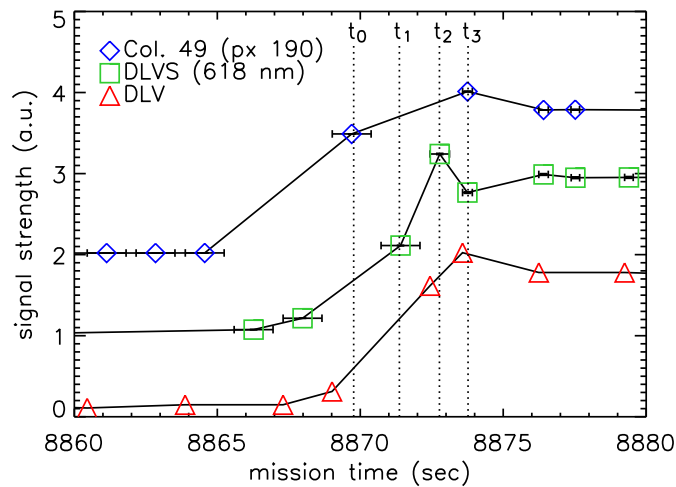Figure 7.6: The observations of the downward looking instruments compared around the time of landing (t_0). Error bars delimit the exposure time. Shown is the signal strength of the DLV, DLVS, and column 49, offset by an arbitrary amount. Also indicated are the three times (t_1, t_2, t_3) discussed in the text.

surface (MRI altitude 46 cm). Light reflected off a surface is observed from the point of view of the MRI. The spotlight beam is circular (not elliptical as for the actual SSL), and its flux drops off with the square of the distance. Before light reaches the surface it may be scattered by dust (if present) to be registered by the camera. POV-Ray offers two ways to simulate dust. The first is with the `media` statement to simulate scattering and extinction by a medium of microscopic scatterers. This type of simulation is not formulated in terms of particles, and it does not model extinction of light reflected off the surface towards the cameras. Hence, its results can only be discussed in qualitative terms. The type of scattering can be specified. I consider both isotropic scattering, and (more realistic) the strongly forward scattering behavior of the *Mie haze* model. Alternatively, I model macroscopic dust particles as tiny spheres, which does take into account extinction of light reflected off the surface. For the sphere diameter I select a value in the range provided by Lorenz et al. (2006b) for particles that may make up the equatorial dunes. Since Huygens landed 30 km south of two dunes (see Figs. 1.10 and 6.3), it is reasonable to assume these particles can be found around the landing site. Figure 7.7 shows the results for the microscopic dust (`media`) simulation. The top figures are simulated MRI views of a variegated surface illuminated by a SSL-type lamp, the bottom figures show simulated column 49 profiles. It is clear that dust absorption darkens the left side of the reflection spot (the approximate location of the DLVS footprint), but it is key to demonstrate that at the same time it can brighten the right side of the MRI image (which spills over into column 49). The figure shows that isotropically scattering dust can do this, where the (more realistically) forward scattering dust fails. In both cases details on the surface remain visible, as required by the column 49 observations. Apparently, to explain the increased brightness of column 49 **790** substantial backscattering is required. Figure 7.8 shows the results of the macroscopic dust (spheres) simulation, with at left simulated MRI views, and at right the associated column 49 profiles. Note that the lamp reflection spot
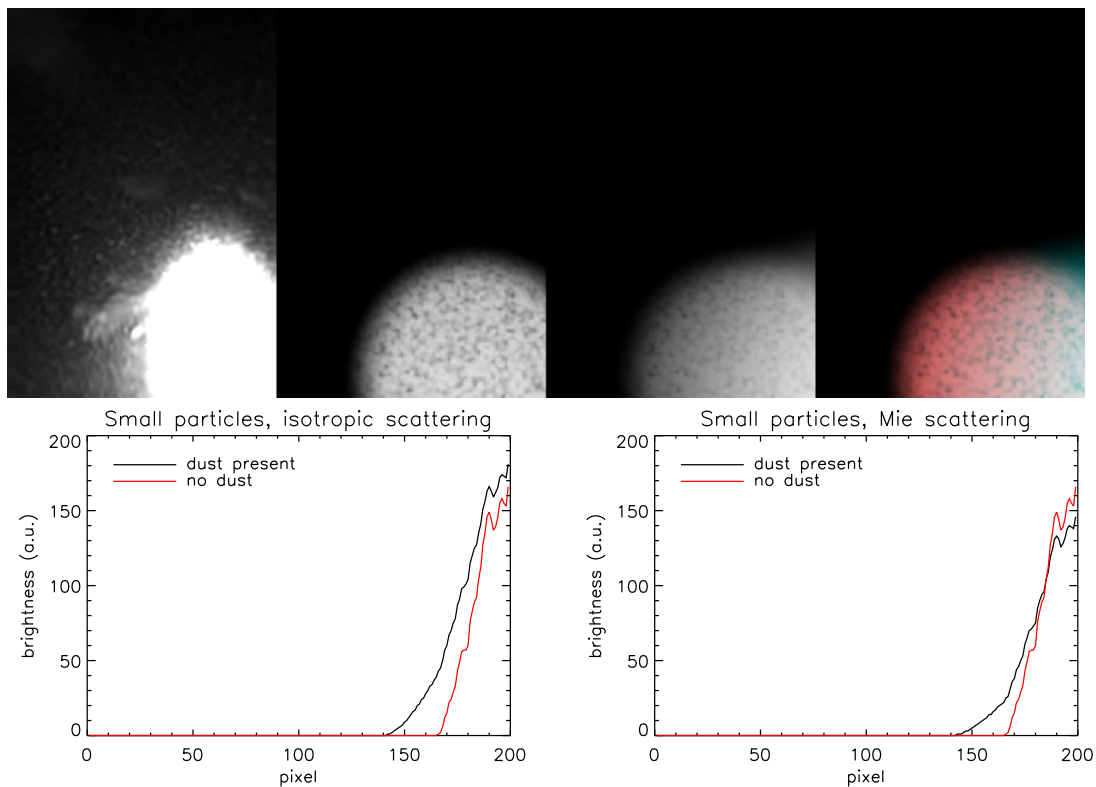
137

Figure 7.7: Simulations of how column 49 would perceive the presence of microscopic dust between DISR and the surface. **Top**: POV-Ray simulations of how the MRI would see the lamp reflection spot. The simulation employs the `media` statement, which does not consider extinction of light reflected from the surface. Far left: MRI image **1011** of the overexposed reflection spot. Center left: No dust. Center right: Dust scattering white light isotropically. Far right: To illustrate the process we let dust scatter green and blue light only (red light is transmitted). The simulated lamp beam is circular, whereas the actual beam is elliptical. **Bottom**: Simulated column 49 profiles (i.e. the top 200 pixels of the rightmost column of the MRI images) in the presence of isotropically (left) and forward (right) scattering dust. Compare these profiles to Fig. 7.3 (left).

is displayed darker than in Fig. 7.7 to accommodate for the high brightness of particles close to the lamp. The particle number density is 3 cm^{-3}, which results in a darkening of 10% at the left side of the lamp spot (as required by DLVS observation **790**). Clearly, the presence of macroscopic particles creates spikes in the column 49 profile, with maxima in brightness due to particles close to the lamp, and minima due to particles close to the camera. In reality, the spikes would not be as pronounced as in Fig. 7.8, because particles close to the camera would be out of focus, and because crossover to column 49 does not only involve the rightmost column of the MRI. Nevertheless, these simple simulations suggest that the brightening of column 49 profile **790** with respect to **791** is definitely not due to large (>0.1 mm) dust particles, as these would lead to spikes in the profile that were not observed. In principle, it may be caused by the presence of very fine particles, which would need to exhibit a substantial degree of backscattering, and have a scattering cross-section independent of wavelength. This would be an unusual type of dust. Scattering by
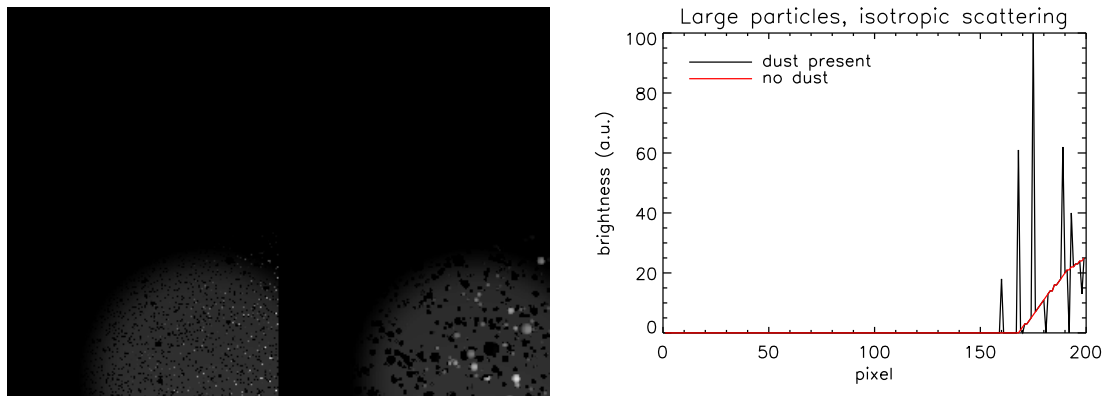
Figure 7.8: Simulations of how column 49 would perceive the presence of macroscopic dust between DISR and a uniform surface. **Left**: POV-Ray simulations of how the MRI would see the lamp reflection spot. Dust is modeled as isotropically scattering 0.25 mm (left) and 2 mm (right) diameter spheres at a number density of 3 cm^{-3}. **Right**: Simulated column 49 profiles (i.e. the top 200 pixels of the rightmost column of the MRI images) for the 0.25 mm diameter spheres at left. Compare this figure to Fig. 7.3 (left).

Titan aerosols, for example, is found to be strong in the forward direction and wavelength dependent (Tomasko and Smith 1982) (Tomasko et al. 2007).

In summary, the downward looking instrument measurements are explained best by the assumption that Huygens was moving and/or rotating for at least 3 seconds, after landing, probably perched on cobbles like those observed in the SLI images. Because the final resting position of the probe was with its bottom on the soil (Karkoschka et al. 2007), it must have slid off the cobbles, or pushed them into the (soft) ground. The DLVS measurements within that interval provide evidence for the presence of materials with different spectral characteristics at the landing site. The measurements at 4 seconds after landing are difficult to explain. They are not caused by the presence of large dust particles in the air between surface and camera, that are thought to make up the equatorial dunes (Lorenz et al. 2006b). Very fine particles are ruled out by the requirement of backscattering and the spectrally neutral character of the putative absorption. Possibly we do not fully understand the crossover mechanism, and/or the post-landing behavior of the CCD. Input from other onboard sensors (radio, accelerometers) could lead to further understanding, and perhaps indicate whether the probe was still moving after 4 seconds after landing.

7.2 Long term variability

After 47 seconds on the surface DISR switched to one of the several surface modes (see Section 4.1). The DLVS returned to the 10-column mode, and the DLIS measurements were once more summed on board as if the spacecraft was still suspended in the air. Some of the DISR instruments observed slow, gradual changes over the hour that Huygens spent immobilized on the surface. In this section I discuss whether these are real, or can be attributed to instrumental effects.
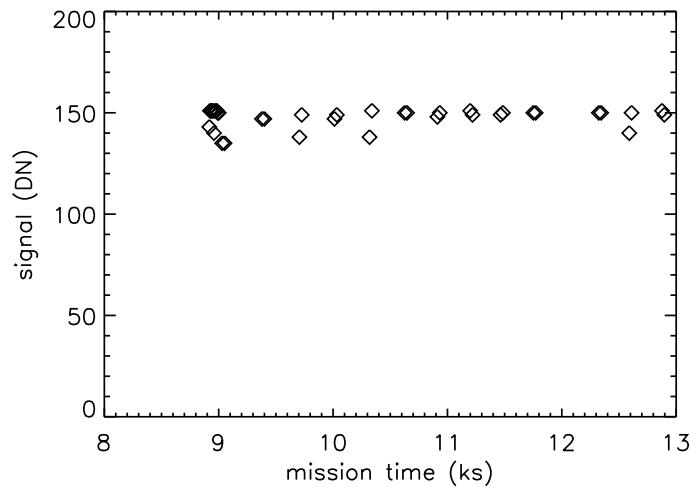
Figure 7.9: The signal of the DLV is virtually constant over time after one minute after landing. The measurements are bimodal due to the dark signal associated with the surface operational mode.

7.2.1   DLV

After the initial variability around landing the DLV signal remained virtually constant. The changes visible in Fig. 7.9 are due to the bimodal distribution of the dark signal (see §3.1.1) in the various surface modes. The expected difference in dark signal is about 10 DN, more or less the value observed.

7.2.2   CCD instruments

The long term behavior of the CCD-based instruments after landing was peculiar. The brightness distribution on the images gradually changed, with the brightest parts of the SLI surface image (the top and bottom part) becoming even brighter over time. The brightness distribution on all SLI surface images is in fact identical. The CCD was not designed to deal with the flood of reflected lamp light it received after landing, and could not get rid of the excess charge completely. The DLVS measurements are affected in a similar way. Furthermore, post-landing CCD measurements were severely affected by stray light, due to the small distance of the fiber to the CCD surface (20 μm).

The other downward looking instruments that use the CCD as light detector indeed behaved similarly. Figure 7.10 shows how the signal of both column 49 and the DLVS gradually increased over time, column 49 mostly where the charge rate is highest, and the DLVS mostly at higher wavelengths, where the intensity is highest. Since the DLV and the DLIS observations, which do not use the CCD as detector, did not exhibit any significant changes over time, the changes observed by column 49 and the DLVS must result from the phenomenon described above. Then it follows that the most accurate measurements are those recorded right after landing.

Figure 7.10: Charge accumulation on the CCD over time. Column 49 (**left**) and the DLVS (**right**) were read out at the same time, and therefore have identica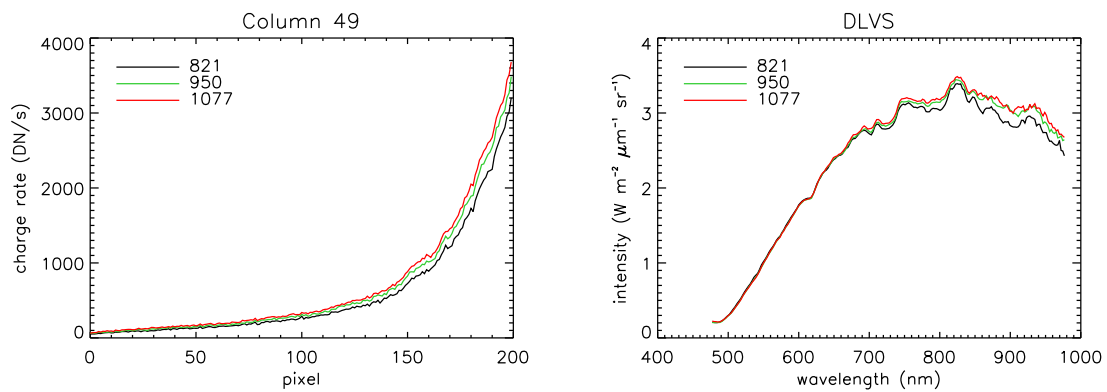l sequential numbers (listed in the legend). The time between the first and last measurement was 4074 sec (1h 8m). The increase is largest where the signal is strongest. Spectra DLVS **821** and **1077** are that of footprint 6 (out of 8) of the first and last correctly exposed 10-column mode spectra recorded after landing.

7.2.3   DLIS

Figure 7.11 (left) compares the first correctly exposed DLIS spectrum recorded after landing (**249**) with the last one (**268**), obtained 66 minutes later. Note that **249** was recorded in the single exposure (unsummed) mode, and **261** and **268** in the summed mode. A few minutes after landing the DLIS switched to the summed mode again, in case the spacecraft was mistaken about having landed and in reality was still suspended in the atmosphere (see Sec. 4.1). In contrast to spectra recorded early in flight, summing while on the surface is of no consequence because the spacecraft was continuously looking in the same direction. The figure shows that the DLIS observed a slight gradual darkening over the course of the hour on the surface. Whether this darkening of about 5% is real cannot be established with certainty, but probably not because it was not observed by any of the other downward looking instruments. Instead, it may emerge from a switch to a different set of responsivities associated with the 14 K increase in detector temperature. Even though the images show that the probe tilted slightly over the hour (Karkoschka et al. 2007), the estimated amount is so small (0.06 degrees), that this could have affected the spectrometer observations. The overall reflectance of the surface was most likely constant, as implied by the DLV measurements.

   Is the depth of the methane absorption lines constant as well? As Fig. 7.11 (right) shows, the $1.16\,\mu$m methane complex does not show any changes in shape over the course of an hour. This implies that the methane mixing ratio in the atmosphere between the DLIS and the lamp reflection spot on the surface was constant. If evaporation of liquid methane from the soil by lamp or probe heat occurred after 90 seconds after landing, it was too little to be observed in the DLIS optical path. The presence of liquid methane on the surface at the landing site is ruled out by the post-landing DLIS spectra (see Section 5.3) and observations by other Huygens instruments (Fulchignoni et al. 2005, Zarnecki et al. 2005). However, there are hints that the subsurface is wet at a depth of several cm (Niemann et al. 2005, Zarnecki et al. 2005, Lorenz et al. 2006a). Most of the energy of the
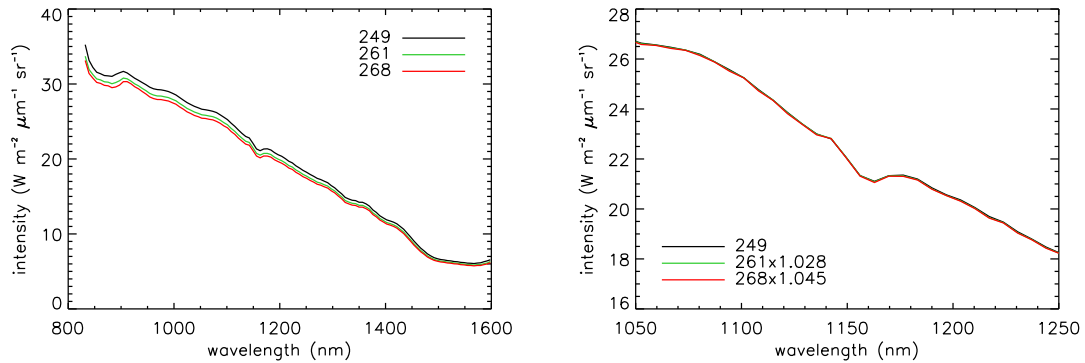
Figure 7.11: Evolution of the DLIS spectra recorded on the surface. **Left**: **249** and **268** are the first and last unsaturated spectra (see Table A.14). The recording times of **249**, **261**, and **268** are 8960, 10943 and 12902 s, respectively, and their detector temperatures 189, 196, and 203 K. All spectra used **202** as background. **Right**: When spectra **261** and **268** are scaled to match **249**, the 1.16 μm methane absorption line complex is found to be invariant.

20 W SSL was deposited on an area of about 80 cm^2, and the heat flow downward may have heated liquid methane in the subsurface to the boiling point at 116 K (at Titan pressure). The results from a simple simulation of the heat flow, using the parameters for a porous icy regolith from Tokano (2005), indicate that the top of the surface would have heated up quickly, possibly to temperatures as high as 170 K depending on the amount of free convection (this temperature assumes air flow velocities of 2 m s^{-1}). Evidence for strong surface heating is found in the post-landing images in the form of changes in seeing (Karkoschka et al. 2007). However, due to the low thermal conductivity of this type of surface, a temperature increase of at least 20 K is reached only in the upper 2 cm of the soil. If liquid methane was present below 3 cm, evaporation would hardly have increased the mixing ratio in the air above the lamp reflection spot. The DLIS was peering directly into the spot (see Fig. 4.7), but the fact that it did not record any changes in the methane absorption lines does not exclude the presence of liquid methane a few centimeters below the surface.

A   Overview of DISR Observations

This appendix provides an overview of selected DISR downward looking instrument observations from data stream 524b. Measurements are listed in 14 tables as follows, DLV: Tables A.1 to A.3, DLVS: Tables A.4 to A.8, column 49: Table A.9, and DLIS: Tables A.10 to A.14. Tables are ranked in chronological order and generally classified according to observation mode (see Chapter 4 for an overview). Tabulated are only those modes that we are concerned with in this thesis: SM1, SM2, MNS, VLNS, and diverse post-VLNS surface modes.

The first column in each table is the sequential number (#) assigned by DISR. Except for these tables, sequential numbers are printed **bold** throughout this thesis. The second column lists the measurement cycle number. Different instruments can have a measurement in the same cycle, as described in the file `Science_Summary`. The third column lists the mission time, counted from the start of the descent. Other columns may contain the probe attitude and altitude, calculated according to the Karkoschka et al. (2007) reconstruction, and exposure details. Exceptions are altitudes below 30 m, which were calculated from the time of landing at mission time 8869.77 s, assuming an impact velocity of 4.60 m s^{-1} as determined by the Surface Science Package (Zarnecki et al. 2005). Azimuth angles are defined counterclockwise with respect to the east. The spectrometer altitude after landing is 46 cm, and the azimuth is 257.0° (Karkoschka et al. 2007).

Table A.1: All VLNS mode DLV measurements transmitted before landing. Instrument readout was instantaneous. The altitudes of **435**, **439**, and **441** were calculated from the time of landing.

#	cycle	mission time (s)	altitude (m)	azimuth angle (°)
403	91	8824.75	205	171.4
411	95	8843.33	119	56.3
413	96	8845.04	111	45.3
417	98	8848.47	96	23.5
419	99	8850.18	88	12.6
423	101	8853.60	74	351.0
427	103	8857.02	57	329.8
431	105	8860.45	42	309.3
435	107	8863.88	27.1	289.6
439	109	8867.30	11.4	270.7
441	110	8869.01	3.5	261.9

Table A.2: All VLNS mode DLV measurements transmitted after landing. Instrument readout was instantaneous.

#	cycle	mission time (s)	#	cycle	mission time (s)
445	112	8872.44	471	125	8893.13
447	113	8873.58	475	127	8895.40
449	114	8876.24	481	130	8900.63
453	116	8879.24	493	136	8909.75
459	119	8883.38	499	139	8914.63
465	122	8888.37	501	140	8815.76

Table A.3: All post-VLNS DLV measurements transmitted from the surface. Instrument readout was instantaneous.

#	cycle	mission time (s)	#	cycle	mission time (s)
503	141	8918.02	554	156	10319.10
505	142	8923.64	556	156	10339.52
507	143	8931.63	561	157	10625.90
509	144	8941.57	563	157	10646.34
511	145	8949.83	568	158	10912.28
513	146	8958.77	570	158	10932.70
515	147	8967.01	575	159	11198.62
517	148	8975.43	577	159	11219.07
519	149	8983.71	581	160	11464.57
521	150	8991.99	583	160	11484.98
523	151	9000.28	589	161	11750.92
526	152	9030.43	591	161	11771.34
527	152	9050.89	603	163	12323.62
533	153	9378.19	605	163	12344.07
535	153	9398.61	609	164	12589.57
540	154	9705.45	612	164	12609.98
543	154	9725.89	617	165	12875.91
547	155	10012.27	619	165	12896.34
549	155	10032.70			

Table A.4: All DLVS Spectrophotometric Map 1 spectra. Mission time listed is halfway through exposure. The phase angle is the average of that of pixel 11 and 12.

#	cycle	mission time (s)	exposure time (s)	altitude (km)	azimuth angle (°)	phase angle (°)
537	52	5536.55	0.85	18.27	190.3	19.1
540	52	5539.98	0.85	18.25	158.1	15.0
541	52	5541.09	0.85	18.24	147.6	16.3
543	52	5543.57	0.85	18.23	124.2	22.6
545	52	5545.81	0.85	18.21	103.1	29.7
547	52	5548.04	0.85	18.20	82.1	36.7
549	52	5550.28	0.85	18.18	61.1	43.1
551	52	5552.75	0.85	18.16	38.0	48.8
553	52	5555.05	0.85	18.15	16.3	52.6
555	52	5557.29	0.85	18.13	355.1	54.6
557	52	5559.60	0.85	18.12	333.0	54.7
559	52	5562.09	0.85	18.10	308.9	52.5
561	52	5564.40	0.85	18.08	286.0	48.4
563	52	5566.72	0.85	18.07	262.7	42.4
565	52	5568.95	0.85	18.05	239.7	35.3

Table A.5: All DLVS Spectrophotometric Map 2 spectra. Mission time listed is halfway through exposure. The phase angle is the average of that of pixel 11 and 12.

#	cycle	mission time (s)	exposure time (s)	altitude (km)	azimuth angle (°)	phase angle (°)
686	61	8046.92	0.85	3.88	330.9	54.0
688	61	8049.17	0.85	3.87	316.2	52.8
690	61	8051.47	0.85	3.86	300.9	50.7
692	61	8053.97	0.85	3.85	284.4	47.5
694	61	8056.27	0.85	3.83	269.1	43.7
696	61	8058.51	0.85	3.82	254.3	39.5
698	61	8060.81	0.85	3.81	239.0	34.7
700	61	8063.22	0.85	3.80	223.1	29.3
702	61	8065.46	0.85	3.79	208.3	24.3
704	61	8067.69	0.85	3.78	193.5	19.5
706	61	8070.00	0.85	3.77	178.2	15.7
708	61	8072.43	0.85	3.75	162.0	14.2
710	61	8074.67	0.85	3.74	147.1	15.8
712	61	8076.90	0.85	3.73	132.1	19.5
714	61	8079.14	0.85	3.72	117.1	24.3
716	61	8081.40	0.85	3.71	101.8	29.5
718	61	8083.82	0.85	3.70	85.5	35.0

Table A.6: All VLNS mode DLVS spectra transmitted before landing. Mission time listed is halfway through exposure. The altitudes of **785** and **786** were calculated from the time of landing.

#	cycle	mission time (s)	exposure time (s)	altitude (m)	azimuth angle (°)	phase angle (°)
768	91	8825.43	1.36	202	167.3	14.2
769	92	8827.14	1.36	194	157.0	14.2
771	94	8842.30	1.36	124	62.9	41.8
772	95	8844.01	1.36	116	51.9	44.7
774	97	8847.44	1.36	101	30.0	49.6
775	98	8849.15	1.36	93	19.1	51.4
777	100	8852.57	1.36	78	357.4	53.6
779	102	8855.99	1.36	62	336.1	54.0
781	104	8859.42	1.36	47	315.4	52.6
785	108	8866.27	1.36	16.1	276.4	45.5
786	109	8867.98	1.36	8.2	267.0	43.0

Table A.7: All VLNS mode DLVS spectra transmitted after landing. Mission time listed is halfway through exposure. Spectra marked with an asterisk were partly overexposed.

#	cycle	mission time (s)	exposure time (s)	#	cycle	mission time (s)	exposure time (s)
788*	111	8871.41	1.36	803	126	8894.41	0.30
789*	112	8872.78	0.68	806	129	8899.03	0.30
790	113	8873.75	0.34	807	130	8900.78	0.30
791	114	8876.41	0.33	809	132	8903.66	0.30
792	115	8877.52	0.30	811	134	8907.31	0.30
793	116	8879.40	0.30	812	135	8908.44	0.30
798	121	8886.65	0.30	813	136	8909.90	0.30
799	122	8888.52	0.30	815	138	8912.91	0.30
801	124	8891.42	0.30	816	139	8914.78	0.30
802	125	8893.28	0.30				

Table A.8: Selected correctly exposed 10-column mode DLVS spectra transmitted from the surface (**1077** was the last). Mission time listed is halfway through exposure.

#	cycle	mission time (s)	exposure time (s)	#	cycle	mission time (s)	exposure time (s)
821	142	8931.13	0.30	905	155	10110.85	0.68
825	144	8949.31	0.36	906	155	10117.67	0.68
827	145	8957.92	1.00	907	155	10141.53	0.68
829	146	8966.49	0.36	909	156	10317.92	0.35
831	147	8974.83	0.50	910	156	10320.69	0.35
833	148	8983.18	0.36	911	156	10330.92	0.35
835	149	8991.47	0.36	950	158	10961.60	0.36
837	150	8999.75	0.36	1077	165	13005.36	0.36

Table A.9: Selected column 49 measurements. Mission time listed is halfway through exposure.

#	cycle	mission time (s)	exposure time (s)	#	cycle	mission time (s)	exposure time (s)
782	105	8861.13	1.36	791	114	8876.41	0.33
783	106	8862.84	1.36	792	115	8877.52	0.30
784	107	8864.56	1.36	821	142	8931.13	0.30
787	110	8869.70	1.36	950	158	10961.60	0.36
790	113	8873.75	0.34	1077	165	13005.36	0.35

Table A.10: All DLIS Spectrophotometric Map 1 spectra. During an operation the instrument acquired two exposures (samples) with shutter subsequently open and closed, which were summed on board. Mission time listed is halfway through the operation. Each spectrum is the average of the two samples.

#	cycle	mission time (s)	sampling time (s)	operation time (s)	altitude (km)	azimuth angle (°)	phase angle (°)
58	52	5538.46	0.13	0.56	18.26	172.4	16.1
59	52	5539.14	0.13	0.56	18.26	166.0	14.7
60	52	5539.83	0.13	0.56	18.25	159.5	13.8
65	52	5543.25	0.13	0.56	18.23	127.2	17.8
68	52	5545.31	0.13	0.56	18.21	107.8	24.3
69	52	5545.99	0.13	0.56	18.21	101.3	26.7
71	52	5547.37	0.13	0.56	18.20	88.4	31.4
72	52	5548.05	0.13	0.56	18.20	82.0	33.7
75	52	5550.11	0.13	0.56	18.18	62.7	40.2
78	52	5552.16	0.13	0.56	18.17	43.5	46.0
79	52	5552.85	0.13	0.56	18.16	37.0	47.7
82	52	5554.91	0.13	0.56	18.15	17.7	52.0
85	52	5556.96	0.13	0.56	18.13	358.3	54.9
86	52	5557.65	0.13	0.56	18.13	351.7	55.5
88	52	5559.02	0.13	0.56	18.12	338.6	56.2
89	52	5559.71	0.13	0.56	18.12	332.0	56.3
91	52	5561.08	0.13	0.56	18.11	318.7	55.8
92	52	5561.77	0.13	0.56	18.10	312.0	55.3
95	52	5563.83	0.13	0.56	18.09	291.8	52.7
96	52	5564.51	0.13	0.56	18.08	285.0	51.4
99	52	5566.57	0.13	0.56	18.07	264.2	46.5
102	52	5568.62	0.13	0.56	18.05	243.1	40.3
103	52	5569.31	0.13	0.56	18.05	236.0	37.9
105	52	5570.69	0.13	0.56	18.04	221.7	32.9

Table A.11: All DLIS Spectrophotometric Map 2 spectra. During an operation the instrument acquired two exposures (samples) with shutter subsequently open and closed, which were summed on board. Mission time listed is halfway through the operation. Each spectrum is the average of the two samples.

#	cycle	mission time (s)	sampling time (s)	operation time (s)	altitude (km)	azimuth angle (°)	phase angle (°)
113	61	8047.21	0.13	0.56	3.88	329.0	56.0
115	61	8048.58	0.13	0.56	3.87	320.0	55.3
116	61	8049.27	0.13	0.56	3.87	315.5	55.0
119	61	8051.33	0.13	0.56	3.86	301.9	53.6
122	61	8053.38	0.13	0.56	3.85	288.3	51.5
123	61	8054.06	0.13	0.56	3.85	283.7	50.6
126	61	8056.12	0.13	0.56	3.83	270.1	47.6
129	61	8058.18	0.13	0.56	3.82	256.5	43.9
130	61	8058.87	0.13	0.56	3.82	251.9	42.6
132	61	8060.24	0.13	0.56	3.81	242.9	39.8
133	61	8060.92	0.13	0.56	3.81	238.3	38.3
136	61	8062.98	0.13	0.56	3.80	224.7	33.6
139	61	8065.05	0.13	0.56	3.79	211.0	28.7
140	61	8065.73	0.13	0.56	3.79	206.5	27.0
142	61	8067.10	0.13	0.56	3.78	197.4	23.7
143	61	8067.79	0.13	0.56	3.78	192.9	22.1
146	61	8069.85	0.13	0.56	3.77	179.2	17.6
149	61	8071.90	0.13	0.56	3.76	165.5	14.1
150	61	8072.59	0.13	0.56	3.75	160.9	13.4
152	61	8073.96	0.13	0.56	3.75	151.8	12.8
153	61	8074.64	0.13	0.56	3.74	147.2	13.0
156	61	8076.70	0.13	0.56	3.73	133.4	15.5
159	61	8078.76	0.13	0.56	3.72	119.6	19.6
160	61	8079.44	0.13	0.56	3.72	115.0	21.1
162	61	8080.81	0.13	0.56	3.71	105.8	24.4
163	61	8081.50	0.13	0.56	3.71	101.1	26.1
166	61	8083.56	0.13	0.56	3.70	87.2	31.2
169	61	8085.61	0.13	0.56	3.69	73.4	36.1

Table A.12: All MNS mode DLIS spectra. During an operation the instrument acquired two exposures (samples) with shutter subsequently open and closed, which were summed on board. Mission time listed is halfway through the operation. Each spectrum is the average of the two samples.

#	cycle	mission time (s)	sampling time (s)	operation time (s)	altitude (km)	azimuth angle (°)	phase angle (°)
171	64	8236.20	1.99	8.02	2.96	93.7	28.8
172	65	8275.82	1.99	8.02	2.77	215.6	30.3
174	67	8324.95	1.99	8.02	2.53	256.9	44.0
176	69	8373.44	1.99	8.02	2.30	279.0	49.5
178	71	8421.82	1.99	8.02	2.08	349.2	54.9
182	75	8520.19	1.68	6.76	1.61	28.5	49.0
184	77	8569.58	1.75	7.05	1.39	52.8	42.6
186	79	8618.70	1.99	8.02	1.15	74.9	35.4
188	81	8668.47	1.99	8.02	0.92	110.5	22.6
190	83	8716.47	1.99	8.02	0.70	162.7	13.5
192	85	8766.83	1.99	8.02	0.47	193.8	22.4

Table A.13: All VLNS mode DLIS spectra transmitted before landing. During an operation the instrument acquired a single exposure (sample) with either shutter open (bright) or closed (dark). Mission time listed is halfway through sampling. The altitudes of **210** and **213** were calculated from the time of landing.

#	cycle	mission time (s)	type	sampling time (s)	operation time (s)	altitude (m)	azimuth angle (°)	phase angle (°)
194	91	8825.69	bright	1.00	1.02	200	165.7	14.0
196	93	8832.53	bright	1.00	1.02	169	124.3	17.9
199	96	8845.55	bright	1.00	1.02	109	42.2	45.5
202	99	8850.68	bright	1.00	1.02	86	9.4	52.6
204	101	8854.10	bright	1.00	1.02	72	347.9	54.9
206	103	8857.53	bright	1.00	1.02	55	326.8	55.4
208	105	8860.95	dark	1.00	1.02	41	-	-
210	107	8864.38	bright	1.00	1.02	24.8	286.9	51.1
213	110	8869.52	dark	1.00	1.02	1.2	-	-

Table A.14: All correctly exposed post-VLNS DLIS spectra transmitted from the surface. During an operation the instrument acquired multiple exposures (samples) with shutter open and closed, which were summed on board. For spectra **261** to **268** the sampling time of two of the eight regions was half the value in the table. The number of samples tabulated is for shutter open. Mission time listed is halfway through the operation.

#	cycle	mission time (s)	sampling time (ms)	samples	operation time (s)
249	146	8960.23	16.13	54	2.05
250	147	8968.43	8.06	100	1.95
251	148	8976.84	8.06	100	1.95
252	149	8985.12	8.06	100	1.95
253	150	8993.41	8.06	100	1.95
254	151	9001.69	8.06	100	1.95
261	158	10942.72	16.13	2144	70.71
262	159	11219.25	8.06	3680	71.48
263	160	11500.50	8.06	3680	71.48
264	161	11781.75	8.06	3680	71.48
265	162	12065.27	8.06	3680	71.48
266	163	12344.25	8.06	3680	71.48
267	164	12625.50	8.06	3680	71.48
268	165	12901.64	8.06	3680	71.48

B   Abbreviations

BRDF	Bidirectional Reflectance Distribution Function
CBOE	Coherent Backscatter Opposition Effect
CCD	Charge Coupled Device
DISR	Descent Imager / Spectral Radiometer
DLIS	Downward Looking Infrared Spectrometer
DLV	Downward Looking Violet photometer
DLVS	Downward Looking Visual Spectrometer
DN	Data Number
ESA	European Space Agency
FWHM	Full Width at Half Maximum
GCMS	Gas Chromatograph / Mass Spectrometer
HASI	Huygens Atmospheric Structure Instrument
HNS	High Near Surface
HRI	High Resolution Imager
ISS	Imaging Science Subsystem
JPL	Jet Propulsion Laboratory
LNS	Low Near Surface
LPG	Laboratoire Planétologie Grenoble
LPL	Lunar & Planetary Laboratory
MNS	Medium Near Surface
MPS	Max-Planck-Institut für Sonnensystemforschung
MRI	Medium Resolution Imager
NASA	National Aeronautics and Space Administration
SAR	Synthetic Aperture Radar
SHOE	Shadow Hiding Opposition Effect
SI	Système International
SLI	Side Looking Imager
SM1	Spectrophotometric Map 1
SM2	Spectrophotometric Map 2
S/N	Signal to Noise
SSL	Surface Science Lamp
SSP	Surface Science Package
ULIS	Upward Looking Infrared Spectrometer
ULV	Upward Looking Violet photometer
ULVS	Upward Looking Visual Spectrometer
VIMS	Visual and Infrared Mapping Spectrometer
VLNS	Very Low Near Surface

Bibliography

Atreya, S. K., Adams, E. Y., Niemann, H. B., Demick-Montelara, J. E., Owen, T. C., Fulchignoni, M., Ferri, F., and Wilson, E. H. (2006). Titan's methane cycle. *Planet. Space Sci.*, 54:1177–1187.

Barnes, J. W., Brown, R. H., Radebaugh, J., Buratti, B. J., Sotin, C., Le Mouelic, S., Rodriguez, S., Turtle, E. P., Perry, J., Clark, R., Baines, K. H., and Nicholson, P. D. (2006). Cassini observations of flow-like features in western Tui Regio, Titan. *Geophys. Res. Lett.*, 33:16204–+.

Barnes, J. W., Brown, R. H., Soderblom, L., Buratti, B. J., Sotin, C., Rodriguez, S., Le Mouèlic, S., Baines, K. H., Clark, R., and Nicholson, P. (2007). Global-scale surface spectral variations on Titan seen from Cassini/VIMS. *Icarus*, 186:242–258.

Barnes, J. W., Brown, R. H., Turtle, E. P., McEwen, A. S., Lorenz, R. D., Janssen, M., Schaller, E. L., Brown, M. E., Buratti, B. J., Sotin, C., Griffith, C., Clark, R., Perry, J., Fussner, S., Barbara, J., West, R., Elachi, C., Bouchez, A. H., Roe, H. G., Baines, K. H., Bellucci, G., Bibring, J.-P., Capaccioni, F., Cerroni, P., Combes, M., Coradini, A., Cruikshank, D. P., Drossart, P., Formisano, V., Jaumann, R., Langevin, Y., Matson, D. L., McCord, T. B., Nicholson, P. D., and Sicardy, B. (2005). A 5-Micron-Bright Spot on Titan: Evidence for Surface Diversity. *Science*, 310:92–95.

Bernard, J.-M., Quirico, E., Brissaud, O., Montagnac, G., Reynard, B., McMillan, P., Coll, P., Nguyen, M.-J., Raulin, F., and Schmitt, B. (2006). Reflectance spectra and chemical structure of Titan's tholins: Application to the analysis of Cassini-Huygens observations. *Icarus*, 185:301–307.

Biemann, K. (2006). Complex organic matter in Titan's aerosols? *Nature*, 444:E6.

Bird, M. K., Allison, M., Asmar, S. W., Atkinson, D. H., Avruch, I. M., Dutta-Roy, R., Dzierma, Y., Edenhofer, P., Folkner, W. M., Gurvits, L. I., Johnston, D. V., Plettemeier, D., Pogrebenko, S. V., Preston, R. A., and Tyler, G. L. (2005). The vertical profile of winds on Titan. *Nature*, 438:800–802.

Bouchez, A. H. and Brown, M. E. (2005). Statistics of Titan's South Polar Tropospheric Clouds. *ApJ*, 618:L53–L56.

Buratti, B. J. (1985). Application of a radiative transfer model to bright icy satellites. *Icarus*, 61:208–217.

Campbell, D. B., Black, G. J., Carter, L. M., and Ostro, S. J. (2003). Radar Evidence for Liquid Surfaces on Titan. *Science*, 302:431–434.

Chandrasekhar, S. (1960). *Radiative transfer*. New York: Dover.

Clark, B. E., Helfenstein, P., Bell, J. F., Peterson, C., Veverka, J., Izenberg, N. I., Domingue, D., Wellnitz, D., and McFadden, L. (2002). NEAR Infrared Spectrometer Photometry of Asteroid 433 Eros. *Icarus*, 155:189–204.

Clark, R. N. (1981a). The spectral reflectance of water-mineral mixtures at low temperatures. *J. Geophys. Res.*, 86:3074–3086.

Clark, R. N. (1981b). Water frost and ice: The near-infrared spectral reflectance 0.65-2.5 μm. *J. Geophys. Res.*, 86:3087–3096.

Cloutis, E. A. (1989). Spectral Reflectance Properties of Hydrocarbons: Remote-Sensing Implications. *Science*, 245:165–168.

Courtin, R. and Kim, S. J. (2002). Mapping of Titan's tropopause and surface temperatures from Voyager IRIS spectra. *Planet. Space Sci.*, 50:309–321.

Coustenis, A., Lellouch, E., Maillard, J. P., and McKay, C. P. (1995). Titan's Surface: Composition and Variability from the Near-Infrared Albedo. *Icarus*, 118:87–104.

Cruikshank, D. P., Allamandola, L. J., Hartmann, W. K., Tholen, D. J., Brown, R. H., Matthews, C. N., and Bell, J. F. (1991). Solid C≡N Bearing Material on Outer Solar System Bodies. *Icarus*, 94:345–353.

Cruikshank, D. P., Owen, T. C., Ore, C. D., Geballe, T. R., Roush, T. L., de Bergh, C., Sandford, S. A., Poulet, F., Benedix, G. K., and Emery, J. P. (2005). A spectroscopic study of the surfaces of Saturn's large satellites: H_2O ice, tholins, and minor constituents. *Icarus*, 175:268–283.

Dimitrov, V. and Bar-Nun, A. (2002). Aging of Titan's Aerosols. *Icarus*, 156:530–538.

Domingue, D. and Verbiscer, A. (1997). Re-Analysis of the Solar Phase Curves of the Icy Galilean Satellites. *Icarus*, 128:49–74.

Elachi, C., Wall, S., Allison, M., Anderson, Y., Boehmer, R., Callahan, P., Encrenaz, P., Flamini, E., Franceschetti, G., Gim, Y., Hamilton, G., Hensley, S., Janssen, M., Johnson, W., Kelleher, K., Kirk, R., Lopes, R., Lorenz, R., Lunine, J., Muhleman, D., Ostro, S., Paganelli, F., Picardi, G., Posa, F., Roth, L., Seu, R., Shaffer, S., Soderblom, L., Stiles, B., Stofan, E., Vetrella, S., West, R., Wood, C., Wye, L., and Zebker, H. (2005). Cassini Radar Views the Surface of Titan. *Science*, 308:970–974.

Fulchignoni, M., Ferri, F., Angrilli, F., Ball, A. J., Bar-Nun, A., Barucci, M. A., Bettanini, C., Bianchini, G., Borucki, W., Colombatti, G., Coradini, M., Coustenis, A., Debei, S., Falkner, P., Fanti, G., Flamini, E., Gaborit, V., Grard, R., Hamelin, M., Harri, A. M., Hathi, B., Jernej, I., Leese, M. R., Lehto, A., Lion Stoppato, P. F., López-Moreno, J. J., Mäkinen, T., McDonnell, J. A. M., McKay, C. P., Molina-Cuberos, G., Neubauer,

F. M., Pirronello, V., Rodrigo, R., Saggin, B., Schwingenschuh, K., Seiff, A., Simões, F., Svedhem, H., Tokano, T., Towner, M. C., Trautner, R., Withers, P., and Zarnecki, J. C. (2005). In situ measurements of the physical characteristics of Titan's environment. *Nature*, 438:785–791.

Gendron, E., Coustenis, A., Drossart, P., Combes, M., Hirtzig, M., Lacombe, F., Rouan, D., Collin, C., Pau, S., Lagrange, A.-M., Mouillet, D., Rabou, P., Fusco, T., and Zins, G. (2004). VLT/NACO adaptive optics imaging of Titan. *A&A*, 417:L21–L24.

Griffith, C. A. (1993). Evidence for surface heterogeneity on Titan. *Nature*, 364:511–514.

Griffith, C. A. and Owen, T. (1990). The Possibility of Probing Titan's Surface in the Near IR. In *Bulletin of the American Astronomical Society*, pages 1084–+.

Griffith, C. A., Owen, T., Geballe, T. R., Rayner, J., and Rannou, P. (2003). Evidence for the Exposure of Water Ice on Titan's Surface. *Science*, 300:628–630.

Griffith, C. A., Penteado, P., Baines, K., Drossart, P., Barnes, J., Bellucci, G., Bibring, J., Brown, R., Buratti, B., Capaccioni, F., Cerroni, P., Clark, R., Combes, M., Coradini, A., Cruikshank, D., Formisano, V., Jaumann, R., Langevin, Y., Matson, D., McCord, T., Mennella, V., Nelson, R., Nicholson, P., Sicardy, B., Sotin, C., Soderblom, L. A., and Kursinski, R. (2005). The Evolution of Titan's Mid-Latitude Clouds. *Science*, 310:474–477.

Griffith, C. A., Penteado, P., Rannou, P., Brown, R., Boudon, V., Baines, K. H., Clark, R., Drossart, P., Buratti, B., Nicholson, P., McKay, C. P., Coustenis, A., Negrao, A., and Jaumann, R. (2006). Evidence for a Polar Ethane Cloud on Titan. *Science*, 313:1620–1622.

Grundy, W., Lemmon, M., Fink, U., Smith, P., and Tomasko, M. (1991). Windows Through Titan's Atmosphere? In *Bulletin of the American Astronomical Society*, page 1186.

Grundy, W. M., Schmitt, B., and Quirico, E. (2002). The Temperature-Dependent Spectrum of Methane Ice I between 0.7 and 5 μm and Opportunities for Near-Infrared Remote Thermometry. *Icarus*, 155:486–496.

Hapke, B. (1981). Bidirectional reflectance spectroscopy. I - Theory. *J. Geophys. Res.*, 86:3039–3054.

Hapke, B. (1984). Bidirectional reflectance spectroscopy. III - Correction for macroscopic roughness. *Icarus*, 59:41–59.

Hapke, B. (1986). Bidirectional reflectance spectroscopy. IV - The extinction coefficient and the opposition effect. *Icarus*, 67:264–280.

Hapke, B. (2002). Bidirectional Reflectance Spectroscopy 5. The Coherent Backscatter Opposition Effect and Anisotropic Scattering. *Icarus*, 157:523–534.

Hapke, B., Nelson, R., and Smythe, W. (1998). The Opposition Effect of the Moon: Coherent Backscatter *and* Shadow Hiding. *Icarus*, 133:89–97.

Hapke, B., Wells, E., Wagner, J., and Partlow, W. (1981). Far-UV, visible, and near-IR reflectance spectra of frosts of H_2O, CO_2, NH_3 and SO_2. *Icarus*, 47:361–367.

Helfenstein, P., Veverka, J., and Hillier, J. (1997). The Lunar Opposition Effect: A Test of Alternative Models. *Icarus*, 128:2–14.

Herschel, J. F. W. S. (1847). *Results of astronomical observations made during the years 1834, 5, 6, 7, 8, at the Cape of Good Hope; being the completion of a telescopic survey of the whole surface of the visible heavens, commenced in 1825.* London, Smith, Elder and co., 1847.

Irwin, P. G. J., Sromovsky, L. A., Strong, E. K., Sihra, K., Teanby, N. A., Bowles, N., Calcutt, S. B., and Remedios, J. J. (2006). Improved near-infrared methane band models and k-distribution parameters from 2000 to 9500 cm^{-1} and implications for interpretation of outer planet spectra. *Icarus*, 181:309–319.

Israël, G., Szopa, C., Raulin, F., Cabane, M., Niemann, H. B., Atreya, S. K., Bauer, S. J., Brun, J.-F., Chassefière, E., Coll, P., Condé, E., Coscia, D., Hauchecorne, A., Millian, P., Nguyen, M.-J., Owen, T., Riedler, W., Samuelson, R. E., Siguier, J.-M., Steller, M., Sternberg, R., and Vidal-Madjar, C. (2005). Complex organic matter in Titan's atmospheric aerosols from in situ pyrolysis and analysis. *Nature*, 438:796–799.

Israël, G., Szopa, C., Raulin, F., Cabane, M., Niemann, H. B., Atreya, S. K., Bauer, S. J., Brun, J.-F., Chassefière, E., Coll, P., Condé, E., Coscia, D., Hauchecorne, A., Millian, P., Nguyen, M. J., Owen, T., Riedler, W., Samuelson, R. E., Siguier, J.-M., Steller, M., Sternberg, R., and Vidal-Madjar, C. (2006). Astrochemistry: Complex organic matter in Titan's aerosols? (Reply). *Nature*, 444:E6.

Karkoschka, E. (1998). Methane, Ammonia, and Temperature Measurements of the Jovian Planets and Titan from CCD-Spectrophotometry. *Icarus*, 133:134–146.

Karkoschka, E., Tomasko, M. G., Doose, L. R., See, C., McFarlane, E. A., Schröder, S. E., and Rizk, B. (2007). DISR Imaging and the Geometry of the Descent of the Huygens Probe within Titan's Atmosphere. *Planet. Space Sci.*, 55:1896–1935.

Kossacki, K. J. and Lorenz, R. D. (1996). Hiding Titan's ocean: densification and hydrocarbon storage in an icy regolith. *Planet. Space Sci.*, 44:1029–1037.

Kuiper, G. P. (1944). Titan: a Satellite with an Atmosphere. *ApJ*, 100:378–+.

Lambert, J. H. (1760). *Photometria sive de mensura et gradibus luminis, colorum et umbrae*. Augsburg: Eberhard Klett; 547 p.

Lebreton, J.-P., Witasse, O., Sollazzo, C., Blancquaert, T., Couzin, P., Schipper, A.-M., Jones, J. B., Matson, D. L., Gurvits, L. I., Atkinson, D. H., Kazeminejad, B., and Pérez-Ayúcar, M. (2005). An overview of the descent and landing of the Huygens probe on Titan. *Nature*, 438:758–764.

Lellouch, E., Schmitt, B., Coustenis, A., and Cuby, J.-G. (2004). Titan's 5-micron lightcurve. *Icarus*, 168:209–214.

Lopes, R. M. C., Mitchell, K. L., Stofan, E. R., Lunine, J. I., Lorenz, R., Paganelli, F., Kirk, R. L., Wood, C. A., Wall, S. D., Robshaw, L. E., Fortes, A. D., Neish, C. D., Radebaugh, J., Reffet, E., Ostro, S. J., Elachi, C., Allison, M. D., Anderson, Y., Boehmer, R., Boubin, G., Callahan, P., Encrenaz, P., Flamini, E., Francescetti, G., Gim, Y., Hamilton, G., Hensley, S., Janssen, M. A., Johnson, W. T. K., Kelleher, K., Muhleman, D. O., Ori, G., Orosei, R., Picardi, G., Posa, F., Roth, L. E., Seu, R., Shaffer, S., Soderblom, L. A., Stiles, B., Vetrella, S., West, R. D., Wye, L., and Zebker, H. A. (2007). Cryovolcanic features on Titan's surface as revealed by the Cassini Titan Radar Mapper. *Icarus*, 186:395–412.

Lorenz, R. D. (1993). Wake-induced dust cloud formation following impact of planetary landers. *Icarus*, 101:165–167.

Lorenz, R. D. (1997). Impacts and cratering on Titan: a pre-Cassini view. *Planet. Space Sci.*, 45:1009–1019.

Lorenz, R. D. (2006). Thermal interactions of the Huygens probe with the Titan environment: Constraint on near-surface wind. *Icarus*, 182:559–566.

Lorenz, R. D., Niemann, H. B., Harpold, D. N., Way, S. H., and Zarnecki, J. C. (2006a). Titan's damp ground: Constraints on Titan surface thermal properties from the temperature evolution of the Huygens GCMS inlet. *Meteoritics & Planetary Science*, 41:1705–1714.

Lorenz, R. D., Wall, S., Radebaugh, J., Boubin, G., Reffet, E., Janssen, M., Stofan, E., Lopes, R., Kirk, R., Elachi, C., Lunine, J., Mitchell, K., Paganelli, F., Soderblom, L., Wood, C., Wye, L., Zebker, H., Anderson, Y., Ostro, S., Allison, M., Boehmer, R., Callahan, P., Encrenaz, P., Ori, G. G., Francescetti, G., Gim, Y., Hamilton, G., Hensley, S., Johnson, W., Kelleher, K., Muhleman, D., Picardi, G., Posa, F., Roth, L., Seu, R., Shaffer, S., Stiles, B., Vetrella, S., Flamini, E., and West, R. (2006b). The Sand Seas of Titan: Cassini RADAR Observations of Longitudinal Dunes. *Science*, 312:724–727.

Lunine, J. I., Elachi, C., Wall, S., Allison, M., Anderson, Y., Boehmer, R., Callahan, P., Encrenaz, P., Flamini, E., Franceschetti, G., Gim, Y., Hamilton, G., Hensley, S., Janssen, M., Johnson, W., Kelleher, K., Kirk, R., Lopes, R., Lorenz, R., Muhleman, D., Orosei, R., Ostro, S., Paganelli, F., Paillou, P., Picardi, G., Posa, F., Radebaugh, J., Roth, L., Seu, R., Shaffer, S., Soderblom, L., Stiles, B., Stofan, E., Vetrella, S., West, R., Wood, C., Wye, L., Zebker, H., Alberti, G., Karkoschka, E., Rizk, B., McFarlane, L., See, C., and Kazeminejad, B. (2007). Cassini radar's third and fourth looks at Titan. Submitted to *Icarus*.

Lunine, J. I. and Stevenson, D. J. (1987). Clathrate and ammonia hydrates at high pressure - Application to the origin of methane on Titan. *Icarus*, 70:61–77.

Lunine, J. I., Stevenson, D. J., and Yung, Y. L. (1983). Ethane Ocean on Titan. *Science*, 222:1229–1230.

McCord, T. B., Carlson, R., Smythe, W., Hansen, G., Clark, R., Hibbitts, C., Fanale, F., Granahan, J., Segura, M., Matson, D., Johnson, T., and Martin, P. (1997). Organics and other molecules in the surfaces of Callisto and Ganymede. *Science*, 278:271–275.

McCord, T. B., Hansen, G. B., Buratti, B. J., Clark, R. N., Cruikshank, D. P., D'Aversa, E., Griffith, C. A., Baines, E. K. H., Brown, R. H., Dalle Ore, C. M., Filacchione, G., Formisano, V., Hibbitts, C. A., Jaumann, R., Lunine, J. I., Nelson, R. M., Sotin, C., and the Cassini VIMS Team (2006). Composition of Titan's surface from Cassini VIMS. *Planet. Space Sci.*, 54:1524–1539.

McWorter, D. and Sunada, D. (1977). *Groundwater Hydrology and Hydraulics*. Water Resources Publications, Ft. Collins, CO.

Muhleman, D. O., Grossman, A. W., Butler, B. J., and Slade, M. A. (1990). Radar reflectivity of Titan. *Science*, 248:975–980.

Niemann, H. B., Atreya, S. K., Bauer, S. J., Carignan, G. R., Demick, J. E., Frost, R. L., Gautier, D., Haberman, J. A., Harpold, D. N., Hunten, D. M., Israel, G., Lunine, J. I., Kasprzak, W. T., Owen, T. C., Paulkovich, M., Raulin, F., Raaen, E., and Way, S. H. (2005). The abundances of constituents of Titan's atmosphere from the GCMS instrument on the Huygens probe. *Nature*, 438:779–784.

Owen, T. (2005). Planetary science: Huygens rediscovers Titan. *Nature*, 438:756–757.

Petrova, E. V., Markiewicz, W. J., and Keller, H. U. (2001). Regolith Surface Reflectance: A New Attempt to Model. *Solar System Research*, 35:278–290.

Pohn, H. A., Radin, H. W., and Wildey, R. L. (1969). The Moon's photometric function near zero phase angle from Apollo 8 photography. *ApJ*, 157:L193–L195.

Porco, C. C., Baker, E., Barbara, J., Beurle, K., Brahic, A., Burns, J. A., Charnoz, S., Cooper, N., Dawson, D. D., Del Genio, A. D., Denk, T., Dones, L., Dyudina, U., Evans, M. W., Fussner, S., Giese, B., Grazier, K., Helfenstein, P., Ingersoll, A. P., Jacobson, R. A., Johnson, T. V., McEwen, A., Murray, C. D., Neukum, G., Owen, W. M., Perry, J., Roatsch, T., Spitale, J., Squyres, S., Thomas, P., Tiscareno, M., Turtle, E. P., Vasavada, A. R., Veverka, J., Wagner, R., and West, R. (2005). Imaging of Titan from the Cassini spacecraft. *Nature*, 434:159–168.

Richardson, J., Lorenz, R. D., and McEwen, A. (2004). Titan's surface and rotation: new results from Voyager 1 images. *Icarus*, 170:113–124.

Rodriguez, S., Le Mouélic, S., Sotin, C., Clénet, H., Clark, R. N., Buratti, B., Brown, R. H., McCord, T. B., Nicholson, P. D., Baines, K. H., and the VIMS Science Team (2006). Cassini/VIMS hyperspectral observations of the HUYGENS landing site on Titan. *Planet. Space Sci.*, 54:1510–1523.

Roe, H. G., Brown, M. E., Schaller, E. L., Bouchez, A. H., and Trujillo, C. A. (2005). Geographic Control of Titan's Mid-Latitude Clouds. *Science*, 310:477–479.

Roush, T. L. and Dalton, J. B. (2004). Reflectance spectra of hydrated Titan tholins at cryogenic temperatures and implications for compositional interpretation of red objects in the outer Solar System. *Icarus*, 168:158–162.

Sagan, C. and Dermott, S. F. (1982). The tide in the seas of Titan. *Nature*, 300:731–733.

Sagan, C. and Khare, B. N. (1979). Tholins - Organic chemistry of interstellar grains and gas. *Nature*, 277:102–107.

Schaller, E. L., Brown, M. E., Roe, H. G., and Bouchez, A. H. (2006). A large cloud outburst at Titan's south pole. *Icarus*, 182:224–229.

Shkuratov, Y., Ovcharenko, A., Zubko, E., Miloslavskaya, O., Muinonen, K., Piironen, J., Nelson, R., Smythe, W., Rosenbush, V., and Helfenstein, P. (2002). The Opposition Effect and Negative Polarization of Structural Analogs for Planetary Regoliths. *Icarus*, 159:396–416.

Smith, P. H., Lemmon, M. T., Lorenz, R. D., Sromovsky, L. A., Caldwell, J. J., and Allison, M. D. (1996). Titan's Surface, Revealed by HST Imaging. *Icarus*, 119:336–349.

Sotin, C., Jaumann, R., Buratti, B. J., Brown, R. H., Clark, R. N., Soderblom, L. A., Baines, K. H., Bellucci, G., Bibring, J.-P., Capaccioni, F., Cerroni, P., Combes, M., Coradini, A., Cruikshank, D. P., Drossart, P., Formisano, V., Langevin, Y., Matson, D. L., McCord, T. B., Nelson, R. M., Nicholson, P. D., Sicardy, B., Lemouelic, S., Rodriguez, S., Stephan, K., and Scholz, C. K. (2005). Release of volatiles from a possible cryovolcano from near-infrared imaging of Titan. *Nature*, 435:786–789.

Stofan, E. R., Elachi, C., Lunine, J. I., Lorenz, R. D., Stiles, B., Mitchell, K. L., Ostro, S., Soderblom, L., Wood, C., Zebker, H., Wall, S., Janssen, M., Kirk, R., Lopes, R., Paganelli, F., Radebaugh, J., Wye, L., Anderson, Y., Allison, M., Boehmer, R., Callahan, P., Encrenaz, P., Flamini, E., Francescetti, G., Gim, Y., Hamilton, G., Hensley, S., Johnson, W. T. K., Kelleher, K., Muhleman, D., Paillou, P., Picardi, G., Posa, F., Roth, L., Seu, R., Shaffer, S., Vetrella, S., and West, R. (2007). The lakes of Titan. *Nature*, 445:61–64.

Stofan, E. R., Lunine, J. I., Lopes, R., Paganelli, F., Lorenz, R. D., Wood, C. A., Kirk, R., Wall, S., Elachi, C., Soderblom, L. A., Ostro, S., Janssen, M., Radebaugh, J., Wye, L., Zebker, H., Anderson, Y., Allison, M., Boehmer, R., Callahan, P., Encrenaz, P., Flamini, E., Francescetti, G., Gim, Y., Hamilton, G., Hensley, S., Johnson, W. T. K., Kelleher, K., Muhleman, D., Picardi, G., Posa, F., Roth, L., Seu, R., Shaffer, S., Stiles, B., Vetrella, S., and West, R. (2006). Mapping of Titan: Results from the first Titan radar passes. *Icarus*, 185:443–456.

Strong, K., Taylor, F. W., Calcutt, S. B., Remedios, J. J., and Ballard, J. (1993). Spectral parameters of self- and hydrogen-broadened methane from 2000 to 9500 cm^{-1} for remote sounding of the atmosphere of Jupiter. *Journal of Quantitative Spectroscopy and Radiative Transfer*, 50:363–429.

Tobie, G., Lunine, J. I., and Sotin, C. (2006). Episodic outgassing as the origin of atmospheric methane on Titan. *Nature*, 440:61–64.

Tokano, T. (2005). Meteorological assessment of the surface temperatures on Titan: constraints on the surface type. *Icarus*, 173:222–242.

Tokano, T., McKay, C. P., Neubauer, F. M., Atreya, S. K., Ferri, F., Fulchignoni, M., and Niemann, H. B. (2006). Methane drizzle on Titan. *Nature*, 442:432–435.

Tomasko, M., Doose, L., Engel, S., Dafoe, L. E., West, R., Lemmon, M., Karkoschka, E., and See, C. (2007). A model of Titan's aerosols based on measurements made inside the atmosphere. Submitted to *P&SS*.

Tomasko, M. G., Archinal, B., Becker, T., Bézard, B., Bushroe, M., Combes, M., Cook, D., Coustenis, A., de Bergh, C., Dafoe, L. E., Doose, L., Douté, S., Eibl, A., Engel, S., Gliem, F., Grieger, B., Holso, K., Howington-Kraus, E., Karkoschka, E., Keller, H. U., Kirk, R., Kramm, R., Küppers, M., Lanagan, P., Lellouch, E., Lemmon, M., Lunine, J., McFarlane, E., Moores, J., Prout, G. M., Rizk, B., Rosiek, M., Rueffer, P., Schröder, S. E., Schmitt, B., See, C., Smith, P., Soderblom, L., Thomas, N., and West, R. (2005). Rain, winds and haze during the Huygens probe's descent to Titan's surface. *Nature*, 438:765–778.

Tomasko, M. G., Buchhauser, D., Bushroe, M., Dafoe, L. E., Doose, L. R., Eibl, A., Fellows, C., Farlane, E. M., Prout, G. M., Pringle, M. J., Rizk, B., See, C., Smith, P. H., and Tsetsenekos, K. (2002). The Descent Imager/Spectral Radiometer (DISR) Experiment on the Huygens Entry Probe of Titan. *Space Science Reviews*, 104:469–551.

Tomasko, M. G. and Smith, P. H. (1982). Photometry and polarimetry of Titan - Pioneer 11 observations and their implications for aerosol properties. *Icarus*, 51:65–95.

Towner, M. C., Garry, J. R. C., Lorenz, R. D., Hagermann, A., Hathi, B., Svedhem, H., Clark, B. C., Leese, M. R., and Zarnecki, J. C. (2006). Physical properties of Titan's surface at the Huygens landing site from the Surface Science Package Acoustic Properties sensor (API-S). *Icarus*, 185:457–465.

Wilson, L. (1973). A photometric investigation of the packing state of Apollo 11 lunar regolith samples. *Planet. Space Sci.*, 21:113–118.

Yung, Y. L., Allen, M., and Pinto, J. P. (1984). Photochemistry of the atmosphere of Titan - Comparison between model and observations. *ApJS*, 55:465–506.

Zarnecki, J. C., Leese, M. R., Hathi, B., Ball, A. J., Hagermann, A., Towner, M. C., Lorenz, R. D., McDonnell, J. A. M., Green, S. F., Patel, M. R., Ringrose, T. J., Rosenberg, P. D., Atkinson, K. R., Paton, M. D., Banaszkiewicz, M., Clark, B. C., Ferri, F., Fulchignoni, M., Ghafoor, N. A. L., Kargl, G., Svedhem, H., Delderfield, J., Grande, M., Parker, D. J., Challenor, P. G., and Geake, J. E. (2005). A soft solid surface on Titan as revealed by the Huygens Surface Science Package. *Nature*, 438:792–795.

Publications

Tomasko, M. G., Archinal, B., Becker, T., Bézard, B., Bushroe, M., Combes, M., Cook, D., Coustenis, A., de Bergh, C., Dafoe, L. E., Doose, L., Douté, S., Eibl, A., Engel, S., Gliem, F., Grieger, B., Holso, K., Howington-Kraus, E., Karkoschka, E., Keller, H. U., Kirk, R., Kramm, R., Küppers, M., Lanagan, P., Lellouch, E., Lemmon, M., Lunine, J., McFarlane, E., Moores, J., Prout, G. M., Rizk, B., Rosiek, M., Rueffer, P., Schröder, S. E., Schmitt, B., See, C., Smith, P., Soderblom, L., Thomas, N., and West, R. (2005) Rain, winds and haze during the Huygens probe's descent to Titan's surface. *Nature*, 438: 765-778

Karkoschka, E., Tomasko, M. G., Doose, L. R., See, C., McFarlane, E. A., Schröder, S. E., and Rizk, B. (2007) DISR Imaging and the Geometry of the Descent of the Huygens Probe within Titan's Atmosphere. *Planet. Space Sci.*, 55: 1896-1935

Schröder, S. E. and Keller, H. U. (2007) The reflectance spectrum of Titan's surface at the Huygens landing site determined by the Descent Imager/Spectral Radiometer. Accepted by *Planet. Space Sci.*

Keller, H. U., Grieger, B., Küppers, M., Schröder, S. E., Skorov, Y. V., and Tomasko, M. G. (2007) The properties of Titan's surface at the Huygens landing site from DISR observations. Accepted by *Planet. Space Sci.*

Acknowledgements

For some, the Ph.D. years are a time of toil and hardship, but for me it was more a time of adventure. I explored a new world (Titan!), traveled to exotic places (Tucson!), and met with legendary scientists (who turned out to be normal people!). That night in Darmstadt when Huygens landed, and when we first saw images from the surface of Titan in that cramped Portacabin was a high point in my life. For this I first and foremost thank my main supervisor Horst Uwe Keller. Herr Keller, you gave me the freedom and resources I needed, and, despite your busy schedule, always found time to discuss my work. One of those defining moments that inspired me to become a planetary scientist was the Giotto flyby of comet Halley in 1986. I vividly remember seeing those colorful (and unintelligible) images live on TV, so thank you for that too. I am also grateful to my other supervisors Michael Küppers and Björn Grieger. Michael, thank you for your active interest in my work and progress. You too always found time for discussion, and I learned from your insights. Furthermore I wish to thank my supervisor at the Georg August Universtität Andreas Tilgner, and the other members of my defense committee: Wolfram Kollatschny, Franz Kneer, Helmut Grubmüller, and Stephan Herminghaus.

During my frequent visits to the LPL of the University of Arizona in Tucson, I enjoyed the hospitality and support of the entire DISR team. I am very grateful to Martin Tomasko, P.I. of the wonderful DISR camera. Many thanks go to Chuck See, for helping me with the DISR#2 experiments, Erich Karkoschka, for valuable discussions and some great hikes around Tucson, and to the other team members: Mike Bushroe, Lyn Doose, Andrew Eibl, Steffi Engel, Katie Holso, Lisa McFarlane, Mike Prout, and Bashar Rizk. I also want to express my gratitude to the French DISR team members: Bernard Schmitt for his hospitality during my visit to the LPG in Grenoble and the calibration target reflectance measurements, Eric Quirico for the tholin sample, Emmanuel Lellouche for the water absorption line strengths, and Bruno Bézard for the recalculated surface reflectances.

In the last three years I have been a member of the International Max Planck Research School (IMPRS) of the MPS. I am grateful to IMPRS coordinator Dieter Schmitt, and the MPS administration (Sabine Stelzer und die Damen der Verwaltung) for their help and support. I also want to thank my present and former office mates Martin Tschimmel, Pedro Russo, Kristofer Hallgren, and Maxim Kramar for the nice atmosphere. Life in the institute is enriched by the presence of many Ph.D. students and postdocs. Thank you all for your enjoyable companionship! And I am looking forward to playing football for many more years.

Finally, I want to thank Huib Henrichs of the Astronomical Institute 'Anton Pannekoek' in Amsterdam for his suggestion to join the IMPRS, my parents for their moral and financial support, and Lisa for being so nice!

Curriculum Vitae

Persönliche Daten

Name: Stefanus Ewoud Schröder
Geburtsdatum: 13. Juni 1970
Geburtsort: Amsterdam, Die Niederlande
Staatsangehörigkeit: holländisch

Schulausbildung

1976 - 1982   Grundschule *Paus Johannes XIII*, Alkmaar, Die Niederlande
1982 - 1988   V.W.O. (Gymnasium) *Bonhoeffer College*, Castricum,
                          Die Niederlande

Studium

1988 - 1994   M.Sc. Biologie, *Vrije Universiteit* (VU), Amsterdam,
                          Die Niederlande
1997 - 2003   M.Sc. Astronomie, *Universiteit van Amsterdam* (UvA),
                          Amsterdam, Die Niederlande
2004 - 2007   Ph.D. Geophysik, Georg-August-Universität, Göttingen, und
                          Max-Planck-Institut für Sonnensystemforschung (MPS),
                          Katlenburg-Lindau

Berufserfahrung

1995 - 1997   Biomathematiker, *Rijksinstitut voor Kust en Zee* (RIKZ),
                          Den Haag, Die Niederlande